MEASUREMENTS AND TIME EVOLUTION OF ATOMIC AND MOLECULAR HYDROGEN IN INTERSTELLAR CLOUDS

A Dissertation

Presented to the Faculty of the Graduate School

of Cornell University

in Partial Fulfillment of the Requirements for the Degree of

Doctor of Philosophy

by

Marko Krčo

May 2015

MEASUREMENTS AND TIME EVOLUTION OF ATOMIC AND MOLECULAR HYDROGEN IN INTERSTELLAR CLOUDS

Marko Krčo, Ph.D.

Cornell University 2015

The timescale over which molecular clouds collapse to form stars is of intense scientific interest. It reflects the support mechanisms which slow collapse such as angular momentum, thermal pressure, turbulence, and ambipolar diffusion, and impacts the chemical make up of the resulting stars and surrounding planets. In this doctoral thesis we obtain lower age limits for a set of molecular clouds by studying the ratio between atomic and molecular hydrogen gas. Clouds are initially entirely, or almost entirely composed of atomic hydrogen (HI), but by the time they form stars they are almost entirely composed of molecular hydrogen (H_2). We measure H_2 column densities using ^{13}CO and dust extinction as tracers. In the clouds' interiors, the HI gas is sufficiently shielded from the external radiation field that it cools to temperatures of approximately 10K to 50K, at which point it can absorb the background 21 cm emission from the warm galactic ISM. This HI Narrow Self-Absorption (HINSA) is simple to observe, yet difficult to analyze due to the complexity of the background emission. We present a novel new method of analyzing HINSA spectra which for the first time offers sufficient confidence in the derived column densities that a more sophisticated analysis of the HI/H_2 ratio in clouds could be undertaken. We have performed the largest survey of HINSA in clouds carried out to date using the Green Bank Telescope (GBT), and the Five College Radio Observatory (FCRAO). We establish HINSA as a useful tool, and with the large body

of data acquired, can move to determine the ages of several clouds. We discovered that the observed HINSA column densities were highly dependent on the unknown shape and orientation of each cloud. Thus we developed a geometry-independent method of determining the density distribution function of molecular clouds. A geometry-independent chemical model then allowed us to determine the lower limits to the ages of 23 clumps within 9 molecular clouds.

BIOGRAPHICAL SKETCH

Marko Krčo was born February 6th, 1980 in Bečej, Yugoslavia. He moved to New York City with his family in search of a better life on Columbus Day, 1991. He was proud to be accepted into the Bronx High School of Science in 1993. In 1994 his family and he opened Krcho Wholesale Inc., allowing them to pursue the American Dream. His family received green cards through the lottery in 1995. He co-founded Web Page Creations, inc. in 1997 with Nigel Singh. They disbanded the company in order to pursue higher education. Marko was admitted to Colgate University as a Physics and Astronomy major. To pay for college, he held a variety of jobs ranging from dish washer at Donovan's Pub, to a campus safety officer, assistant to the fire chief, and even as a "financial adjuster" at Chrysler Financial. Ultimately he relied on his entrepreneurial skills. In 1998, he purchased, renovated, and resold Bay View Deli on City Island, Bronx, NY. In 1999 he negotiated an agreement with Colgate University through which they would support him in rebuilding a defunct campus business (Cecelie's Coffee House) with funds, and a legal umbrella under the condition that he would return ownership of the premises to the University upon graduation. In 2000 he founded the Colgate Student Charity Program, a non-profit organization comprised mostly of student volunteers who collected funds locally to sponsor needy children overseas. His first scientific research was to measure the rotational period of the asteroid 202 Chryseis with Stephen Slivan in 2000. He then continued working with Dr. Slivan on determining the spin solutions of the Koronis family of Asteroids. A paper in Nature was published as a result of this research, and Marko received the 1894 Colgate University Department Founders Award. In 2001, he was accepted as an REU student at the Arecibo Observatory, where he worked with Snezana Stanimirovic on 21 cm mapping

of the Magellanic Stream. Expanding his interests, he developed a theoretical multi-party quantum clock synchronization protocol in collaboration with Prabasaj Paul. This research resulted in his first peer-reviewed paper as primary author. The protocol is currently being used to construct the first quantum communications networks, and the first generation of quantum computers. In 2002, Marko was proud to be accepted as a doctoral student at Cornell University. In 2004, he worked with Paul F. Goldsmith on determining the observability of ultra-cold CH in molecular clouds. In 2005, they began working on this doctoral thesis research. In 2010, his family began experiencing difficulties with Krcho Wholesale. Marko thus was forced to pause his research and assist his parents, by helping them to retire. He returned to NYC and liquidated his property to contribute to their retirement. In 2013 they used their available funds to purchase an apartment building (under Star M. Properties, LLC) that would provide sufficient retirement income for his family. They then executed a merger between Krcho Wholesale Inc, and Harold Levinson Associates. In 2014, Star M. Properties, LLC was sufficiently well established that Marko could delegate responsibilities and return to research, whereupon this thesis was completed.

Mojoj majci, koja me je lepo slagala kad nisam hteo ići na prvi dan prvog razreda: "Ajde bre, samo ćeš jednom morati da ideš, it to za samo 45 minuta. Posle nikad nećes morati nazad u školu ponovo. Posle 28 godina ....

Mom ocu, koji me je večito vodio na dolmu i uvek me učio o svetu.

Polu, koji je uvek u mom srcu. Deo njega je u svemu što radim.

I svim nama bivšim Jugoslovenima, kojima je vaznije kakav je čovek nego odakle je. Možemo bilo šta dostignuti.

To my mother, who lied to me when I didn't want to go on my first day of first grade by saying: "You'll only have to go once, for 45 minutes. Then it'll be over and you'll never have to go to school again". 28 years later...

To my father, who took me on all those walks to the Tisa river, and inspired me to seek to understand the world around me.

To Paul Spector, who is with me always.

To my friends, who stood by me even during the most difficult times.

Ultimately, to Paul F. Goldsmith for having the patience to work with me for 11 long years. And for helping out a nervous, lonesome undergrad at his first AAS.

ACKNOWLEDGEMENTS

This research was supported in part by the National Science Foundation through grants AST 0404770 and AST 0407019, as well as the National Radio Astronomy Observatory Student Support Program. The research was carried out at the Jet Propulsion Laboratory, California Institute of Technology, under a contract with the National Aeronautics and Space Administration. The data used in this paper were obtained with the Five College Radio Observatory which is supported by the National Science Foundation with permission of the Metropolitan District Commission, and with the Greenbank Telescope of the National Radio Astronomy Observatory.

We thank Mark Heyer and Jay Lockman for assistance in carrying out the observations at the FCRAO and the GBT. We thank Rebecca Oppenheimer and the American Museum of Natural History for providing a working environment where a portion of this work could be completed.

The program used for regridding the data in this work was modified from the original version developed by Tim Robishaw. The research makes use of the MPFIT program designed by C.B. Markwardt.

TABLE OF CONTENTS

LIST OF TABLES

LIST OF FIGURES

CHAPTER 1

INTRODUCTION

The general picture of star formation is felt to be well understood. Diffuse gas and dust are compressed or coalesce into clouds which are dense enough to collapse under their own gravity and eventually form stars. However, many of the details of this picture are poorly known. Of special importance is the process of evolution from the point of sufficient self-shielding to produce molecules, to the point where gravitational collapse is inevitable. Which support mechanisms - thermal pressure, turbulence, magnetic fields - exist to prevent or slow down collapse has a direct bearing on the star formation rate and the mass distribution of the stars that are formed. Another question is the composition of the stellar nebula, as it relates to the prevalence and composition of any planetary bodies, comets, asteroids, etc. that are formed in the resulting solar systems. A key question is the abundance of water and other building blocks which might condense onto smaller bodies and eventually be deposited onto planets. The chemical processes in molecular clouds are thus of significant interest, as are the conditions within such clouds. By the time stars are formed, clouds have almost entirely converted their atomic hydrogen (HI) into molecular form (H_2). But what about other molecules, such as water, poly-aromatic hydrocarbons (PAHs), or complex organic molecules? We can observationally measure the abundances of many molecules that are present in the gas phase, but what about those which are stuck on dust grains?

A common thread in these two lines of inquiry is the question of how long the collapse process takes. The support mechanisms directly influence the collapse time, which is inversely proportional to the star formation rate. Con-

straints on the collapse timescale provide limits on the support mechanisms, thus helping us determine the basic conditions (density, temperature, pressure, etc.) within the molecular clouds during collapse. Ambipolar diffusion, which is the process by which material falls into the center of a cloud that is supported by magnetic pressure, offers an excellent example. The ambipolar diffusion rate (dependent on magnetic field strength, ionization rate, etc.) and the collapse time have a direct influence on how star and planet formation proceed. After collapsing sufficiently to be shielded from the external UV-field, molecular clouds become increasingly chemically complex. A key question then is just how much time is available for those processes to take place, and thus determine the abundances of complex molecules, stars, and planets.

The processes within molecular clouds are highly inter-dependent and ultimately determine the availability of the building blocks of life in the resultant star systems. Observational measurement of the collapse timescale would provide a critical piece of information toward understanding these processes. Cloud ages, and the collapse timescale have long been studied ([Shu (1973), Heiles et al. (1988), van der Werf et al. (1988)], and many others). Advances in observational techniques have renewed intense recent interest in the field. [Goldsmith & Li (2005), Pineda et al. (2010), Pagani et al. (2013), Brunken et al. (2014)] represent some of the most recent efforts to measure cloud ages using four independent methods: the atomic to molecular Hydrogen ratio, ^{13}CO depletion onto dust grains, deuterium fractionation of N_2H^+, and the ratio of ortho-H_2D^+ to para-H_2D^+ respectively. It is the goal of this research to provide constraints on this particular piece of the puzzle. We do this by observing the abundance of HI in molecular clouds which have not yet begun forming stars. In this chapter we describe fundamental concepts, the state of understanding in

the field prior to the beginning of this research, an outline of how to obtain such timescale estimates, and a description of the specific questions which we aim to answer. While general descriptions are included here, more detailed discussions are included in the Introductory section of each of the subsequent chapters.

1.1 Fundamental Concepts and the State of Knowledge in the Field

The diffuse Interstellar Medium (ISM) consists primarily of atomic gas and dust. Temperature and the radiation field (primarily in the UV) inhibit the existence of any significant quantities of molecular gas. As clouds collapse their column density increases, thus providing shielding in the interior. This typically occurs as extinction due to dust reaches approximately 1 magnitude ($A_v \approx 1$). The dust extinction permits for the formation and persistence of molecules. In this regime, molecular lines become the dominant cooling mechanism, further enabling collapse. $A_v \approx 1$ forms a convenient boundary by which to define the birth of a molecular cloud. It is not clear how long it takes for a cloud to collapse from the diffuse ISM to a state where it has $A_v \approx 1$. Nor is it certain that all clouds which reach $A_v \approx 1$ will collapse to form stars, in fact it seems likely that many never do so. Depending on support mechanisms it is also possible that clouds may "hang around" for an extended period of time with $A_v > 1$ before ultimately collapsing and forming stars.

What is clear however, is that the clouds which we do observe with $A_v > 1$ are composed almost entirely of molecular Hydrogen (H_2), hence they are called molecular clouds. This was evident since the very earliest observations of the

ISM and immediately raises the question of how did such a state come about if H_2 cannot persist in the diffuse ISM. All clouds must have begun composed entirely, or almost entirely of atomic Hydrogen (HI), and over time must convert that HI to H_2. Part of the answer lies in the ability of H_2 to shield itself against photodestruction (self-shielding). Another part is the process by which atomic hydrogen is converted to H_2. The obvious avenue of study is to look at the ratio of HI to H_2 in existing clouds in order to understand their age. As we will describe, this has been a field of intense study since the 1950s, but the effort has been hampered by a number of serious challenges which must first be overcome.

Two body formation of H_2 by radiative association of two hydrogen atoms is extremely slow [Bates (1951), Latter & Black (1991)]. In the universe today, dust grains act as a catalytic surface on which two hydrogen atoms can get rid of excess angular momentum and form an H_2 molecule. Since the size distribution and composition of dust particles in the ISM is poorly known, and likely variable over time throughout the lifetime of a cloud, the HI to H_2 conversion rate is difficult to estimate [Hollenbach & Salpeter (1971)](also see Appendix A of [Goldsmith & Li (2005)]). Section 6 of [Goldsmith & Li (2005)] gives a comprehensive treatment of the H_2 formation process, and in this work we adopt the same value for the formation rate coefficient ($k_{H_2} = 1.2 cm^3 s^{-1}$) such that the H_2 formation rate due to dust grains can be described by

$$R_{H_2} = k_{H_2} n_{HI} n_0 \ , \tag{1.1}$$

where n_0, and n_{HI} represent total proton and HI number densities. Thus the rate of H_2 formation is dependent on density squared. As a cloud collapses

sufficiently to provide shielding from the external UV field, the highest density regions of the cloud will convert their HI to H_2 more quickly than the outer, more diffuse regions. As a result we should see a variation in the HI to H_2 abundance not only as a function of time, but also as a function of position within a cloud. Therefore it is necessary for us to obtain maps of both HI and H_2 within a cloud in order to determine its age.

H_2 has no observable emission lines in the temperature regime present within shielded molecular clouds (10 - 100 K), and there are insufficient background sources to map an entire cloud in H_2 absorption. Therefore we must use H_2 tracers such as ^{13}CO emission, or total proton column densities derived from stellar reddening due to dust extinction. Both methods are employed in this research, where appropriate. The strengths and weaknesses of each method are described in detail in subsequent chapters.

The HI content of these clouds is much more difficult to determine however. Since HI is the most common constituent of the ISM, the 21 cm emission line is present across most of the sky and especially along lines of sight near the galactic plane. Therefore, when observing at 21cm wavelengths toward the direction of a particular cloud it is difficult to determine which portion of the observed HI belongs to a given cloud and not foreground or background material. One way to isolate the HI gas associated with a particular cloud is to examine HI self-absorption. Most of the background HI emission in the galaxy is due to the warm ISM ($\approx$ 100K). The HI gas in a cloud's interior is shielded from the external UV field, and is thus cools along with the rest of the cloud's gas to temperatures of 10K - 50K. The cool foreground HI gas within molecular clouds will then absorb the background 21cm emission from warm, galactic HI to produce

HI Self-Absorption (HISA). This phenomenon has long been studied, with the aim of determining the HI abundance of molecular clouds.

[Garzoli & Varsavsky (1966)] were the first to discover that observed HI column densities decreased in regions of high extinction (an observation which is also reflected in Figure 3.10b). [Heiles (1969)] found clear evidence for self-absorption during a larger survey with a narrow absorption feature over a wider emission line in a source in Taurus. [Shu (1973)] was among the first to point out that the HI observed in molecular clouds may in fact be a remnant of the formation process. The possibility of detecting remnant HI spurred many surveys since that time which are detailed in subsequent chapters. However, they were all plagued by difficulties arising from the nature of the background HI emission.

HI is the most common constituent of the ISM. As such, 21 cm emission is evident to some degree at all directions, most especially near the galactic plane. The 21 cm emission arises from so many sources that its on-sky, and kinematic structure can be quite complex with many emission components often superimposed over one another along the same line of sight. Further, the emission lines can be tens of km/sec wide due to turbulence, the low mass of the hydrogen atom and the temperature of the warm ISM. The many studies of HISA could detect localized reductions in HI emission, but it is difficult to determine whether individual reductions are just due to temperature variations, kinematic effects, or simply the result of the superposition of two or more velocity components [Gibson et al. (2000), Kavars et al. (2003)]. Interferometric maps, like the one by [van der Werf et al. (1988)] of L134, help to ascribe specific HISA features to individual molecular clouds with a fair degree of certainty due to correlation

with sky position.

With improved observations it became possible to directly correlate HISA features with molecular emission arising from individual clouds. [Li & Goldsmith (2003)] were the first to use the term HI Narrow Self-Absorption (HINSA) to describe those HISA features which correlated strongly in sky position, center velocity, and non-thermal linewidth with molecular emission from constituents such as OH,^{12}CO,^{13}CO,$C^{18}O$, and others. As such, HINSA features form a subset of HISA which can be attributed with high confidence to the cold HI gas present in the interiors of molecular clouds. [Li & Goldsmith (2003)] found that ^{13}CO emission was most closely correlated to HINSA features in sky position, center velocity, and non-thermal linewidth. They focused their survey on clouds located within the relatively nearby (140 pc) Taurus Molecular Cloud Complex, where they found that 77% of the observed positions with molecular emission showed HINSA features. They found that the HINSA column densities, when compared to the total proton column densities, are of order 10^{-3}. Their survey revealed that in general HINSA abundances were lower in the central, densest regions of molecular clouds which is consistent with the expected dependence of the H_2 formation rate on density.

[Goldsmith & Li (2005)] applied a chemical model to estimate cloud ages. This model consisted only of H_2 formation on dust grains, and dissociation by cosmic rays. The model could not account for the change in density over time as a cloud may have collapsed, and thus formed only a lower limit on the age estimate. The same constraint was necessary for this research, as discussed in Chapter 5. Since energetic cosmic rays are able to penetrate even into the densest regions of molecular clouds, they found that a certain steady state volume

number density for cold HI ($\approx 2\ cm^{-3}$) should exist even in clouds which have already completed their conversion process. They used the on-sky cloud sizes to estimate depths, and the resulting volume densities. This methodology led them to conclude that all of the clouds in their survey exhibited HINSA abundances at, or near steady-state values. Thus it was difficult to assign age estimates to those clouds, leading to one of the major motivations for this research: to find clouds which exhibited HINSA abundances higher than steady-state.

[Goldsmith et al. (2007)] improved upon the previous chemical model from [Goldsmith & Li (2005)] by including photo-dissociation from external UV-fields using a one-dimensional slab model with variable density and temperature. They found that within 10^5 years the densest core regions of a cloud would convert nearly all of their HI to H_2, however it would take approximately 10^7 years for an entire cloud to reach steady state. Since [Goldsmith & Li (2005)] found that all of their clouds were near steady-state, they concluded that 10^7 years could be used as a minimum age for these clouds. They defined age as the time since the clouds first collapsed sufficiently to provide shielding and begin forming molecules. We use a similar definition in our study. Further, they modelled the expected 21 cm line profiles and how they might evolve over time. They were particularly interested in searching for young clouds which had not yet reached steady-state, and discovered that according to their models young clouds should exhibit a characteristic double-dip HINSA feature. This expected feature was due to remnant, warm HI within the modelled clouds which would exhibit a wider emission feature along with the narrower absorption feature. At that time, and in subsequent observations (including the survey presented here), no clear, convincing examples of such features were found. Therefore it was necessary to conduct further surveys, and devise other methods to search

for young clouds.

While Helium is a major constituent of molecular clouds, they do not directly affect the evolution of the HI to H_2 ratio in any known manner aside from its contribution to the total proton count and the resultant effects on the H_2 formation rate. We have thus chosen to omit Helium from the following discussion, except where it is accounted for by the total proton count.

The above section describes in general terms the state of knowledge in the field at the time when this doctoral research began. More detailed discussions are included in subsequent chapters. Several motivations were borne out of the previous efforts, and are described in the following section.

1.2 Questions, and Motivations

While HISA had been a long studied phenomenon, very few HISA features could be attributed to molecular clouds due to a lack of accompanying molecular data. Therefore, HINSA features were only identified in a small number of nearby ($\leq$ 200 pc) clouds, most of which were located within the Taurus Molecular Cloud Complex. It had long been expected [van der Werf et al. (1988)] that foreground HI emission would attenuate HISA features, leading to a maximum distance at which HISA (and HINSA) features could be detected. Before any large, comprehensive study utilizing HINSA features such as this one could be undertaken it was important to first establish HINSA as a viable tool of study and understand its limitations and constraints. This led to the first set of questions which this research aimed to answer:

- **Are HINSA features visible in other regions, and complexes?**

  The first observations were constrained mostly to the Taurus Molecular Clouds Complex, and a small number of other nearby clouds (like L134). It was important to first establish that HINSA features are not a peculiarity of these regions, and whether they might exist within isolated clouds not part of larger complexes.

- **Is there a maximum distance at which HINSA features are detectable within the Galaxy?**

  All previous HINSA detections were in clouds within approximately 200 pc. As foreground HI emission would increase with distance, searching for HINSA at greater distances would require a new survey.

- **Are HINSA features detectable at high latitudes? How does the background emission affect HINSA detections?**

  The strength of the background 21 cm emission is expected to affect the visibility of any HINSA features. It was unknown whether high-latitude clouds (with little background emission) would still exhibit HINSA.

- **What fraction of clouds with molecular emission exhibit HINSA features?**

  The data in [Li & Goldsmith (2003)] and [Goldsmith & Li (2005)] presented the first survey of HINSA sources. While they were confined to the Taurus Molecular Cloud Complex they found that 23% of their clouds did not exhibit HINSA features. Since the reasons for these non-detections are unknown, it was important to establish whether this ratio persisted outside of Taurus.

- **Are there any nearby HI emission sources which might obscure HINSA features from particular directions?**

Since no large survey existed, it was not possible to tell whether HINSA detectability might depend on sky position.

Only once HINSA could be established as a viable tool for large-scale study, could we consider using it for more sophisticated analysis. Previous methods, such as those employed by [Li & Goldsmith (2003)] and others used mathematical functions fitted over the observed 21 cm spectra to derive HINSA column densities. These methods all suffered from uncertainties inherent in selecting masking regions, and the choice of functions fitted. These choices could significantly alter the measured HINSA column densities, and as a result the confidence in the results was so low as to discourage further analysis based on those results. We developed an improved technique, which is not only independent of fitting functions, but is capable of measuring HINSA column densities from multiple, overlapping velocity components along the same line of sight. With this new ability we could begin an analysis that allows for further fundamental questions to be answered.

- **Do clouds within complexes share similar HINSA abundances?**

  If cloud complexes are formed through a single event, such as a shock wave, we might expect that individual clouds within a complex will have similar ages and thus similar HINSA abundances.

- **Do different components within a cloud exhibit the same HINSA abundances?**

  Most clouds exhibit multiple velocity components along the same line of sight. If the gas is mixed, or if the components are spatially separated but were formed at the same time, we would expect to see the same HINSA column densities in all components.

- **Where are the young clouds?**

  [Goldsmith & Li (2005)] found that all of their clouds were near steady-state HINSA abundances. Only approximate estimates of the collapse timescale could be made without the detection of younger clouds. A major goal of this research was to determine whether we could detect younger clouds.

Each of these questions leads to the ultimate goal of this research: whether we can use HINSA features to estimate the ages of molecular clouds, and the timescale for collapse. Obtaining confident answers for these questions would yield a significant advance in this field of study. To address this question we had to overcome several challenges.

1.3 Research Outline, Constraints, and Motivations for Chosen Methodologies

To improve confidence in HINSA column density measurements we had to devise a new method of data analysis. [Li & Goldsmith (2003), Goldsmith & Li (2005)] noted a strong correlation between ^{13}CO emission and HINSA features in sky position, center velocity, and non-thermal linewidth. In Chapter 2 we describe a new technique which uses associated ^{13}CO emission to create molecular templates that are used to assist in extracting HINSA column densities. Since the thermal component of HINSA linewidths is much wider than that of ^{13}CO, many velocity components which overlap in 21 cm can be distinguished in ^{13}CO emission. This allows us to, for the first time, measure

the HINSA abundances for each velocity component along a line of sight. This technique required us to obtain molecular data in addition to 21 cm data.

We conducted a new survey using the Green Bank Telescope (GBT) to observe HI, and OH lines. We obtained accompanying ^{12}CO, ^{13}CO, and $C^{18}O$ data at the Five College Radio Observatory (FCRAO). With these data we completed the first large-scale survey of HINSA features outside of Taurus, allowing us to examine HINSA behaviour, and establish HINSA as a viable tool of study (Chapter 3). We noted that clouds within the same complexes tended to exhibit similar HINSA abundances, and that HINSA abundances could often be quite different within two velocity components along the same line of sight. These observations provided additional hints that HINSA abundances might reflect cloud ages.

Our original intent was to measure the relationship between HINSA and total proton column densities within each cloud and clump in order to obtain ages. Our simple, spherical models showed that this relationship should evolve over time as the densest portions of each cloud converted their HI to H_2 more quickly than the diffuse regions. We thus expected that HINSA abundances should always decrease with increasing total proton column density. The survey described in Chapter 3 showed that this was not always the case. Further modelling showed that because significant portions of each cloud are at steady-state, constant HI volume density, the cloud's geometry could significantly affect this relationship. It was necessary to devise a geometry-independent method of measuring cloud ages. One way to do so is to compare the total proton and HINSA masses of each cloud/clump in its entirety. To derive ages from such mass ratios it was necessary to obtain the density distribution for each clump in

a geometry-independent way.

Previous studies showed that molecular cloud radial volume density profiles typically obeyed power laws. However, the power law exponents derived in the past varied depending on which regions of clouds were studied, and all depended on geometric assumptions regarding cloud shapes. To gain a better understanding of the density distributions within clouds we derived a new method for determining the shape of clouds' radial volume density profile functions which is geometry-independent. This method is detailed in Chapter 4. Unfortunately, 21 cm data from the GBT do not have a sufficiently small beam size for this method to be useful. Similarly, when we obtained our FCRAO data we had intended to convolve it to the 9.5' GBT beam and thus did not have sufficiently good signal to noise ratio at smaller beam sizes to use this new profile technique on that data either. We therefore used 2MASS extinction data to derive the radial profiles for several clouds. The 2MASS data has several limitations, especially at high optical extinctions. As a result, we were not able to apply it to any of the clouds in our HINSA survey. Instead we applied it to other, similar clouds which fit the criteria described in Chapter 4. We found that molecular clouds are best approximated using attenuated power law functions, and were able to obtain typical parameter values in Chapter 4.

Using the improved understanding of clouds' internal structure we developed a new chemical model to determine the time evolution of the HINSA to total proton mass ratio for an entire cloud. This chemical model, described in Chapter 5 could only provide lower limits on age estimates. As the exact structure of the specific clouds studied could not be determined we used a range of reasonable parameters, derived from Chapter 4, for each model. The models

with those parameters that produced the lowest age estimates were adopted for the final age limits. We found that clouds are typically at least several hundred thousand years old. Particularly in the case of L204, we found that our estimates agreed well with previous, independently measured age estimates for that cloud. In general, our estimates agreed with the recent results from [Brunken et al. (2014)] who measured the age of L183 (not part of our survey).

In Chapter 6 we summarize the scientific conclusions which were derived from this work. We find that we were ultimately able to answer nearly all of the questions with which we began this inquiry, as well as others which arose during the course of research.

CHAPTER 2

AN IMPROVED TECHNIQUE FOR MEASUREMENT OF COLD HI IN MOLECULAR CLOUD CORES

2.1 Introduction

Star formation occurs in molecular clouds which are thought to have evolved from diffuse atomic hydrogen (HI) regions to form dense, cold, well–shielded regions composed primarily of molecular Hydrogen (H_2). Our quantitative understanding of cloud evolution and specifically the conversion process (from HI to H_2 gas) has been hindered by our inability to measure confidently the HI abundance in evolving clouds. In this paper we present a new technique for measuring HI column densities in dark clouds offering a significant improvement over previous methods. In the interests of brevity this paper includes the results from only a few clouds on which this technique has been applied in order to demonstrate the technique. The results of a much larger survey of observational data and analysis are to follow in a subsequent publication.

The ability to determine accurately the HI component of molecular clouds could have a variety of benefits. Measurement of HI/H_2 ratios in clouds, used in conjunction with astrochemical models, allows us to determine the chemical ages of individual clouds or entire molecular complexes (e.g. Taurus, Perseus, etc.). This will greatly expand our understanding by constraining star formation models thus yielding insights into the collapse process and the interplay of magnetic fields, ambipolar diffusion, turblence, and various potential sources of cloud support. By studying age distributions in large scale regions we can learn about the processes that may trigger the collapse of large complexes. In

contrast to previous methods, our technique allows us to determine the HI/H_2 ratios for individual velocity components within a cloud thus yielding unique information about cloud kinematics. Further, the technique allows for the absolute measurement of quantities such as HI column density, in contrast to many previous studies which were limited to comparative measurements.

HI is the dominant constituent of the diffuse ISM and its 21cm emission line is prevalent everywhere throughout the sky, especially near the galactic plane. Typical HI emission spectra are composed of numerous superimposed velocity components. The emission linewidths of the overall features are typically on the order of a few 10s of kms^{-1}. They include velocity variations owing to galactic rotation as well as very significant peculiar velocities resulting from localized phenomena. It is rare to find a molecular region for which one can confidently claim that the HI emission observed along the line of sight to the cloud is associated with the cloud, and is not due to background or foreground sources. Owing to such velocity crowding it is difficult or impossible to disentangle HI emission originating from a particular cloud from the background galactic HI emission.

The situation for HI absorption is different. HI within a galactic cloud of any type can absorb the continuum emission from distant (galactic or extragalactic) radio sources. Because the HI optical depth varies inversely with the cloud temperature, the absorption by galactic HI is stronger in cold, galactic HI clouds. The integrated optical depth of all the clouds along the line of sight through the galactic disk can exceed unity as demonstrated in [Kolpak et al. (2002)], and [Garwood & Dickey (1989)].

These cold, interstellar HI clouds may also be identified through their ab-

sorption of warm background HI emission originating within the galaxy. Because the emission being absorbed by cold HI clouds in this case is galactic HI emission, the resultant spectral absorption features are referred to as HI self-absorption (HISA). There have been many surveys with HISA detections over the years including [Garzoli & Varsavsky (1966)], [Heiles (1969)], [Knapp (1975)], [Heiles & Gordon (1975)], [Wilson & Minn (1977)], [McCutcheon et al. (1978)], [Myers et al. (1978)], [Bowers et al. (1980)], [Batrla et al. (1981)], [Shuter et al. (1997)], [van der Werf et al. (1988)], [Feldt & Wendker (1993)], [Montgomery et al. (1995)], [Gibson et al. (2000)], and [Kavars et al. (2003)], among others. It is important to emphasize that the term HISA refers to an observable spectral absorption feature rather than being a description of a specific physical process.

Molecular spectral emission lines provide an independent view of that subset of interstellar clouds that are cold and composed primarily of molecular species. These "molecular clouds" are expected to maintain a residual abundance of atomic hydrogen if for no other reason than the cosmic ray dissociation of H_2. This applies even when the chemical evolution of the cloud has reached equilibrium [Solomon & Werner (1971), Goldsmith & Li (2005)]. With the residual HI co–existing throughout the cloud with molecular species, the observed spatial and velocity (kinematic) structure of the molecular cloud will be similar whether observed in molecular emission or HI self-absorption lines. Thus, we expect to observe HI self-absorption features along the lines of sight of molecular clouds which share the spatial distribution and kinematics (non–thermal line width) of molecular emission lines. Such localized association between molecular emission and HI self-absorption is observed for many nearby clouds as reported by [Li & Goldsmith (2003)] and [Goldsmith & Li (2005)]. The

specific case in which the HI absorption features observed in the direction of a molecular cloud share the spatial and kinematic structure seen in the molecular lines is called HI Narrow Self-Absorption (HINSA) as defined in [Li & Goldsmith (2003)]. The term *Narrow* arises from the typically small non-thermal linewidths (on the order of 0.1 kms^{-1}) of HINSA features, very similar to the similarly small nonthermal linewidths of molecular tracers along the same lines of sight. HINSA can be considered to be a subset of HISA, but it is a subset derived from an understanding of a specific, observable physical phenomenon in molecular clouds.

While both are simply acronyms for spectral absorption features, HISA can be caused by a variety of different conditions and processes, but HI Narrow Self-Absorption (HINSA) is that subset of HISA in which the atomic HI absorption correlates well with molecular emission of certain tracers (most notably ^{13}CO) in sky position, central velocity, and nonthermal line width. Based on our current understanding of cold molecular clouds, the most satisfactory picture is that HINSA features are a result of HI gas located within these cold, dense, well–shielded regions. Some early examples of HINSA studies that predate the use of this term are those of [Wilson & Minn (1977)], [van der Werf et al. (1988)], and [Jackson et al. (2002)]. The technique which we describe in this paper pertains only to the extraction of HI data from HINSA features.

The general picture which emerges, as found in [Li & Goldsmith (2003)] and [Goldsmith & Li (2005)], is that the HI gas located within cold, quiescent cores of dark clouds produces HINSA absorption features. The well–defined center velocities and narrow line widths allow us to separate the HI gas associated with individual clouds from the galactic background. However, the complexity

of the background emission spectra that are frequently encountered makes extracting accurate data (especially in terms of obtaining the cold HI column density) from the absorption features difficult. Several methods (discussed in §2.4) have been used previously, but all are recognized to introduce significant uncertainties in the results. We here present a new technique that aims to improve the situation by using the properties of molecular emission to characterize the region producing the HINSA features, and then employes the HINSA spectral features to derive HI column densities.

In §2.2 we present selected data and show the results of applying the new technique to them, and in §2.3 we contrast this with previous methods for analyzing HINSA data. In §2.4 and §2.5 we describe the technique and the combination of molecular data with the HINSA spectra. In §2.6 and §2.7 we verify the validity of our technique using simulated data and also examine its limitations.

2.2 Results Using Observational Data

In this section we demonstrate the utility of our procedure by showing some results of its implementation based on observations of two molecular clouds. While a full discussion of the implications of these results is reserved for another publication, we hope that the results obtained encourage careful consideration of the technique described here.

An observational survey, whose complete results and analysis are presented elsewhere, was performed using the Green Bank Telescope (GBT) and the Five College Radio Observatory (FRCAO) to obtain HI, OH, ^{13}CO, ^{12}CO, and C^{18}O maps of more than 30 dark clouds which exhibit HINSA features. Figure 2.1

shows sample HI spectra from two well known clouds, Lynds 134 (L134) and L1757. HINSA absorption features are prominent in both sources. The red lines represent the recovered background spectra after HINSA has been removed. This representation is reassuring in that the smooth, natural looking background spectra indicate that the HINSA removal process has not produced marked distortions in the background. While L134 represents a simple case of a single emission component, in L1757 our technique is able to discern two emission components closely spaced in velocity. Previous methods based solely on the HI line profile would have significantly overestimated the HI optical depth by assuming there was only a single emission component. By utilizing the associated molecular data as described below, the possibility of a single emission component is largely eliminated.

The technique we use here assumes that the cold HI and molecular constituents are well–correlated spatially, so that we can assume that the line center velocity and nonthermal line width for the cold atomic gas and the molecular gas in a particular direction are the same. This is justified by previous studies of HINSA and CO isotopologues, including [Li & Goldsmith (2003)] and [Goldsmith & Li (2005)]. Our technique depends on use of these spectra to calculate the HI optical depths and column densities. In conjunction with observations of molecular tracers this allows us to obtain HI column densities in dark clouds with improved accuracy. Further, we are able to obtain unprecedented detail by examining individual velocity components within each cloud, even when their velocity separations are small enough to make individual components difficult to distinguish in HI spectra. Additional details are given in §2.4

Figures 2.2, 2.3, and Tables 2.1 and 2.2 show measured HI, H_2, and total pro-

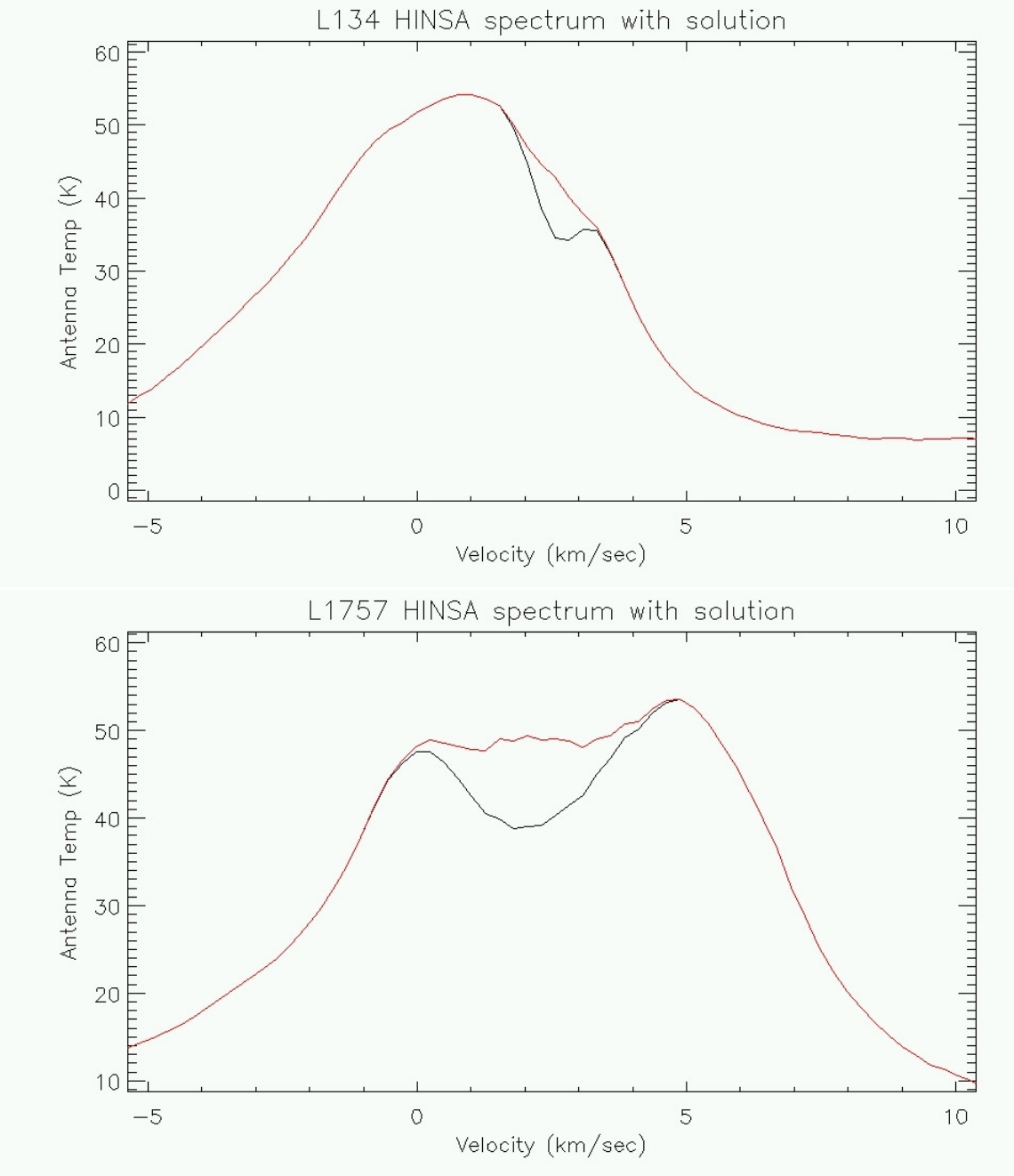

Figure 2.1: Sample HI spectra in the directions of the molecular clouds L134 (upper) and L1757 (lower). We show the original observed spectra (black) and the recovered background spectra after HINSA removal (red), using the technique described in this paper.

ton column densities, and the HI/H_2 ratios for individual velocity components throughout numerous positions in clouds L134 and L1757. No such analysis has previously been carried out. The choice of these two sources indicates the importance and possible rewards of such studies in that the two clouds exhibit very different properties. While in L134 all the velocity components have similar HI/H_2 abundances in the relatively narrow range between 10^{-4} and 10^{-2}, in L1757 the situation is quite different, with ratios varying systematically as a function of velocity and extending over a much greater range. The most likely explanation for this phenomenon is that L134 is a mature cloud in which the chemical evolution of all of the velocity components has proceded to the point where HI abundances have approached their equilibrium values. In contrast, L1757 represents a much younger cloud in which each component is evolving at a different rate governed by its total density. This information yields valuable insight into the dynamics and chemistry of dark clouds, but has never before been available. A complete discussion of the results for a large sample of clouds will be presented in a forthcoming paper as a proper analysis requires more space than is available here.

2.3 Limitations of Previous HI Self-Absorption Analysis Techniques

Owing to the complexity of HI background emission along most lines of sight, it is clearly quite arbitrary to fit a straight line across the absorption feature. It is equally problematic to use OFF source observations since the HI background spectra change significantly over the angular size of the foreground cloud as

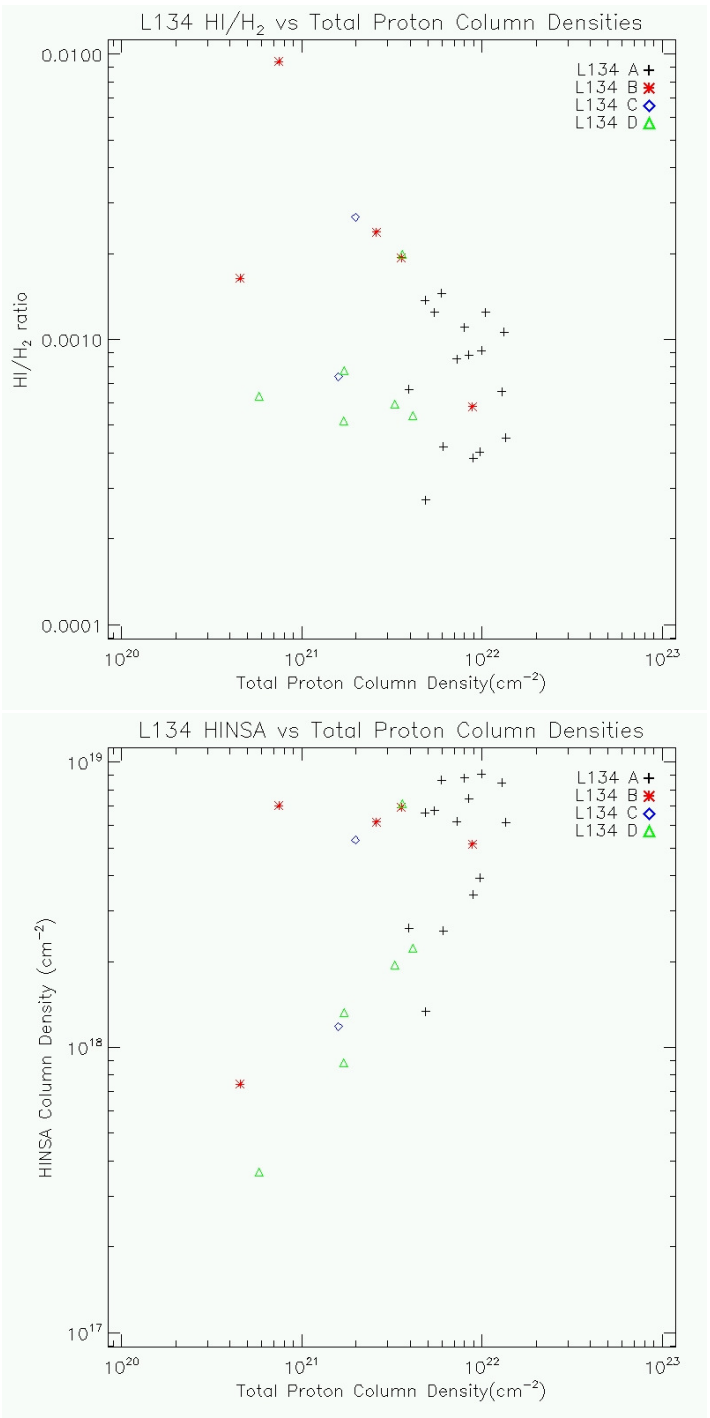

Figure 2.2: Atomic to molecular abundance ratios in the molecular cloud L134. Each point represents a single velocity component at different position within the cloud. The 2.55–3.5, 1.65–2.55, 1.55–1.65, 0.25–1.55, and -1.00–0.25 kms^{-1} velocity components are represented by black, red, blue, green, and cyan dots, respectively. These points are Nyquist sampled relative to the GBT HI beam and are thus independent. There are no systematic differences in the HI/H_2 ratio among the different velocity components.

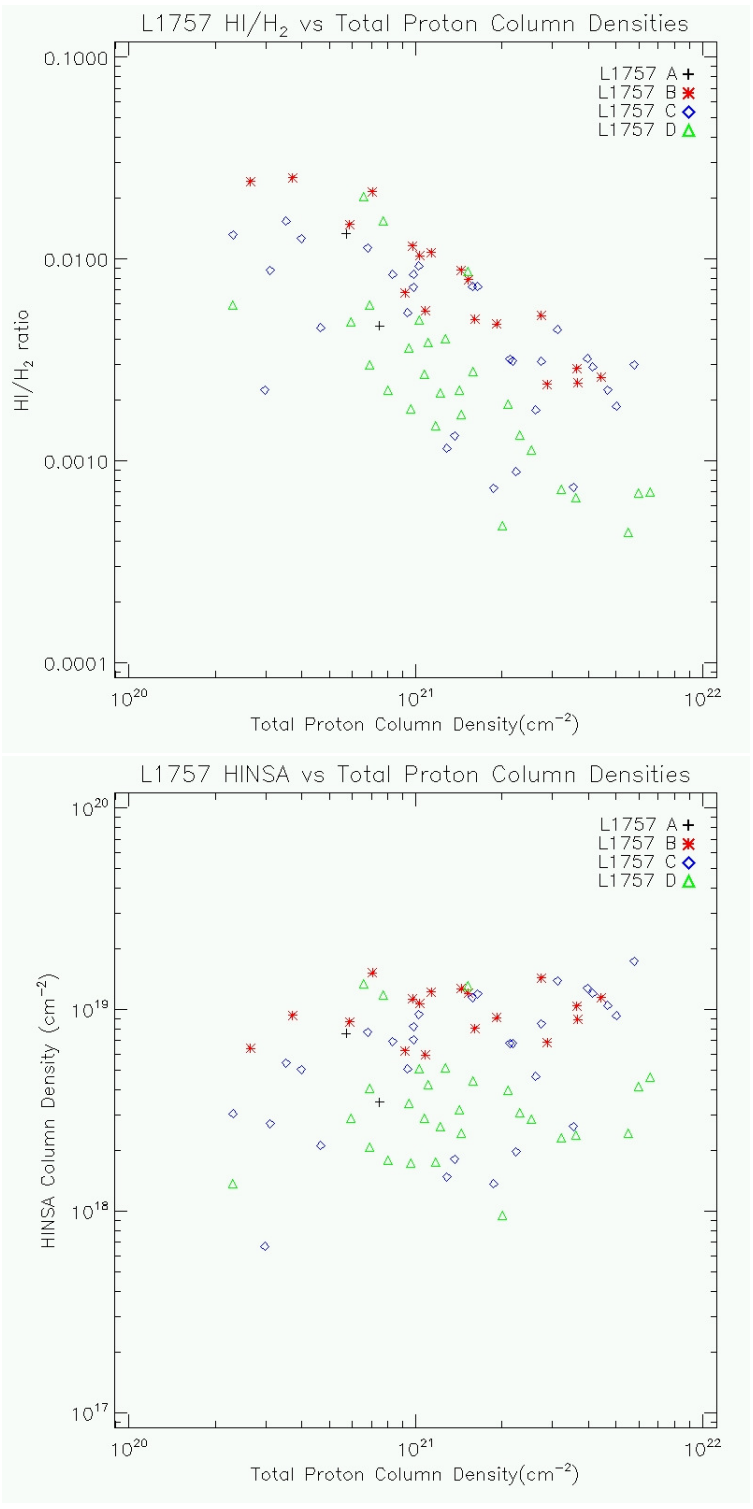

Figure 2.3: Atomic and molecular hydrogen column densities and ratios in L1757, presented as in Figure 2.2. The 4.3–6.7, 2.0–4.0, 1.0–2.5, -0.5–1.3 kms^{-1} components are represented by black, red, blue, and green points, respectively. Unlike L134, the various velocity components of L1757 show fairly well–defined but systematically different different relationships between HI and H_2.

sampled by the telescope beams that have been employed. Several methods for extracting HI column densities from HISA absorption have been tried in the past. These can be classified into two groups, each with its own set of limitations. The most commonly–used methods rely on fitting simple mathematical functions such as gaussians or polynomials over the observed spectra while masking the absorption features. As discussed in [Li & Goldsmith (2003)] these techniques result in significant uncertainty because the analysis is underconstrained. Arbitrary choices for the degree of the fitted polynomial and the masking ranges must be made, and these greatly affect the final results.

Recently, [Kavars et al. (2005)] implemented an automated algorithm for measuring HISA which relies on spotting the characteristic HISA features (the dip) in HI spectra. However, this technique (as pointed out by its authors) suffers from several limitations. The [Kavars et al. (2005)] technique, as well as function fitting methods, are unable to determine the gas temperature and the optical depth without assuming a value for one of these important quantities. These methods are thus limited to comparative measurement of one quantity, such as HI column density, over large regions recognizing that absolute values cannot be obtained.

Owing to the complexity of the galactic HI background, and lacking additional information, it is often impossible to tell which dips in the spectra are genuine absorption features and which are produced simply by the superposition of two emission features. Both phenomena may be spatially extended with continuous velocity distributions. Molecular observations can be used to distinguish between these two scenarios. In molecular clouds there are often multiple components along the same line of sight with closely spaced central

velocities. The lower mass of atomic hydrogen compared to molecular tracers (and consequently greater thermal line width) means that it is often possible for multiple components which are distinguishable in molecular spectra to merge into a single HI absorption feature. Using the molecular gas as a template for the HINSA analysis has the potential to greatly enhance the accuracy of the HI/H_2 comparison since the ratio may be different in each velocity component.

Previous analysis techniques have been applied to both HISA and HINSA sources without distinguishing between the two. Our technique is limited to HINSA sources for which (by definition) there is molecular data available. Limiting our scope in this manner allows us to utilize observational data from various molecular tracers to assist in extracting meaningful results from HINSA features. As will be shown in what follows, to the extent that our assumption that HI is mixed with the molecular gas is valid, we are able to measure both the temperature and optical depth of the HI gas without any ambiguities regarding fitting functions. In this way we may treat each velocity component in a cloud separately.

2.4 The Technique

2.4.1 Analytic Representation

An idealized HINSA spectrum can be represented by the radiation transfer equation as

$$T_A(v) = (T_b(v) + T_c)e^{-\tau(v)} + T_H\left(1 - e^{-\tau(v)}\right) \ , \tag{2.1}$$

where v corresponds to velocity, $T_A(v)$ is the observed spectrum, $T_b(v)$ is the background emission due HI emission clouds, T_c represents the continuum emission along the line of sight at 21 cm including the 2.7K microwave background(§2.4.2), T_H is the gas temperature of the foreground absorbing cloud producing HINSA, and $\tau(v)$ is the optical depth of the absorbing HI gas at 21cm which we can describe as $\tau(v) = \tau_0 e^{\frac{-(v-v_H)^2}{2\sigma_H^2}}$, where τ_0 is the peak optical depth, v_H is the central velocity of the HINSA component, and σ_H is the HINSA linewidth. In this particular representation we have assumed that there is no intervening HI emission originating between us and the absorbing HINSA cloud; this topic is further discussed in §2.4.3. When multiple absorption components overlap in velocity within the same line of sight, the transfer equation must be applied consecutively for each component from farthest to nearest.

HINSA absorption features are typically Gaussian-like dips with much smaller amplitudes and linewidths than the characteristics of the emission spectra ($T_b(v)$) on which they reside. These features can be so small in comparison to the background emission that they can be difficult to distinguish by eye. However, by utilizing a fundamental property of gaussians we can obtain a much better representation of the data in which the HINSA becomes more apparent.

The derivatives in velocity or frequency of a gaussian function can be written as:

$$f(v) = f_0 e^{(-v^2/2\sigma^2)} \quad \frac{df(v)}{dv} = -\frac{v}{\sigma^2}f(v) \quad \frac{d^2f(v)}{dv^2} = -\frac{1}{\sigma^2}f(v) + \frac{v^2}{\sigma^4}f(v) \ , \tag{2.2}$$

where it is apparent that higher order derivatives show a stronger dependence on linewidth. For conceptual purposes we can temporarily approximate the HINSA absorption and background emission features as gaussians. Because the linewidths for HINSA features (typically ~ 1 kms^{-1}) are much narrower than the linewidths for the background emission components, in the first and second derivative representations, even a low-amplitude absorption feature will become readily apparent in comparison to the bright background emission. This is illustrated in Figure 2.4. In the second derivative representation, HINSA becomes the dominant feature in the spectrum thus making it easier to isolate and quantify.

One could in principle use higher derivative representations to search for the best fit as the HINSA becomes progressively more prominent. However with real data the noise also rises with higher derivatives. The second derivative representation has been found to be the optimum choice for our GBT and Arecibo observations. It would be possible to take the second derivative representation of any HINSA spectrum and attempt to fit a simple function to it to extract the absorption. However, HINSA spectra are rarely so simple as to lend themselves to this kind of fitting and we would have very limited information on the temperature of the HI gas. Furthermore, the large thermal linewidths of HI spectra tend to blend all the velocity components along a single line of sight. Unless we are convinced that all the velocity components in a cloud can be characterized by the same HI/H_2 ratio, we must find a way to extract the HINSA using additional constraints based on physical parameters.

The primary benefit of limiting our technique to HINSA features is that we can use data from molecular tracers in order to constrain the analysis. If we can

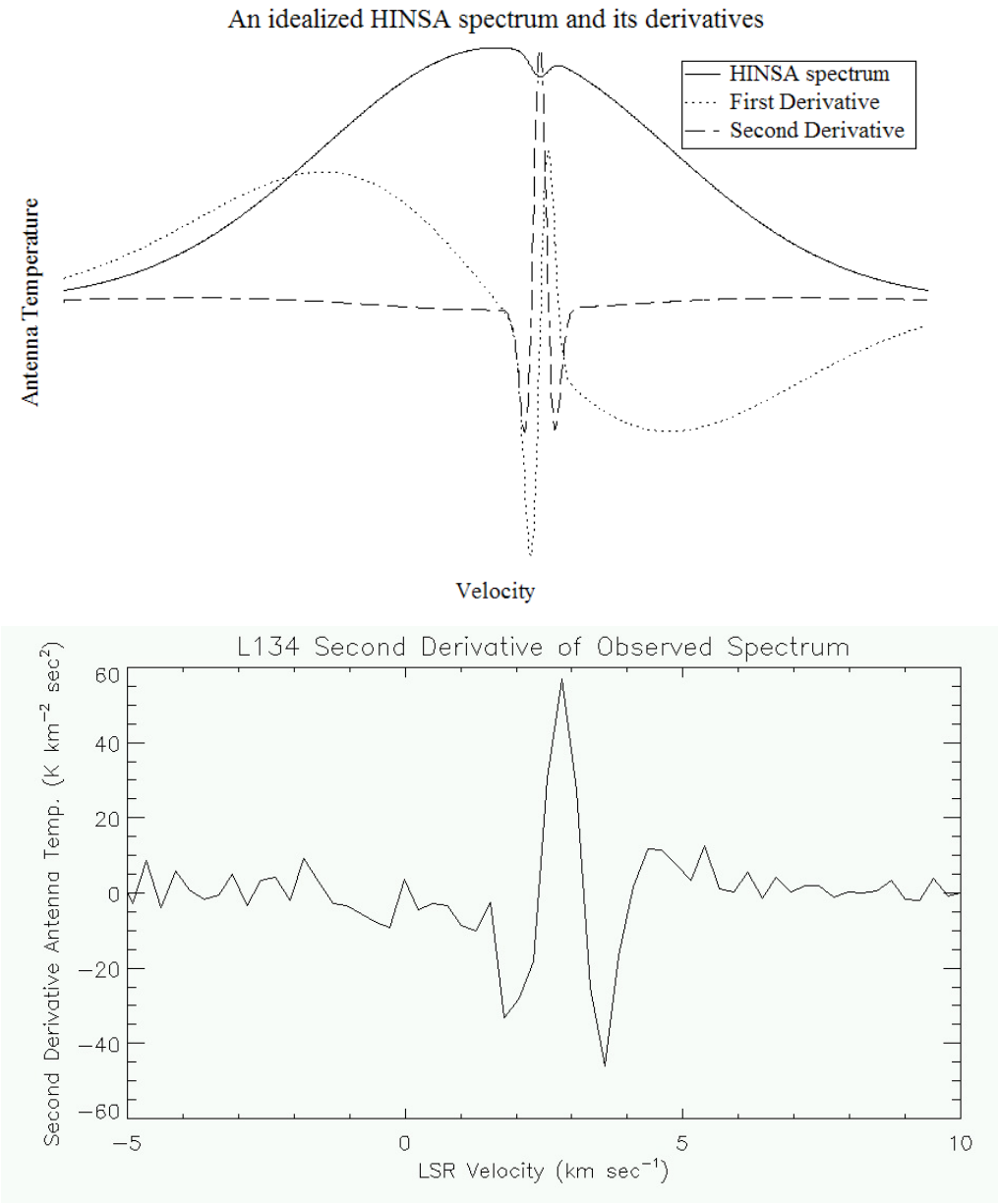

Figure 2.4: (upper) An idealized HINSA spectrum with typical observed properties along with its first and second velocity derivatives. The scales have been normalized for demonstration purposes. (lower) Second derivative representation of the observed spectrum toward L134 shown is Figure 2.1. It is apparent that a small HINSA dip becomes the dominant feature in the second derivative representation

determine the values of all the other parameters (linewidth, center velocity, and temperature) for each velocity component then we can ideally limit ourselves to searching for that value of τ_0 which produces the T_b emission spectrum whose second derivative best removes the HINSA feature. Minimizing the integrated squared sum of the second derivative background spectrum is sufficient to extract the HINSA feature (see §2.4.5).

2.4.2 Continuum Emission at HI wavelengths

There are various sources of continuum emission (T_c) in equation 2.1 throughout the galaxy that contribute to the sky brightness at 21cm. The emission may originate from a variety of sources such as synchroton emission within the galaxy and continuum emission from ionized gas such as that in the Galactic Halo. Continuum emission can also originate from individual discrete galactic and extra-galactic sources, such as pulsars, HII regions, AGNs, accretion disks, and quasars. These sources will typically produce emission whose intensity is constant across the observed HI band. Observing techniques such as frequency switching as well as software baseline removal algorithms remove the continuum emission and the 2.7K background along a particular line of sight from the reduced spectrum. The continuum emission component should ideally be included when calculating HINSA since the temperature of the cold gas clouds (10K) is comparable to the antenna temperature produced by the continuum emission. Several galactic surveys have been performed which have measured the value of the 21cm continuum including [Reich et al. (1997)], [Uyaniker et al. (1999)], and [Reich & Reich (1986)], among others. These data can be utilized to determine the expected continuum emis-

sion along any HINSA source. Typical values are on the order of a few K. According to equation 2.1, the value of T_c, while significant, becomes critical only when the HINSA optical depths are high and gas the temperature is low.

2.4.3 Foreground HI Emission

Usually there will be HI emission between the observer and the HINSA cloud due to intervening HI gas. To assess the importance of the effect this intervening gas might have on our HINSA measurements we must expand equation 2.1 to include all three gas components, that of the HI emission behind the HINSA cloud, absorption due to the HINSA cloud itself, and emission between us and the HINSA cloud.

$$T_I(v) = T_c e^{-\tau_b(v)} + T_{ex\ b}(1 - e^{-\tau_b(v)}) \tag{2.3}$$

represents the emission component due to the warm HI gas behind the HINSA cloud whose excitation temperature is $T_{ex\ b}$ and optical depth is $\tau_b(v)$. At this stage, only the background continuum emission T_c is attenuated.

The HINSA cloud then attenuates the background emission, while also adding its own contribution as in

$$T_{II}(v) = T_I(v) e^{-\tau_H(v)} + T_{ex\ H}(1 - e^{-\tau_H(v)}) \ , \tag{2.4}$$

where τ_H and $T_{ex\ H}$ represent the optical depth and excitation temperature of the cold HI gas within a molecular cloud. Similarly, any foreground gas will attenuate the spectrum further as well as adding its own emission to produce

the final observed spectrum:

$$T_{III}(v) = T_A(v) = T_{II}(v)e^{-\tau_f(v)} + T_{ex\ f}(1 - e^{-\tau_f(v)}) \,, \tag{2.5}$$

where τ_f and $T_{ex\ f}$ represent the optical depth and excitation temperature of the foreground HI gas between us and HINSA cloud.

We now have two new terms, τ_f and $T_{ex\ f}$, describing emission due to HI gas between us and the HINSA cloud. There is no way to operationally disentangle which portion of the observed emission spectrum originates from in front or behind the molecular cloud, but clearly any foreground emission we observe will attenuate the HINSA features and we must somehow correct for this. To get a sense of the effect and scale of the attenuation, we can assume that both the background and foreground emission gas have the same excitation temperature $T_{ex\ tot} = T_{ex\ b} = T_{ex\ f}$. We can further assume the HI gas is distributed uniformly throughout the galaxy along the line of sight so that a linear relationship can be established between τ_b and τ_f such that $\tau_b = p\tau_{tot}$ and $\tau_f = (1 - p)\tau_{tot}$ where τ_{tot} is the total optical depth of all the emitting HI gas behind and in front of the HINSA cloud and p represents the fractional distribution between the two which we can estimate using

$$p(b) = \left(1 - \frac{D_{cloud} sin(b)}{R_{disk}}\right) . \tag{2.6}$$

Here, D_{cloud} is the distance to the HINSA cloud, b is the galactic longitude along the given line of sight, and R_{disk} represents the distance from Earth to the edge of the galactic disk as defined by its HI content. With a typical scale height of 100pc near the Sun's position within the Milky way we take this value to be 200pc [Stahler & Palla (2004)]. For a more complete discussion see [van der Werf et al. (1988)] or [Li & Goldsmith (2003)]. In this case we are using geometry of the local galactic disk, and the HINSA cloud's position within the

disk to estimate how much of the HI emission visible along a particular line of sight is in fact located in front of a HINSA source attenuating the HINSA feature.

This emission, if located at the same velocity as the HINSA feature, will have the effect of washing out the absorption feature and thus the apparent HINSA optical depth will be lower than the intrinsic value. In fact, it can be shown from the above formulation that for optically thin HINSA, $p(l,b) \propto \tau^{-1}$ as shown in in [van der Werf et al. (1988)], where τ now represents the observed apparent optical depth of any HINSA feature. Thus to obtain the intrinsic HINSA optical depth of a cloud we must divide the apparent optical depth by $p(l,b)$. Due to the uncertainties in the HI distribution it is impractical to directly model the effects of foreground clouds when trying to extract HINSA profiles. Instead HINSA optical depths are computed on the assumption that there is no intervening emission and are subsequently adjusted using the factor $p(l,b)$ which itself depends only on the cloud's position and is calculated independently of the observed emission spectrum.

The observed spectra thus give us an apparent optical depth which then must be adjusted by p to yield an estimate of the intrinsic optical depth. For most nearby clouds this correction factor is in fact small in comparison to other sources or error. It must be true that $p(l,b)$ is not much less than unity if a significant HINSA feature is to be observed otherwise the foreground emission would obscure the HINSA absorption. For the two sample clouds in this paper, L134 and L1757 the correction factor has values of 0.5 and 0.7 accordingly.

2.4.4 Obtaining Constraints Using Molecular Parameters

It is possible to obtain data from molecular tracers which can provide us with reliable estimates of the HINSA feature properties for each velocity component by utilizing certain assumptions justified by previous work. [Li & Goldsmith (2003)] showed a very strong correlation between the line center velocity of each HINSA component and those of its molecular counterparts using the OH, ^{13}CO, and C^{18}O molecules as tracers. Thus, once each molecular component has been identified and separated using traditional fitting we can assume that each velocity component visible in molecular emission has an accompanying HINSA component whose optical depth may yet turn out to be 0. We can use the central velocity from any of the above molecules as an estimate of the number of HINSA components present and their center velocities (v_H).

Spectral linewidths are composed of both thermal and nonthermal(turbulent) components. The two components add according to $\sigma_{obs} = \sqrt{\sigma_{th}^2 + \sigma_{nt}^2}$, where σ_{obs}, σ_{th}, and σ_{nt} are the observed linewidth and the thermal and nonthermal components respectively. The thermal component arises from the random motions of individual particles within the gas and will be different for varying atomic or molecular tracers due to the different particle masses. The nonthermal component results from turbulence and bulk motions within the cloud. If two species of gas were uniformly mixed throughout a cloud one would expect their spectra to share similar non-thermal linewidths. [Li & Goldsmith (2003)] showed a good correlation between the nonthermal linewidths of HINSA and the accompanying ^{13}CO emission. We can use ^{13}CO to estimate our expected HI linewidths, but first we must disentangle the thermal components using information about the gas temperature within the cloud.

Under the assumption that the cold HI is in thermal equilibrium with the surrounding molecular gas we can use the kinetic temperature of a molecular tracer to estimate the HI gas temperature (T_H). The $J = 1 - 0$ transition of ^{12}CO has been used in the past to estimate gas temperatures because it usually appears as optically thick in molecular clouds. Equation 2.1 is valid for molecular emission as well as HI absorption as it describes generic radiative transfer. In the case of ^{12}CO there is generally no background or continuum emission and so the equation reduces to

$$T_A(v) = T_{^{12}CO}\left(1 - e^{-\tau_{^{12}CO}(v)}\right) \ , \tag{2.7}$$

where $T_A(v)$, $T_{^{12}CO}$, and $\tau_{^{12}CO}(v)$ describe the observed ^{12}CO antenna temperature, the ^{12}CO gas excitation temperature (which in high density regions can be taken to equal the kinetic temperature), and the optical depth. If the optical depth is taken as $\gg 1$ then the equation reduces simply to $T_A = T_{^{12}CO}$. Thus ^{12}CO provides us with estimates of the HI gas temperature allowing us to estimate the HINSA optical depths, column densities, and thermal and non-thermal linewidths. Some derived ^{12}CO temperatures for L134 and L1757 are given in Table 2.2. Since ^{12}CO emission has been shown to exist wherever there is ^{13}CO emission and HINSA we can measure the ^{12}CO temperature at each position and use it to estimate the ^{13}CO and HINSA temperatures at each position in the cloud. Using these constraints we are left with only one free parameter, the peak optical depth of the cold HI gas.

Due to the uncertainties in the assumptions made the constraint parameters cannot be taken as exact values of the HI gas properties. Instead they can be used as close guess values to help us constrain the fit. By using ^{13}CO and ^{12}CO data we are also able to estimate H_2 column densities using fractional abundances of carbon monoxide that are well–determined in many nearby dense

clouds [Stahler & Palla (2004)].

2.4.5 The Fitting Procedure

As explained in section 2.4 any narrow HINSA feature will be the dominant feature in the second derivative representation of the observed spectrum. As such, once guess parameters for the center velocity, line-width and temperature of the HI gas have been obtained from molecular tracers the remaining task is to find the value of τ_0 for each velocity component which minimizes the resulting area under the curve of the second derivative of the recovered background emission spectrum after HINSA is removed in accordance with the discussion in §2.4.1. This is done by first using the trial values of the HINSA linewidth, center velocity, temperature, and optical depth and using those on a particular observed spectrum ($T_A(v)$) to obtain the recovered background spectrum without HINSA ($T_b(v)$) as described in Equation 2.1. According to §2.4.1 the HINSA feature will be revealed as a large feature in the second derivative representation of any observed spectrum. To find the best trial $T_b(v)$ spectrum the algorithm must search for one whose integraded intensity in the second derivative representation is minimized. The second derivative of the recovered spectrum ($T_b(v)$) is calculated numerically through traditional methods. Since the second derivative representation will have negative values as well as positive ones, it is squared prior to integration. We thus minimize the value of I as described by the function

$$I = \int \left(\frac{d^2 T_b(v)}{dv^2} \right)^2 dv \ . \tag{2.8}$$

which is simply the squared integrated intensity of the second derivative of the background spectrum (T_b) that is recovered after trial values of the HINSA op-

tical depths and other parameters are removed from the observed spectrum. Finally, determining the smallest value of I will give us the best-fit values of the HINSA parameters. It is possible to use a more sophisticated minimizing function, but the HINSA feature is so dominant in the second derivative representation that this has proven not to be necessary.

Previous studies have shown that the correlation between HI and ^{13}CO center velocities is strong [Li & Goldsmith (2003)]. Hence, the v_H parameter is held fixed for each velocity component. The T_F estimates obtained from ^{12}CO do not carry as much confidence (as discussed in the next section), however the temperature is still kept as a fixed parameter during our fit. For optically thin spectral lines such as HINSA the temperature cannot sufficiently constrain the shape of the absorption feature to be allowed as a free parameter since a wide range of combinations of temperatures and optical depths would be able to fit the data. Thus the gas temperature must be specified in any fits.

The linewidths obtained from ^{13}CO observations can only be applied to the HI gas under the assumption that the two species are coextensive throughout the cloud. This assumption, while strongly suggested by the previously–referenced studies, is clearly not exact. Hence the molecular linewidths for each velocity component are used as guess values for the HI fit. The HI linewidths are allowed to vary in value during the fit near the initial guess values.

In practice, τ_0 is left as a free parameter, and σ_H as a constrained parameter for each component. For every trial value of τ_0 a T_b spectrum is constructed and its second derivative is checked for the fitting parameter as specified by equation 2.8. All velocity components along the same line of sight must be fitted simultaneously to account for obscuration due to overlapping. There are a

variety of fitting algorithms that can be used for the final fitting. In the present case a variation of the Levenberg–Marquardt method was implemented. In the interest of clarity, we give in appendix A a step-by-step description of the entire process including the determination of molecular parameters and HINSA extraction.

2.5 Coming to Terms with Variable Beam Sizes and Unresolved Sources

Our technique combines observations from different telescopes with different frequencies and beam sizes. The HI data presented in this paper was obtained using the 100 m Greenbank Telescope (GBT) having a 9′ beam size, while the ^{12}CO and ^{13}CO data were obtained using the Five College Radio Observatory (FCRAO) 14 m telescope having a 45″ beam size. Combining these data sets is non-trivial. Convolving the CO data directly to a 9′ beam has the effect of smoothing out a great deal of structure, kinematically as well as spatially, which is neither necessary nor desirable.

By fitting the molecular data prior to convolution we preserve information regarding individual velocity components which may otherwise disappear or be distorted in an HI beam. It is not necessary for all molecular components to have accompanying HINSA features. Maintaining this information is crucial to studying the comparative composition of different velocity components within a cloud as well as properly determining their HI/H_2 ratios. High-resolution molecular data should only be convolved to a beam size which results in sufficient signal–to–noise to produce good fits to the individual emission compo-

nents. Following this argument and a series of numerical experiments, our FCRAO spectra were convolved to a 2 arcminute beam size. Parameters including center velocity, linewidth, temperature, and optical depth for each molecular emission velocity component are derived using conventional fitting techniques. Corresponding guess parameters for the HI gas are then constructed by convolving the molecular fit parameters to the HI beam. This approach allows us to measure the HINSA column densities for each individual molecular component, as well as to utilize the high spatial resolution information on the molecular constituents of the cloud.

Many sources are unresolved when observed with available single-dish HI beams. Previous studies ([Li & Goldsmith (2003)], and [Goldsmith & Li (2005)]) have shown strong spatial and linewidth correlations between HINSA and ^{13}CO. With this information we may make the assumption that HINSA and ^{13}CO are well mixed throughout a cloud. This affords us the opportunity to make estimates of the HI beam filling factors by assuming that HINSA is present wherever significant ^{13}CO emission is observed. This assumption, while not precise, is useful. In the case of resolved sources the beam filling factor plays a minimal role. In unresolved sources, or the edges of larger clouds, the beam filling factor as implemented by the present technique, does not alter the calculated HI/H_2 ratio, but only alters the total column densities of both species.

2.6 Example Solutions Using Simulated Data

A controlled way to assess the validity of our technique is to apply it to synthetic, yet realistic data and compare the derived results with the known input

values. Simulated data does not allow us to test the assumptions on the relations between molecular and atomic gas that are used by this technique. It is possible however to assume those relations to be correct and to test the validity of the HINSA fitting technique by itself. Further it is possible to observe the effects on the HINSA fit of having incorrectly determined the fitting parameters based on molecular data.

2.6.1 A Simple Case

The simplest case consists of a single emission component obscured by a single HINSA absorption feature as in Figure 2.5. As expected, HINSA is the dominant feature in the second derivative representation. For the simulated run, the center velocity and temperature of the cold HI gas are provided as precisely known quantities. The linewidth, however, is given only as a guess parameter. The task then is to search for those values of the linewidth and the peak optical depth which minimize the squared sum of the second derivative background spectrum after HINSA is removed. Figure 2.6 shows the original observed spectrum as well as the recovered background spectrum after fitting. The resulting computed optical depth of 0.198 compares favorably to the original inputed value of 0.2. It is apparent from the second derivative representation of the recovered spectrum that the HINSA which was prominent in the original spectrum (Figure 2.5) has been effectively removed.

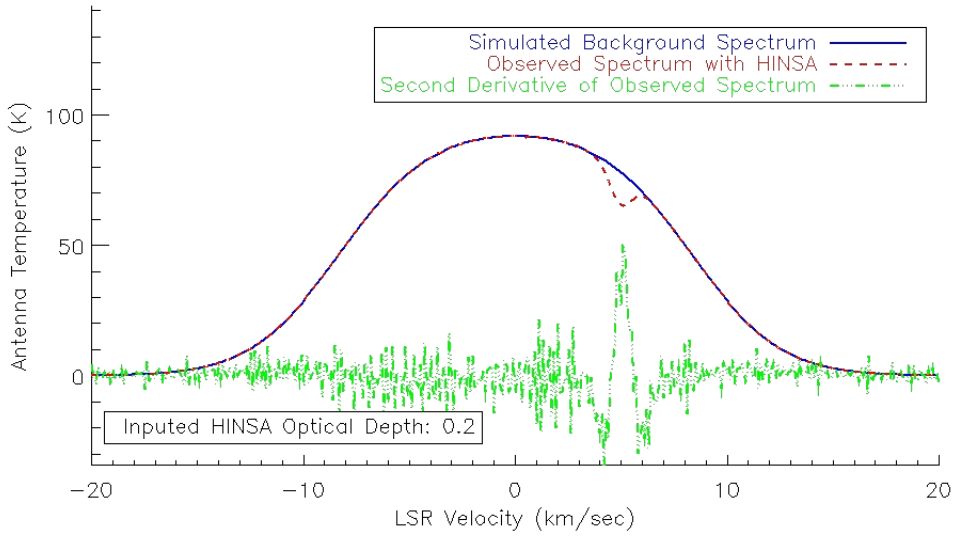

Figure 2.5: An idealized HINSA spectrum (red) from simulated data. The blue line represents the background HI emission spectrum, while the green line represents the second velocity derivative of the observed HINSA spectrum. The spectra include typical radiometric noise. The HINSA feature has a peak optical depth of 0.2 and gas temperature of 10K.

2.6.2 Effects of Faulty Parameter Determination from Molecular Data

It is clear from the previous simulation that in an idealized case where the properties (center velocity, linewidth, and temperature) of the HI gas are well known, the HINSA optical depths can readily be determined to a high degree of accuracy. However in practice, the properties of the HI gas are not known but are instead surmised with some uncertainty from observations of molecular tracers. Hence it is necessary to examine the impact of incorrectly deriving the HI properties from molecular data. One concern is the gas temperature, which we obtain from ^{12}CO. It is reasonable to assume that the HI excitation temperature is equal to the kinetic temperature of the gas. However, temperature gradients

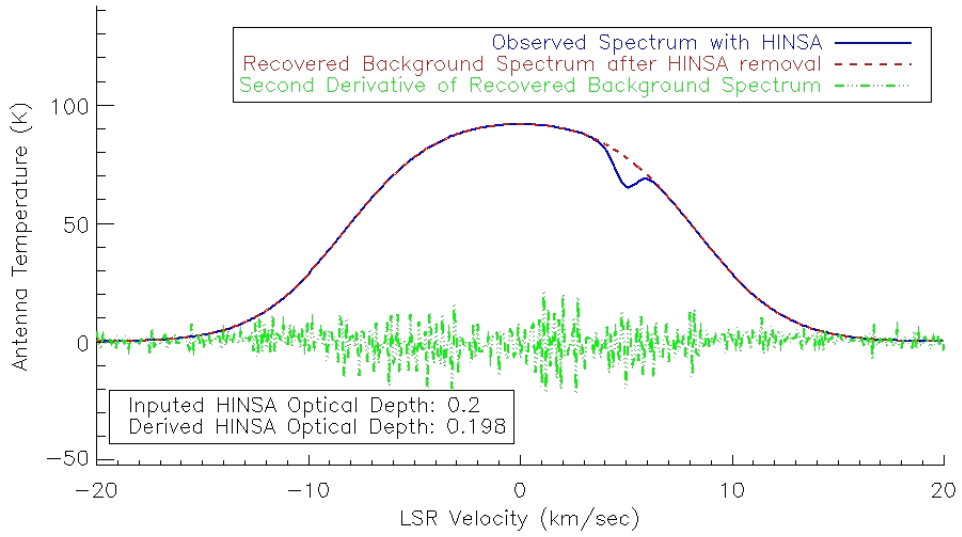

Figure 2.6: The original observed spectrum (blue) along with the derived background spectrum after HINSA removal (red) using the same simulated data as in Figure 2.5. The recovered background spectrum, and the calculated optical depth of 0.198 are nearly identical to the input parameters. The second derivative representation of the recovered background spectrum (green) shows no signs of the HINSA feature.

may exist resulting in the average temperature appropriate for analyzing the HINSA being different from that determined from the optically thick common isotopologue of carbon monoxide. Since HINSA features are typically optically thin, an incorrect estimate of the HI gas temperature would not strongly alter the shape of the fitted HINSA, but would only affect the derived optical depths and column densities. Thus, incorrect temperature estimates would be difficult to detect through fitting alone.

Incorrect estimates of the HI linewidths based on ^{13}CO data are plausible since the relation between them is only approximate. Here we investigate the effect of such an error by forcing our fitting routine to find the best fit HINSA optical depth while being constrained to use an incorrect value for the HI linewidth.

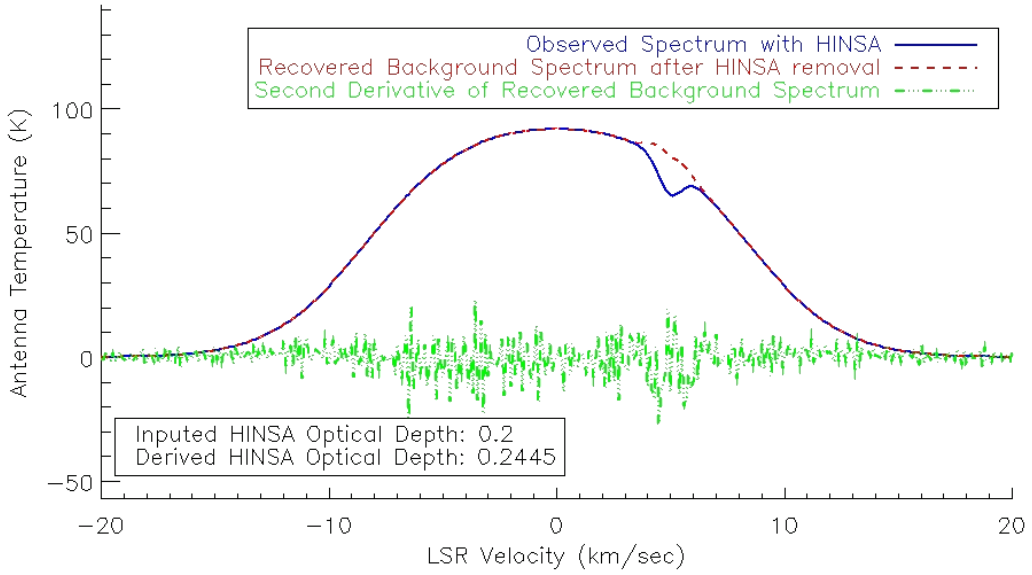

Figure 2.7: Using a HINSA linewidth 20% greater than the correct value when fitting the same simulated HINSA spectrum as in Figure 2.5 (blue) produces a distorted recovered background spectrum (red). The second derivative representation has a clear signature at the velocity of the HINSA absorption feature observed, and both its apearance and that of the the recovered background spectrum are unlikely to be representative of a realistic system.

[Li & Goldsmith (2003)] showed a variance of roughly 20% in the observed relation between HINSA and ^{13}CO nonthermal linewidths. Figure 2.7 shows the resulting fit when forced to utilize a HINSA linewidth 20% larger than the actual value of the same simulated data as in the previous example. It is no longer possible for the algorithm to produce a smooth recovered background spectrum, regardless of the optical depth assumed. This is a key indicator of an error in the input information. Figure 2.8 shows that the new best fit HINSA optical depth is 0.245 rather than 0.20. Similarly inaccurate solutions result when a faulty center velocity is used.

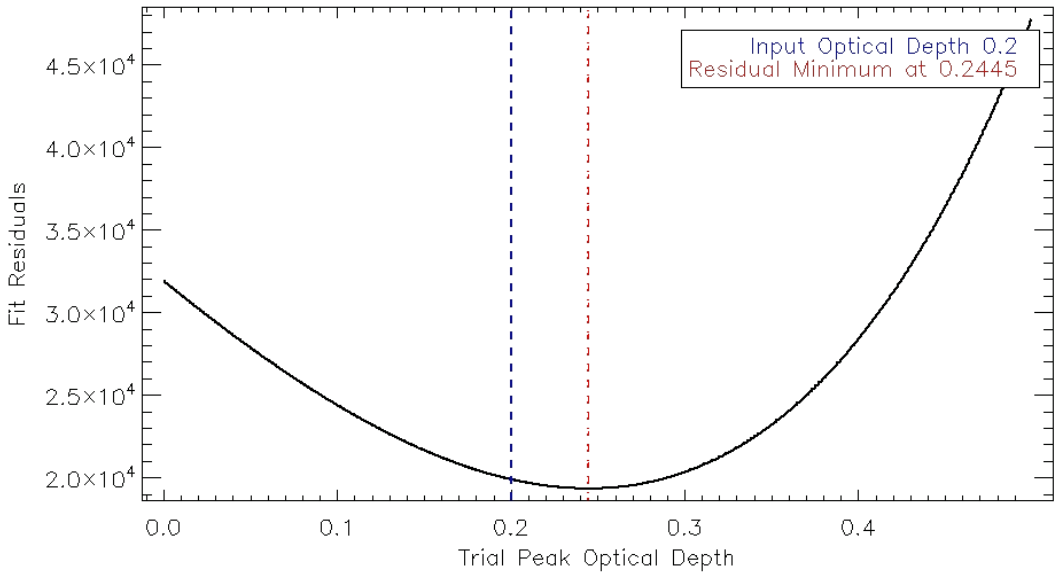

Figure 2.8: The squared sum residuals of the second derivative of the recovered background spectra for different trial values of the optical depth using the same data, and incorrect linewidth as in Figure 2.7. This function I represents the quantity to be minimized in our fitting procedure described in §2.4.5. The minimum value of I is considered to be the best fit, and in this case corresponds to an optical depth of 0.245, compared to the correct optical depth of 0.20. Realistic simulated statistical noise is included in this plot, and while the range in optical depth corresponding to a specified increase in the residuals may be significant, there are no localized minima to confuse the results.

2.6.3 Complex Examples

It is often the case that two emission components may overlap at the velocities at which HINSA may be expected, thus obscuring the absorption feature and increasing the uncertainty in the analysis. In such cases, previous techniques have had great difficulty in determining whether any HINSA is present at all. Our technique attempts to recover the smoothest, most gaussian-like background spectrum while being constrained by the HI gas parameters de-

rived from molecular observations. It is unlikely for emission components to appear over a HINSA features in such a way as to completely obscure the absorption.

As an example, Figure 2.9 shows that our technique is able to accurately extract HINSA features which on visual inspection might be ambiguous. In this simulation, the HINSA feature with an optical depth of 0.20 was placed in between two identical emission components. The recovered HINSA optical depth had a value of 0.208 which is well within the error limits of other uncertainties as discussed in the section. Figure 2.10 shows further examples with more complex geometry in which our technique is still able to pick out HINSA features with good precision.

2.6.4 Distorted Emission Components

The technique we present here is based on the assumption that the background emission is composed primarily of a superposition of gaussian–like components. Significant deviations from this assumption can lead to incorrect results. Figure 2.11 shows the case in which the background spectrum is complex, due to the superposition of overlapping components. The presence of a background component of width only modestly greater than that of the HINSA feature, in combination with the broader emission feature, results in a noticeable error in the derived HINSA optical depth. On casual inspection, there may be little indication that the solution is problematic (as shown in the lower panel of Figure 2.12). When dealing with real data, where the actual background spectrum is not known beforehand, there is no simple way to determine when such distor-

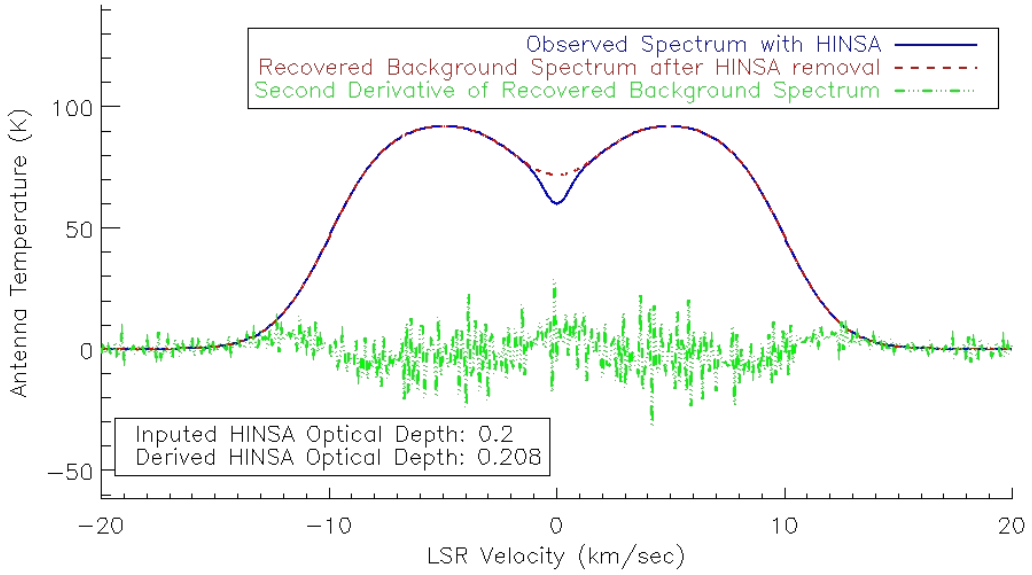

Figure 2.9: Two relatively broad identical emission components combined with a HINSA feature located midway between them yield the simulated observed spectrum (blue). The recovered background spectrum (red) and accompanying second derivative representation (green) illustrate the results after HINSA extraction. The derived optical depth is 0.208, which compares very well with the input optical depth of 0.20.

tions may occur, or what their effect might be on our derived HINSA optical depths. Though instances such as this are likely to be rare, it is worthwhile to be especially wary of HINSA measurements when the absorption feature seems to lie in the trough between two emission components.

2.6.5 Confidence in Derived HINSA Optical Depths from Simulated Data

It may be tempting to take Figure 2.8 and use standard methods for determining the uncertainties in least-squares linear fitting problems to determine the uncer-

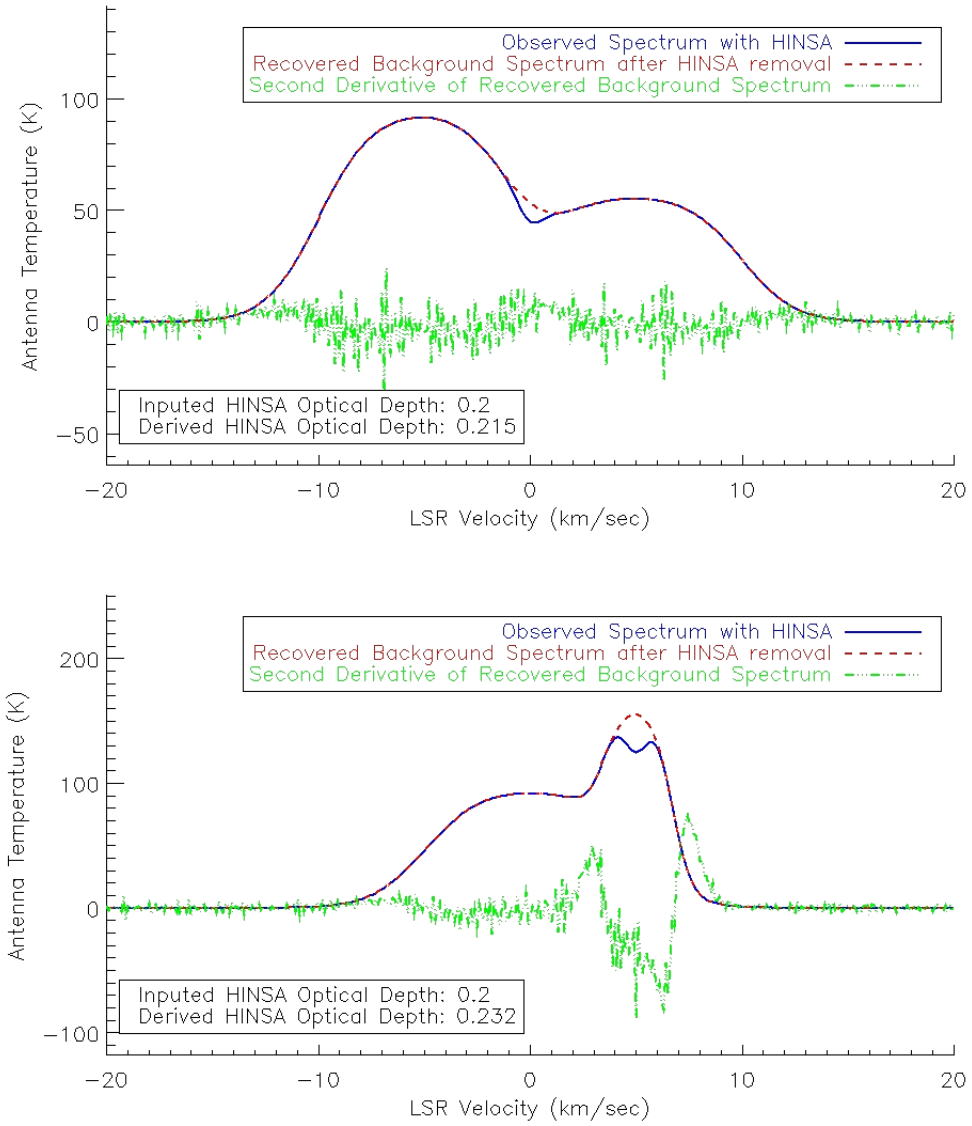

Figure 2.10: Upper: Two unequal emission components together with a 0.20 peak optical depth HINSA feature result in the simulated observed spectrum (blue). The recovered HINSA optical depth is 0.215, and the HINSA extraction results in the recovered background spectrum (red), which is nearly identical to the input background spectrum. Lower: A similar case where the HINSA feature has been placed to coincide with a narrow emission component whose shape is slightly distorted by the presence of another emission component. The derived HINSA optical depth of 0.232 is still close to the value 0.20 that was input to the calculation. The second derivative representation of the recovered background spectra (green) shows that there is still significant structure left after HINSA extraction. This structure is the result of the interaction between two emission components. 48

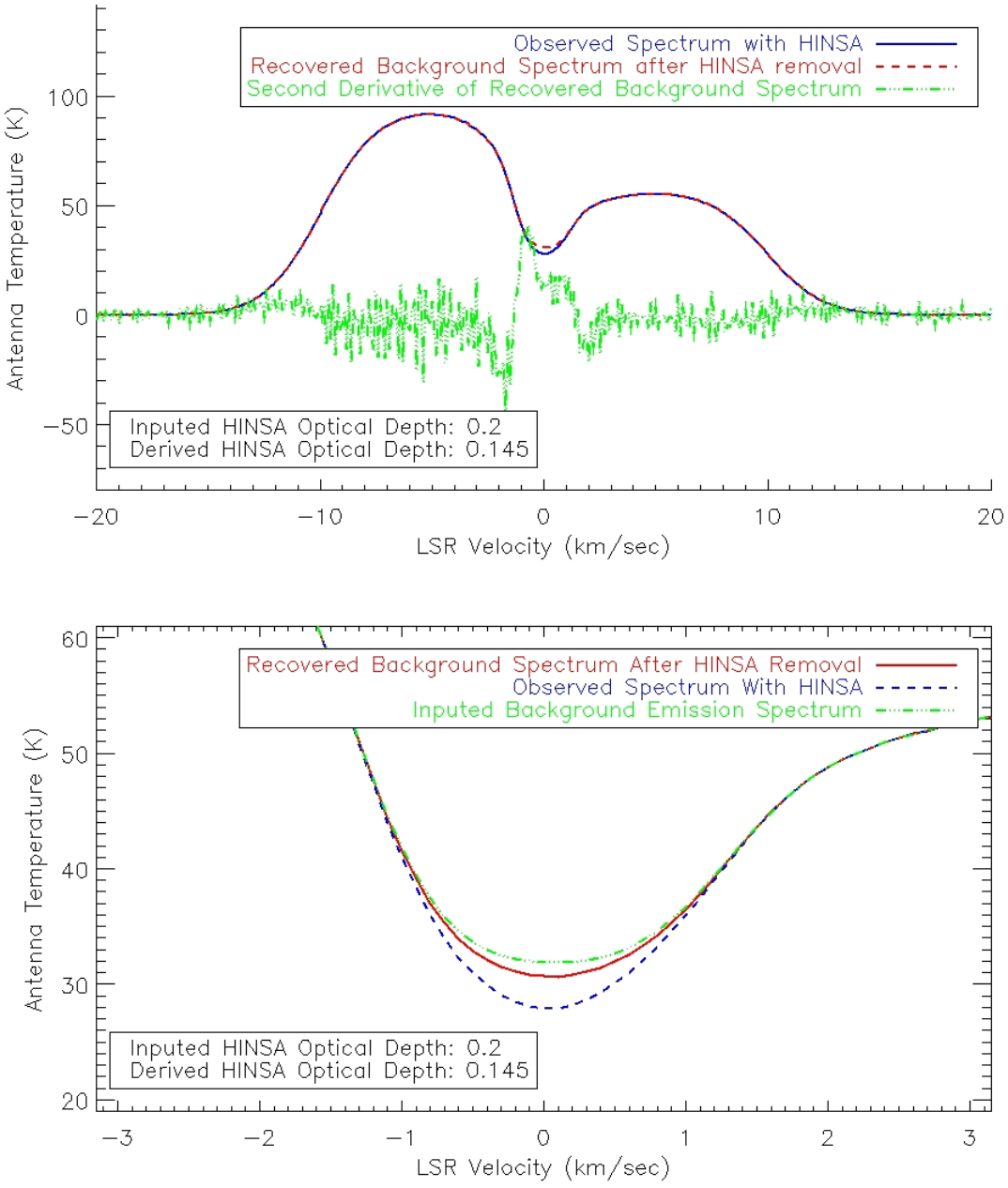

Figure 2.11: Upper: For comparison with Figure 2.10, a third emission component with brightness temperature of 30 K and center velocity of 0 kms^{-1} has been introduced to distort the shape of the emission spectrum at the location of the simulated HINSA feature. In this instance the derived HINSA optical depth of 0.145 differs considerably from the inputed value of 0.2. Lower: An expanded view of the region of interest showing the recovered and inputed background emission spectra.

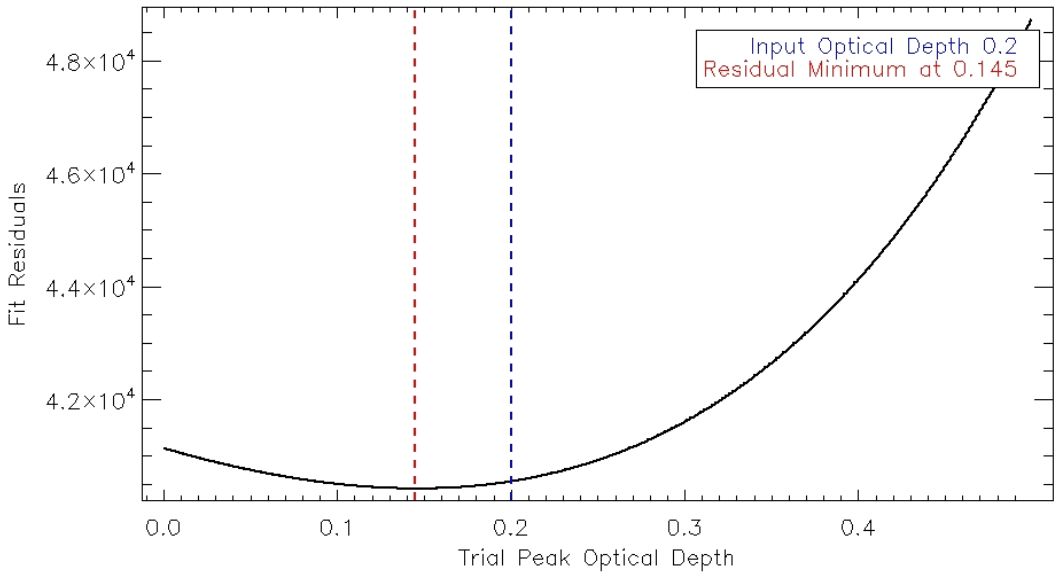

Figure 2.12: A similar residuals plot as in Figure 2.8 as applied to the solution in Figure 2.11. The behavior of the residuals is the same here even though the error in the solution is clearly evident (τ = 0.15 compared to 0.20). This demonstrates the difficulty in identifying incorrect fits in cases such as in Figure 2.11.

tainties in our estimates of τ based on the width of the trough of the fit residuals. But our problem does not strictly allow such analyses. There are two components that contribute uncertainty to our estimates of τ. The first is radiometric noise. The simulated data in this section all include realistic simulated noise for observations made with a large single-dish telescope such as Arecibo or the GBT. This source of uncertainty is in fact linear in nature and could be treated using traditional least-squares linear fitting analyses. However, as HI spectra are typically bright and easily obtainable with only a few seconds of integration time this source of uncertainty is insignificant compared to the other uncertainties. If we were to look directly at Figure 2.8, then the uncertainties due to radiometric noise would appear as small, narrow localized minima. However, in the case of this and all our simulations this contribution is smaller than even

the thickness of the line in the plot.

The dominant source of uncertainty which produces the trough is non-linear and somewhat systematic. The fundamental principle on which our technique depends, as discussed in §2.4.1, requires that our observed spectra resemble the superposition of multiple (positive and negative) gaussians. According to the radiative transfer equation however this is not strictly the case. When multiple emission and absorption components are superimposed they attenuate one another in a non-linear fashion. Hence our observed spectra will never strictly represent gaussians, but will only resemble them. This introduces a somewhat systematic, "nonlinearity" error which is much greater than that introduced by radiometric noise.

As an example, if we were to re-run the simulation from Figure 2.8 numerous times with all the same parameters for emission and absorption components but different radiometric noise (of the same average amplitude), the measured optical depth would always be very close to 0.245, the only variation in the results would be due to radiometric noise which in these realistic cases is insignificant. This represents a 22.5% error (not an uncertainty) relative to the original inputed value of 0.20 which is produced not by random local minima which would confuse the results, but by a systematic shifting of the entire residuals trough. This systematic error is produced when several emission and absorption components are superimposed in such a way that the final spectra no longer resemble simple superpositions of gaussians. Throughout this section we have shown successively more complex superpositions of this nature in an attempt to test the limits of this systematic error. We have found that for the vast majority of observations likely to be encountered, this error will be only a few percent. In

an attempt to find the limits, we constructed the most complex superpositions that would likely be observed in real data and found that in the very worst cases the systematic error reached only about 50%. Figures 2.9, 2.10, and 2.11 represent some of those complex cases. For the majority of observations, this nonlinearity error will be minor in comparison to other sources of error due to uncertainties in physical conditions in the cloud. In the most extreme cases, the nonlinearity error will be on a par with, but not dominant compared to these other sources of uncertainty, which are discussed in the following section.

These simulations cannot directly test the validity of our assumptions regarding the relations between atomic and molecular gas properties as those are inherently non–statistical uncertainties whose properties are currently not well known. However, the simulations do show that the solutions are modestly sensitive to any such errors in that errors in our ^{13}CO–based estimes of either the HI linewidths or center velocities neccessarily produce visible artifacts in the recovered background spectra after HINSA extraction, as shown in Figure 2.7. This allows us to identify faulty fits, where we can then go back to the molecular data and construct better templates for the HINSA extraction. Hence it is important to understand all the possible sources of uncertainty in our estimates of the HINSA properties based on molecular templates as discussed in the following section.

2.7 Limitations: Sources of Ambiguity and Uncertainty

While it has been shown in the previous section that our technique is able to produce good fits to the HI data when the HI gas properties are correctly de-

rived, there are several factors which limit the accuracy of our technique. These sources of error are non–statistical in nature in that they arise from our reliance on the association between HI and molecular tracers. As such, they make the placement of simple error bars on derived HI optical depths impossible. While it is certainly possible to place uncertainty estimates numerically through standard least-squares fitting methods, and compound those with estimates of the uncertainties due to measurements of the molecular parameters and their relation to the HI gas, any such numbers would be meaningless and misleading. The best way to estimate the uncertainties in our results is to examine the spread in the results in Figures 2.2 and 2.3 and assume that in an ideal case each component would be represented by a single line (of certain shape) which would be governed by the physical processes within the cloud such as the HI to H_2 conversion process. This would give us an upper limit on our uncertainty in deriving the HI/H_2 ratio. However, the present models of cloud evolution do not yet offer us sufficient confidence to make such estimates with certainty. More detailed observations and modeling of molecular cloud processes are necessary before such estimates can be made with confidence. It is our hope that the technique described in this paper will help in this regard. This development is likely to be an iterative process. It is important to note that the sources of uncertainty in previous techniques, while inherently somewhat different, are not smaller nor better determined than those in the method presented here. It is, however, of critical importance to quantify and to understand each of these sources of uncertainty in order to understand the level of confidence in the results obtained using this new technique.

2.7.1 Gas Temperature

Knowledge of the HI gas temperature is necessary for estimating the non-thermal linewidths of ^{13}CO as well as the observed linewidths of the HI gas, the measurement of the HI optical depth, and column densities both for HI and molecular tracers. As such, accurate temperature estimates are critical. At the present time the most practical method for estimating the HI gas temperature in these dark cloud cores is through obtaining the ^{12}CO temperature. Typically, ^{12}CO emission is optically thick, and thus if large scale velocity gradients are absent, as is generally the case in dark clouds, this measurement represents only the surface temperature of the cloud and does not necessarily reflect the average HI gas temperature in the interior of the cloud. The cores of these clouds are shielded from the external UV radiation field and thus are likely to be at a lower temperature than the surface. While this bias introduces overestimates of the HI gas temperature by only a few degrees, typical core temperatures are on the order of 10K thus the effect is significant. It may be possible to use alternate means to estimate the temperatures of other molecular tracers which share similar distributions as HI within a cloud. One promising candidate is the inversion transitions of ammonia. Detailed comparison of this or other tracers with ^{12}CO would require a better understanding of the spatial distribution of cold HI necessitating interferometric maps of HINSA features.

2.7.2 Radiometric Noise and Baselines

21cm spectra with high signal to noise ratios are relatively easy to obtain with short integration times. Radiometric noise should thus not significantly af-

fect HINSA measurements. Obtaining good baselines on the HI spectra is important in that any artificial slopes can significantly alter the derived optical depths. Since HI emission is highly variable spatially, ON-OFF observations are impractical. Total power ON measurents are ideal if system stability permits this approach to be used, as reported by [Li & Goldsmith (2003)]. Frequency-switched observations can yield sufficiently good baselines, but only if system bandpass and calibration are sufficiently good. A very successful combination of these techniques is available with the recently installed Arecibo L-Band Feed Array (ALFA) in conjunction with the Galactic-ALFA (GALFA) spectrometer at Arecibo. Least-Squares Frequency Switching (LSFS) allows the RF and IF bandpasses to be separately determined so that total power observations produce sufficiently good baselines for HINSA observations.

2.7.3 Choice of Molecular Tracer

[Li & Goldsmith (2003)] showed good correlations between the central velocities, nonthermal linewidths and spatial distributions of HINSA and both ^{13}CO and C^{18}O. In many cases, ^{13}CO shows a better spatial correlation, but C^{18}O shows a better linewidth correlation. This would not be expected if the relative abundances of HI, ^{13}CO, and C^{18}O were constant throughout the cloud. The variations may be a reflection of the higher critical density of C^{18}O, the density dependence of the HI/H_2 conversion process, and possibly CO depletion onto dust grains at high densities. Thus the choice of which molecule makes the best template for the HINSA linewidth is complex. Based on experience, using ^{13}CO fits provides somewhat better results. As a practical matter, the ^{13}CO lines are much brighter and easier to observe than those of C^{18}O. As a result, we have

selected ^{13}CO as the template molecule for HINSA extraction.

2.7.4 Distances and Foreground Gas

The presence of intervening HI emission sources between the observer and the HINSA source will tend to wash out the absorption and introduce underestimates of the HINSA optical depth. [van der Werf et al. (1988)] introduced an adjustment factor to compensate for this effect, however its precise value is poorly known. This approach was followed by [Li & Goldsmith (2003)], but these authors found it to be relatively unimportant for the relatively nearby clouds in the Taurus Molecular Cloud Complex. A more detailed study of the relation between HINSA features and distance is required when dealing with more distant sources.

2.7.5 Component Order

Several velocity components are often observed in molecular clouds. It is assumed that there are correspondingly multiple HINSA components. Equation 2.1 indicates that when multiple overlapping HINSA components are present along the same line of sight with appreciable optical depths, there is significance in which component is placed in the background, and which is in the foreground. There is no simple way to determine the sequence of multiple components along the same line of sight. Since the typical optical depths for HINSA are on the order of 0.1, the resulting ambiguity for the HI column densities is below 10%, smaller than the other sources of error in our technique.

2.7.6 Molecular Emission Fits and the Uniqueness Problem

The center velocities of an individual molecular component may vary significantly within a cloud. It is often the case that two components may be widely separated in velocity at one point in the cloud while being nearly indistinguishable in another region. This poses a problem when trying to make measurements on individual components and is especially pronounced when working with HI spectra with high thermal linewidths. Further, it is difficult to predict how a specific implementation of the technique proposed here might react when working with such spectra. When working with a sufficiently small number of spectra it is possible to recognize and dismiss the affected spectra by eye. However, in larger regions, where there may be many thousands of spectra, and where fully automated fitting algorithms must be used, the problem becomes more pronounced. Thus we have developed a method for partly alleviating the uniqueness problem and allowing for easier identification of overlapping emission spectra. This is a problem most often avoided in many projects involving complex emission spectra since usually only the total integrated intensity is used. For the technique presented here however, the individual properties of each emission component are necessary.

Molecular emission spectra are typically characterized by (overlapping) gaussian components. It is a property of gaussians that taking any gaussian function to the fourth power effectively reduces its linewidth by a factor of 2. Therefore, by taking all our molecular spectra to the fourth power prior to fitting, the individual emission components become significantly more apparent. However, doing this also greatly magnifies the noise in the spectra. Thus it is necessary to perform some filtering by removing the high-frequency Fourier

components of each spectrum. The magnification and filtering processes can significantly alter the amplitude, shape, and linewidths of the final spectra. However, the final center velocities remain the same. Thus, the filtered spectra may be used to identify the number and center velocity of the emission components within a spectrum. Subsequently, the known velocities can be used to constrain the fitting of the original data. While not yielding a unique solution, this method does allow more accurate fitting of molecular emission components using automated algorithms and dealing with large spectral data sets.

2.8 Summary

The significance of accurately measuring the HI content of dark clouds and star forming regions has long been recognized. HINSA features have been shown as a promising method to achieve this goal, but the difficulty in confidently disentangling HINSA from the galactic background emission has limited research efforts in this field. The technique described here builds upon previous work to provide new opportunities. By utilizing a second derivative representation in which HINSA becomes the dominant feature in the spectrum, and using information from associated molecular tracers to constrain our fits, we are able to obtain HI column densities with greater confidence than previously possible. This technique enables us to study individual velocity components within a cloud. Several uncertainties and sources of error still remain, most notably the errors inherent in temperature determination through ^{12}CO, and the precise relations between the properties of cold HI and molecular tracers such as ^{13}CO. As shown in §2.6 the purely statistical errors derived from our constructed data were only a few percent in simple cases which represent the majority of observed spectra.

The nonlinearity error may be as large as 50 percent in the extreme cases.

While the scope of this paper is limited to a demonstration of the new technique, the improved confidence in the results have the potential to yield significant scientific advances in the field of molecular cloud and star formation studies which are deferred to a subsequent publication. The two astronomical sources discussed briefly here for demonstration purposes are part of a much larger survey of over 30 dense cloud cores. In conjunction with numerical modeling these data provide us with the chemical ages of the clouds and individual components therein, thus providing a significant constraint on theoretical models of star formation. Large maps have been collected with the Arecibo L-Band Feed Array (ALFA) of the Taurus and Perseus star forming regions. These regions show plentiful HINSA features whose analysis may shed light on the dynamics of such complexes including the processes which may have triggered their formation.

	V_{LSR}(kms^{-1})	HI Mass($M_\odot$)	H_2 Mass($M_\odot$)	Mean HI/H_2	Peak H_2 Dens.(cm^{-3})	Mean H_2 Dens.(cm^{-3})
L134 A	2.35 – 3.40	$4.0 \cdot 10^{-2}$	71	$1.1 \cdot 10^{-3}$	2490	910
L134 B	1.80 – 2.75	$9.5 \cdot 10^{-3}$	41	$4.7 \cdot 10^{-4}$	2390	660
L134 C	0.50 – 2.75	$4.7 \cdot 10^{-3}$	8.4	$1.1 \cdot 10^{-3}$	1530	310
L134 D	–0.7 – 1.10	$5.1 \cdot 10^{-3}$	12	$8.5 \cdot 10^{-4}$	1230	480
L1757 A	4.70 – 6.00	$1.6 \cdot 10^{-2}$	31	$1.0 \cdot 10^{-3}$	840	310
L1757 B	2.50 – 3.35	$2.7 \cdot 10^{-1}$	45	$1.1 \cdot 10^{-2}$	540	270
L1757 C	1.50 – 2.20	$3.0 \cdot 10^{-1}$	106	$5.7 \cdot 10^{-3}$	1560	305
L1757 D	0.80 – 1.50	$1.7 \cdot 10^{-1}$	95	$3.5 \cdot 10^{-3}$	880	290

Table 2.1: Derived Component Properties for L134 and L1757. The component radii are estimated by the extent of the ^{13}CO emission and are used to estimate cloud depths and thus volume densities. In L1757, the fact that some components have roughly the same H_2 density but very different HI abundances suggests that the different components may have formed at different times.

	Peak HINSA optical depth	Peak ^{13}CO optical depth	Peak ^{12}CO T_{ex} (K)	Mean continuum at 21cm (K)
L134 A	0.53	0.84	19	3.1
L134 B	0.20	0.67	17	
L134 C	0.20	0.24	17	
L134 D	0.19	0.22	14	
L1757 A	0.20	0.31	16	3.2
L1757 B	0.35	0.29	17	
L1757 C	0.36	0.74	19	
L1757 D	0.30	0.35	15	

Table 2.2: Derived Component Properties for L134 and L1757 continued. The ^{12}CO temperature, derived directly from the ^{12}CO spectra, is used as an estimate of the HI temperature represented by T_H in Equation 2.1.

CHAPTER 3

A SURVEY OF HI NARROW SELF-ABSORPTION IN MOLECULAR CORES

3.1 Introduction

Molecular clouds must have been composed of primarily atomic material when at some time in the past their density and extinction were not high enough to provide sufficient shielding against external radiation to allow molecules to form. Similarly, regions within clouds where stars form are primarily molecular so that at some point they must have converted the majority of their material to molecular form. The primary process responsible for this atomic to molecular conversion is the formation of molecular hydrogen (H_2) on dust grains, but our understanding of this process is limited by several factors including uncertainty regarding grain composition, atomic sticking and mobility coefficients, as well as gas temperature.

As a cloud collapses its fractional abundance of atomic hydrogen (HI) will decrease with time. If this HI gas coexists at the same cloud depths as molecular material then it too will be shielded from external UV fields and will cool. Furthermore, modeling has shown that even after a cloud has converted the majority of its gas to molecular form it will retain a small steady-state abundance of HI due to dissociation of H_2 by cosmic rays which are able to penetrate even the cloud's core [Solomon & Werner (1971), Goldsmith & Li (2005)]. Such cold HI gas will be visible at 21cm in absorption against the warmer galactic background HI emission. Cold HI gas which is associated with the molecular material is expected to show correlation with the spatial distribution,

line of sight velocity, and non-thermal linewidth of molecular tracers such as ^{13}CO. These absorption features have been termed HI Narrow Self-Absorption (HINSA) and have been observed and studied in previous studies in a number of clouds [Li & Goldsmith (2003), Goldsmith & Li (2005), Krco et al. (2008)]. A distinction should be made in that HINSA features are that subset of HI Self-Absorption (HISA) features where molecular gas is highly correlated with HI gas in position, velocity, and non-thermal linewidth. HISA features have been studied extensively in a number of works such as [Garzoli & Varsavsky (1966), Heiles (1969), Knapp (1975), Heiles & Gordon (1975), Wilson & Minn (1977), McCutcheon et al. (1978), Myers et al. (1978), Bowers et al. (1980)], [Batrla et al. (1981), Shuter et al. (1997), van der Werf et al. (1988)], [Feldt & Wendker (1993), Montgomery et al. (1995), Gibson et al. (2000)], [Kavars et al. (2003)], among others. HISA features features may be the result of a number of phenomena, while HINSA features are believed to be specific to associated molecular clouds.

Due to the complex nature of the background galactic HI emission it is very difficult to obtain accurate column density measurements from HINSA features. A new technique has been developed for extracting HI column densities which takes advantage of the observed correlations between molecular tracers (such as ^{13}CO) and the cold HI gas that produces HINSA. A detailed discussion of the new technique, its strengths and weaknesses, and limitations of previous analysis methods can be found in [Krco et al. (2008)]. The new technique allows us to determine the HI to H_2 ratio in molecular clouds in greater detail, and permits us to measure the atomic to molecular ratio in individual velocity components within a cloud.

Understanding the HI to H_2 ratio in molecular clouds and individual velocity components can lead to significant insight on the formation process of H_2 on dust grains and provide limitations on star formation models. One outstanding question is whether all portions of a molecular cloud or larger molecular complexes are at the same stage in their atomic to molecular conversion process. Differences in the HI to H_2 ratio could indicate different chemical ages, compositions, dust grain properties, or environmental effects which might affect the HI to H_2 conversion process, for different regions within a cloud.

The study presented here aims to answer several questions relating to the viability of using HINSA features as a tool for studying star formation, and what information can be obtained from such studies. The most important issues addressed by this study are:

- What fraction of molecular clouds exhibit visible HINSA features? (Section 3.3)
- Are HINSA features present outside of the Taurus Molecular Cloud Complex? (Section 3.3)
- Is this fraction consistent with the notion that all molecular clouds contain at least steady state abundances of cold HI? (Section 3.3)
- Does distance play a significant role in the detectability of HINSA due to foreground emission as expected [van der Werf et al. (1988)], and if so, is there a limiting distance to which we can detect HINSA features? (Section 3.5.1)
- Is there a spatial correlation between the fraction of HINSA-visible clouds in relation to position or inclination from the galactic plane? (Section 3.5.1)

- Do clouds belonging to similar molecular complexes exhibit similar HI to H_2 ratios and is there any relation between the HI to H_2 ratios and the nature of the given complexes? (Section 3.5.2)
- How does the HI abundance vary as a function of position, and of density within a cloud? (Section 3.6)
- Do individual molecular clouds exhibit variations in the HI to H_2 ratio spatially or as a function of velocity? (Section 3.6)

Sections 3.2, 3.3, and 3.4 describe the survey, the prevalence of HINSA features, and data analysis methods used throughout this work. Section 3.5 gives a summary of the data results throughtout the survey while Section 3.6 focuses on individually mapped clouds. Section 3.7 summarizes the obtained data to answer the most important questions as stated above.

3.2 Current Survey

To provide appropriate data to answer the questions stated in Section 3.1 we selected 48 clouds at a wide range of positions and distances (ranging from 140 to 700 parsecs). It was expected that the presence of active star formation may hinder the detection of HINSA due to heating of the HI gas by internal radiation. For this reason cores known to have stars present were excluded. The bulk of the chosen sources were selected from the Lynds catalog [Lynds (1962)] having peak optical extinction of 6 magnitudes or more. In order to minimize overlap with past and planned future surveys, all sources were chosen to be outside of the field of view of the Arecibo telescope.

3.2.1 GBT Observations

In accordance with the technique described in [Krco et al. (2008)], it was necessary to obtain at least HI, and OH single spectrum (SS) observations using the Green Bank Telescope (GBT) for the purpose of distinguishing HINSA features associated with molecular clouds from other dips that may be present in the HI spectra. The Spectral Processor was used as the backend with a 0.1 kms^{-1}channel width at 1440 MHz and 1667 MHz on 4 bands which were dedicated to observing the corresponding lines of HI and OH simultaneously. Telescope pointings were performed at the beginning of each day of observation against known compact continuum sources. Data and baselines were obtained using in-band frequency switching for all sources. However, in many cases the observed background HI emission was so wide in velocity that out-of-band frequency switching was required. All SS observations had ON-source initial integration times of at least 60 seconds. However, subsequent observations were obtained and averaged together on sources where the OH line was not apparent with only 60 seconds of integration.

Where possible, initial pointings for SS observations were selected to target peaks in previously observed ^{13}CO emission. However, such data were not available for most clouds and core positions were estimated using extinction in optical images, or using extinction maps from the 2 Micron All Sky Survey (2MASS). Several sources have multiple SS pointings which were used to better determine the positions of the molecular cloud cores where initial OH data seemed to indicate that the beam had missed the center of the molecular cloud.

Upon completion of the SS pointings, 9 clouds were selected which exhibited the most unambiguous HINSA features. These clouds were mapped at 21cm

using On-The-Fly (OTF) mapping and out-of-band frequency switching. The map sizes for individual clouds varied from .014 to 1.67 square degrees on the sky.

3.2.2 FCRAO Observations

To fully utilize the HINSA analysis technique described in [Krco et al. (2008)] it was necessary to obtain ^{13}CO (J = 1 - 0) maps to use as a molecular template for associated HI spectra obtained with the GBT. Similarly, ^{12}CO (J = 1 - 0) data were obtained to estimate cloud temperatures. These 3mm data were obtained using the Five College Radio Astronomy Observatory (FCRAO) with the 32 pixel SEQUOIA backend using OTF mapping. The Dual Channel Correlator (DCC) was used with a 25 MHz bandwith and 25kHz channel spacing.

The contrast between the 45″ FCRAO and 9′ GBT beams required us to obtain small FCRAO maps even in positions where there were only GBT SS observations available. Time and weather limitations prevented us from obtaining complete data for all the GBT sources, and as such, the most interesting sources were observed by priority. 26 of the GBT sources have 20′ x 20′ ^{13}CO and ^{12}CO maps available centered on at least one GBT SS position. All sources mapped at the GBT in HI have large ^{13}CO maps with partial coverage ^{12}CO maps. Tables 3.1 and 3.2 contain a listing of all pointings at each SS source where FCRAO data was available. Table 3.3 lists all SS sources observed at the GBT for which no FCRAO observations were made. Table 3.4 lists the 9 clouds for which extended maps were made with the GBT.

3.3 Prevalence of HINSA Features

Previous studies have focused almost exclusively on identifying HINSA features within the Taurus Molecular Cloud Complex where HINSA was found to be present in roughly 80% of the observed molecular cores [Goldsmith & Li (2005)]. An important goal of this survey is to determine whether HINSA features are unique to Taurus, or other nearby molecular cloud complexes or whether they represent a more general phenomenon to be found in more distant complexes or even isolated cores. Determining whether a HINSA feature is present can be accomplished through visual inspection of HI and associated OH spectra.

Figure 3.1 shows overlaid HI and OH spectra for 4 of our clouds. In order for an absorption feature to be identified as HINSA it must be centered at the same velocity and have a similar linewidth as the molecular emission at the same sky position. The presence of other dips in the HI spectra underscores the necessity of obtaining complementary molecular data to determine which features are due to cold HI gas associated with molecular clouds. It should be noted that L1780 and L63 have significantly lower background HI emission temperatures and thus would require much higher cold HI optical depths in order to display HINSA features comparable to those seen in some of the other clouds in the survey.

The prevalence of HINSA features and what factors may affect their visibilty are important questions, as noted in section 3.1. This survey found 40 HINSA sources in 48 clouds (83% detection rate) which is comparable to the detection rate of 77% found in Taurus [Li & Goldsmith (2003)]. Previous sur-

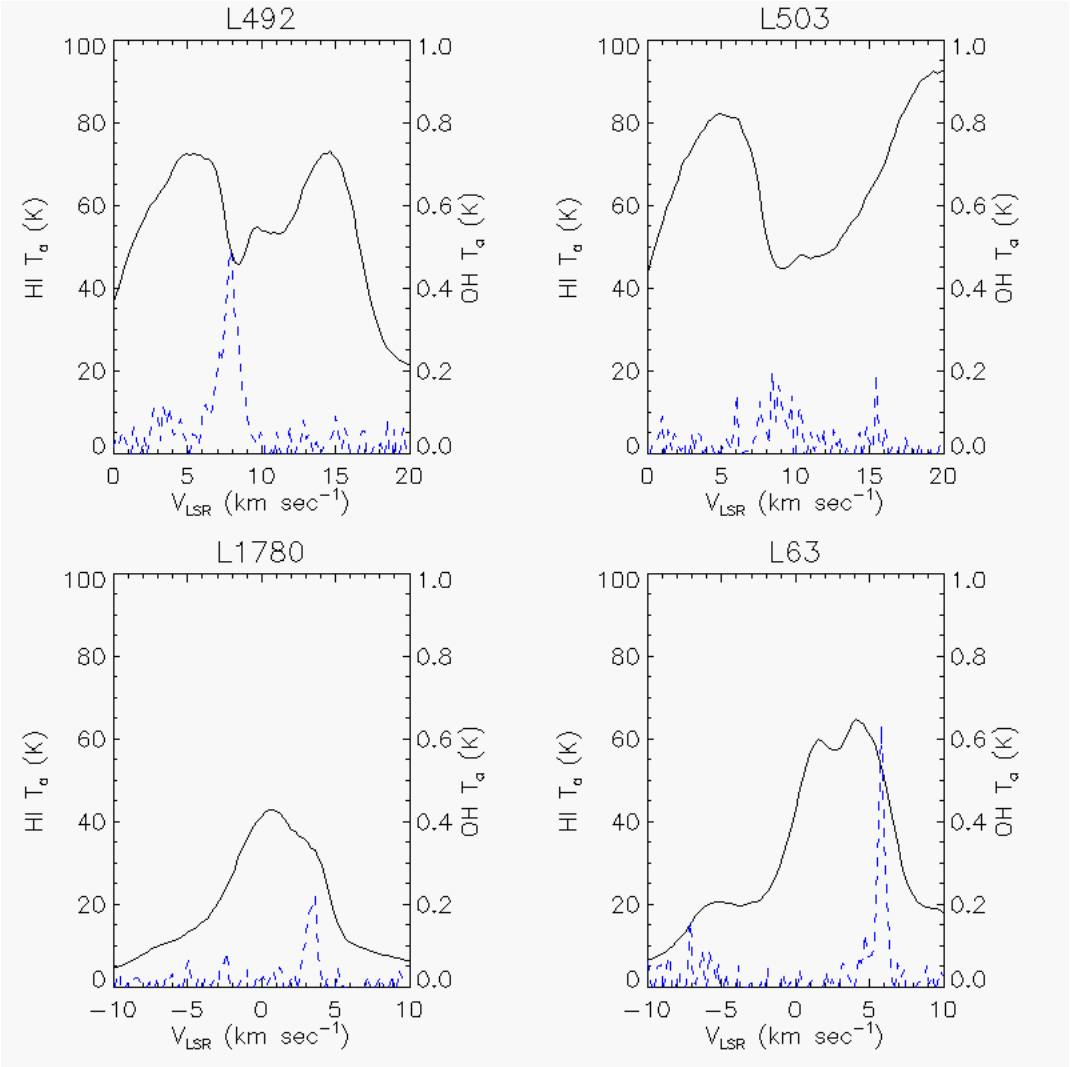

Figure 3.1: HI (solid) and OH (dashed) spectra toward 4 clouds from our survey. L492 and L503 exhibit clear HINSA features with the same velocities, and similar line widths as the OH emission. In contrast L1780 and L63 display no such features even though they show OH lines of similar intensity as the other two clouds. L492 and L503 exhibit similar HI absorption depths with very different OH line intensities. This contrast provide a suggestion that the atomic to molecular gas ratios may differ significantly from one cloud to another.

veys, such as [Knapp (1974)], found absorption features toward roughly a half of the surveyed clouds. However, those survey were conducted with significantly larger beam sizes and velocity resolutions reducing the number of possible detections. In each of the 8 sources with HINSA non-detections, there were OH emission components of comparable intensity to those in clouds where HINSA was found. It is expected that HINSA features would be more difficult to detect in clouds which are further away since at a greater distance there is a greater chance of intervening warm HI emission which would mask the absorption feature. In addition, more distant clouds have smaller angular sizes and fill a smaller portion of any HI beam. Figure 3.2a shows clearly that, within the 700pc range of this survey, no such effect is observed. The fact that HINSA non-detections are not clearly concentrated at the largest observed distances implies that HINSA features can probably be observed at even greater distances. Figure 3.2a does however show that most non-detections are located toward the Galactic center. It is possible that there is some physical reason for this, but Figure 3.2b shows that a large portion of the surveyed clouds are in the direction of the Galactic center and that the non-detections are all located near other clouds that do display HINSA feaures. This makes the existence of a directional influence on HINSA detections unlikely.

The depth and detectability of HINSA features against a background HI emission spectrum (T_{bg}) is expectedly dependent on the brightness of the HI emission at the velocity of the molecular emission components. Where the background HI emission is weaker the cold HI associated with a molecular cloud would have to be colder or have a higher optical depth in order to produce an absorption feature or the same depth as that with a stronger HI background. Figure 3.2c shows that non-detections are concentrated in regions where T_{bg} is

less than 100K, while at higher T_{bg} the percentage of non-detections drops off significantly. All 8 of the clouds with no detected HINSA have molecular emission at velocities and positions where T_{bg} is less than 100K which is consistent with the idea that HINSA features are more difficult to detect in front of weaker background HI emission.

It is reasonable to expect that clouds which have lower molecular column densities would also tend to have less accompanying cold HI available to produce absorption features. Figure 3.2d compares T_{bg} with derived H_2 column densities (N_{H2}) for all velocity components and all positions where ^{13}CO is available. This plot shows not only that non-detections are more common at lower T_{bg} but also that they occur more frequently within clouds that exhibit low H_2 column densities. For T_{bg} of 50K or less (where half of our clouds with no detections lie) there are no detections where N_{H2} is less than $10^{21} cm^{-2}$. None of the 8 clouds without HINSA detections has accompanying ^{13}CO data from which H_2 column densities could be derived, and the OH observations were only made with the intent of identifying molecular line velocities and are thus insufficient to derive proper OH column densities. Consistent with Figure 3.2d we assume that those clouds probably have H_2 column densities below $10^{21} cm^{-2}$.

Figure 3.2 does not provide any single clear answer to the question why certain clouds and velocity components within clouds exhibit HINSA features while others do not. The lack of any non-detections in Figure 3.2d at $T_{bg} > 100K$ and $N_{H2} > 10^{21} cm^{-2}$ may indicate that there is some abundance of cold HI gas located in all molecular clouds. This is consistent with the concept of a minimal HI abundance due to cosmic ray dissociation of H_2 as discussed in [Goldsmith et al. (2007)]. Figure 3.2d also shows that HINSA features are un-

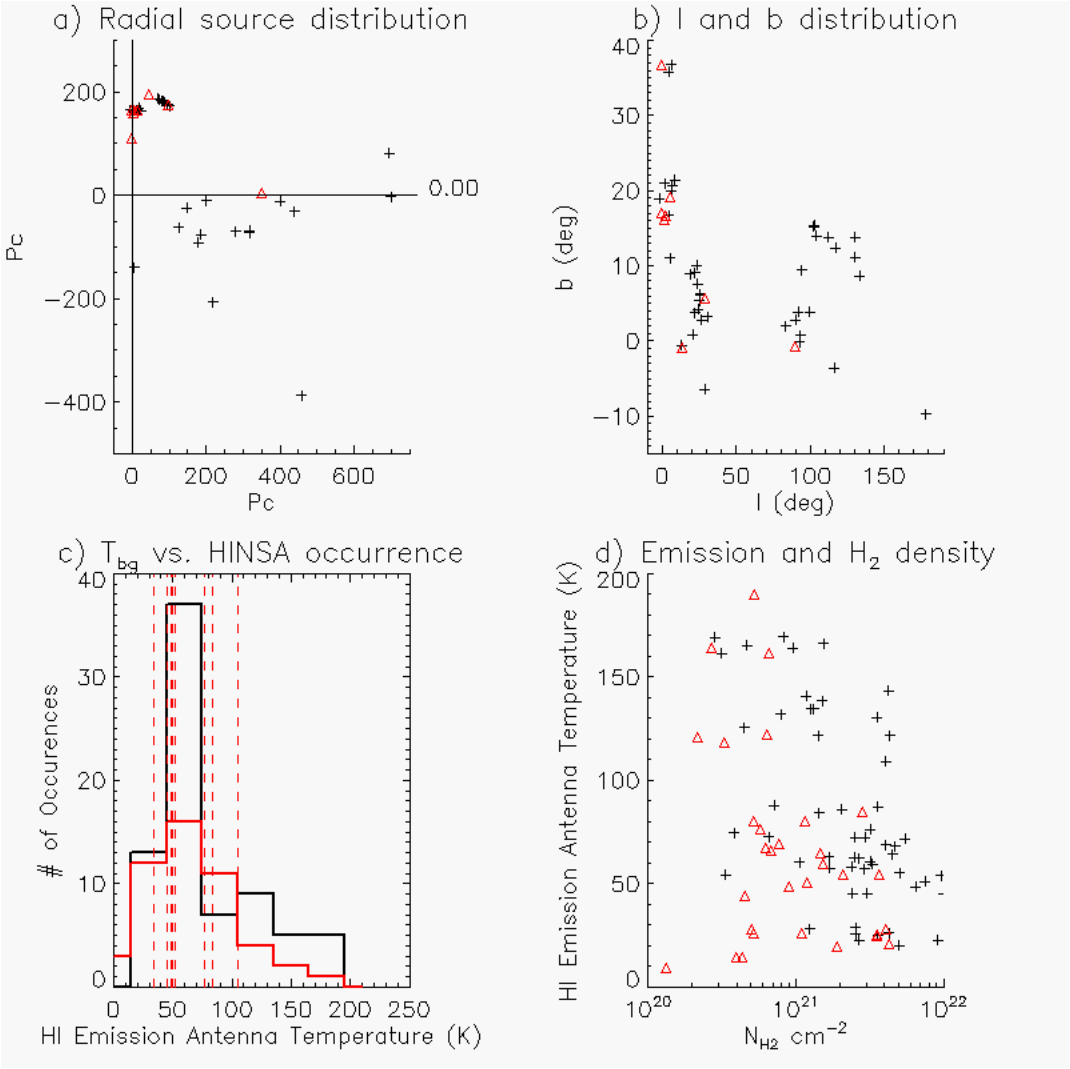

Figure 3.2: a) Positions of all observed clouds within the survey within the Galactic disk relative to the Sun. The Sun is located at (0,0), the Galactic center is located toward the top of the page with Galactic longitude increasing clockwise. Black crosses represent HINSA detections while red diamonds represent non-detections. b) Galactic longitude (l) and latitude (b) of all clouds within the survey. c) Histogram of HINSA detections (black, solid) and non-detections (red, solid) with respect to the background HI emission temperature at the velocities of molecular emission for all velocity components of all clouds within the survey. The dashed vertical lines represent the HI antenna temperatures of the 8 clouds with no HINSA detections. d) Background HI emission temperature vs. estimated H_2 column density for all velocity components of all clouds where ^{13}CO is available. The derivation of H_2 column densities is discussed in more detail in §3.4.2.

detectable in cloud where $N_{H2} < 10^{21} cm^{-2}$ at positions and velocities where $T_{bg} < 50K$ using the techniques and observing methods of this survey. However, the extensive co-existence of detections and non-detections in the intervening parameter space is a strong indication that there may be very different abundances of cold HI among molecular clouds which would indicate rather different chemistries and physical conditions which need to be studied further.

3.3.1 Detection Limit of HINSA features

Since Figure 3.2d implies that all molecular clouds are likely to have some cold HI present, it is important to be able to place upper limits on HI column densities where HINSA features are not detected. As discussed in [Krco et al. (2008)], the brightness of HI emission lines with large radio telescopes such as the GBT or Arecibo means that the detectability of HINSA features is generally not limited by systematic noise in the spectra, but by the ability to distinguish absorption dips from features in the emission spectrum. This holds true in the current survey as well. Further, the depth of any HINSA feature is dependent not only on the column density of HI present but also on the temperature of the absorbing HI relative to that of the warm HI background emission at the velocity and position of molecular emission. As discussed in [Krco et al. (2008)] the detectability of HINSA features is also dependent on the shape of the background emission. Thus, estimating HI column density upper limits is a non-trivial problem *which is largely independent of observing parameters*.

The total integrated intensity of the HINSA feature (I_{HINSA}) is determined by subtracting the observed HI spectrum (T_a) from the derived HI background

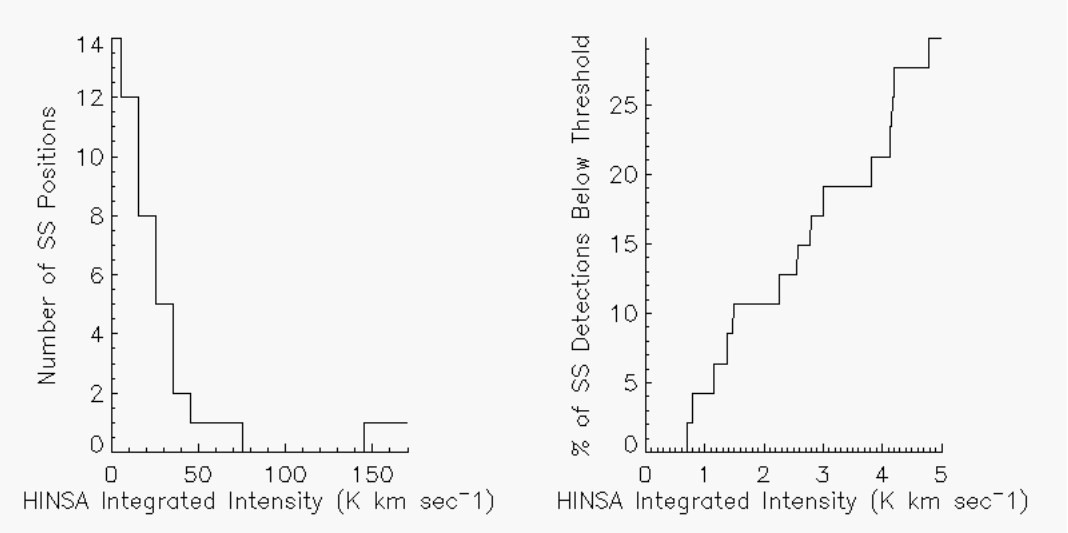

Figure 3.3: (left) A histogram of all Single-Spectrum (SS) positions where HINSA features are observed in 10 $K\ km\ sec^{-1}$ bins based on the total HINSA integrated intensity of each spectrum. (right) The percentage of SS HINSA detections (vertical axis) that have HINSA integrated intensities (horizontal axis) below a specific value. For example, only 5% of our HINSA detections have HINSA integrated intesities below $1K\ km\ s^{-1}$, and 30% below $5K\ km\ s^{-1}$. The lowest HINSA integrated intensity detected is of $0.7K\ km\ s^{-1}$.

spectrum (T_{bg}) received after all the HINSA features present are removed, and integrating over all velocities. The survey contains a sufficiently large sample of HINSA detections that we can gain a rough estimate of the minimum observable value of I_{HINSA}. Figure 3.3 shows that the bulk of HINSA features are small ($I_{HINSA} < 30K\ km\ s^{-1}$) with only a few exceptions having lower values. The smallest observed I_{HINSA} is 0.70 $K\ km\ s^{-1}$ while 95% of all observed HINSA features occur at $I_{HINSA} > 1K\ km\ s^{-1}$. While the comparison is not strictly accurate, it could be said that $1K\ km\ s^{-1}$ is a representative 2 standard deviation detection limit, for it encompasses 95% of the observed data. Thus, any derived HI column density upper limit based on a I_{HINSA} detection limit of $1K\ km\ s^{-1}$ will similarly have 95% statistical significance.

Choosing a specific I_{HINSA} as a detection limit permits evaluation of minimum detectable HINSA column densities. The general radiative transfer equation can be written as

$$T_a(v) = T_{bg}(v) \cdot e^{-\tau(v)} + T_F \left(1 - e^{-\tau(v)}\right) \ , \tag{3.1}$$

where v represents velocity, $T_a(v)$ and $T_{bg}(v)$ represent the observed and expected background antenna temperatures, T_F is the gas temperature of the foreground HI gas, and $\tau(v)$ is the optical depth of the foreground HI gas which produces the HINSA feature. This is a simplified expression which does not include any terms for continuum emission, beam dilution, or any foreground HI emission in front of the cold absorbing cloud. Those factors are discussed in detail by [Krco et al. (2008)] and are accounted for in all resultant HI column densities derived in this work, but are unnecessary for the present derivation. Excluding these factors, the integrated intensity of the HINSA feature can then be expressed as

$$I_{HINSA} = \int_{-\infty}^{\infty} T_{bg}(v) - T_a(v)\, dv = \int_{-\infty}^{\infty} \left(1 - e^{-\tau(v)}\right)\left(T_{bg}(v) - T_F\right)\, dv \ , \tag{3.2}$$

which represents a daunting integral without fore-knowledge of the shape of $T_{bg}(v)$ or $\tau(v)$. Since in HINSA non-detections there is very little information on the velocity position or width of any HINSA features, it is reasonable to assume that if a HINSA feature existed, it would occur at the same velocity as the associated molecular emission (v_{me}). It is then reasonable to assume that the HI background temperature remains approximately constant over the linewidth of any HINSA feature, thus $T_{bg}(v)$ can be treated as a constant ($T_{bg} = T_{bg}(v_{me})$). Expanding the exponential in equation 3.2 yields

$$I_{HINSA} = (T_{bg} - T_F) \int_{-\infty}^{\infty} \tau(v)\, dv \ , \tag{3.3}$$

where only the first two terms of the expansion are necessary since HINSA optical depths are typically less than 1. HINSA column densities are directly related to emission integrated intensities by the well known relation

$$N_{HI} = 1.82 \cdot 10^{18} \left(T_F \int_{-\infty}^{\infty} \tau(v)\, dv \right) \left(K\ km\ s^{-1} \right)^{-1} cm^{-2} \quad . \tag{3.4}$$

The critical HI column density required for detection (N_{crit}) based on a critical HINSA integrated intensity (I_{crit}) can be written as

$$N_{crit} = 1.82 \cdot 10^{18}\ I_{crit}\ \frac{T_F}{T_{bg} - T_F}\ K^{-1}\ km^{-1}\ sec\ cm^{-2} \ . \tag{3.5}$$

Substituting the integrated intensity limit for the detectable HINSA column densities derived earlier ($I_{crit} = 1 K\ km\ s^{-1}$ yields

$$N_{crit} = 1.82 \cdot 10^{18}\ cm^{-2}\ \frac{T_F}{T_{bg} - T_F} \ . \tag{3.6}$$

Equation 3.6 permits the estimation of the minimum observable HINSA column density for a cloud with a given gas temperature T_F and background HI emission T_{bg} at the velocity where HINSA is expected. It is important to note that this relation is independent of observing parameters under the assumption that the noise in any observed HI spectra is neglible. In particular, the presence of any foreground HI gas which would dilute any absorption features can be accounted for by using the p-parameter [van der Werf et al. (1988)] which would serve to increase the minimum detectable column density. All of the clouds

with no HINSA detections also do not have any accompanying ^{12}CO data and thus an estimate of the gas temperature of 15K is used. Tables 3.1,3.2, and 3.3 give N_{crit} estimates for all SS observations adjusted for beam fill and foreground gas effects [Krco et al. (2008)]. In cases where no HINSA is detected, this value serves as an upper limit on the HINSA column density. It would not be entirely correct to say that N_{crit} is a measure of the uncertainty in any HINSA detection as there are other, less quantifiable factors present which are discussed in [Krco et al. (2008)] and section 3.5.3.

3.4 Reduction and Data Analysis Methods

[Krco et al. (2008)] describe in detail the technique used for identifying HINSA features and deriving HI column densities as well as other parameters from HI, ^{13}CO, and ^{12}CO observations. Here we will present only a brief description of each step with examples from the present survey.

3.4.1 Reconciling 21cm and 3mm Beam Sizes

Figure 3.1 shows that OH spectra, which can be obtained simultaneously and with a similar beam size as HI spectra, can be used for a cursory differentiation of HINSA features from other background emission properties. [Goldsmith & Li (2005)] showed that OH is a less reliable tracer of HINSA features than ^{13}CO. However, ^{13}CO data obtained at FCRAO has an inherent beam size of 45″ compared with the 9′ HI GBT beam. This presents a challenge in that the technique described in [Krco et al. (2008)] is strongly dependent on a direct

comparison between ^{13}CO and HI spectra. Since the linewidths of HINSA features are often dominated by their thermal components, it is important to properly identify and fit all the velocity components in a ^{13}CO emission spectrum in order to derive proper HINSA non-thermal linewidths. Further, the HINSA technique utilized here makes fundamental assumptions about the gaussian nature of both HI and ^{13}CO optical depths and any deviations from those assumptions introduce uncertainties in the final derivation.

To facilitate a direct comparison between the 45″ ^{13}CO and 9′ HI data it is necessary to synthesize a 9′ ^{13}CO beam using the 45″ data. This is done by muliplying the ^{13}CO map by a function which approximates the GBT beam response. In cases where HI maps with multiple positions are present this process is commonly known as regridding. However, the same process is applied in cases where only a single HI spectrum exists whereby the associated ^{13}CO map is multiplied by the GBT beam response at the position of the HI observation. Due to the uncommon nature of the direct HI to ^{13}CO comparison required by this research, it is useful to identify some of the more subtle difficulties with this approach.

Figure 3.4 shows how convolving 45″ ^{13}CO spectra to a 9′ beam has the effect of averaging together several emission features to form a spectrum with a smaller number of identifiable velocity components which are not neccessarily gaussian. The fact that in many cases velocity for a single ^{13}CO emission component can shift significantly across a 9′ beam contributes to the production of 9′ ^{13}CO spectra with non-gaussian emission components thus hampering the HINSA analysis technique utilized here. One approach to mitigate this problem would be to fit the ^{13}CO emission components on the original 45″ spectral map,

and thus produce maps of the fit parameters such as linewidth, center velocity, etc. for each emission component. These fit maps could then be convolved with the GBT beam response at one or more positions to syntesize 9′ fit maps that could be utilized at templates for HINSA analysis. This approach was found to have a serious shortcoming. At 45″ the signal to noise ratio in the ^{13}CO maps used in the this research was low enough to hide many ^{13}CO emission features within any individual spectrum. It was often found that HINSA features may be visible in the HI 9′ beam at positions and velocities where no ^{13}CO emission could be identified in any individual 45″ spectrum. However, using synthesized 9′ ^{13}CO spectra would reveal the missing ^{13}CO emission components. This is evident in Figure 3.4 where the emission component at 4 kms^{-1} is evident in the synthesized spectrum but not in any of the individual 45″ spectra.

An intermediate approach would be to first convolve the 45″ ^{13}CO maps with a somewhat larger synthesized beam (2′ was the size we attempted to use) in order to increase the signal-to-noise ratio prior to fitting of emission components. Those fits could then be convolved to the 9′ HI beam and positions to use as templates for HINSA analysis. This process requires that convolution be performed twice, once on the 45″ spectra, and then again on the 2′ fit parameters to arrive at a 9′ map of fit parameters required for creating templates. Since no function can perfectly duplicate the GBT beam response each convolution necessarily introduces biases and artifacts into the synthesized results. When convolution is performed twice these artifacts are significantly magnified to the point where this approach is undesirable. It was also found that this approach tended to identify many ^{13}CO emission components which were very closely spaced in position and velocity to the point where their HI counterparts could not be distinguished in the 9′ HI beam due to the smoothing inherent in us-

ing such a large beam and the inherently larger HINSA linewidths. This effect results in the uniqueness problem discussed in [Krco et al. (2008)].

With all three approaches posing their own difficulties, it was decided that the least problemmatic approach would be to convolve the original ^{13}CO 45″ maps with the 9′ beam response at one or more positions where neccessary, and then fit gaussian functions to the resultant ^{13}CO spectra to use as templates for HINSA analysis. This is done with the understanding that the final synthesized emission spectra may be non-gaussian, and that some of the fitted emission components may in fact be the mergers of two or more velocity components which are only distinguishable at smaller beam sizes. The understanding of these and other limitations resulted in some of the elimination criteria cited in Section 3.4.3. Data where these limitations made the HINSA fits unreliable have been removed.

3.4.2 Obtaining Templates by Fitting ^{13}CO and ^{12}CO Emission Spectra

Previous methods for estimating HINSA column densities relied on fitting functions such as gaussians or polynomials to 21cm spectra in order to obtain the ”background” emission spectrum. The choice of fitting function, masking regions, or other parameters could significantly affect the final results in a somewhat arbitrary fashion. The technique described in [Krco et al. (2008)] seeks to utilize the established relation between ^{13}CO emission and HINSA features to create fits which do not utilize any arbitrary functions or parameters and is capable of measuring the atomic to molecular ratio for each individual ve-

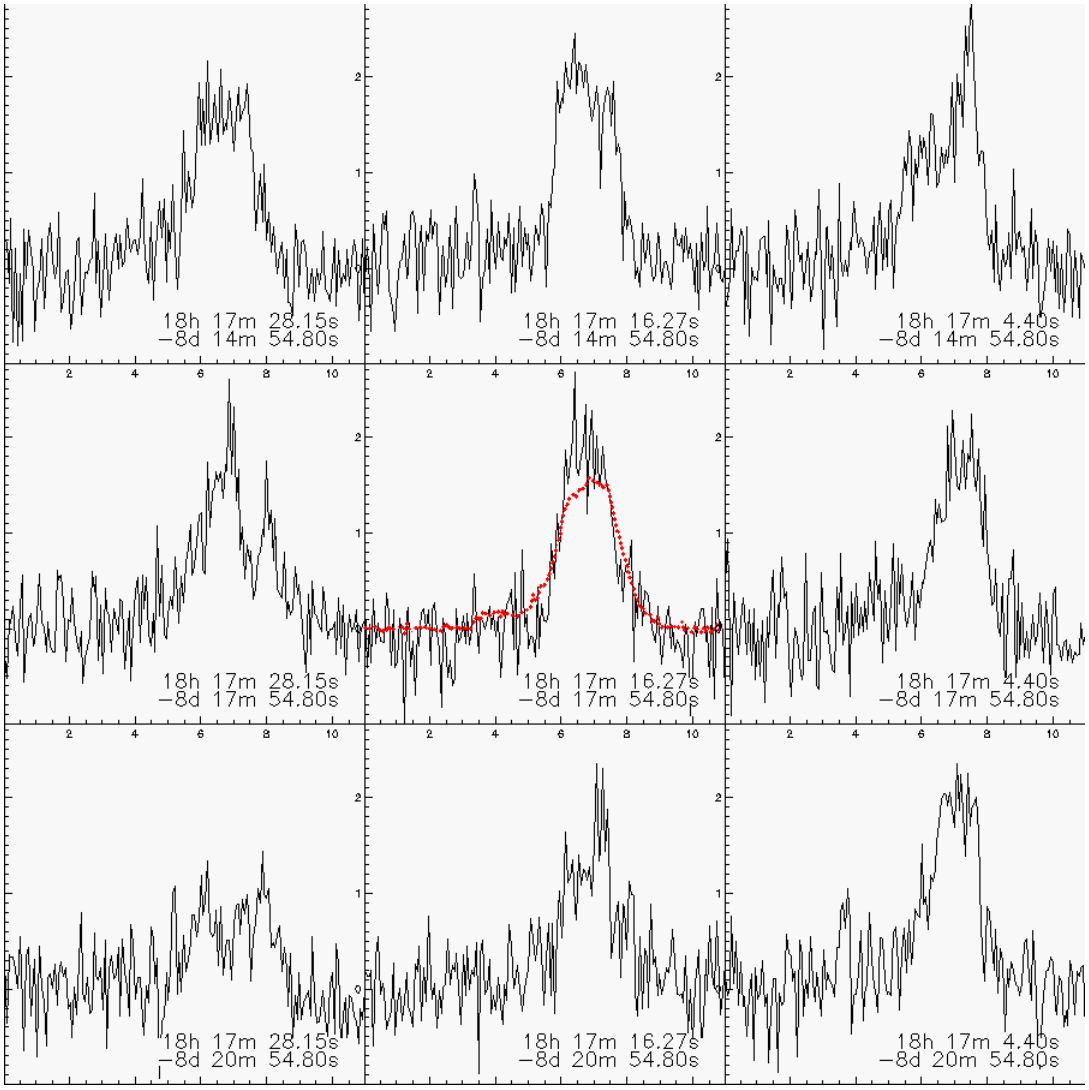

Figure 3.4: Nine ^{13}CO spectra in the L429 cloud observed with the FCRAO 14m telescope (45″ beam) spaced by approximately 3′. The horizontal and vertical axes represent velocity, and FCRAO antenna temperature, respectively. The red dotted line represents the convolved 9′ spectrum at the central position. L429 exhibits an uncommonly complex kinematic structure consisting of several velocity components which are blended together to form the single non-gaussian emission feature seen in the synthesized 9′ beam. A smaller emission feature is also visible at 4 $km\ s^{-1}$ which is too small to be detected in the noise of individual 45″ spectra.

locity component. This technique directly compares all ^{13}CO emission components to associated HINSA features by determining the ^{13}CO center velocities, linewidths, and where available, gas temperatures, and then utilizing those parameters as a template with which to fit the HINSA features.

Since ^{13}CO emission spectra are often composed of two or more velocity components which may overlap with non-negligible optical depths, the spectra are fitted according to the full radiative transfer equation as described in Equation 3.1. It is assumed that each velocity component has a gaussian optical depth and a given temperature. An arbitrary assumption is made that velocity components with greater recessional velocities are further away and thus form a part of the background spectrum (T_{bg}) for any foreground emission components. As HINSA features are typically optically thin this assumption has a rather small effect and is discussed further in [Krco et al. (2008)]. ^{12}CO emission at the center velocity for each component gives an estimate of the gas temperature for ^{12}CO under the assumption that the ^{12}CO emission is optically thick. This same temperature is then used to derive ^{13}CO optical depths, column densities, and non-thermal linewidths. There are several limitations to estimating the ^{13}CO excitation temperature using ^{12}CO emission which are discussed in more detail in [Krco et al. (2008)]. ^{12}CO data are not available for all positions with all sources and a 15K temperature is used in those cases. The absence of ^{12}CO data predominantly occurs on the outer edges of mapped clouds where temperatures are expected to be higher. Gas temperatures derived from ^{12}CO emission will sometimes appear unreasonably low due to the ^{12}CO not being optically thick, thus a minimum gas temperature of 10K is applied to all data.

Figures 3.5 and 3.6 show ^{13}CO and ^{12}CO spectra for positions in 8 selected

clouds. The HI lines presented in the figures are discussed in Section 3.4.3. These clouds were selected to show a wide variety of molecular emission and HI absorption spectra representative of the entire survey. Detailed results of the fits are presented in Tables 3.1 and 3.2. H_2 column densities are derived from ^{13}CO column densities using a constant ratio of $7.5 \cdot 10^{-5}$ [Stahler & Palla (2004)].

3.4.3 Fitting HINSA features to Molecular Templates

Guess values for center velocity, non-thermal linewidth, and temperature are derived from associated molecular data for all HI spectra to determine HINSA optical depths and column densities. In accordance with the technique developed in [Krco et al. (2008)], this is performed by finding those fit parameters which result in the recovered HI background spectrum with the smallest integrated intensity of the second derivative of the spectrum with respect to velocity. Sample fits are presented in Figures 3.5 and 3.6. As described in [Krco et al. (2008)] fitting HINSA features requires the use of four parameters for each corresponding molecular emission velocity component in a given spectrum. While ^{13}CO fitting provides initial guess values for some of these components it is necessary to allow certain parameters to float between a prescribed range of values while others stay fixed during the HINSA fitting process.

- Center velocities for each molecular emission component can be determined well through fitting. Further, the correlation between ^{13}CO and HINSA velocities has been found to be strong [Li & Goldsmith (2003)]. It has been found that allowing HINSA center velocities to deviate from ^{13}CO center velocities by a small amount (one tenth of the component's

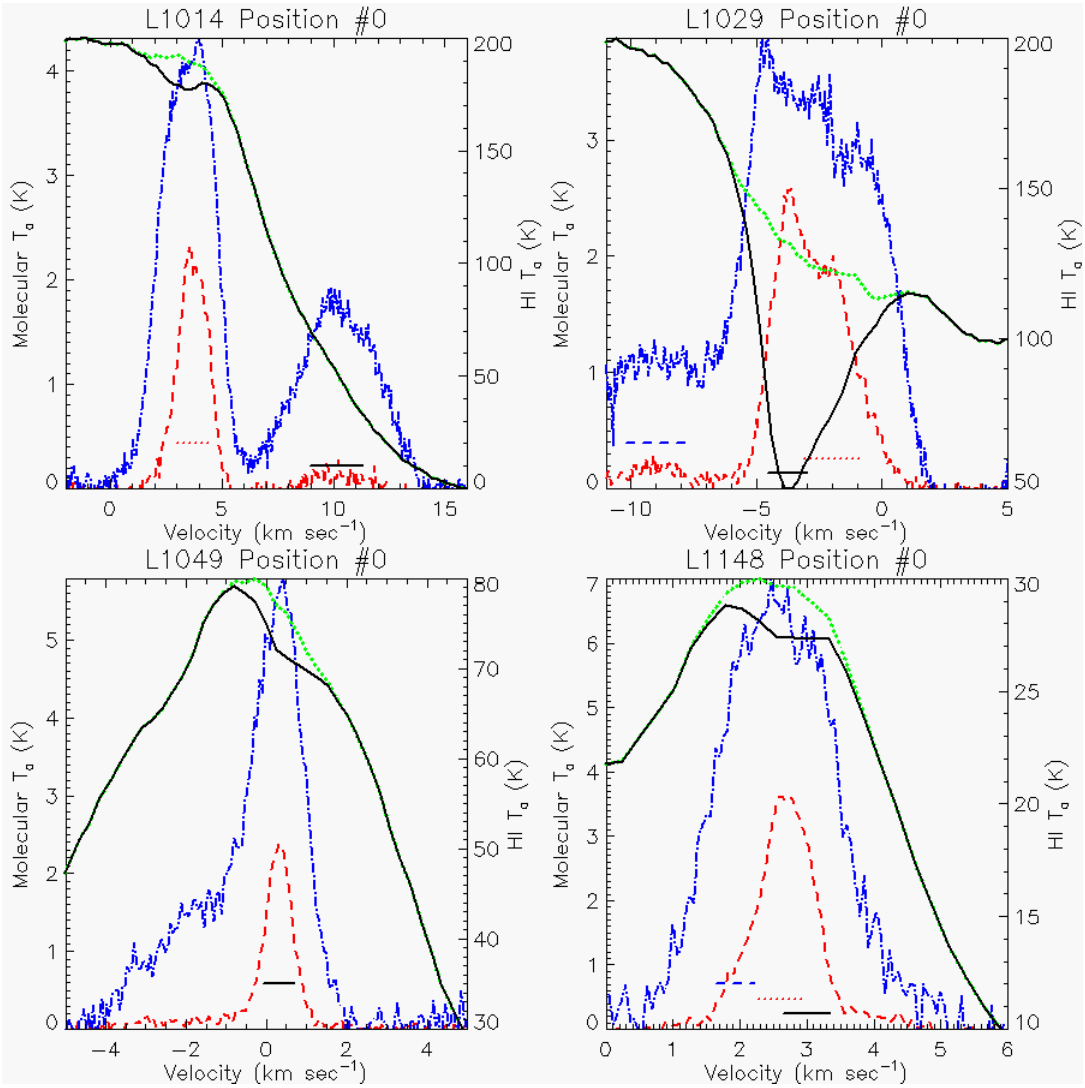

Figure 3.5: ^{13}CO (red, dashed), ^{12}CO (blue, dash-dot-dash), Observed HI (black, solid), and derived HI T_{bg} (green, dotted) spectra for 4 selected clouds. Antenna temperatures for ^{13}CO and ^{12}CO emission are indicated by the left vertical axis, while HI antenna temperatures are indicated on the right. The horizontal lines represent the center velocities and FWHM linewidths of each fitted molecular emission velocity component.

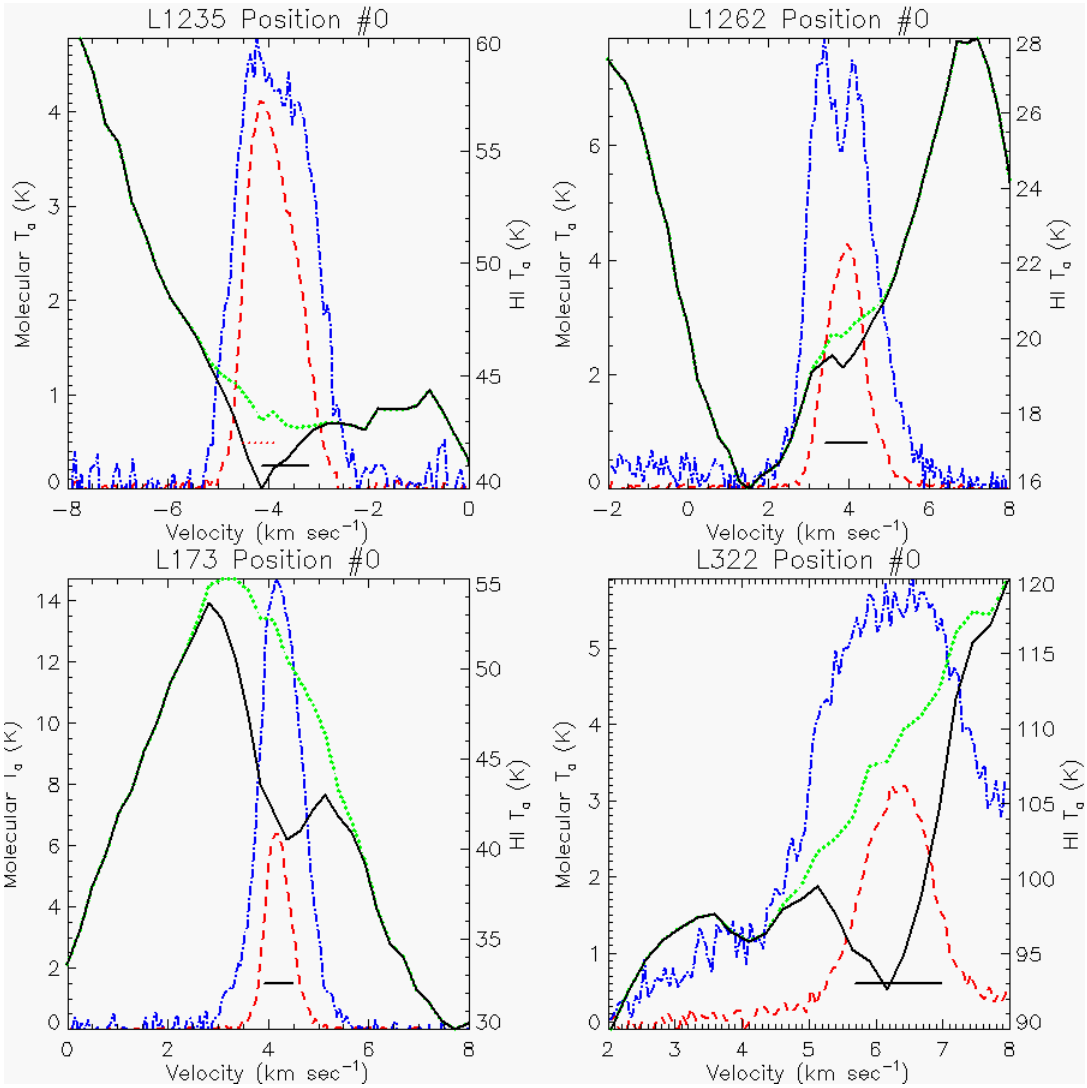

Figure 3.6: ^{13}CO (red, dashed), ^{12}CO (blue, dash-dot-dash), Observed HI (black, solid), and derived HI T_{bg} (green, dotted) spectra for 4 selected clouds. Antenna temperatures for ^{13}CO and ^{12}CO emission are indicated by the left vertical axis, while HI antenna temperatures are indicated on the right. The horizontal lines represent the center velocities and FWHM linewidths of each fitted molecular emission velocity component.

linewidth) can improve the final HINSA fits. In only 2% of the spectra analyzed in this survey it was necessary to allow center velocities to deviate by as much as 30% of the linewidth in order to obtain satisfactory HINSA fits.

- The nonthermal components of HINSA and ^{13}CO linewidths are expected to be well correlated [Li & Goldsmith (2003)]. However, deriving expected HINSA linewidths from fitted ^{13}CO linewidths is dependent on estimating the thermal components using temperatures derived from ^{12}CO which are not always reliable. As a result derived HINSA non-thermal linewidths are allowed to deviate by as much as 50% from the fitted ^{13}CO non-thermal linewidths for each component.
- Gas temperatures derived from ^{12}CO emission are used for both ^{13}CO and HINSA gas as well and are kept constant during HINSA fitting.
- No a priori information exists to provide guess values for HINSA optical depths; Thus an initial guess value of 0.1 is used for all velocity components.

In order for a HINSA fit to be considered satisfactory it must fulfill three criteria. 11% of the HINSA fits in this survey have been excluded due to failing one of the following criteria:

- The recovered background spectrum (T_{bg}) must be consistant with HI spectra observed in surrounding regions where no molecular emission is detected.
- T_{bg} spectra must not show any ”kinks” as described in [Krco et al. (2008)] which would be indicative of improperly derived center velocities or linewidths.

- It has been found that this technique does not always produce unique solutions, especially in cases where several overlapping velocity components are spaced close together in velocity. The stability of each solution is tested by randomizing the guess parameters for center velocity, non-thermal linewidth, and optical depth for all velocity components within a given spectrum to ensure that at least 95% of the initial parameter space converges to the same final solution. Only 1.4% of the spectra analyzed in this survey failed this criterion and have been excluded from the survey as ambiguous.

HINSA column densities are derived from fit parameters according to equation 3.4. It is necessary to adjust any column densities for foreground HI emission using the p-parameter discussed in [van der Werf et al. (1988)] and [Krco et al. (2008)]. This parameter effectively increases any observed HINSA column densities to account for foreground HI gas.

3.4.4 Adjusting Column Densities for Beam Fill

To calculate accurate HINSA and ^{13}CO column densities it is necessary to determine what fraction of the 9′ beam is filled. It has been found that HINSA features only occur in regions where $A_v > 1$. Beam fill maps have been constructed for all clouds on a 45″ beam using a 30″ pixel spacing on a grid identical to any ^{13}CO maps obtained. A value of 1 is assigned to any pixels where ^{13}CO signal is detected above the 3 σ detection limit and a value of 0 otherwise. This binary map is then convolved to 9′ using methods identical to those for ^{13}CO to give an estimate of the beam fill factor for each position where HI data are

available. Column densities for HINSA, ^{13}CO (and thus H_2) are then adjusted for this factor. Any determinations of the HI to H_2 ratio are unaffected by determinations of the beam fill factor as both both constituents are adjusted by the same value. Absolute values for the column densities are affected. Positions where the ^{13}CO fills less than 50% of the GBT beam have been excluded from this survey in order to minimize the introduction of new uncertainties through this process. Excluding these regions effectively removes the low-density regions on the edges of mapped clouds from the data set. It has been tested that this process does not create any significant biases, but does reduce the variance in measured HINSA column densities over an entire cloud.

3.5 Survey Results

3.5.1 HINSA Column Densities

It is important to detail the general characteristics of HINSA detections. Figure 3.7 shows the distributions of N_{HINSA} and N_{H_2} measurements in this survey. HINSA column densities are typically of order $10^{19} cm^{-2}$. Both distributions show similar features in that both have a tail at lower values while exhibiting a sharp drop off at higher column densities. It is important to note that the HINSA column density distribution is significantly wider than that of H_2, having a standard deviation in log space of 0.53 compared to 0.32 for H_2. Possible explanations are discussed in section 3.5.3.

Figure 3.8 shows the spatial distribution of HINSA column densities for all clouds in the survey. A wide range of column densities is evident, even along

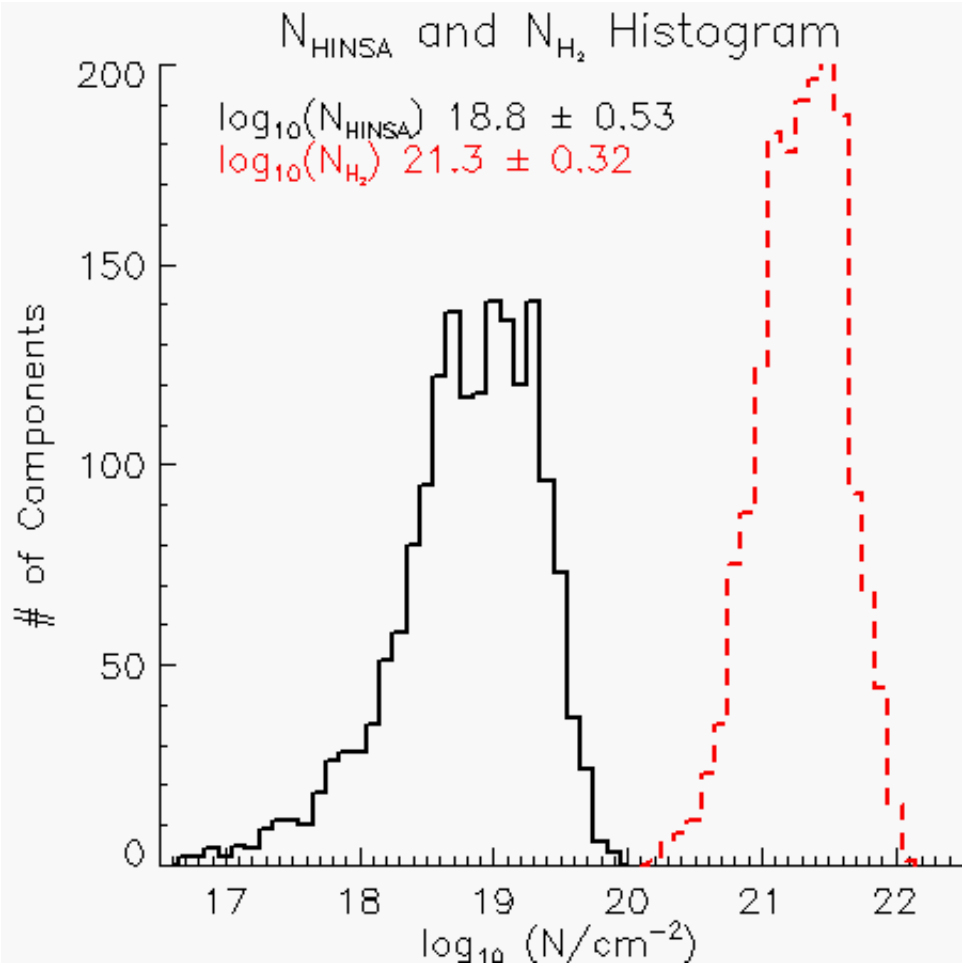

Figure 3.7: Derived HINSA column densities (N_{HINSA}) are represented by the black, solid histogram on the left. Associated H_2 column densities (N_{H_2}), as derived from ^{13}CO emission, are represented by the red, dashed histogram on the right. All measurements, for all velocity components in the survey, forming a total of 1746 data points for each constituent, are included. Column densities for both are represented on a logarithmic scale on the horizontal axis. The legend specifies the derived logarithmic mean and standard deviation for each constituent.

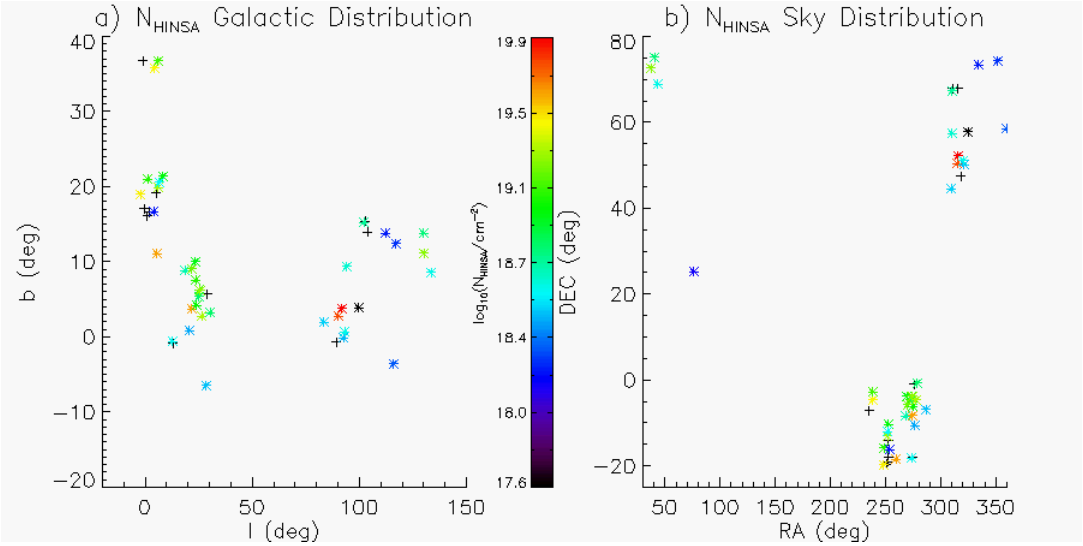

Figure 3.8: Color coded representations of detected HINSA column densities in Galactic (a) and celestial (b) coordinates. Each point represents an individual cloud, with the color representing the total HINSA column density measured along the line of sight with the maximum ^{13}CO column density measured. Crosses represent clouds where no HINSA was detected.

nearby lines of sight showing no clear correlations between HINSA column densities in Galactic and sky coordinates. This is consistent with the idea that we are measuring a physical property of the clouds unaffected by biases which could be produced by the intensity of the background HI emission (which is stronger near the galactic plane), or any significant spatially large local foreground HI emission which would serve to reduce the measured HI optical depths in a certain region of our sky. It is evident that certain groupings of clouds (such as that at a declination of -5 degrees and R.A. of 283 degrees) exhibit very similar HINSA column densities. All the clouds in this grouping are believed to lie at the same distance (approximately 200 pc).

Figure 3.9 shows that our sources cover a wide variety of objects; Some are isolated globules whereas others are part of larger structures. It is evident that

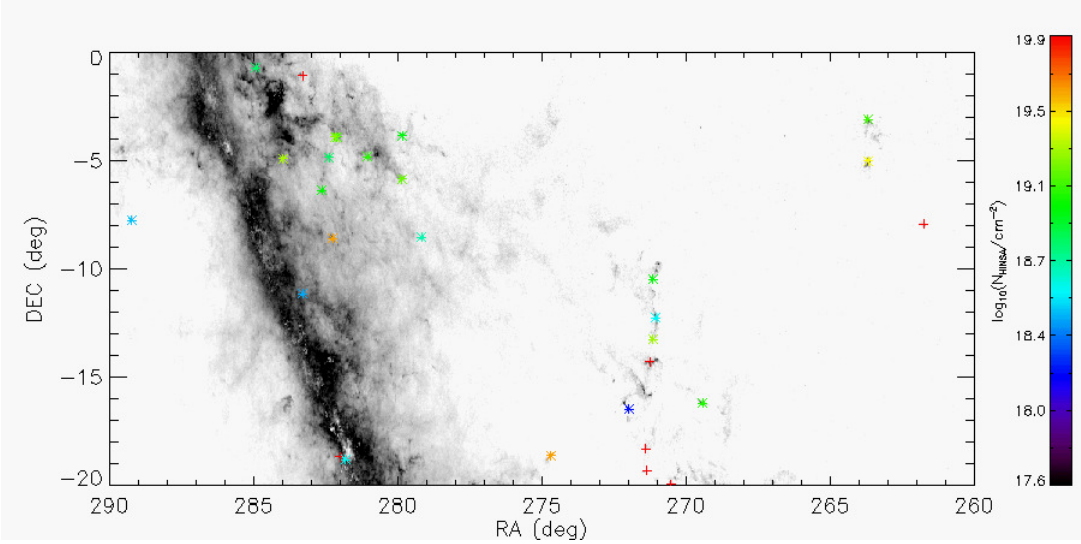

Figure 3.9: The HINSA column density of each cloud in the region is represented by an asterisk color coded according to the scale on the right. HINSA non-detections are illustrated by crosses. The background is optical extinction map made from 2MASS stellar reddening data. Darker regions represent greater optical extinction. The band represents the galactic plane.

the grouping at 283 deg R.A. and -5 deg declination with similar HINSA column densities could be part of one larger physical structure. Alternatively, the filamentary structure at 272 deg R.A. and -12 deg declination exhibits a large variation in HINSA column densities. HINSA column densities alone do not provide sufficient information to determine whether a group of clouds are chemically similar, it is necessary to look at the relation between HINSA and H_2.

3.5.2 The Relationship of Atomic and Molecular Gas

To better understand the chemical properties of the clouds in this survey it is necessary to compare the fractional abundance of cold HI as expressed by the gas ratio N_{HINSA}/N_0, where the total proton column density (N_0) includes only

the atomic and molecular hydrogen gas and is calculated as $N_0 = N_{HINSA} + 2N_{H_2}$. H_2 column densities are inferred from ^{13}CO observations and compared directly to their associated HINSA features for all velocity components. Figure 3.10a shows that cold HI manifested as HINSA features comprises on average 0.1% of the total proton column density, which makes it the third most abundant constituent of molecular clouds by number density after H_2 and He. As discussed in [Goldsmith et al. (2007)], it is expected that at higher volume densities the HI abundance will decrease as the increased availability of dust accelerates the atomic to molecular conversion process. Even in steady-state where the HI volume density is independent of time and density, the HI fractional abundance will be lower in denser regions. This hypothesis is confirmed by Figure 3.10b which shows a decrease in HI abundance at higher total proton column densities with a five standard deviation statistical significance for a linear fit.

While this relation is apparent when comparing individual velocity components as in Figure 3.10b, it is not evident when summing over all velocity components along a single line of sight as in Figure 3.10d. This hints at the possibility of different HINSA abundances in velocity components along the same line of sight and underscores the importance of a HINSA analysis technique which is able to derive HINSA column densities for all velocity components such as that used here. Further, Figures 3.10c and 3.10d show a wide range of HINSA abundances indicating that there is likely no common, universal HINSA abundance but that, in fact, the HINSA abundance is a property of each individual cloud and can yield useful information.

Figures 3.10c and 3.11 show that the same grouping of clouds discussed in §3.5.1 also exhibits similar HINSA abundances. It is unlikely, considering the

wide range of HINSA column densities and abundances observed throughout the survey, that this grouping shares such a similar chemistry by chance. If HINSA abundances are primarily environmentally driven then this grouping could indicate similarities in dust properties, cosmic ray fluxes, or any other factors that influence the HI to H_2 conversion process. If HINSA abundances are primarily determined by the age and chemical evolution of a cloud then this grouping would indicate that the surrounding dust and gas structure was likely formed in a single event and that all the clouds therein would share a similar age. There is insufficient information currently presented to make a determination, but this would be an important direction for a future study. To gain a better understanding of the processes which determine the HINSA abundance of molecular clouds it would be useful to examine specific clouds in detail as is done in §3.6.

3.5.3 Empirical Determination of HINSA uncertainties

As discussed in [Krco et al. (2008)], determining the uncertainties in HINSA measurements experimentally is made difficult by a number of unknowns which can only be approximated. The most significant of these arise from determining ^{13}CO and HI gas temperatures from ^{12}CO data, and from uncertainties inherent in the assumption that the HI and ^{13}CO gas are co-existant. It was suggested in [Krco et al. (2008)] that the only meaningful way to estimate the uncertainties in HINSA measurements was through a survey. Assuming that figure 3.7 approximates normal gaussian distributions, a simple upper limit on the N_{HINSA} uncertainty of 0.53 in log space can be derived. This is under the unphysical assumption that there is a single real HI column density value for

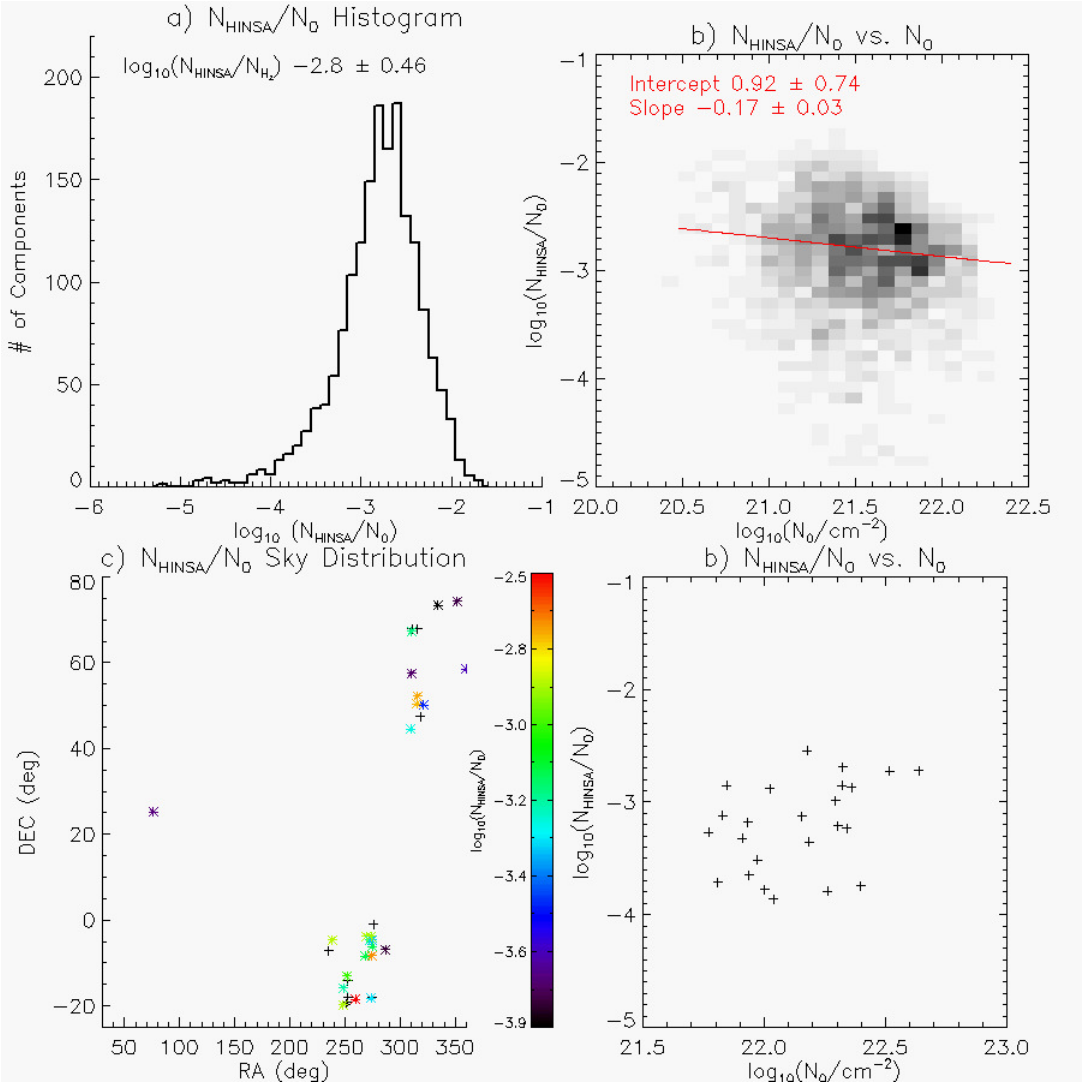

Figure 3.10: a) A histogram of the atomic to molecular gas column density ratio for all velocity components at all positions in the survey. The legend gives values of the mean and standard deviation. b) HI to total proton column density ratio as a function of total proton column density, for all velocity components at all positions in the survey. Darker pixels indicate a greater number of measurements. c) The sky distribution of the gas column density ratio for the highest ^{13}CO column density region measured in each cloud. The color of each asterisk represents the ratio according to the color map on the right. Black crosses represent HINSA non-detections. Clouds for which there is no ^{13}CO data available are excluded. d) Column density ratios as a function of total proton column density summed over all velocity components along the highest ^{13}CO column density lines of sight for each cloud with HINSA detections and available ^{13}CO data.

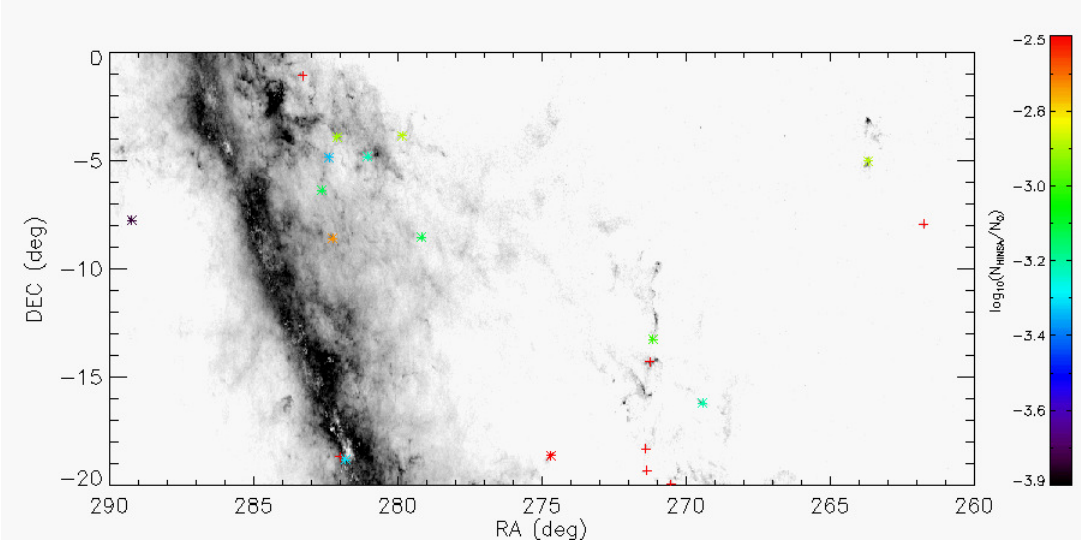

Figure 3.11: The HINSA to total proton column density ratio of each cloud in the region is represented by an asterisk according to the color scale on the right. The background is an optical extinction map made from 2MASS stellar reddening data similar to Figure 3.9. Darker regions represent greater optical extinction. The band represents the galactic plane. HINSA non-detections are presented as crosses. Clouds for which there is no ^{13}CO data available are excluded.

all clouds along all lines of sight, and that the width of the distribution is represented entirely by measurement uncertainties. In fact the histogram represents a convolution of the real HI column density distribution and the uncertainty in our measurements. If we assume that both elements can be approximated by gaussians, then their widths would add in quadrature to create the convolved distribution apparent in Figure 3.7.

The H_2 column density, and HI abundance distributions presented in Figures 3.7 and 3.10a provide additional information which can be used to improve our estimate of the uncertainty in N_{HINSA}. Under the assumption that each distribution can be separated into component elements that add in quadrature, each of which is approximated by a gaussian distribution, it is possible to elimi-

nate common elements to better determine the N_{HINSA} measurement uncertainty. This assumption is not ideal but is sufficient for a first-order estimate.

The width of the H_2 column density distribution can be approximated by

$$\sigma^2_{^{13}CO} + \sigma^2_T + \sigma^2_{^{13}CO_{nt}} + \sigma^2_{H_2} = 0.32^2 \ , \tag{3.7}$$

where $\sigma_{^{13}CO}$ represents the width of the real distribution of ^{13}CO column densities across all clouds and all positions in the survey, σ_T represents the width contribution through using ^{12}CO to determine gas temperatures, $\sigma_{^{13}CO_{nt}}$ represents the contribution of all other ^{13}CO measurement uncertainties not related to gas temperature, and σ_{H_2} represents any contribution that may arise from using a single value to determine H_2 column densities from those of ^{13}CO.

The width of the N_{HINSA} distribution can similarly be approximated by

$$\sigma^2_{HINSA} + \sigma^2_T + \sigma^2_{HINSA_{nt}} = 0.53^2 \ , \tag{3.8}$$

where σ_{HINSA} and $\sigma_{HINSA_{nt}}$ represent the width contributions due to the real distribution of HINSA column densities over all clouds and positions in our survey, and all uncertainties in N_{HINSA} measurements unrelated to the gas temperature determination. σ_T can be assumed to be the same for both the HINSA and H_2 distributions since the column densities of both are,to first order, similarly proportional to the temperature and the same temperature was used for both species.

The width of the HI abundance distribution can be approximated by

$$\sigma^2_{^{13}CO} + \sigma^2_{^{13}CO_{nt}} + \sigma^2_{H_2} + \sigma^2_{X_{HINSA}} + \sigma^2_{HINSA_{nt}} = 0.32^2 \ , \tag{3.9}$$

where $\sigma_{X_{HINSA}}$ represents the real distribution of HINSA abundances over all clouds and positions in our survey. Since both HINSA and H_2 column densities are similarly dependent on the same temperature there is no σ_T contribution to the width.

Figure 3.10b shows that there is a correlation between the HINSA abundance and the total proton column density. However, the slope is small over the range of measured column densities compared to the spread in HI abundances. Thus it can be assumed when measuring distribution widths that there is no strict correlation and that the width of the abundance distribution is primarily due to the widths of the HINSA and H_2 column density distributions. The distribution of H_2 column densities when convolved with the HINSA abundance distribution will approximate the N_{HINSA} distribution whose width can be written as

$$\sigma^2_{HINSA} = \sigma^2_{^{13}CO} + \sigma^2_{X_{HINSA}} + \sigma^2_{HINSA_{nt}} \ . \tag{3.10}$$

This set of equations can be solved to yield

$$\sigma^2_T - \sigma^2_{^{13}CO_{nt}} = 0.26^2 \tag{3.11}$$

and

$$\sigma^2_{HINSA_{nt}} + \sigma^2_{X_{HINSA}} = 0.42^2 \ . \tag{3.12}$$

$\sigma_{^{13}CO}$ and $\sigma_{HINSA_{nt}}$ have been completely removed and $\sigma_{^{13}CO_{nt}}$ is due only to the instrumental uncertainties in measuring ^{13}CO and is presumed to be small in comparison to other uncertainties. A lower limit estimate on the uncertainties due to temperature determination (σ_T) of 0.26 has thus been derived. However the total HINSA uncertainties must also include the uncertainties not related to temperature ($\sigma_{HINSA_{nt}}$) which cannot be presently determined due to being entangled with the unknown distribution of HINSA abundances ($\sigma^2_{X_{HINSA}}$).

The total HINSA column density uncertainty ($\epsilon_{N_{HINSA}}$) in log space can be written as

$$0.26 < \epsilon_{N_{HINSA}} = \sqrt{\sigma^2_{HINSA_{nt}} + \sigma^2_T} < 0.53 \ , \tag{3.13}$$

where the lower and upper limits are determined from equations 3.11 and 3.8. Since σ_T and $\sigma^2_{X_{HINSA}}$ are expected to be dominant in equations 3.11 and 3.12 a single value of $\epsilon_{N_{HINSA}} = 0.3$ in log space is used for statistical analysis where necessary.

3.6 HINSA Abundances in Mapped Sources

To better understand the cold HI content of molecular clouds it is necessary to look at its spatial distribution within an entire cloud. Figures 3.12 through 3.29 show results for the sources mapped in our survey. Each source has 2 accompanying figures. The first figure (such as Figure 3.12) is composed of two plots showing measured HINSA column densities and abundances with respect to total proton column densities. Each symbol/color represents an individual velocity component while each point represents a map position where the relevant

velocity component is present. The legend on top provides information on each velocity component. The second figure is a spectral map (such as Figure 3.13) showing the observed HI, and ^{13}CO spectra in each map as well at the derived HINSA optical depths. Each spectrum's horizontal axis represents velocity, and each spectrum is positioned in the figure based on its sky position.

In the spectral maps, HINSA solutions are only displayed for spectra which meet the criteria described in §3.4.3. The bulk of the excluded spectra are due to small beam fill factors. The spectral maps show that HINSA features are closely correlated with ^{13}CO emission. Only in a small fraction of cases was it necessary to allow the velocity of the HINSA solutions to deviate significantly from that of the ^{13}CO emission in order to produre proper solutions.

The Spectral map for L392 in Figure 3.17 shows a strong correlation between ^{13}CO and HINSA in not only sky position, velocity, and linewidth but in the relation between HINSA optical depths and ^{13}CO emission implying a direct correlation between H_2 and HINSA column densities as evidenced in Figure 3.16 by the fact that the HINSA to N_0 slope is close to 1. Similarly, the cold HI abundance seems to remain roughly constant throughout the cloud. In contrast, the spectral map for L429 (Figure 3.19) shows large variations in HINSA optical depths compared to ^{13}CO emission, both for the individual components themselves and between the two main ^{13}CO emission components throughout the cloud. Figure 3.18 shows that the two main components, numbered 0 and 1, both have an N_{HI} slope of approximately 0.6 which is in stark contrast to L392. When examining all the mapped clouds in the survey it becomes evident that while there is a general trend for the cold HI abundance to decrease at higher total proton column densities, this is not always the case and the range in N_{HI}

slopes is quite large (ranging from -1.6 to 1.75). Further these slopes may vary not only between different clouds but within different velocity components of a particular cloud. No explanation for this phenomenon is immediately apparent. It is expected that, when working with non-spherical clouds, there will be a variation in N_{HI} slopes due to the orientation of a given cloud due to the fact that HI abundances are expected to vary significantly at different depths and column density measurements will sample different portions of a cloud at different orientations. More detailed modeling of both the geometry and chemistry of these clouds is required, and will be discussed in a future paper.

Nearly all of the clouds in the survey that exhibit multiple velocity components show differences in the HINSA abundances between different velocity components that overlap spatially. In the case of L429, components 0 and 1, which overlap both in velocity and spatially exhibit similar N_{HI} slopes as well as a similar range of total proton column densities, yet their HI column densities differ by half an order of magnitude. Most of our mapped clouds exhibit similar characteristics while L1029 and L1757 show velocity components with HI column densities a full order of magnitude different than other components within the same cloud.

It is difficult to imagine a set of circumstances under which velocity components with such different HI abundances as evidenced in this survey could be co-extensive in all three spatial dimensions and well mixed. It seems more likely that these individual velocity components are in fact physically separated and are evolving chemically independent of one another. It is possible that certain velocity components which overlap spatially may be quite well separated in fact, and form different clouds. However in the case of L429, the two pri-

mary components do seem to be spatially co-located, sharing similar borders and peak intensity locations, while at the same time producing HINSA features of very different depths.

It is possible that the differences in cold HI abundance are indicative of different evolutionary stages (and chemical ages) for different clumps within the cloud, where by clouds and velocity components with lower HI abundances would be older. Having such information for individual clumps within a cloud would be of great value in understanding the dynamical processes which form molecular clouds and complexes. A detailed chemical model examining this possibility is reserved for a future publication.

A number of environmental factors could similarly affect HI abundances. An increased rate of cosmic ray dissociation of H_2 would increase the amount of available HI within a cloud. As discussed in [Goldsmith & Li (2005)], the HI volume density is proportional to the cosmic ray abundance in a steady-state cloud. The observed differences in HI abundance in the velocity components of individual clouds having similar total proton column densities would necessitate differences in cosmic ray dissociation of between one half to one order of magnitude for different velocity components within a cloud. There are several mechanisms which could account for variations in cosmic ray flux such as attenuation on irregularly shaped surfaces, or the presence of strong magnetic fields. However, no single physical process is immediately apparent that could produce localized variations in cosmic ray flux of such magnitude that in this picture would be indicated in nearly all the clouds observed by this survey.

External UV radiation fields could also significantly affect HI abundances, especially in regions of low optical depth. In a spherical cloud most of the ma-

terial would be shielded from external UV radiation. If a cloud were clumpy, irregularly shaped, contained internal UV sources (such as stars), or hollow regions then the total surface area for incident radiation and the depth to which that radiation could penetrate would be increased. This would result in greater HI column densities. It is not yet clear whether this effect would be sufficient to explain the variations in HI abundances in column density evidenced here.

3.7 Discussion and Conclusions

This work comprises the first large survey of the cold HI gas internal to molecular clouds through HINSA features in 21cm spectra. HINSA features are present in at least 80% of the clouds surveyed but cold HI gas is likely to be present in all molecular clouds. The results of this survey support the hypothesis discussed in [Goldsmith & Li (2005)] and [Goldsmith et al. (2007)] among others that a minimum residual HI abundance due to cosmic rays should be present in all clouds. Starting with [van der Werf et al. (1988)], it has been postulated that foreground HI emission should obscure HINSA features at larger distances and lower Galactic latitudes; Compounded with the difficulty in resolving distant clouds using 21cm beam sizes, this would suggest a limiting distance beyond which HINSA features could not be observed. Previous studies were limited to clouds of up to 200pc distance. This survey has shown that HINSA features are measurable to distances of at least 700pc and the lack of non-detections at that range suggests that detection of HINSA at larger distances is not excluded.

Due to the limited number of sources in previous surveys there was uncertainty as to whether HINSA features were ubiquitous throughout molecular

clouds or peculiar properties of a few clouds such as L134, or regions like the Taurus Molecular Cloud Complex. The clouds surveyed in this work cover a large range of sky and Galactic positions, and sample individual clouds and Bok globules as well as groupings of clouds that belong to larger structures as shown in Figures 3.9 and 3.11. It can be concluded from this work that cold HI gas can exist in all molecular clouds regardless of sky position, or environment and is detectable even at lines of sight with total proton column densities as low as $10^{21}\ cm^{-2}$. As a result, it has become evident that the study of molecular clouds through their internal atomic hydrogen content is feasible for all nearby molecular clouds and complexes. Toward that goal, an improved technique for measuring HINSA column densities was derived in [Krco et al. (2008)], while previously unavailable uncertainty estimates for HINSA measurements are derived in §3.5.3. Along with the HINSA detection limit discussed in §3.3.1, the fundamental tools for studying the HI content of molecular clouds through HINSA features using the technique described in [Krco et al. (2008)] have been developed.

Beyond confirming that cold atomic hydrogen comprises the third most abundant constituent of molecular clouds, the large range of HINSA column densities and abundances determined by this survey indicate that the measured column densities can yield significant information on the properties of individual clouds. Several factors which could affect HINSA abundances and the manner in which they vary with different total proton column densities have been discussed throughout. While the observed HINSA abundances here agree in general with predictions put forth in [Goldsmith et al. (2007)], no fully satisfactory explanation currently exists for the large differences in HINSA abundance between individual velocity components in a particular cloud, or for the varia-

tions in the slopes of the HINSA to total proton column density relation. More detailed modeling of individual clouds is required to understand how geometric, dynamical, and chemical factors could produce the wide variety of HINSA profiles seen here. A more complete understanding should allow us to measure the chemical ages of these clouds yielding significant information on molecular cloud evolution and the time scale for the process of star formation as discussed in §3.1.

3.8 Acknowledgements

This research was supported in part by the National Science Foundation through grants AST 0404770 and AST 0407019, as well as the National Radio Astronomy Observatory Student Support Program. The research was carried out at the Jet Propulsion Laboratory, California Institute of Technology, under a contract with the National Aeronautics and Space Administration. The data used in this paper were obtained with the Five College Radio Observatory which is supported by the National Science Foundation with permission of the Metropolitan District Commission, and with the Greenbank Telescope of the National Radio Astronomy Observatory. We thank Mark Heyer and Jay Lockman for assistance in carrying out the observation. The program used for regridding the data in this work was modified from the original version developed by Tim Robishaw.

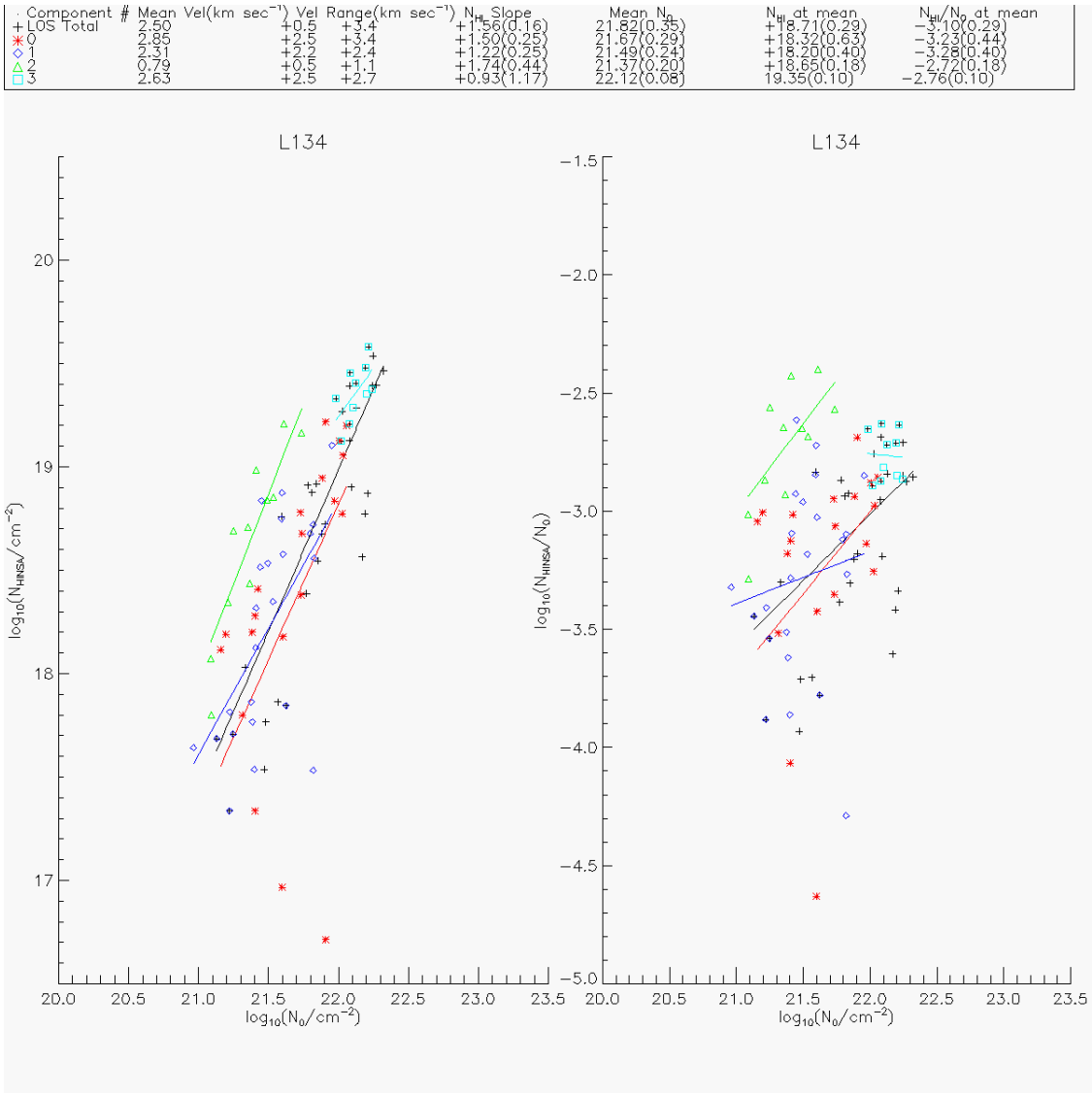

Figure 3.12: L134 HINSA column densities (left) and abundances (right). Each velocity component within the cloud is represented by an individual symbol and color as indicated by the legend. Each point represents an independently measured position on the sky for each velocity component, though many overlapping components may share the same sky position. Each line represents a linear fit through all measurements for a given velocity component. The legend gives velocity ranges, mean total proton column densities (N_0) , HINSA column densities (N_{HINSA}) and abundances (N_{HINSA}/N_0) at the mean value of N_0, and the slopes of the HI column density fits for each velocity component, with uncertainties in parentheses. These have been derived using the estimates in Section 3.5.3. The N_{HINSA}/N_0 slope in each case is exactly 1 smaller than the given N_{HINSA} slope. The LOS component refers to the summation of all velocity components present along a given line of sight.

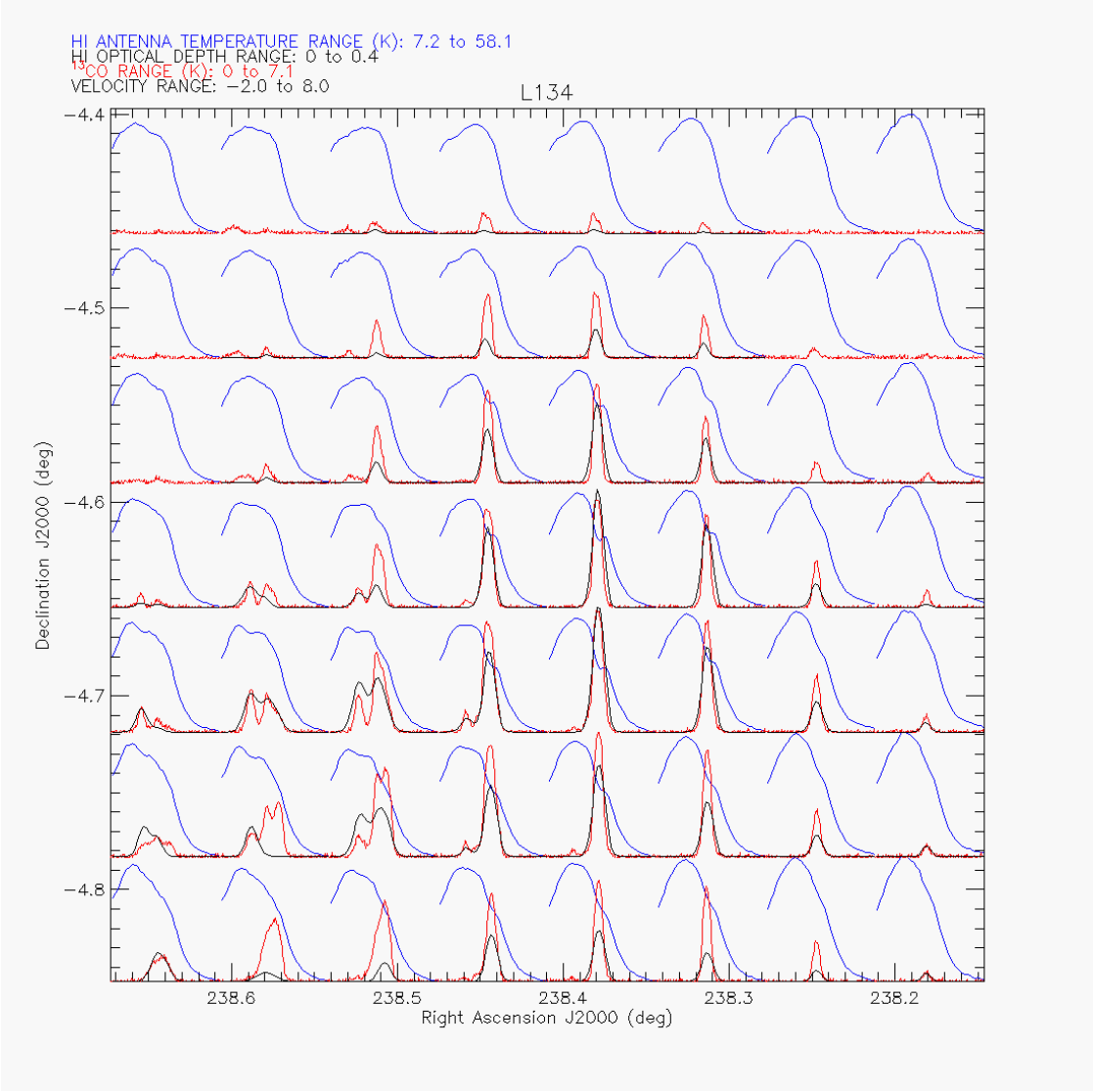

Figure 3.13: ^{13}CO (red), observed HI (blue), and determined HINSA optical depth spectra (black) for all positions within the map. The overall horizontal and vertical axes represent sky position. The horizontal axes for each spectral plot represent the velocity range given in the legend. The vertical axes in each spectral plot represent the range of antenna temperatures for HI, HINSA optical depths, and ^{13}CO antenna temperatures given by the legend.

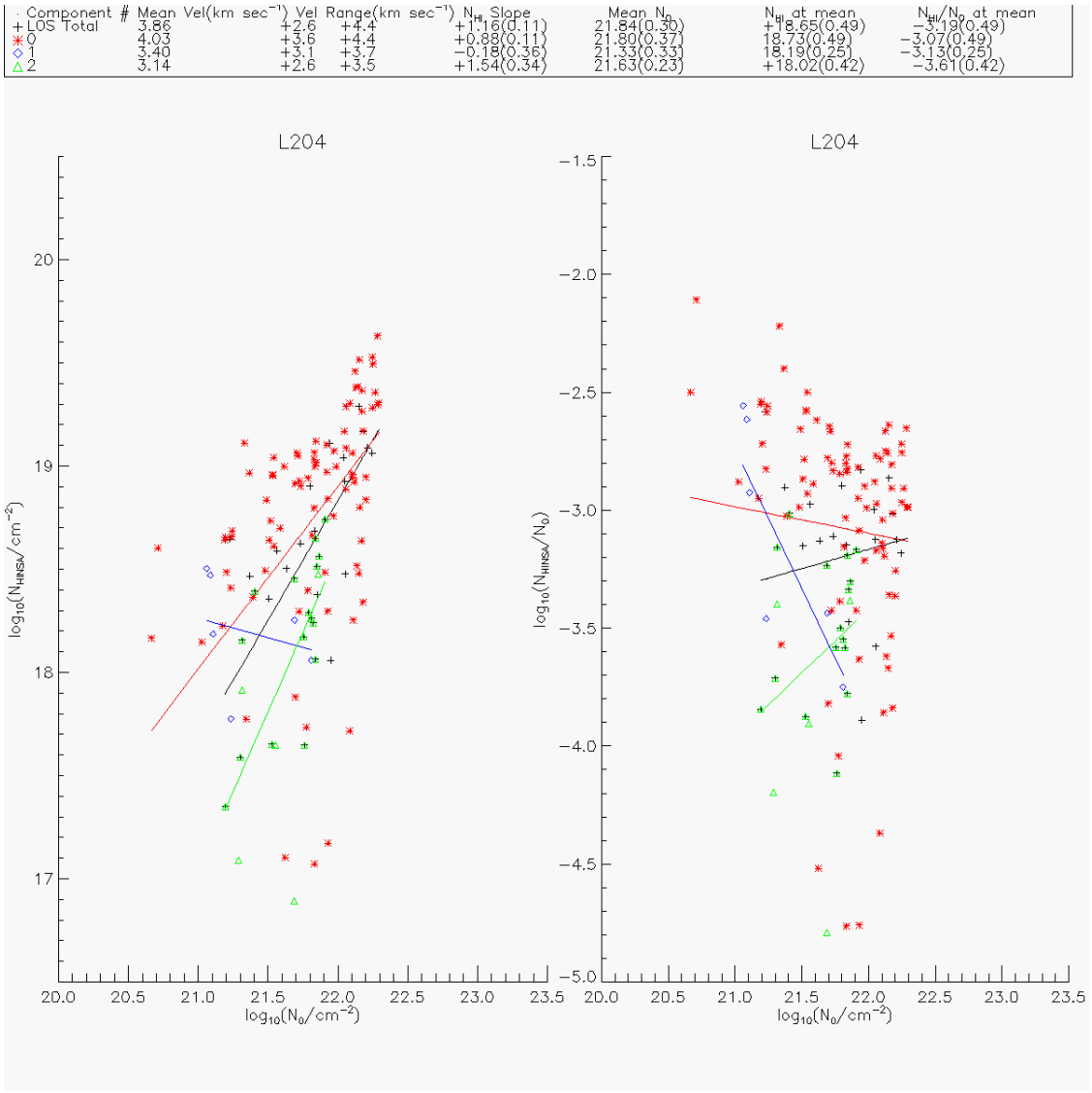

Figure 3.14: A similar representation to that in Figure 3.12 for the cloud L204.

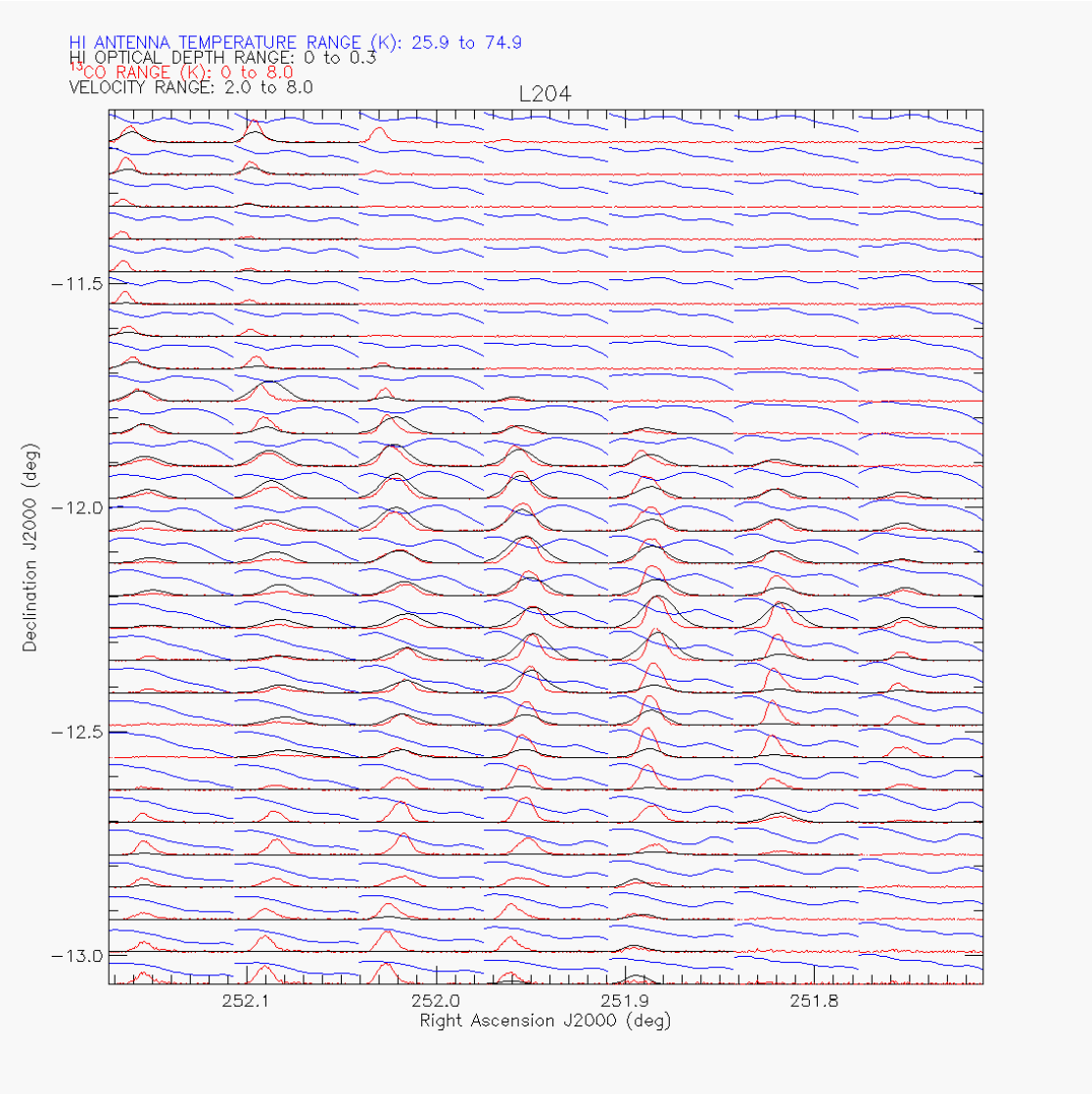

Figure 3.15: A similar representation to that in Figure 3.13 for the cloud L204.

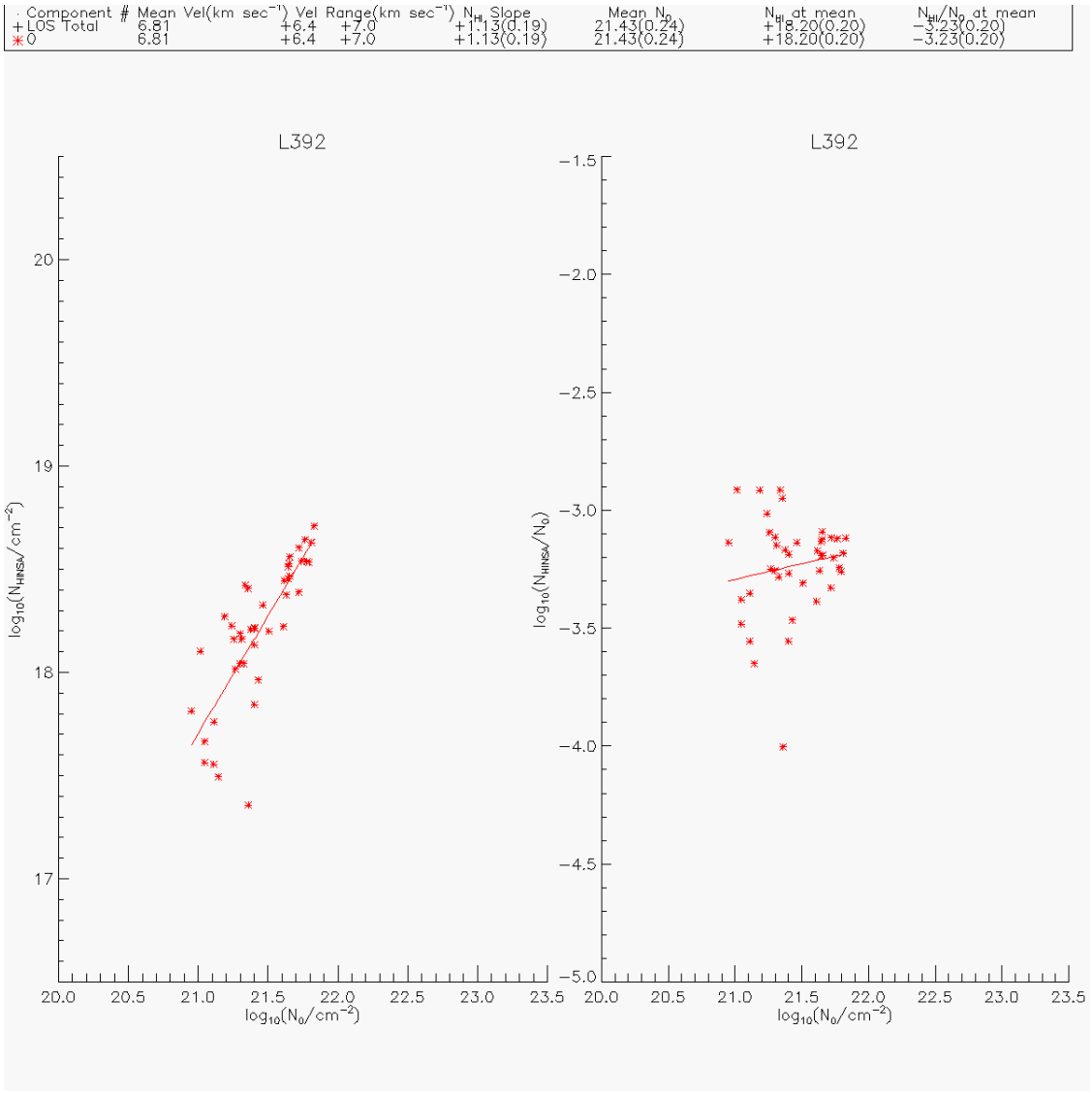

Figure 3.16: A similar representation to that in Figure 3.12 for the cloud L392.

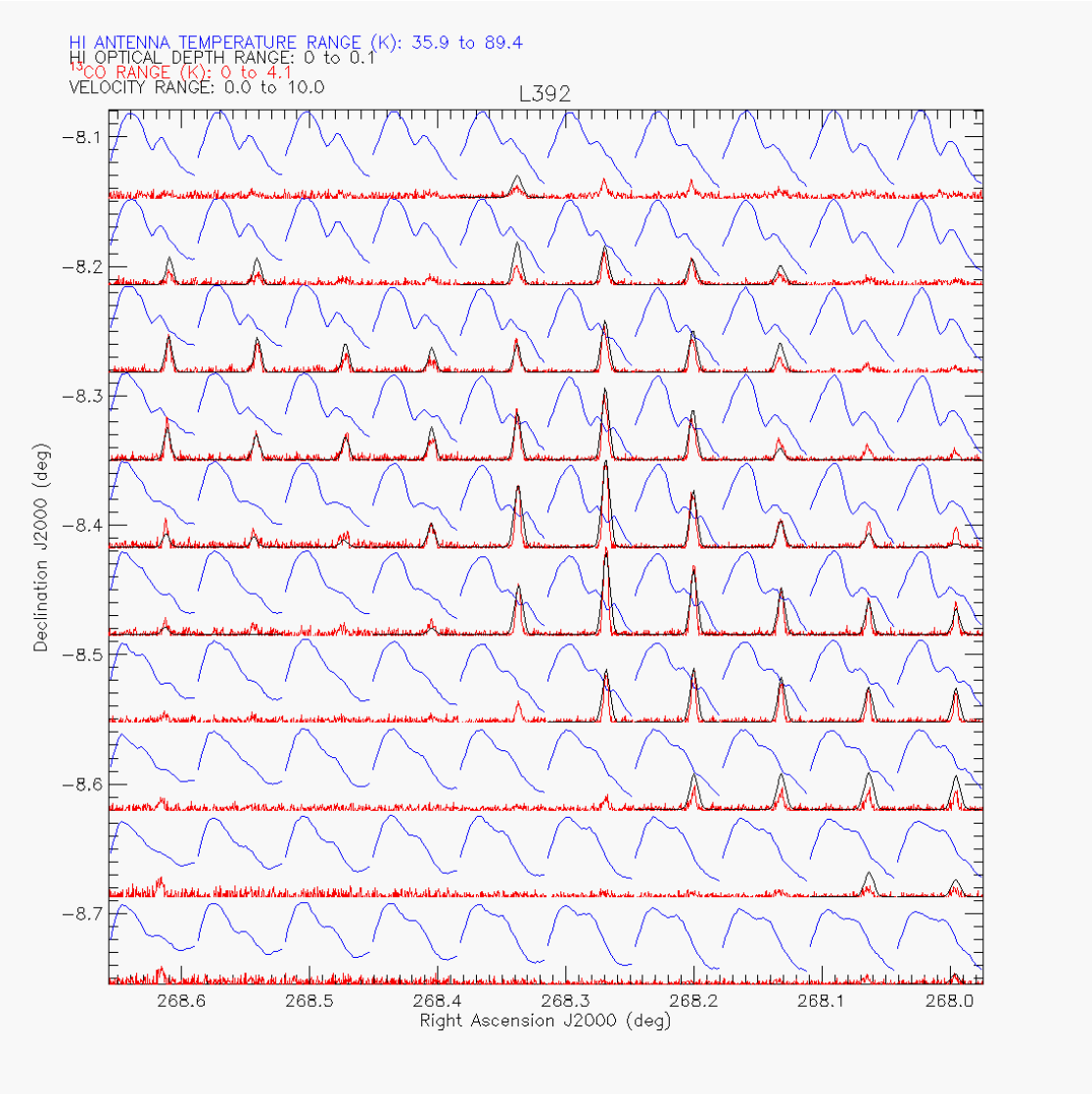

Figure 3.17: A similar representation to that in Figure 3.13 for the cloud L392.

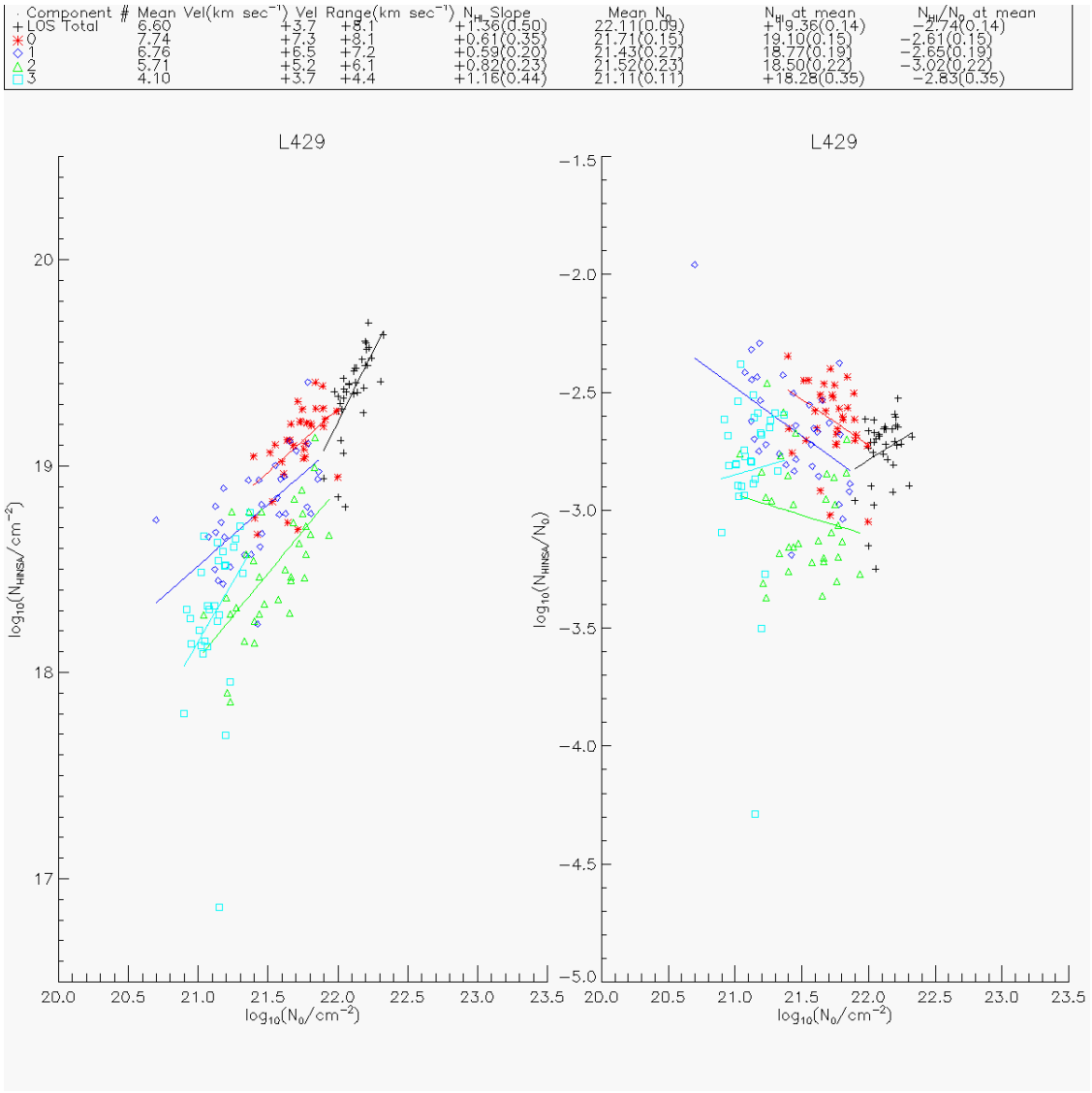

Figure 3.18: A similar representation to that in Figure 3.12 for the cloud L429.

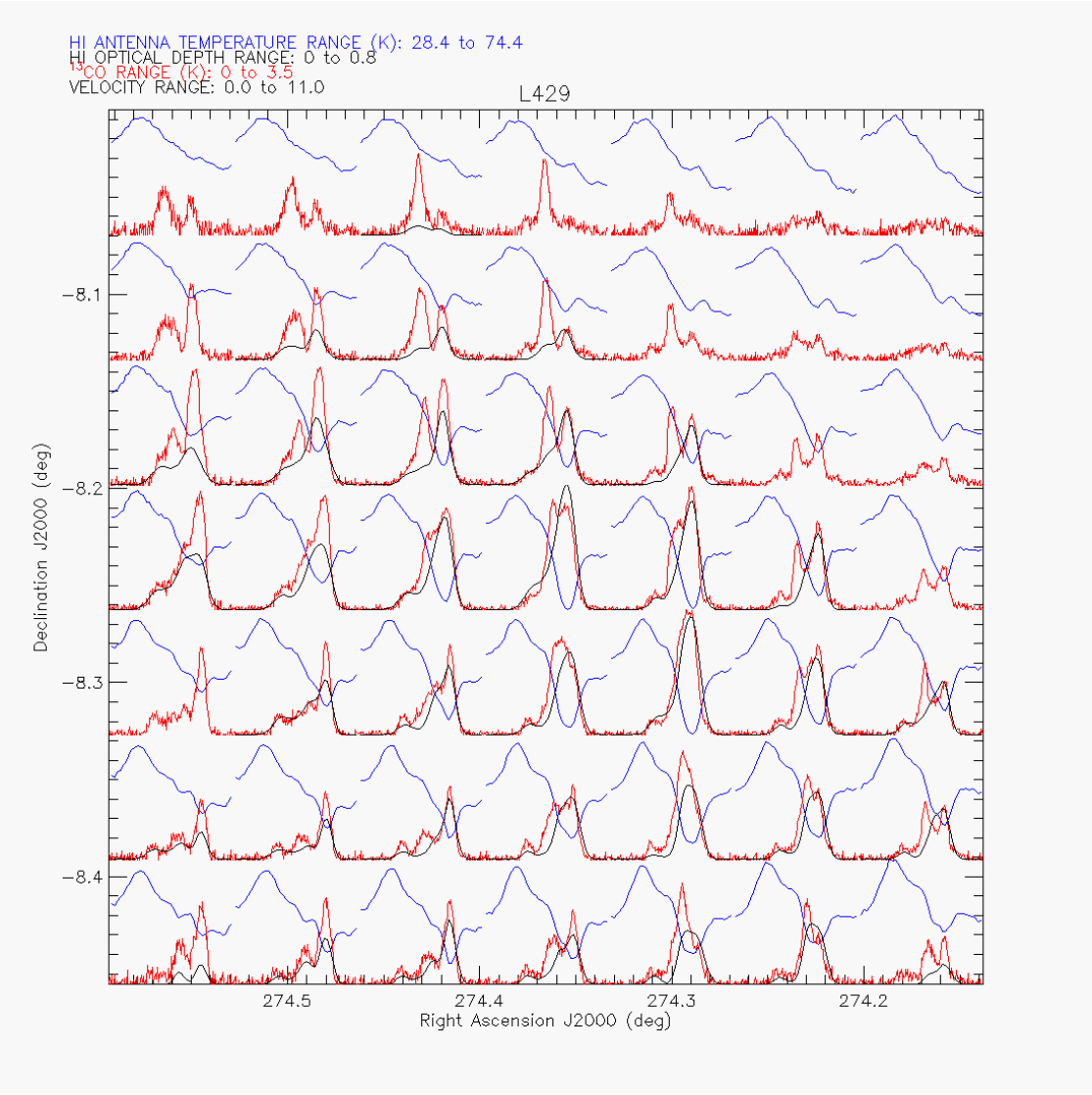

Figure 3.19: A similar representation to that in Figure 3.13 for the cloud L429.

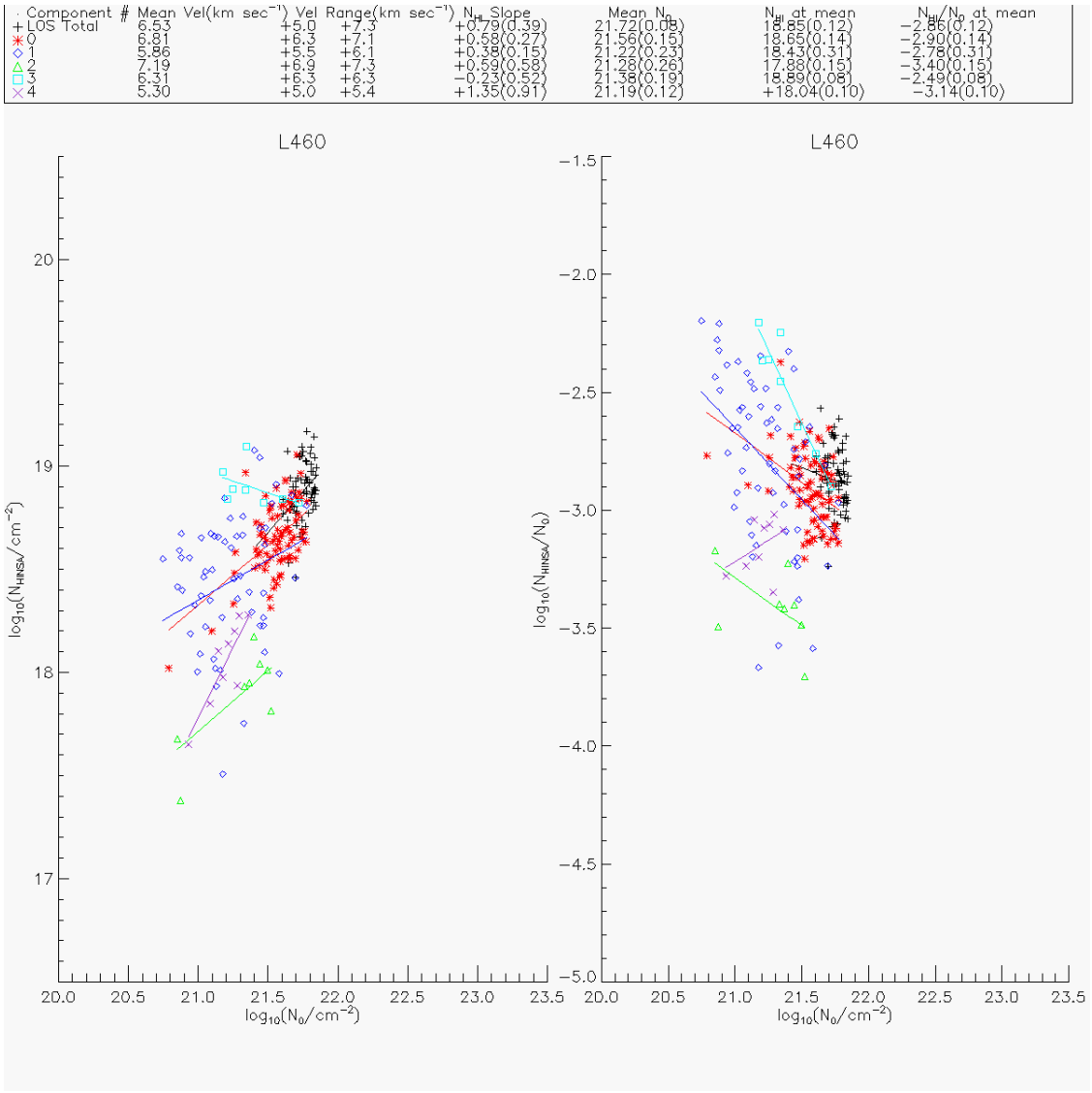

Figure 3.20: A similar representation to that in Figure 3.12 for the cloud L460.

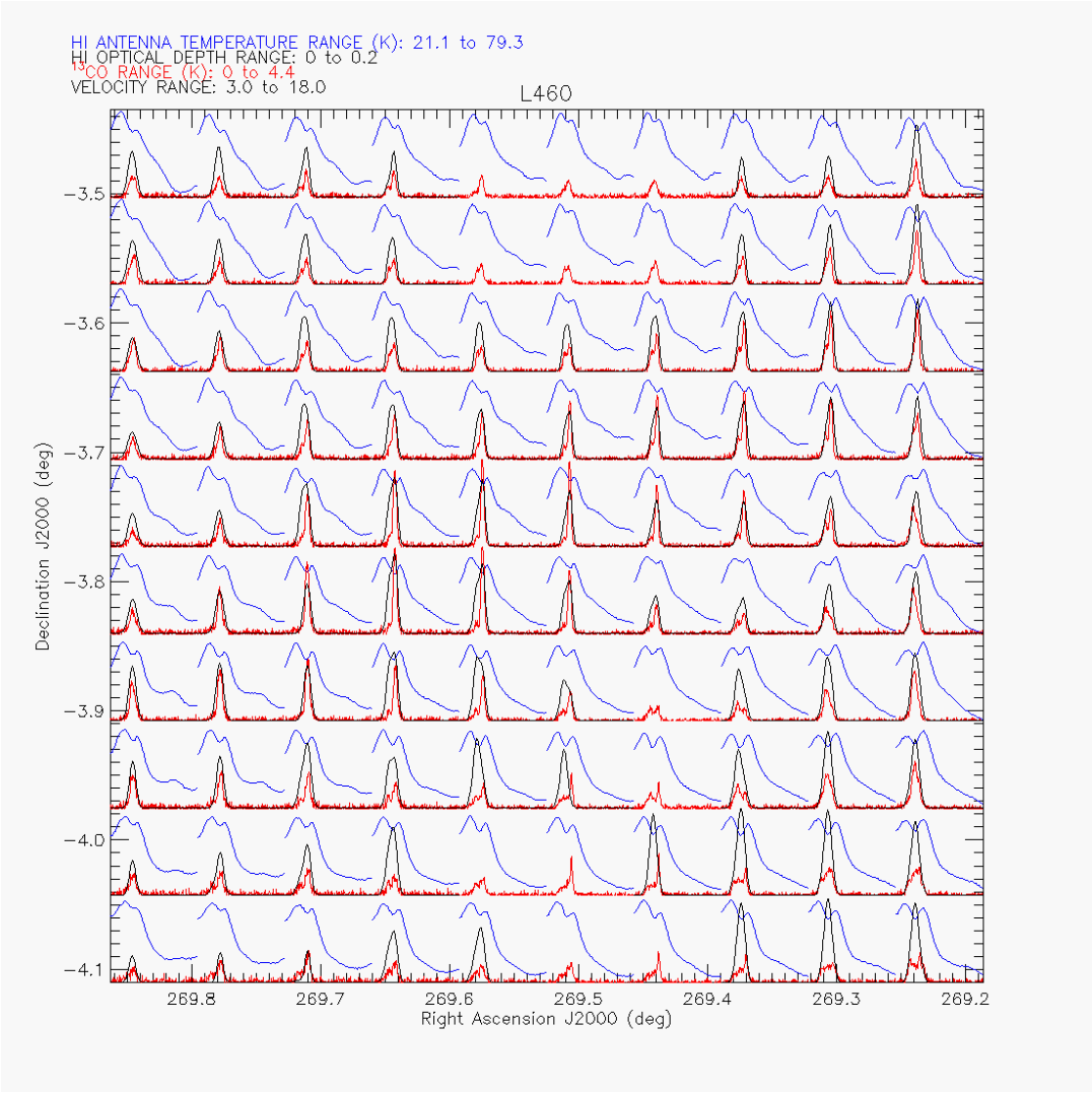

Figure 3.21: A similar representation to that in Figure 3.13 for the cloud L460.

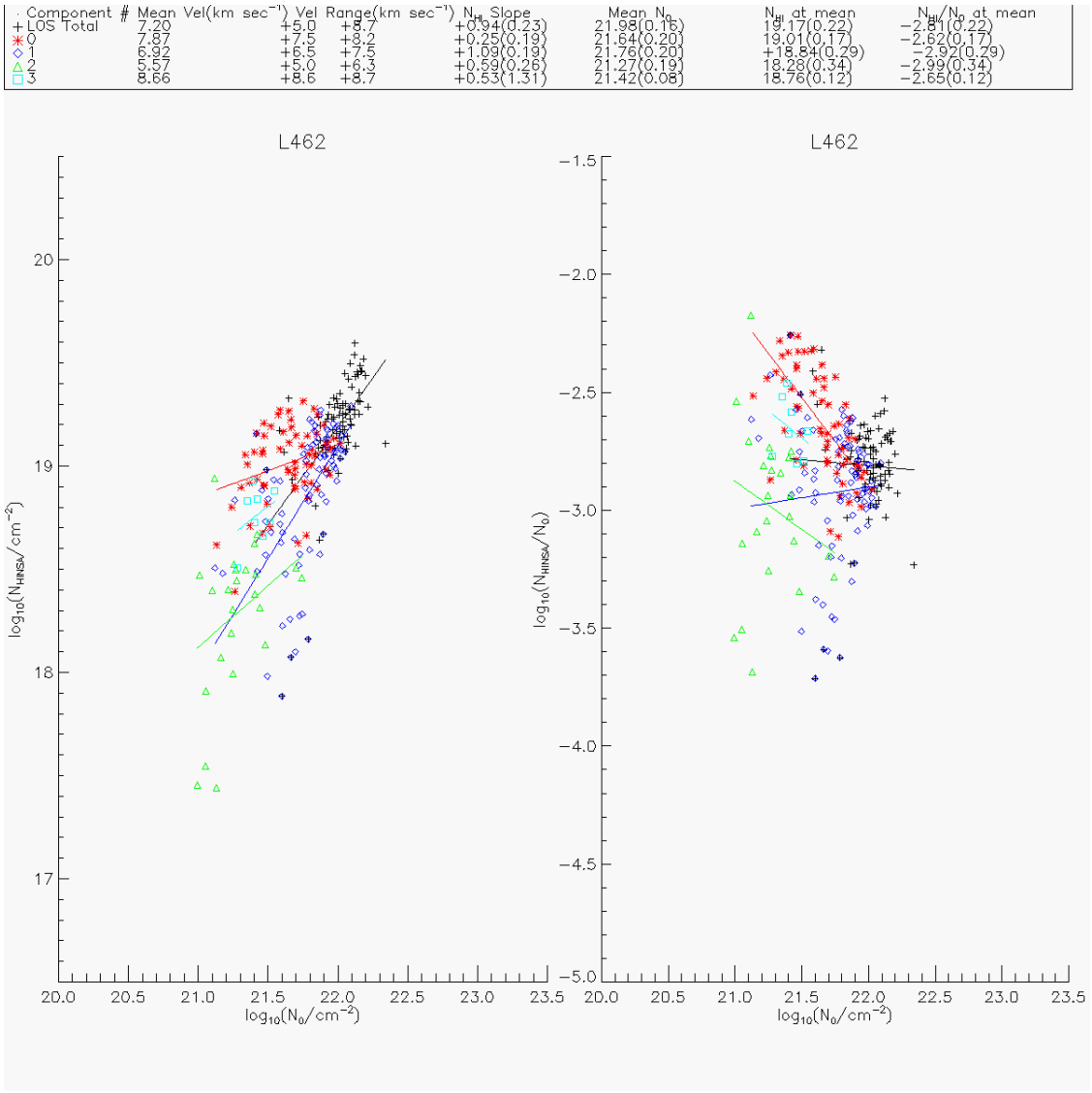

Figure 3.22: A similar representation to that in Figure 3.12 for the cloud L462.

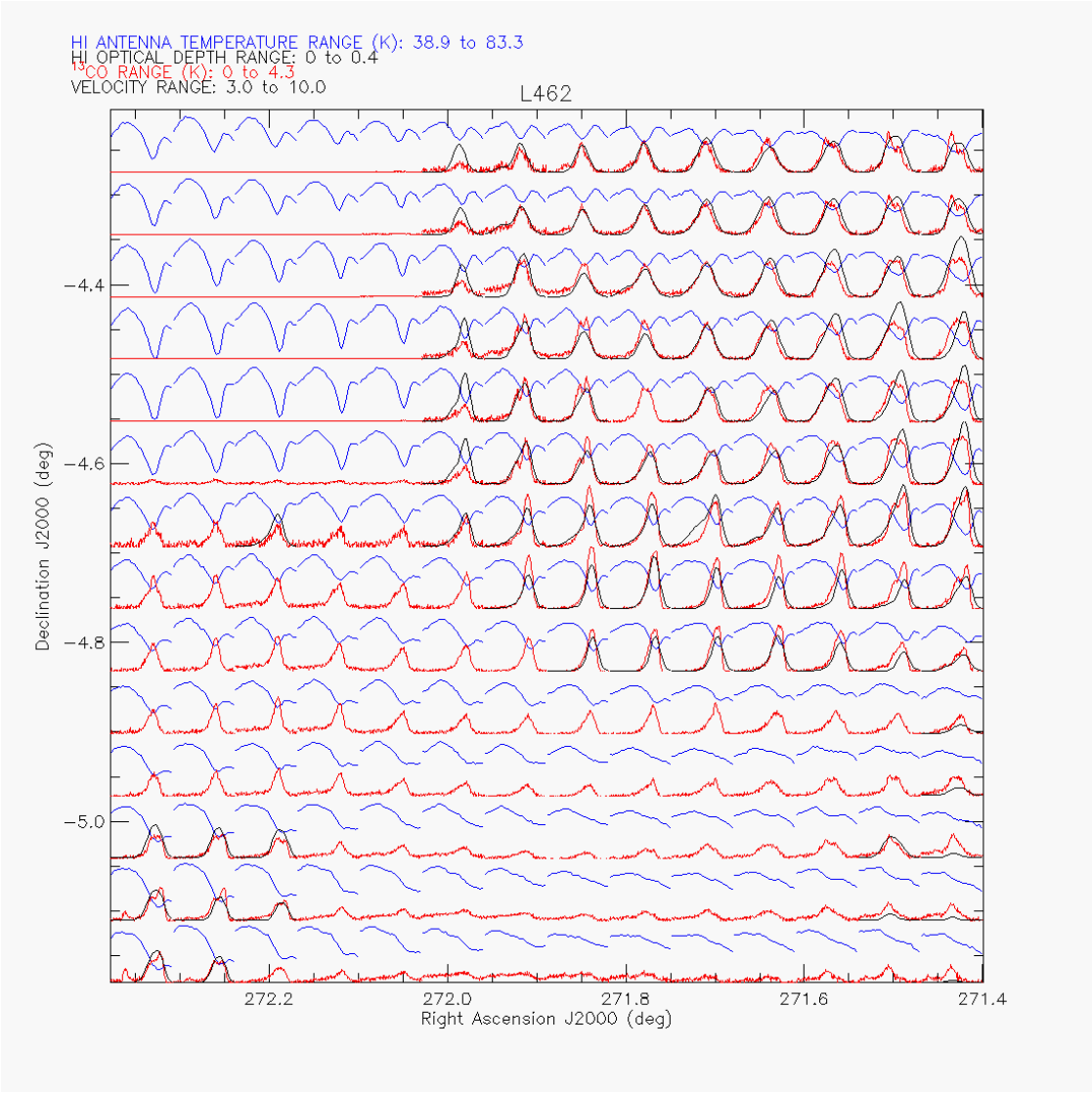

Figure 3.23: A similar representation to that in Figure 3.13 for the cloud L462.

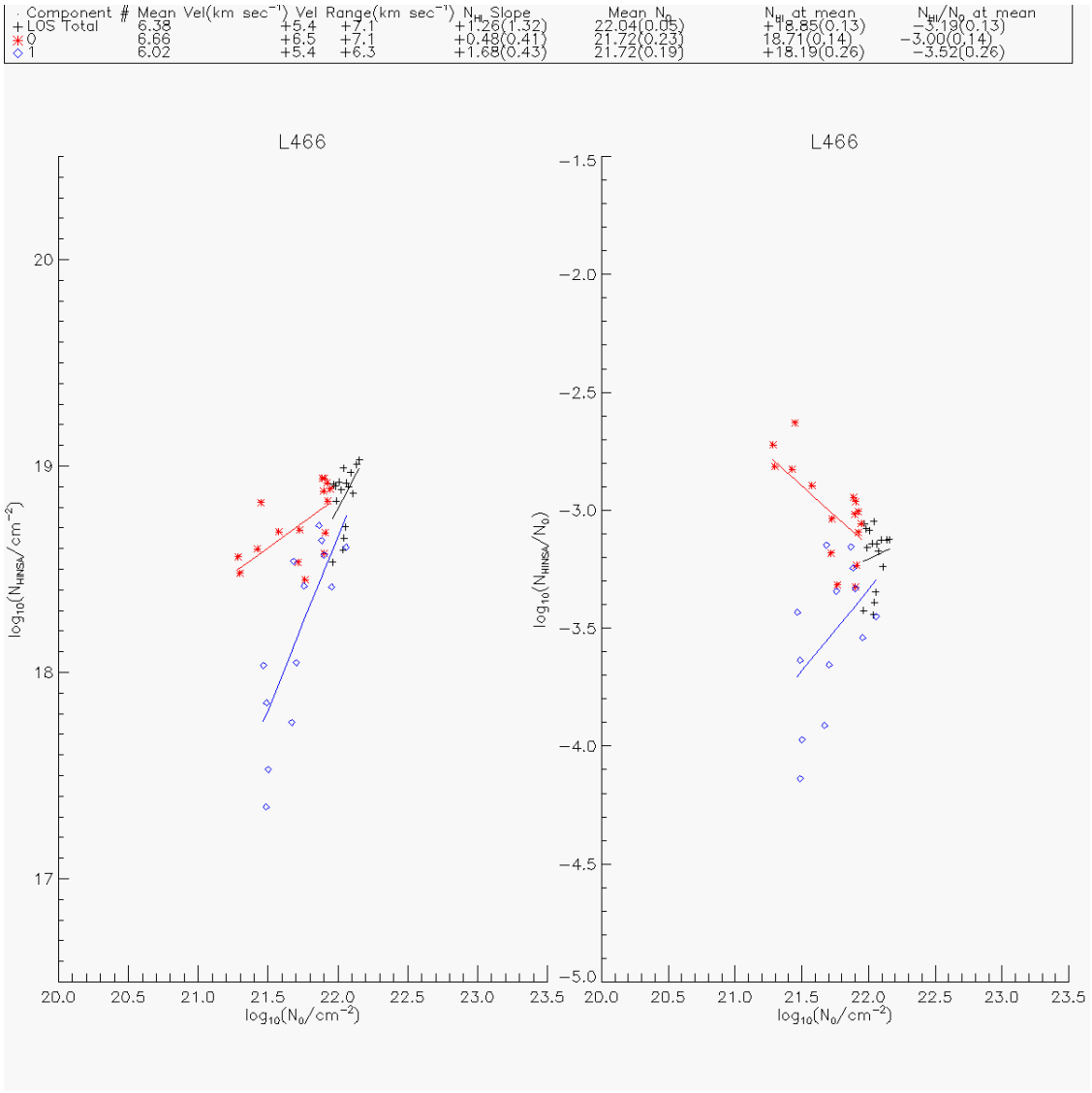

Figure 3.24: A similar representation to that in Figure 3.12 for the cloud L466.

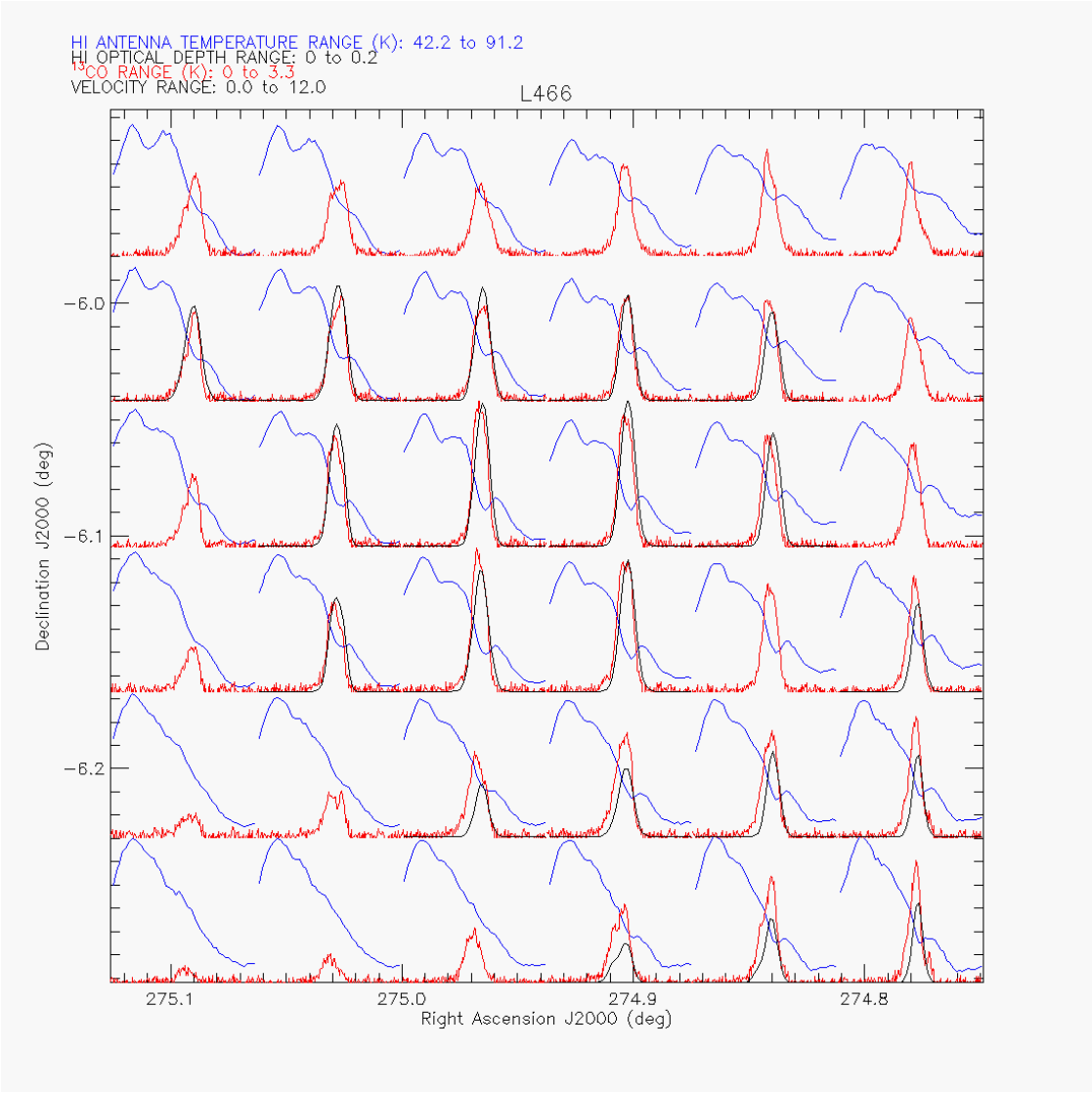

Figure 3.25: A similar representation to that in Figure 3.13 for the cloud L466.

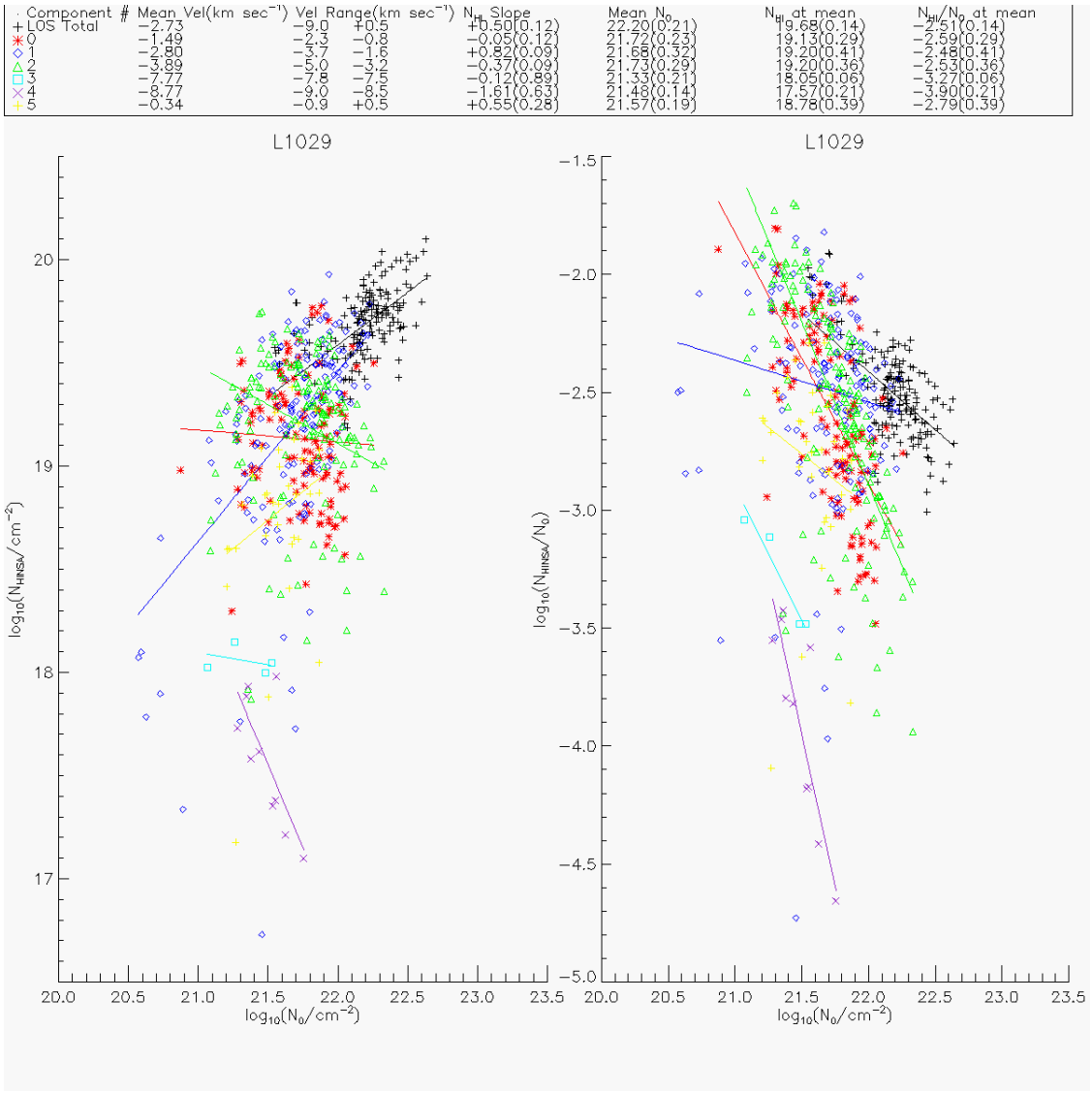

Figure 3.26: A similar representation to that in Figure 3.12 for the cloud L1029.

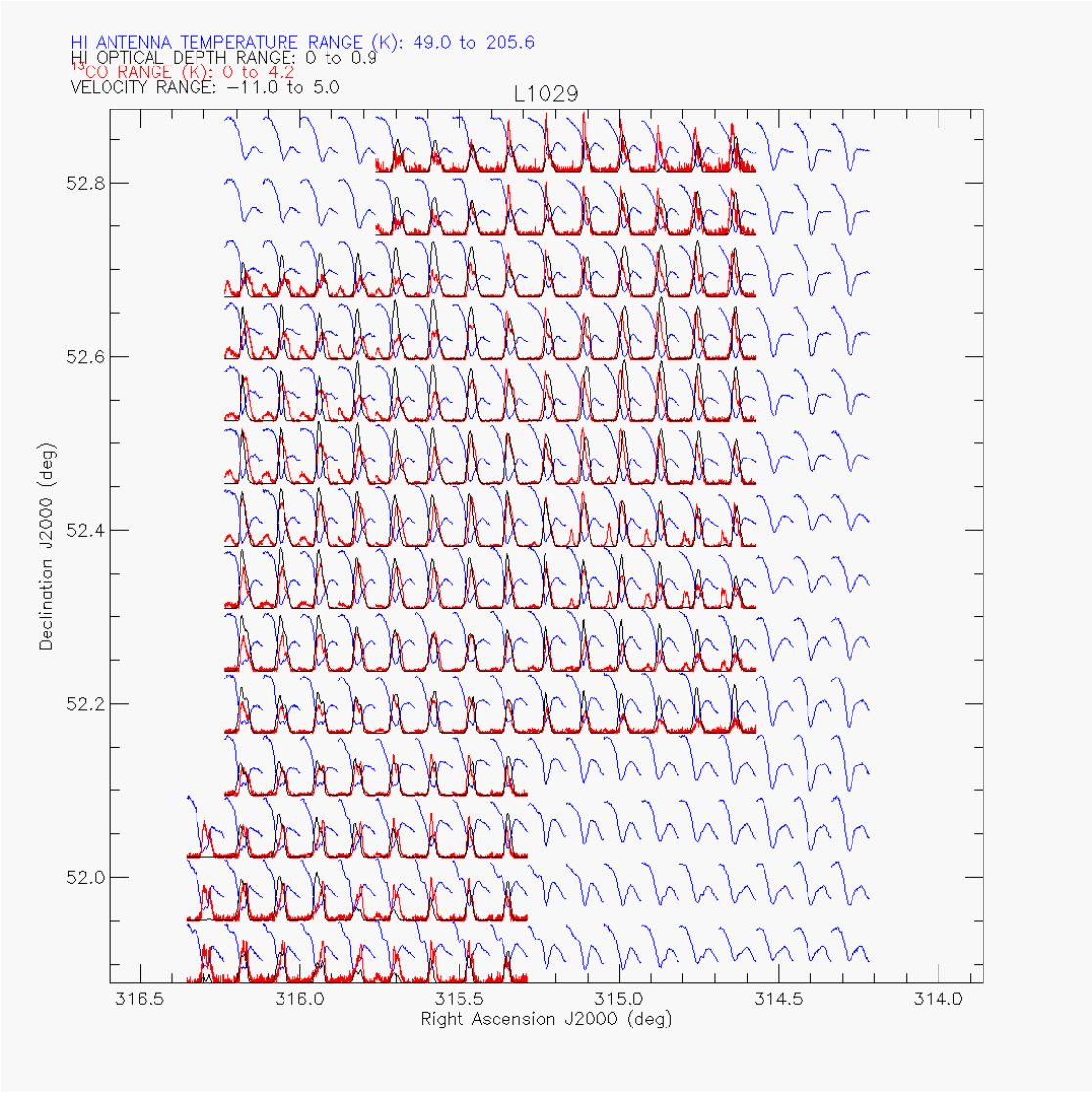

Figure 3.27: A similar representation to that in Figure 3.13 for the cloud L1029.

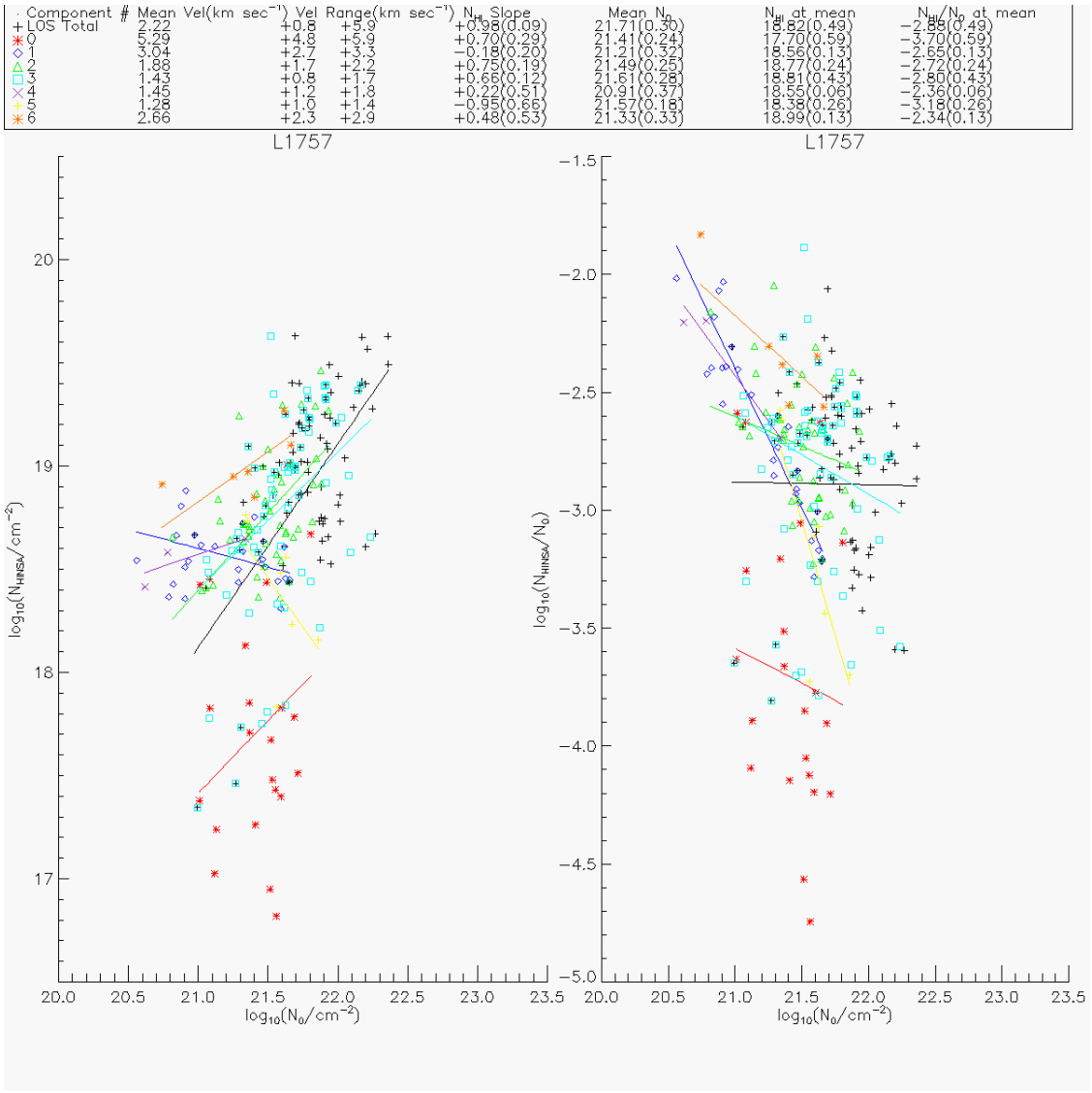

Figure 3.28: A similar representation to that in Figure 3.12 for the cloud L1757.

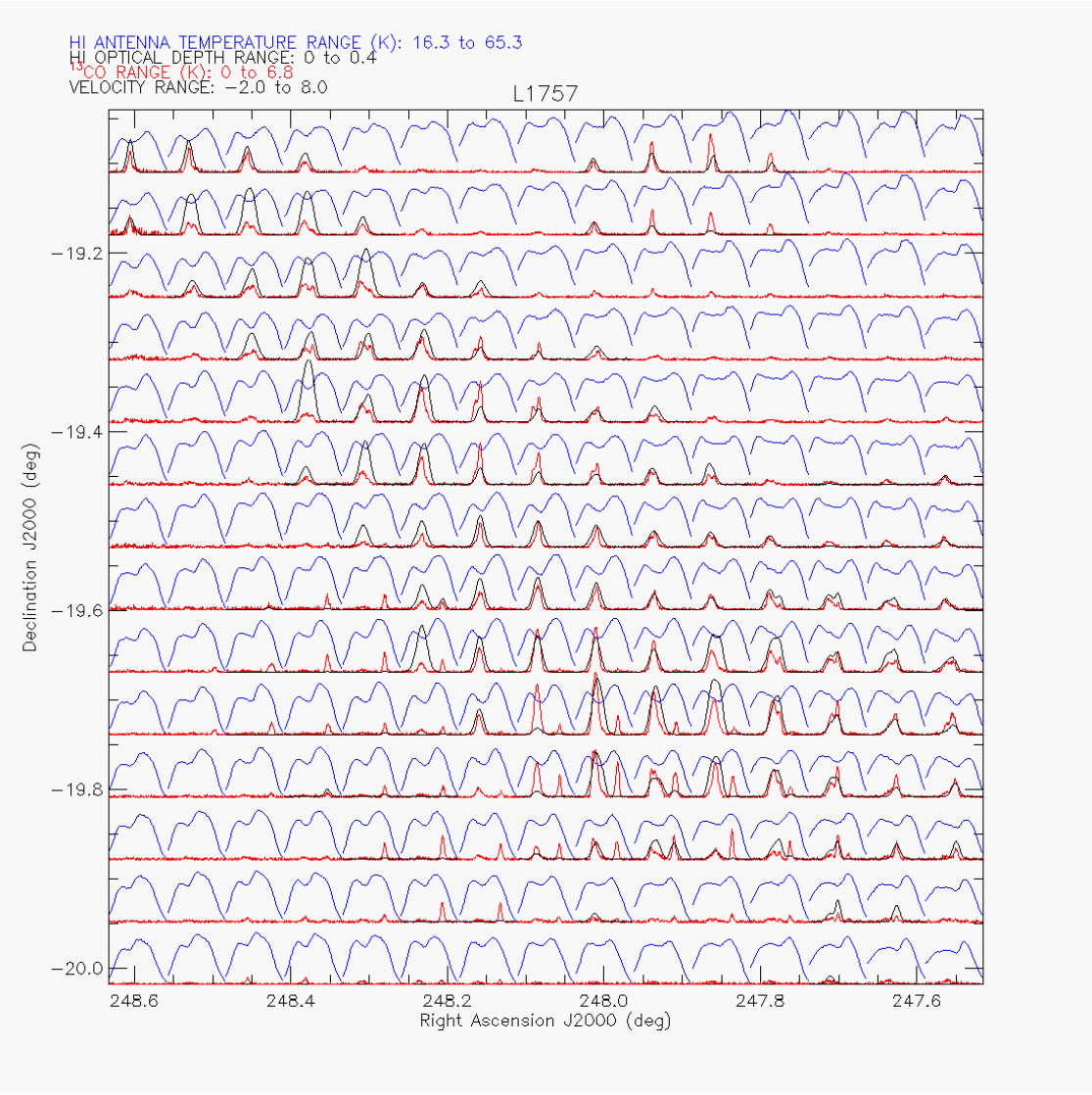

Figure 3.29: A similar representation to that in Figure 3.13 for the cloud L1757.

Source	SS Number	R.A. (J2000)	Dec (J2000)	Velocity ($kmsec^{-1}$)	$N_{HINSA}/(10^{19}cm^{-2})$	$N_0/(10^{21}cm^{-2})$	$N_{HINSA}/N_0/10^{-3}$	$\sigma_{HINSA}(kmsec^{-1})$	$T_{^{12}CO}(K)$	$T_{bg}(K)$	Distance (pc)
B133	0	19h 6m 19.25s	-6d 54m 22.60s	12.04	0.29	9.14	0.32	0.05	10.8	22.7	200 [Kim & Hong (2002)]
L1014	0	21h 24m 3.86s	50d 9m 49.71s	10.14	≤ 0.05	0.45	≤ 1.18	0.00	10.0	44.2	200 [Leung et al. (1982)]
-	-	-	-	3.72	0.28	4.24	0.68	0.07	10.0	143.5	-
-	1	21h 24m 5.76s	49d 59m 7.55s	4.01	0.09	1.52	0.64	0.03	10.0	138.6	-
L1029	0	21h 1m 33.17s	52d 11m 48.93s	-3.79	2.51	3.57	7.04	0.70	10.0	130.6	400 [Simonson & van Someren Greve (1976)]
-	-	-	-	-1.96	3.04	4.36	6.97	0.50	10.0	121.7	-
-	-	-	-	-9.01	≤ 0.01	0.52	≤ 0.19	0.00	10.0	190.2	-
L1049	0	20h 41m 5.00s	57d 27m 31.67s	0.31	0.45	12.50	0.36	0.06	11.3	68.4	440 [Felli et al. (1992)]
L1148	0	20h 41m 10.63s	67d 20m 32.63s	3.00	0.05	1.23	0.40	0.01	11.7	28.2	325 [Straizys et al. (1992)]
-	-	-	-	2.62	0.52	2.54	2.04	0.09	13.1	28.8	-
-	-	-	-	1.93	≤ 0.12	0.50	≤ 2.48	0.00	11.3	27.9	-
L1155	0	20h 43m 29.88s	67d 52m 39.42s	2.87	≤ 0.27	4.28	≤ 0.65	0.00	12.8	21.2	325 [Straizys et al. (1992)]
-	-	-	-	1.31	≤ 0.14	3.57	≤ 0.39	0.00	10.9	25.1	-
-	1	20h 43m 49.35s	67d 37m 9.09s	2.48	0.27	3.59	0.77	0.04	12.0	25.3	-
-	-	-	-	0.93	≤ 0.11	1.10	≤ 1.02	0.00	10.0	26.3	-
-	2	20h 44m 17.59s	67d 41m 59.52s	2.31	1.06	4.28	2.48	0.15	13.3	26.1	-
-	-	-	-	0.54	≤ 0.11	0.51	≤ 2.23	0.00	10.0	26.0	-
L1172	0	21h 2m 18.51s	67d 53m 53.27s	3.40	≤ 0.35	1.89	≤ 1.77	0.00	12.7	19.6	288 [Straizys et al. (1992)]
-	-	-	-	2.72	≤ 0.25	3.56	≤ 0.70	0.00	14.4	24.9	-
-	1	21h 1m 50.05s	67d 46m 24.92s	3.29	0.52	2.67	1.95	0.09	14.8	22.8	-
-	-	-	-	2.63	0.82	2.56	3.21	0.16	13.3	25.6	-
-	2	21h 4m 3.23s	67d 41m 7.69s	2.83	≤ 0.20	4.06	≤ 0.50	0.00	14.9	28.2	-
L1235	0	22h 15m 39.84s	73d 23m 1.91s	-3.67	0.01	3.05	0.04	0.13	10.0	45.2	200 [Snell (1981)]
-	-	-	-	-4.20	0.13	2.41	0.56	0.04	10.0	45.4	-
L1253	0	23h 56m 42.37s	58d 34m 12.12s	-0.31	0.08	1.43	0.60	0.02	12.6	84.4	140 [Snell (1981)]
-	-	-	-	-0.80	0.16	2.04	0.78	0.05	10.0	85.9	-
-	1	23h 57m 51.22s	58d 34m 10.52s	0.06	0.11	3.60	0.31	0.01	10.9	87.1	-
-	-	-	-	-0.58	0.08	0.71	1.12	0.01	10.0	87.8	-
-	2	23h 56m 42.33s	58d 43m 10.57s	-0.03	≤ 0.03	0.51	≤ 0.51	0.00	10.0	80.2	-
-	-	-	-	-1.09	≤0.03	1.16	≤0.22	0.00	10.0	80.0	-
-	3	23h 56m 42.53s	58d 25m 12.47s	-0.39	≤0.02	2.81	≤0.09	0.00	10.0	85.1	-
-	4	23h 55m 33.62s	58d 34m 10.92s	-0.66	0.05	2.51	0.23	0.12	10.9	72.3	-
L1262	0	23h 25m 44.78s	74d 17m 59.43s	3.91	0.16	5.01	0.33	0.05	12.6	20.2	200 [Snell (1981)]
L134	0	15h 53m 38.20s	-4d 37m 18.76s	2.57	3.17	6.54	4.84	0.43	16.5	48.4	165 [Chini (1981)]
L1544	0	5h 4m 4.72s	25d 13m 9.95s	7.17	0.12	3.21	0.38	0.04	10.0	76.1	140 [Elias (1978)]
L173	0	17h 17m 20.94s	-18d 30m 54.40s	4.19	4.28	7.54	5.68	0.32	29.1	51.2	165 [Chini (1981)]
L1757	0	16h 32m 58.19s	-19d 19m 55.62s	2.79	0.18	0.33	5.40	0.03	15.0	54.5	165 [Nozawa et al. (1991)]
-	-	-	-	1.56	3.52	5.09	6.91	0.37	15.0	55.1	-
-	1	16h 32m 0.56s	-19d 42m 51.15s	5.35	≤0.11	1.18	≤0.98	0.00	19.8	50.8	-
-	-	-	-	1.47	7.62	9.68	7.87	0.53	24.0	53.9	-
L204	0	16h 48m 55.29s	-12d 42m 29.79s	4.04	≤0.05	0.90	≤0.52	0.00	10.0	48.5	170 [McCutcheon et al. (1986)]
-	-	-	-	3.59	≤0.04	2.09	≤0.20	0.00	10.0	54.6	-
-	1	16h 48m 27.81s	-13d 5m 34.83s	3.57	≤0.04	3.64	≤0.11	0.00	10.0	54.4	-
L322	0	18h 15m 34.73s	-18d 10m 43.13s	6.33	0.38	4.07	0.95	0.13	11.2	109.1	unknown
L392	0	17h 53m 16.63s	-8d 25m 1.53s	6.80	0.36	2.39	1.51	0.18	10.0	58.2	300 [Kim & Hong (2002)]

Table 3.1: A summary of the observational results for non-mapped sources where ^{13}CO data are available. Each SS number refers to an individual pointing at the specified position. The velocity, HINSA and total proton column densities (N_{HINSA} and N_0), the non-thermal component of the HINSA linewidth (σ_{HINSA}), derived ^{12}CO excitation temperature ($T_{^{12}CO}$), and the antenna temperature of the background HI emission at the given velocity and position (T_{bg}) are given for each ^{13}CO emission component along each line of sight as well as the estimated distance to each source. Upper limits for N_{HINSA} and N_{HINSA}/N_0 are specified according to Equation 3.6.

Source	SS Number	R.A. (J2000)	Dec (J2000)	Velocity ($kmsec^{-1}$)	$N_{HINSA}/(10^{19}cm^{-2})$	$N_0/(10^{21}cm^{-2})$	$N_{HINSA}/N_0/10^{-3}$	$\sigma_{HINSA}(kmsec^{-1})$	$T_{^{12}CO}(K)$	$T_{bg}(K)$	Distance (pc)
L429	0	18h 17m 16.27s	-8d 17m 54.80s	7.68	1.32	1.71	7.70	0.45	10.9	57.5	200 [Dame & Thaddeus (1985)]
-	-	-	-	7.00	2.07	3.21	6.43	0.63	10.9	60.7	-
-	-	-	-	6.12	0.38	2.49	1.52	0.11	12.1	62.5	-
-	-	-	-	4.20	≤0.03	0.62	≤0.51	0.00	10.0	67.1	-
-	1	18h 17m 34.26s	-8d 14m 6.02s	7.50	2.30	2.95	7.79	0.73	11.1	57.2	-
-	-	-	-	6.72	0.68	1.06	6.37	0.25	12.0	60.5	-
-	-	-	-	6.02	0.60	2.68	2.25	0.15	14.4	62.4	-
-	-	-	-	4.50	≤0.03	0.67	≤0.48	0.00	10.0	66.3	-
-	2	18h 17m 48.44s	-8d 8m 52.90s	7.47	1.99	3.34	5.98	0.60	11.2	59.5	-
-	-	-	-	5.83	0.21	1.68	1.26	0.07	11.7	62.9	-
-	-	-	-	5.01	≤0.03	1.47	≤0.22	0.00	10.0	64.9	-
L43	0	16h 34m 19.97s	-15d 49m 6.82s	0.49	1.23	10.04	1.22	0.12	22.0	44.9	165 [Chini (1981)]
L460	0	17h 58m 5.87s	-3d 46m 23.88s	6.93	0.51	2.94	1.72	0.18	10.7	72.4	200 [Kim & Hong (2002)]
-	-	-	-	5.89	0.20	0.38	5.38	0.07	10.0	74.5	-
L462	0	18h 7m 33.40s	-4d 41m 34.03s	7.88	1.15	4.06	2.84	0.35	11.1	68.7	200 [Dame & Thaddeus (1985)]
-	-	-	-	6.66	0.23	0.66	3.49	0.08	10.0	72.7	-
L466	0	18h 19m 45.21s	-6d 6m 18.28s	6.45	0.93	4.71	1.98	0.28	10.1	68.3	200 [Dame & Thaddeus (1985)]
L483	0	18h 17m 34.00s	-4d 39m 14.25s	7.82	≤0.04	1.52	≤0.24	0.00	10.0	59.4	200 [Dame & Thaddeus (1985)]
-	-	-	-	5.58	0.67	5.53	1.21	0.23	12.3	71.9	-
-	-	-	-	3.48	≤0.03	0.57	≤0.48	0.00	10.0	76.6	-
L490	0	18h 15m 20.53s	-3d 46m 12.25s	8.15	1.38	4.50	3.07	0.47	10.0	64.3	200 [Dame & Thaddeus (1985)]
-	-	-	-	3.85	≤0.03	0.77	≤0.40	0.00	10.0	69.4	-
L922	0	20h 38m 29.79s	44d 31m 59.88s	7.48	0.08	0.46	1.75	0.03	10.0	165.1	700 [Dame & Thaddeus (1985)]
-	-	-	-	6.62	0.23	1.55	1.51	0.09	10.0	166.1	-
-	-	-	-	5.82	≤0.01	0.66	≤0.18	0.00	10.0	161.7	-
-	-	-	-	4.41	≤0.01	0.26	≤0.45	0.00	10.0	163.9	-
-	1	20h 38m 47.63s	44d 35m 56.60s	7.56	0.03	0.31	1.13	0.01	10.0	161.3	-
-	-	-	-	6.53	0.18	0.96	1.96	0.07	10.0	163.9	-
-	-	-	-	5.72	0.08	0.82	1.06	0.03	10.0	169.3	-
-	-	-	-	4.04	0.07	0.28	2.73	0.02	10.0	169.1	-
L981	0	21h 0m 13.32s	50d 20m 7.06s	11.47	≤0.42	0.40	≤10.60	0.00	10.0	14.3	700 [Clark (1986)]
-	-	-	-	2.44	≤0.02	0.33	≤0.51	0.00	10.0	118.4	-
-	-	-	-	-0.07	1.70	1.36	12.51	0.34	10.0	134.6	-
-	-	-	-	-2.11	1.29	1.22	10.59	0.22	10.0	140.7	-
-	1	21h 0m 14.94s	50d 16m 55.12s	11.50	≤0.41	0.43	≤9.62	0.00	10.0	14.4	-
-	-	-	-	2.47	≤0.02	0.21	≤0.78	0.00	10.0	120.8	-
-	-	-	-	0.04	1.73	0.82	21.14	0.38	10.0	132.1	-
-	-	-	-	-1.83	1.15	1.28	9.00	0.20	10.0	134.6	-
-	2	21h 0m 59.76s	50d 21m 24.48s	12.14	≤0.24	0.14	≤17.10	0.00	10.0	17.6	-
-	-	-	-	1.54	≤0.02	0.69	≤0.23	0.00	10.0	122.4	-
-	-	-	-	0.18	1.00	0.49	20.26	0.20	10.0	126.2	-
-	-	-	-	-1.55	2.43	1.56	15.54	0.30	10.0	131.1	-

Table 3.2: A continuation of Table 3.1

Source	SS Number	R.A. (J2000)	Dec (J2000)	Velocity ($kmsec^{-1}$)	$N_{HINSA}/(10^{19}cm^{-2})$	$\sigma_{HINSA}(kmsec^{-2}$	$T_{bg}(K)$	Distance (pc)
B361	0	21h 12m 25.30s	47d 22m 52.87s	2.12	≤0.03	0.00	76.7	350 [Schmidt (1975)]
L1021	0	21h 22m 15.77s	51d 3m 6.32s	0.48	0.40	0.07	174.4	200 [Leung et al. (1982)]
L1111	0	21h 40m 26.41s	57d 48m 1.80s	-0.51	0.03	0.00	105.6	150 [Leung et al. (1982)]
L129	0	16h 55m 1.26s	-16d 18m 54.61s	5.73	0.14	0.02	55.2	165 [Lee & Myers (1999)]
L1333	0	2h 41m 57.63s	75d 8m 22.89s	-1.37	0.48	0.13	44.5	unknown
-	-	-	-	-3.24	0.17	0.05	35.5	-
-	1	2h 8m 45.10s	76d 5m 38.24s	3.23	0.36	0.11	30.0	-
L1340	0	2h 28m 20.66s	72d 38m 35.28s	-14.43	0.44	0.03	64.7	600 [Kun et al. (1994)]
-	1	2h 30m 48.31s	72d 59m 56.56s	-14.75	1.03	0.08	62.6	-
-	2	2h 31m 42.65s	72d 38m 57.36s	-14.84	1.87	0.12	67.7	-
L134N	0	15h 54m 6.38s	-2d 52m 23.01s	2.47	1.38	0.22	35.6	165 [Chini (1981)]
L1355	0	2h 53m 11.42s	68d 55m 53.05s	-3.92	0.41	0.09	69.2	300.0[Lindblad et al. (1973)]
-	1	2h 54m 51.70s	68d 55m 46.21s	-3.92	≤0.03	0.00	69.4	-
-	2	2h 53m 12.97s	69d 4m 49.92s	-3.92	0.26	0.06	66.7	-
-	3	2h 53m 10.75s	68d 46m 53.57s	-3.92	≤0.03	0.00	77.8	-
-	4	2h 51m 32.37s	68d 55m 54.97s	-3.92	≤0.03	0.00	73.7	-
L158	0	16h 49m 8.87s	-14d 7m 11.79s	3.73	≤0.05	0.00	48.8	165 [Nozawa et al. (1991)]
L1780	0	15h 39m 52.57s	-7d 9m 37.10s	3.36	≤0.08	0.00	33.6	110 [Hilton & Lahulla (1995)]
L1782	0	16h 42m 38.94s	-19d 34m 18.21s	5.41	≤0.06	0.00	40.5	165 [Nozawa et al. (1991)]
-	1	16h 41m 25.50s	-19d 11m 3.84s	5.46	≤0.05	0.00	49.2	-
L255	0	16h 48m 44.07s	-10d 20m 16.89s	3.24	0.66	0.08	62.1	165 [Chini (1981)]
-	1	16h 47m 44.51s	-9d 52m 3.04s	3.72	1.02	0.18	49.1	-
L260	0	16h 47m 39.55s	-12d 6m 22.81s	3.35	≤0.04	0.00	58.2	165 [Nozawa et al. (1991)]
-	1	16h 47m 1.33s	-9d 35m 52.40s	3.35	0.37	0.07	54.6	-
L31	0	16h 49m 31.86s	-19d 2m 40.57s	4.68	≤0.05	0.00	43.6	160 [Nozawa et al. (1991)]
-	1	16h 50m 15.58s	-19d 5m 39.83s	4.69	≤0.05	0.00	45.6	-
L328	0	18h 17m 0.87s	-18d 1m 59.56s	6.78	≤0.02	0.00	105.0	200 [Bok & McCarthy (1974)]
L416	0	18h 25m 33.02s	-10d 39m 38.53s	6.04	0.27	0.07	89.4	200 [Dame & Thaddeus (1985)]
L432	0	17h 58m 26.60s	-5d 43m 55.37s	7.36	1.66	0.37	59.9	200 [Dame & Thaddeus (1985)]
L492	0	18h 15m 49.80s	-3d 46m 13.55s	7.83	1.88	0.38	63.6	200 [Dame & Thaddeus (1985)]
L503	0	18h 29m 28.45s	-4d 38m 44.86s	8.71	2.12	0.34	60.1	200 [Dame & Thaddeus (1985)]
L539	0	18h 23m 40.47s	-1d 2m 52.85s	8.43	≤0.03	0.00	80.4	200.0[Dame & Thaddeus (1985)]
-	1	18h 24m 21.35s	-0d 59m 24.76s	8.60	≤0.03	0.00	83.8	-
L588	0	18h 35m 21.28s	-0d 41m 27.08s	10.87	≤0.02	0.00	87.2	200 [Dame & Thaddeus (1985)]
-	-	-	-	7.96	≤0.03	0.00	79.2	-
-	1	18h 35m 52.56s	-0d 30m 55.08s	10.80	0.69	0.13	86.3	-
-	2	18h 36m 13.77s	-0d 38m 5.45s	7.44	≤0.02	0.00	86.6	-
L63	0	16h 50m 2.26s	-18d 3m 22.89s	5.79	≤0.04	0.00	52.1	165 [Nozawa et al. (1991)]

Table 3.3: Summary of results for non-mapped sources where only OH data are available. The velocity, HINSA column density (N_{HINSA}), the non-thermal component of the HINSA linewidth (σ_{HINSA}), and the background HI emission antenna temperature at the specified position and velocity (T_{bg}) are given for each OH emission component identified as well as the estimated distance to each source. Emission components at multiple velocities could only be identified along two lines of sight due to the lower signal to noise ratio in the OH observations. HINSA column densities were derived using OH emission as a template instead of ^{13}CO. Upper limits on N_{HINSA} are determined for all non-detections according to Equation 3.6.

Source	Center R.A. (J2000)	Center Dec (J2000)	Map Dimensions (arcmin)	Component	M_0/M	M_{HINSA}/M	$M_{HINSA}/M_{H_2}/10^{-3}$
L1029	21h 0m 57.85s	52d 23m 10.45s	100 x 60	LOS	6189.43	18.643	3.01
-	-	-	-	0	1659.70	4.635	2.79
-	-	-	-	1	1923.50	7.337	3.81
-	-	-	-	2	2158.18	6.058	2.80
-	-	-	-	3	24.69	0.009	0.40
-	-	-	-	4	69.51	0.010	0.14
L134	15h 53m 38.31s	-4d 37m 20.20s	32 x 27	LOS	143.73	0.177	1.23
-	-	-	-	0	49.39	0.038	0.77
-	-	-	-	1	33.09	0.024	0.75
-	-	-	-	2	11.46	0.026	2.29
L1757	16h 32m 18.23s	-19d 31m 45.85s	63 x 59	LOS	261.54	0.442	1.69
-	-	-	-	0	38.00	0.011	0.29
-	-	-	-	1	20.94	0.037	1.78
-	-	-	-	2	61.75	0.126	2.04
-	-	-	-	3	122.62	0.232	1.89
-	-	-	-	4	1.17	0.003	3.39
-	-	-	-	5	11.19	0.008	0.71
L204	16h 47m 46.29s	-12d 5m 17.30s	27 x 117	LOS	425.07	0.338	0.79
-	-	-	-	0	332.69	0.321	0.96
-	-	-	-	1	32.70	0.004	0.13
L392	17h 53m 15.81s	-8d 25m 1.01s	41 x 41	LOS	163.48	0.104	0.63
L429	18h 17m 27.74s	-8d 13m 48.83s	27 x 27	LOS	252.41	0.484	1.91
-	-	-	-	0	98.63	0.244	2.48
-	-	-	-	1	59.07	0.125	2.12
-	-	-	-	2	71.48	0.072	1.01
L460	17h 58m 5.97s	-3d 46m 21.17s	41 x 41	LOS	256.53	0.359	1.39
-	-	-	-	0	166.89	0.207	1.24
-	-	-	-	1	59.87	0.106	1.78
-	-	-	-	2	10.28	0.003	0.35
-	-	-	-	3	11.58	0.034	3.00
L462	18h 7m 33.38s	-4d 41m 31.98s	59 x 59	LOS	486.98	0.809	1.66
-	-	-	-	0	163.73	0.372	2.27
-	-	-	-	1	277.09	0.377	1.36
-	-	-	-	2	34.56	0.032	0.94
L466	18h 19m 44.98s	-6d 6m 15.58s	23 x 23	LOS	96.98	0.064	0.66
-	-	-	-	0	51.29	0.048	0.94

Table 3.4: The center position and map dimensions are provided for each mapped source. The total proton (M_0) and HINSA (M_{HINSA}) masses summed over an entire map are given for each velocity component in units of solar masses (M). The LOS component refers to the integrated line of sight values along each position over all present velocity components.

CHAPTER 4

GEOMETRY-INDEPENDENT DETERMINATION OF DENSITY DISTRIBUTIONS IN ASTRONOMICAL OBJECTS SUCH AS MOLECULAR CLOUDS

4.1 Introduction

A perennial problem in Astrophysics is a result of our inability to view distant objects from multiple perspectives in order to determine their three-dimensional structure. We have often been forced to utilize geometric assumptions leading to the proliferation of spherical farm animals. Applying geometric assumptions to objects of study is often both useful, and mathematically tractable. In particular, assuming that an object is spherically symmetric, or has some other simple geometry, often permits us to describe the object's internal structure using one or more radial profile functions. Radial profiles may be used to describe mass densities, emission, extinction, or other parameters. Such radial profiles are frequently used to examine or model the physics and chemistry which govern such objects.

It is relatively safe to make assumptions such that stars and planets are spherical, or that a spiral galaxy has a disk and a bulge. However, when studying less symmetric objects, geometric assumptions are often problematic. Molecular clouds exhibit a great variety of shapes which very rarely resemble simple geometries. Hence, determining their internal structure while using a geometric assumption will always yield some bias in any derived radial profile. In this paper we describe a technique which may be used to obtain limited, yet useful information about an object's radial profile function without making any

assumptions about the object's shape, orientation, or the nature of the radial profile function, while using a single two-dimensional column density map as the total available data on the source.

This technique improves on previous methods by discarding the assumption of geometry, as well as any a priori assumptions about the nature of the radial profile function used to do any kind of fitting. There are certain limitations to the technique as well as criteria which must be fulfilled. These are discussed in detail in Section 4.2. The most important limitation and constraint may be summarized as follows.

- Since a two dimensional projection cannot uniquely define a three-dimensional object without additional information, it is impossible to obtain absolute values for the radial profile function without additional information or assumptions. It is however possible to obtain the shape of the function.
- The internal structure of the object in question must be describable using a single radial profile function.

In theory the technique may be used to study spectral line emission, absorption, continuum emission, extinction, etc. It may be applied to any object from a molecular clouds, to an accretion disk, or even the stellar distributions in a galaxy, provided it is consistent with the assumptions described in Section 4.2.

To illustrate and validate the technique we have chosen to apply it to maps of the dust extinction in molecular clouds using publicly available 2MASS column density maps derived using stellar reddening. Dust extinction maps were chosen as the properties of the 2MASS data are well-known, and the distribution

of dust in molecular clouds is a long-studied and currently active field of study. This paper is formulated so as to introduce a novel methodology by presenting an analytical derivation, testing it against simulated data, and finally applying it to real data. Section 4.2 describes the initial assumptions which must be fulfilled in order for the technique to be applicable to a given object. The assumptions ultimately lead the reader to critical relationships which illustrate the key aspects of this technique. Section 4.3 derives the technique analytically using two different methods. Section 4.4 applies the technique to a set of simulated data designed to test its validity as well as expose its performance under a wide range of circumstances. Section 4.5 discusses the choice of using 2MASS dust extinction maps and applies the technique to such maps of several clouds. Once the technique has been fully described and demonstrated, a comparison is made with previous methods for measuring radial profiles in Section 4.6. The results, and performance of this new technique are discussed in Section 4.7.

4.2 Assumptions

The goal of this research is to extract the maximum available information regarding the internal volume density structure of a source using a single column density map observed from one line of sight direction, while making the fewest possible assumptions. We show how it is possible under certain conditions to obtain the shape of an object's volume density profile function without assuming a specific geometry, or making any assumptions about the function that governs the radial density profile. To this end it is necessary to detail the assumptions used in this work.

The method described here only relies on the three assumptions below which are made explicitly for all cases.

Assumption 1: The object studied must be optically thin in whatever observable quantity is being measured in the sense that

$$N(y,z) = \int_{-\infty}^{\infty} n(x,y,z)dx \ , \tag{4.1}$$

where $N(y,z)$ is the measured column density at position (y,z) and $n(x,y,z)$ represents the volume density at position (x,y,z). The observed column density must correspond to the total column density of whatever quantity is being measured. The x axis is arbitrarily chosen to represent the line of sight direction throughout this paper.

Assumption 2: The volume density of the object can be characterized entirely using a single function for the volume density profile.

Previous methods have made assumptions about either the shape of the object or the of the function which governs the volume density in addition to the two assumptions above. No such additional assumptions are made here.

The following assumptions arise wholly as a direct consequence of assumption 2, however they are rarely explicitly stated in the literature.

Assumption 2a: Any object which satisfies assumption 2 must be described using two functions; One function describes the cloud's geometry and a second describes its radial volume density profile.

We define the object's shape using a core function

$$a(\alpha,\theta) = a_c f_c(\alpha,\theta) \ , \tag{4.2}$$

where $a(\alpha, \theta)$ has units of length and describes the size of the object's core along each direction (represented by spherical coordinates (α, θ)) originating from the object's center. a_c is a constant with units of length, and $f_c(\alpha, \theta)$ is a dimensionless function which scales the core radius along each (α, θ) to produce a core shape for the object. In the case of a sphere, $f_c(\alpha, \theta) = 1$ while a_c represents the sphere's radius. Spherical (α, θ), or cartesian (x, y, z) coordinates may be used to describe the core, however the spherical coordinates were chosen here to denote the fact that the core function depends entirely on a direction from the object's center, and not on distance.

Simple radii are a convenient and sufficient parameter by which to characterize objects with simple symmetries such as spheres. When working with arbitrary shapes it is more convenient to define a new, dimensionless parameter r_{rc} which is equal to the ratio between the distance from some point (x, y, z) to the object's center, and the core radius $a(\alpha, \theta)$ along the same direction. If the object's center is located at the origin of the coordinate system $(0, 0, 0)$, then

$$r_{rc}(x, y, z) = \frac{\sqrt{x^2 + y^2 + z^2}}{a(\alpha, \theta)} \ . \tag{4.3}$$

(x, y, z) represent an arbitrary Cartesian coordinate system where x corresponds to the line of sight, and the object's center is located at the origin. In the case of a sphere $r_{rc}(x, y, z) = \sqrt{x^2 + y^2 + z^2}/a_c$. In order to fully describe the geometry of an object which meets Assumption 2, $f_c(\alpha, \theta)$ must be defined, and not equal to zero for all values of (α, θ). Further, it is necessary for $f_c(\alpha, \theta)$ to describe a closed surface such that a vector from the object's center along any direction will cross the surface exactly once. This permits the definition of a radial volume density function which is dependent on r_{rc} that governs the volume density distribution

of the entire cloud. We choose to define

$$n(x, y, z) = n_0 f_n(r_{rc}) \ , \tag{4.4}$$

where $n(x, y, z)$ represents the volume density of the observable quantity at position (x, y, z), and $f_n(r_{rc})$ is a dimensionless function which governs the radial volume density profile. n_0 is a constant scalar representing the volume density at those positions where $f_n(r_{rc}) = 1$.

$r_{rc}(x, y, z)$ and $n(x, y, z)$ can fully characterize any object which satisfies assumption 2. It is reasonable to conclude that neither $r_{rc}(x, y, z)$ or $n(x, y, z)$ can ever be fully determined from a single column density map using only one observable quantity without additional information since a column density map in and of itself can not uniquely define a three-dimensional object. An object which is shallow along the line of sight and possesses high volume density can produce the same column density map as an object which is deeper and less dense. However, it is possible to determine the function f_n as well as certain properties of $a(\alpha, \theta)$ by taking advantage of the self-similarity imposed on the object by assuming the validity of assumption 2. Any object which satisfies assumption 2 can be described in the above manner, and necessarily must conform to the implied assumptions below.

Assumption 2b: Specific values of r_{rc} describe three-dimensional surfaces of equal volume density. The left side of Figure 4.1 illustrates three such surfaces belonging to an arbitrary object, with three distinct values of r_{rc}. All volume density surfaces share the same shape, orientation, and center position. Since each surface is defined by a specific value of r_{rc}, each may be defined to have a specific volume density. The only variation between surfaces of different r_{rc} is in their size, and volume density. The volume

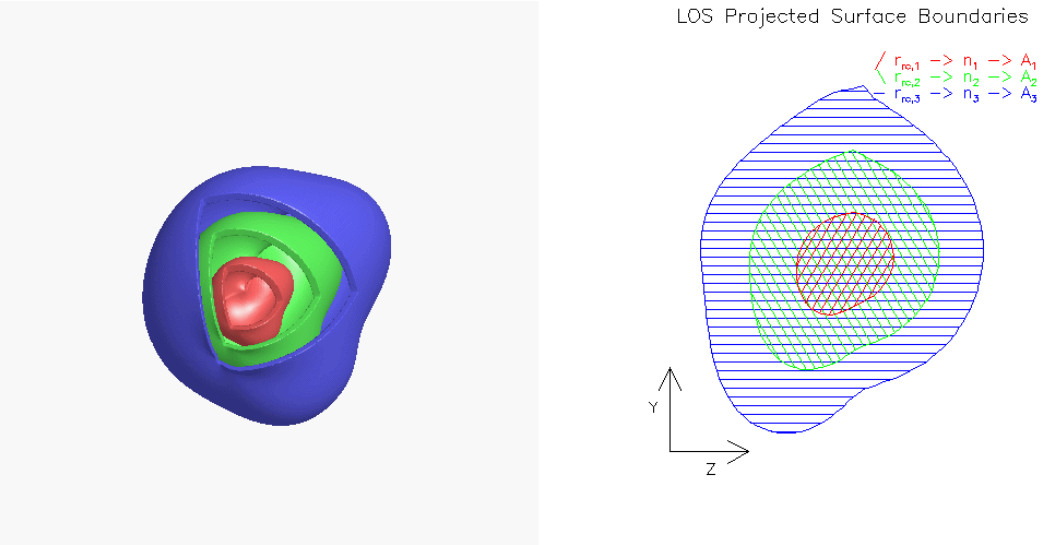

Figure 4.1: (Left) A three-dimensional representation of surfaces with three specific values of r_{rc} for an arbitrary object which satisfies assumption 2. Each surface shares the same shape and orientation, while differing only in scale. (Right) Projections along the line of sight (LOS) of the three surfaces. Each surface is characterized by a specific value of r_{rc}, its projected Area (A), and is defined by its own volume density (n) as in Equation 4.4. Each projected area also has the same shape and orientation, while differing only in scale. Since the object is assumed to be optically thin, the projected column densities from each surface are additive.

enclosed by each surface, and its surface area are directly proportional to r_{rc}^3 and r_{rc}^2 respectively.

Assumption 2c: Each volume density surface, when projected onto a plane perpendicular to the line of sight produces a two-dimensional boundary whose area is directly proportional to r_{rc}^2. The right side of Figure 4.1 describes such projections of three surfaces with independent values of r_{rc}. All such surface boundaries are identical except in their size and the corresponding volume densities they represent. Each surface, defined by a specific value of r_{rc} forms a projection with a specific Area (A), and vice versa.

Self-similarity between different volume density surfaces is a critical conclusion of assumptions 2b and 2c. Aside from certain constants, the only parameters which differentiate the projected boundaries of different volume density surfaces are the area, which is expressable in terms of r_{rc}^2, and the corresponding volume density, which is determined by $f_n(r_{rc})$. Therefore there must be a relationship between the area of each projected boundary and its volume density which is dependent on $f_n(r_{rc})$, but is, aside from some constants, independent of $f_c(\alpha, \theta)$. *$f_c(\alpha, \theta)$ determines the shape and orientation which are identical for each surface, while the relationship between the projected area and volume density of each surface is governed by the radial density profile function ($f_n(r_{rc})$).*

The observable column density map is a superposition of all the volume density surfaces projected onto a plane perpendicular to our line of sight. Thereby the column density map should exhibit the same self-similarity seen among the individual volume density surfaces. If assumptions 1 and 2 hold for a given object, then the following must be valid as well

Assumption 3: Comparing the column densities and areas of different column density contours should yield a relationship which is, aside from some constants, independent of the object's geometry.

Assumption 3 is in fact confirmed analytically by equation 4.25 in Section 4.3.2. The following section shows how the function $f_n(r_{rc})$ may be derived using that relationship.

4.3 Derivation

No truly general proof which would apply to all possible shapes is evident at this time. Therefore it is necessary to restrict this analytic derivation to those geometries which can be described by a quadratic definition of r_{rc}. Geometries which do not conform to equation 4.5 are tested numerically in Section 4.4. A useful form for r_{rc} is

$$r_{rc}(x, y, z) = \sqrt{x^2 a + x b(y, z) + c(y, z)} \ , \tag{4.5}$$

where a is a constant while $b(y, z)$ and $c(y, z)$ are any functions that conform to assumption 2. The above quadratic representation, while not universal, can describe a wide variety of geometries encountered in nature including triaxial ellipsoids. No specific values for $a, b(y, z)$, and $c(y, z)$ are invoked in the following derivation except where noted for purposes of illustration. In such cases, a spheroid model with axial ratio α, inclined by an angle i through a rotation about the y axis will be used. A spheroid is chosen because it is mathematically tractable yet versatile enough to demonstrate changes in shape and orientation by varying α and i respectively. Such a spheroid may be described using

$$a = \frac{\omega^2}{a_c^2 \alpha^2} \ , \ \omega^2 = \alpha^2 cos^2(i) + sin^2(i) \ , \tag{4.6}$$

$$b(z) = \frac{2z cos(i) sin(i)(1 - \alpha^2)}{a_c^2 \alpha^2} \ , \tag{4.7}$$

$$c(y, z) = \frac{y^2 \alpha^2 + z^2(\alpha^2 sin^2(i) + cos^2(i))}{a_c^2 \alpha^2} \ . \tag{4.8}$$

Specific values of r_{rc} describe individual surfaces of equal volume density within the object. Since the line of sight is chosen to be along the x axis it is

useful to express the x positions of each surface with a specific r_{rc} as

$$x_{r_{rc},\pm}(y,z) = \frac{-b(y,z) \pm \sqrt{b(y,z)^2 - 4ac(y,z) + 4ar_{rc}^2}}{2a} \ . \tag{4.9}$$

Defining a new function

$$E(y,z) = \frac{4ac(y,z) - b(y,z)^2}{4a} \ , \tag{4.10}$$

yields

$$x_{r_{rc},\pm}(y,z) = \frac{-b(y,z)}{2a} \pm \frac{\sqrt{r_{rc}^2 - E(y,z)}}{\sqrt{a}} \ . \tag{4.11}$$

$x_{r_{rc},\pm}(y,z)$ represents the two line of sight (x) positions for a surface defined by a particular value of r_{rc} at sky position (y,z). Functions a, $b(y,z)$, and $c(y,z)$ are defined by the geometry of the object in question. Equations 4.6, 4.7, and 4.8 describe the appropriate functions representing a spheroid with axial ratio α and inclination i. $E(y,z)$ is a function that is entirely dependent on the object's shape; its conceptual meaning is expanded upon in the following section.

4.3.1 Discrete Derivation

An object may be considered to be composed of an infinite number of surfaces such as those defined by equation 4.11, with each surface possessing a specific value of r_{rc} and therefore volume density. It is possible to define the object as a discrete series of shells, each of which is defined as the region between an inner ($r_{rc,i}$) and an outer ($r_{rc,o}$) surface with an average volume density ($n_{i,o}$) within the shell. Each such shell will have varying depths along the x axis at different (y,z) positions.

$$D(y,z)_{i,o} = (x_{r_{rc,o},+}(y,z) - x_{r_{rc,o},-}(y,z)) - (x_{r_{rc,i},+}(y,z) - x_{r_{rc,i},-}(y,z)) \ , \tag{4.12}$$

where $D(y,z)_{i,o}$ is the total depth along the line of sight at position (y,z) for the shell made up of two surfaces defined by $r_{rc,i}$ and $r_{rc,o}$. Substituting equation 4.11 into equation 4.12 yields,

$$D(y,z)_{i,o} = \frac{2}{\sqrt{a}}\left(\sqrt{r_{rc,o}^2 - E(y,z)} - \sqrt{r_{rc,i}^2 - E(y,z)}\right) \ . \tag{4.13}$$

Equation 4.13 describes the depth of each shell, however this representation is of limited use since r_{rc} is merely a mathematical construct, and not an observable quantity. Similarly, $E(y,z)$, is a function which is directly dependent on the object's shape, which is unknown. Equation 4.13 must be put in terms of observable quantities. It was concluded in Section 4.2 that the observed column density map would exhibit the same self-similarity as the projected boundaries of individual surfaces. This conclusion leads to two related observable quantities, one is the observed column density, and the other is the area under each column density contour.

Each surface, as described by equation 4.11, when projected onto the line of sight, produces a closed boundary composed of those (y,z) positions where $x_{r_{rc},+}(y,z) = x_{r_{rc},-}(y,z)$. In view of Equation 4.11 the projected boundaries of each shell are then defined by

$$E(y,z)_{boundary} = r_{rc}^2 \ . \tag{4.14}$$

Solving for $E(y,z)$ using the spheroid model above, yields a readily recognizable relation,

$$E(y,z)_{spheroid} = \frac{1}{a_c^2}\left(\frac{z^2}{\omega^2} + y^2\right) \ , \tag{4.15}$$

which is a simple ellipse that results from projecting a three dimensional spheroid surface onto a two dimensional plane. Equation 4.14 makes clear that each contour of equal $E(y,z)$ corresponds to the boundary of a particular volume density surface, with a specific value or r_{rc} and possesses a unique projected area. In general, the projected area made by a surface of a particular r_{rc} can be expressed as

$$A = \epsilon r_{rc}^2 \ , \tag{4.16}$$

where ϵ is a geometry-dependent, unknown constant($\epsilon_{sphere} = \pi a_c^2, \epsilon_{spheroid} = \omega\pi a_c^2$). All positions with equal $E(y,z)$ can be said to correspond to the projected boundary of a surface with $r_{rc,c}$ with corresponding area A_c.

Therefore, equation 4.13 can be reformed in terms of areas as

$$D_{i,o,c} = \frac{2}{\sqrt{a\epsilon}}\left(\sqrt{A_o - A_c} - \sqrt{A_i - A_c}\right) \ , \tag{4.17}$$

where $D_{i,o,c}$ represents the depth along the line of sight of the shell between surfaces defined by $r_{rc} = r_{rc,i}$ and $r_{rc} = r_{rc,o}$ at all positions defined by the contour formed by the projected boundary of the surface defined by $r_{rc,c}$. The observed column density can then be defined as

$$N_c = \sum_{k=c}^{\infty} n_{k,k+1} D_{k,k+1,c} = \sum_{k=c}^{\infty} n_{k,k+1} \frac{2}{\sqrt{a\epsilon}}\left(\sqrt{A_{k+1} - A_c} - \sqrt{A_k - A_c}\right) \ . \tag{4.18}$$

N_c represents the column density at all positions (y,z) defined by the projected boundary of the $r_{rc,c}$ surface. $n_{k,k+1}$ represents the mean volume density within the shell whose surfaces are defined by $r_{rc,k}$ and $r_{rc,k+1}$. The column density and area are observable quantities, however $n_{k,k+1}/(a\epsilon)$ are unknowns. One method of obtaining the relationship between column density and area is to create column density contours on the observed map, yielding a discrete series of contour column densities and associated areas. Using such data it should be possible to obtain information on the quantity $n_{k,k+1}/(a\epsilon)$.

It is useful to define two new variables which will represent the derived volume density profile function.

$$r' = \sqrt{\frac{A}{\pi}} = \sqrt{\frac{\epsilon}{\pi}} r_{rc} \ , \tag{4.19}$$

$$n'(r') = n(r_{rc}) \sqrt{\frac{\pi}{a\epsilon}} = n_0 \sqrt{\frac{\pi}{a\epsilon}} f_n \left(r' \sqrt{\frac{\pi}{\epsilon}} \right) \ , \tag{4.20}$$

permitting equation 4.18 to be rewritten as

$$N_c = \frac{2}{\sqrt{\pi}} \sum_{k=c}^{\infty} n'_{k,k+1} \left(\sqrt{A_{k+1} - A_c} - \sqrt{A_k - A_c} \right) \ . \tag{4.21}$$

The observed column density map can yield a series of contours denoted by their column density (N_c) and area (A_c). Beginning with the outermost contour with the largest area, and moving recursively inward it is possible to derive a series of $n'_{c,c+1}$ measurements for the object using equation 4.21. Equation 4.19 yields a series of r'_c measurements derived from the contour Areas (A_c), yielding a derived relation $n'(r')$. Equation 4.20 shows that $n'(r')$ is related to $n(r_{rc})$ and $f_n(r_{rc})$ through a series of constants (ϵ, n_0, a) which are all unknowns. Knowledge of the object's geometry would yield values for ϵ and a allowing the determination of n_0 and the full definition of the object's radial volume density profile $n(r_{rc})$. Similarly, knowledge of n_0 and f_n could yield knowledge of the object's geometry.

Without such a priori information there are limits to the knowledge which may be obtained from a single column density map, however $f_n(r_{rc})$ can be determined to within 2 unknown scalars related to the dependent and independent variable. Thus it is possible to obtain the shape of the volume density profile function solely from a column density map. This is done without assuming a specific geometry for the object, nor are any assumptions made regarding the nature of $f_n(r_{rc})$. As discussed in Section 4.1 this information can yield sig-

nificant insight into the physics of the object being measured. This derivation is dependent on obtaining valid N_c vs. A_c measurements from the column density map which may be a non-trivial process when working with real data. Methods for obtaining such measurements are discussed in Section 4.5 along with examples of the derivation applied to simulated data.

4.3.2 Analytic Derivation using Gaussians and Attenuated Power Laws

Equation 4.21 is useful for deriving $n'(r')$ from real data, and is used in all practical examples in this paper with both simulated and real data, however it is not necessarily the most insightful. Any practical application of this algorithm requires a strict understanding of the relation between $n'(r')$ and $n(r_{rc})$ with respect to the two scalars which separate them. To this end an analytic derivation is invoked in this section that is equivalent to that in Section 4.3.1, yet qualitatively different in that it may illustrate different aspects of the derived $n'(r')$ function. This derivation does not invoke discreteness, but instead uses integration. The presence of integrals prohibits the use of a truly general form for $f_n(r_{rc})$, thus two radial density profiles are invoked for illustrative purposes along with the same spheroid geometry from Section 4.3.1. A gaussian and an attenuated power law are selected as mathematically tractable radial volume density profiles that are frequently observed in nature. They may be described as

$$n_g(x,y,z) = n_0 e^{-\frac{r_{rc}(x,y,z)^2}{2}}, n_p(x,y,z) = n_0(r_{rc}(x,y,z)^2 + 1)^{\frac{-\gamma}{2}} \quad , \tag{4.22}$$

where n_g and n_p represent the gaussian and attenuated power law functions respectively. γ is a constant that is greater than 1.

If Assumption 1 holds then according to equation 4.1 the observed column density map for each profile may be described by

$$N_g(y,z) = \int_{-\infty}^{\infty} n_g(x,y,z)dx,\ N_p(y,z) = \int_{-\infty}^{\infty} n_p(x,y,z)dx\ , \tag{4.23}$$

where we assume x represents the line of sight coordinate.

Since specific radial density profile functions are used it is possible to directly perform each integral, yielding

$$N_g(y,z) = n_0\sqrt{\frac{2\pi}{a}}e^{\frac{-1}{2}E(y,z)},\ N_p(y,z) = n_0\sqrt{\frac{2\pi}{a}}\sqrt{2\pi}\binom{\gamma-2}{\frac{\gamma-2}{2}}(E(y,z)+1)^{\frac{-\gamma+1}{2}}\quad , \tag{4.24}$$

where $\binom{\gamma-2}{\frac{\gamma-2}{2}}$ is the binomial coefficient. $E(x,y)$ represents the geometry dependent function that describes the projection onto the sky plane of each individual surface as in Equation 4.15. Similarly to Section 4.3.1 the above may be used to express column density in terms of the area covered by each column density contour resulting in

$$N_g(A) = n_0\sqrt{\frac{2\pi}{a}}e^{\frac{-A}{2\epsilon}},\ N_p(A) = n_0\sqrt{\frac{2\pi}{a}}\sqrt{2\pi}\binom{\gamma-2}{\frac{\gamma-2}{2}}\left(\frac{A}{\epsilon}+1\right)^{\frac{-\gamma+1}{2}}\quad . \tag{4.25}$$

Since no specific shape has yet been invoked, Equation 4.25 verifies Assumption 3 by showing that the relationship between column density and the area of its contours is, aside from some constants, independent of the object's geometry.

Alternatively, using equations 4.24 and 4.11 along with the relation

$$\frac{dx_{r_{rc}}}{dr_{rc}} = \frac{r_{rc}}{\sqrt{a(r_{rc}^2 - E(y,z))}} \tag{4.26}$$

yields the following expression for the column density which is equivalent to the derivation in section 4.3.1

$$N(r_{rc}) = \int_{r_{rc}}^{\infty} n(r_{rc,e})\frac{2r_{rc,e}}{\sqrt{a(r_{rc,e}^2 - r_{rc}^2)}}dr_{rc,e}\ . \tag{4.27}$$

Equation 4.27 specifies the observed column density at all positions (y, z) described by the projected boundary of the shell defined by r_{rc}. $r_{rc,e}$ is the integration variable, where the e subscript denotes that the integration is performed over all surfaces exterior to r_{rc}. Solving equation 4.27 for the gaussian and attenuated power law profiles yields

$$N_g(r_{rc}) = n_0 \sqrt{\frac{2\pi}{a}} e^{-\frac{r_{rc}^2}{2}}, N_p(r_{rc}) = n_0 \sqrt{\frac{2\pi}{a}} \sqrt{2\pi} \binom{\gamma - 2}{\frac{\gamma-2}{2}} \left(r_{rc}^2 + 1\right)^{\frac{-\gamma+1}{2}} \quad . \tag{4.28}$$

Equation 4.28, when converted to Areas using Equation 4.16, is identical to Equation 4.25, thus confirming that the discrete derivation in Section 4.3.1 is equivalent to simply integrating the volume density along the line of sight. With Equations 4.25, and 4.28 it is now possible to obtain better understanding of the relationship between the derived function $n'(r')$ and the object's original radial profile defined by $n(r_{rc})$.

4.3.3 Understanding $n'(r')$

The previous sections have shown how limited information may be obtained on the density profile function based on limited assumptions and information. Since column density maps do not uniquely define an object it is inevitable that some information is unknown. Deriving $n'(r')$ through the method defined above yields a function with the same shape as the original $n(r_{rc})$. For interpretation purposes it is important to understand the relation between the derived and actual density profile functions. This relationship may be defined as

$$n'(r') = Gn(r_{rc}) = Gn\left(\frac{r'}{\chi}\right) \quad , \tag{4.29}$$

where G and χ are unknown constants. Applying the above method to the spheroid model with gaussian and power-law profiles yields derived volume density functions described by

$$n'_g(r') = Gn_0 e^{\frac{-r_{rc}^2}{2\chi^2}},\ n'_p(r') = Gn_0\left(\frac{r_{rc}^2}{\chi^2}+1\right)^{\frac{-\gamma}{2}} \quad . \tag{4.30}$$

Equations 4.19, and 4.29, in conjunction with Equation 4.30 show that for a spheroid model,

$$G = \sqrt{\frac{\pi}{a\epsilon}} = \frac{\alpha}{\omega^{\frac{3}{2}}}, \chi = \sqrt{\frac{\epsilon}{\pi}} = \sqrt{\omega}a_c \ . \tag{4.31}$$

G is dimensionless, while χ has dimensions of length. It is important to note that G and χ are completely geometry dependent and thus identical in both the power law and gaussian cases. Neither parameter can be fully determined by the method described here without knowledge of the object's geometry, further data, or assumptions. G and χ are not independent quantities as evidenced by Equation 4.31 due to their dependence on ω, and prevent us from fully determining the object's volume density and geometry. Aside from scalars G and χ, the derived $n'(r')$, and the original $n(r_{rc})$ are identical. It can be shown that for a sphere, $G = 1$ and $\chi = a_c$. These scalars contain all of the unknown geometric information for the observed object. We may derive $n'(r')$ from an observed column density map, however this function will differ from the object's volume density profile ($n(r_{rc})$) by the two unknown scalars G and χ. The shape of $n'(r')$ will however be identical to $n(r_{rc})$ regardless of the two scalars. If an object's geometry is known, G and χ may be calculated for any geometric shape (values for the spheroid are shown in Equation 4.31). In the most general terms, G may most often be viewed as the ratio between the depth and the width of an object along the line of sight, though this interpretation will rarely be strictly true. If G is greater than 1, then the object is more deep than it is wide, and the derived

n_0' will be greater than the actual value of n_0. Several examples using simulated data are presented in the following section.

4.4 Examples using simulated data

It is necessary to produce numerical models using simulated data in order to validate the technique described in Section 4.3, as well as to illustrate the behaviour of G and χ under various conditions. Numerical models of several objects are constructed using known geometries and volume density profiles in order to create simulated column density maps. These maps are then used to derive $n'(r')$ which are finally compared to the original, known, volume density functions used to construct the model.

4.4.1 Model Construction and Analysis

Figure 4.2 illustrates how such a model is constructed and analyzed using the simplest case of a sphere with a gaussian volume density profile and only minimal noise. To produce a column density map such as in Figure 4.2a it is necessary to first choose a geometry (in this case a sphere) and a volume density profile function (in this case a gaussian) and construct a three-dimensional array whose elements represent the object's volume density. This array is then integrated along the line of sight to produce a column density map. Normally distributed noise with mean zero and a certain standard deviation (1% of the maximum column density in the case of Figure 4.2a) is then added to the column density map. A small number of contour levels are drawn for illustration

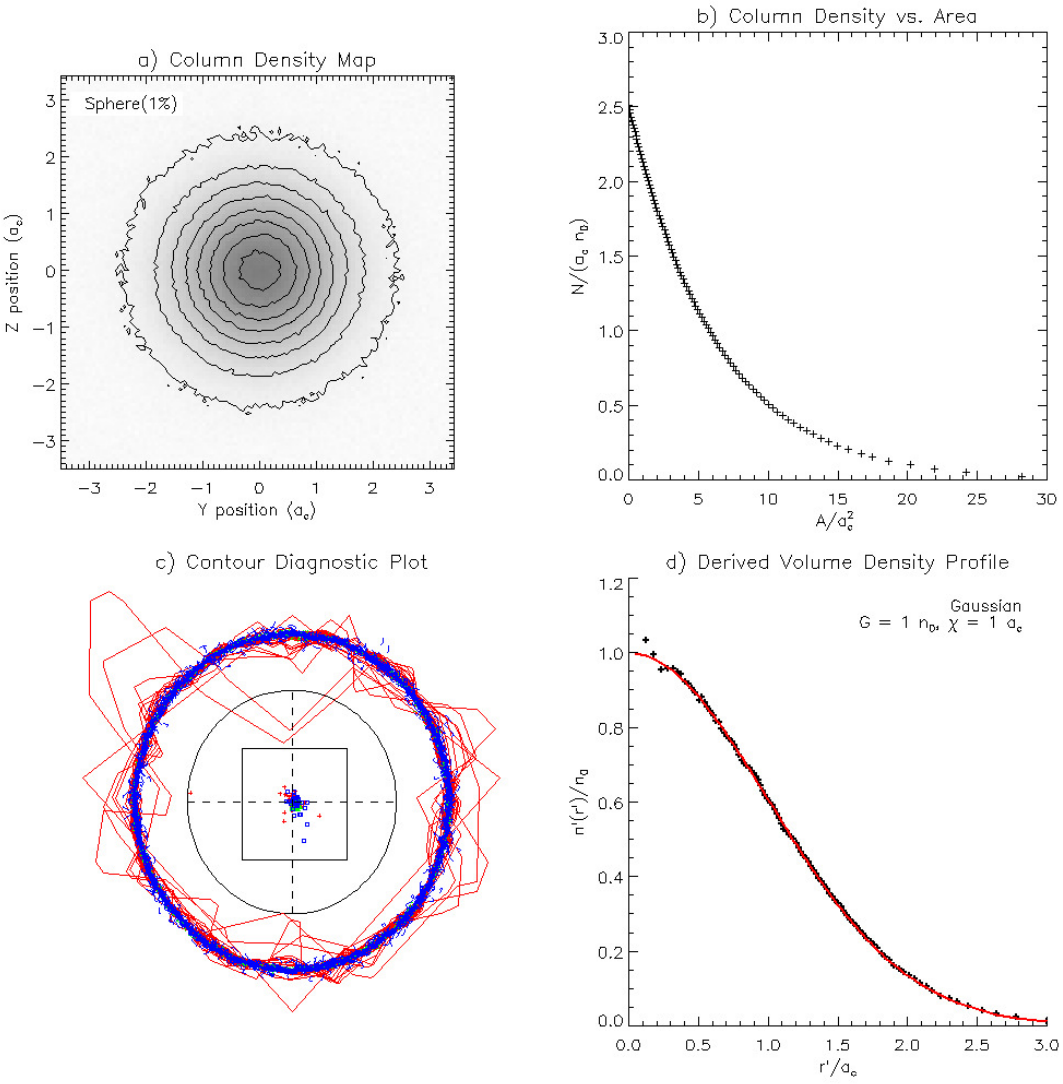

Figure 4.2: A modeled object with spherical geometry ($a = 1/a_c^2, b = 0, c = (y^2 + z^2)/a_c^2$), and a radial volume density profile described by a gaussian ($n(r_{rc}) = n_0 e^{-r_{rc}^2/2}$). a) A simulated column density map with sample contours. Gaussian noise is added equivalent to 1% of the maximum column density. Y and Z coordinates are represented in units of a_c. b) Column Density (N) and corresponding Area (A) for each contour (not displayed) used in the analysis. c) A contour diagnostic plot for the object, as described in Section 4.4. d) The derived volume density profile function ($n'(r')$). Black points represent the values derived from each N and A contour pair. The red line represents the original function $n(r_{rc})$ used by the model as scaled by G and χ.

purposes to produce a map as in Figure 4.2a. Such column density maps are the only source of information for further model analysis, foreknowledge of model scalars such as a_c and n_0 is used only for the purposes of scaling the plots.

Many column density contours (not drawn) are measured on the map in order to produce a plot of column density (N) versus contour area (A) as in Figure 4.2b. There is a choice in how to space the levels of the contours, and how many contours to use due to sampling. It is impossible to properly sample the whole range of column densities without a priori knowledge of the volume density profile function. It has been found most appropriate to measure the same number of contours as the number of pixels that span the object, and to space them equally in column density. This choice often results in oversampling, as discussed in Section 4.4.3, but has been experimentally found to be the most useful.

The technique described here requires implicitly that all column density contours share the same or similar shape, orientation, and center position. The suitability of an object to this analysis technique may be verified by comparing the contours. Similarly, it is necessary to remove from consideration any contours which are created by noise in the column density map. Figure 4.2c illustrates how these goals are implemented. Each contour is scaled to the same size and translated to the same center position. All such contours are then plotted so as to overlap as in Figure 4.2c. The innermost third of the contours with the smallest area are colored red, while the outermost third are colored blue, and intermediate contours are colored green. In the case of Figure 4.2c the simulated noise is quite low and thus only the innermost (smallest) contours display any deviations from a circle. These variations are due to the small number of

pixels within the smallest contours. This representation is useful in that any deviations from a single contour shape and orientation may be easily identified.

A simple method for numerically filtering out noise-induced contours from consideration is to compare the geometric centers of each contour to the geometric center of mass for the object from the column density map. Any contours whose centers exceed some small distance from the center of mass are excluded. Figure 4.2c represents the object's center of mass as the dashed cross in the center. The center positions of each contour are plotted in relation to the center of mass with the green, red, and blue colors representing the contours with the smallest, intermediate, and largest areas respectively. The solid black circle represents the radius used to filter out questionable contours. The square represents the relative position and scale of the pixel from the column density map which contains the object's center of mass. This diagnostic plot is useful in determining how well a given object complies with assumption 2, as well as which contours are suitable for analysis.

Once all unsuitable column density contours are removed from consideration it is possible to apply Equations 4.19 and 4.21 recursively to the N and A pairs in order to derive $n'(r')$ as in Figure 4.2d. Since modeled data is used here it is possible to directly determine the values of G and χ as well as to scale r' and $n'(r')$ using the known values of a_c and n_0 as in Figure 4.2d. Since the original profile density function is known with modeled data it can be scaled by G and χ and compared to the derived $n'(r')$ values as with the red line in Figure 4.2d.

4.4.2 Tests Using Various Geometries and Profile Functions

Figure 4.2 verifies that the derived $n'(r')$ has the same shape as the original $n(r_{rc})$ function to a very high degree for the low-noise, sphere, with a gaussian profile function. As expected for a sphere, $G = 1$ and $\chi = a_c$. The technique described in Section 4.3 should apply for any profile function, as well as any geometries which fulfill the requirements described in Section 4.2. To that end, Figures 4.3a-b, 4.3c-d, and 4.4a-b present three cases beyond the simple gaussian sphere in Figure 4.2. Figures 4.3a-b, and 4.3c-d represent the spheroid defined in Section 4.3 at two different orientations, while Figure 4.4a-b represents a tri-axial ellipsoid. The derived and original volume density profile function shapes agree to a great extent, verifying that the technique is valid for tri-axial ellipsoids of any shape and orientation as expected by the derivation. Several other geometries using both simple geometric shapes such as tapered cylinders, as well as irregular shapes which satisfied the assumptions in Section 4.2 were tested and were all shown to produce valid results using the technique described here.

The derivation in Section 4.3 requires that a is a constant (Equation 4.5). Any geometry which involves a definition of a that is dependent on spatial coordinates y and z results in an object which does not conform to the assumptions in Section 4.2, and thus is not suitable to the analysis presented here. This is due to the variation in the depth of each shell resulting from an inhomogeneous $a(y, z)$ as in Equation 4.17. If the object has a non-constant value of $a(y, z)$ then the relationship between the area and depth of each shell is no longer a constant, and the technique described by Equation 4.18 fails as a would be dependent on the shell number k. It would then be necessary to know the form of $a(y, z)$ (and thus the object's geometry) in order to accurately describe a_k and derive an accurate

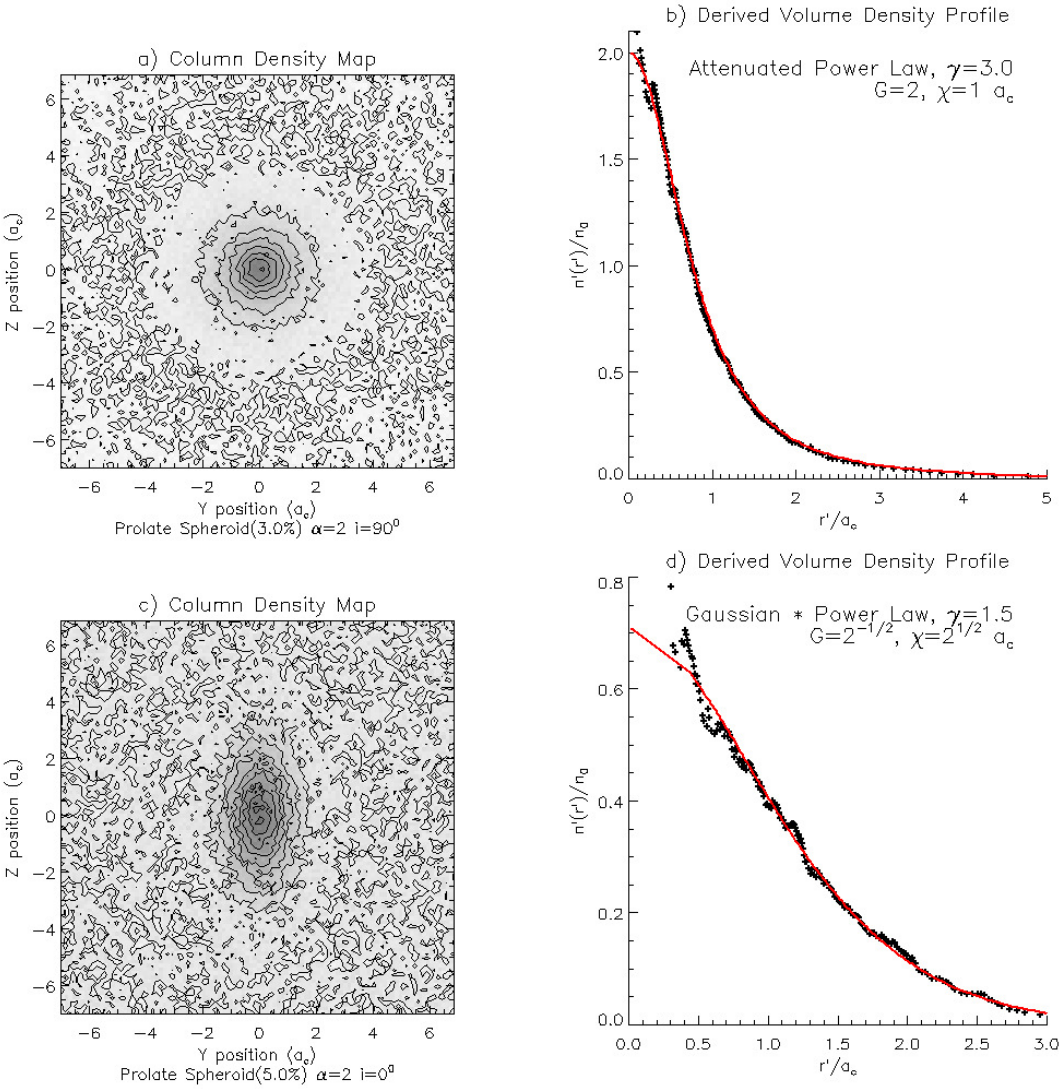

Figure 4.3: a) Simulated column density map of a prolate spheroid as described by Equations 4.6, 4.7, and 4.8 with $\alpha = 2$, $i = 0^o$, and 3% noise added. b) Actual (red line) and derived (black dots) volume density profile for the object in a. An attenuated power-law as in Equation 4.22 with $\gamma = 3$ is used to construct the object in a and b. c) Simulated column density map of an object using the same geometry as in a, except that the object is rotated 90^o and 5% noise is added. d) Actual (red line) and derived (black dots) volume density profile for the object in a. The radial volume density profile used in c and d is described by $n(r_{rc}) = n_0 e^{-r_{rc}^2/2}(r_{rc}^2 + 1)^{\frac{-\gamma}{2}}$ with $\gamma = 1.5$.

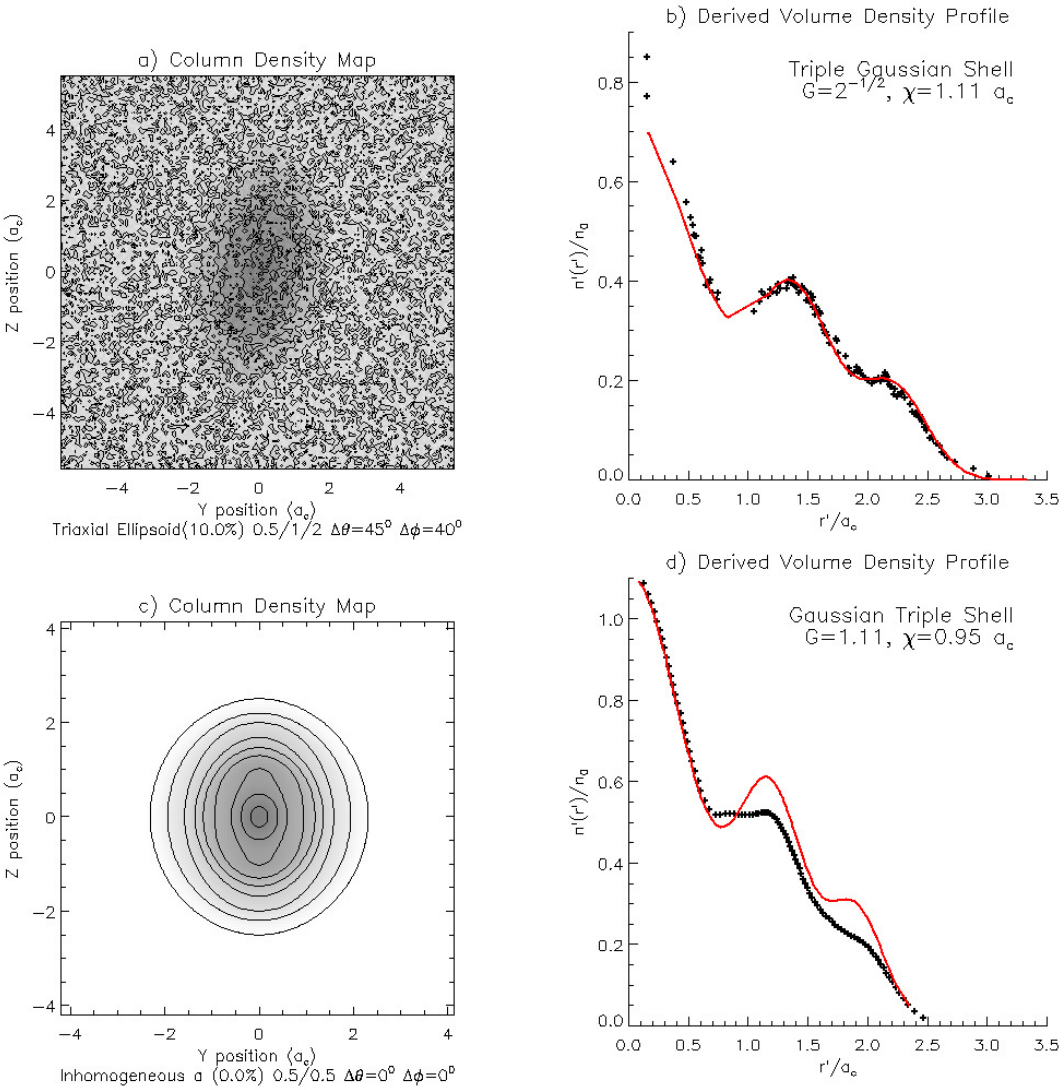

Figure 4.4: a) Simulated column density map of a tri-axial ellipsoid with axis dimensions of 0.5,1, and 2 a_c and 10% noise added. b) Actual (red line) and derived (black dots) volume density profile for the object in a. A triple gaussian volume density profile function is used to construct the object in a and b. c) Simulated column density map of an object with inhomogeneous a (Equation 4.6). d) Actual (red line) and derived (black dots) volume density profile for the object in a. The radial volume density profile used in c and d is described by the same triple gaussian as in a and b.

measurement of $n'(r')$.

It is possible to determine from the column density map whether the object in question has a geometry which is dependent on a constant value of a. Equation 4.16 shows that the projected area of each shell is dependent on ϵ. From the spheroid definition it can be shown that $\epsilon_{spheroid} = \omega\pi a_c^2 = \sqrt{a}a_c\alpha\pi a_c^2$. If a is not homogeneous then neither is ϵ, meaning that the relationship between a shell's area and r_{rc}^2 is no longer constant. This implies that the projected boundary of each shell, and thus each column density contour, has a different shape. *Inhomogeneities in contour shape invalidate this technique*. Figures 4.4c-d show such a geometric shape which utilizes the same quadratic definition for r_{rc} as in Equation 4.5 where

$$\beta = 0.5, \gamma = 0.5 \ , \tag{4.32}$$

$$a(y) = 1 + \gamma y^2 \ , \tag{4.33}$$

$$b(y) = -2\beta^2\gamma y^2 \ , \tag{4.34}$$

$$c(y,z) = (1 + \beta^2\gamma)y^2 + z^2 \ . \tag{4.35}$$

In this case, a is not a constant, the object does not produce self-similar contours, and our technique fails to reproduce the correct radial profile. The reason for the failure is that changing contour shapes result in a value of ϵ which is not constant for all the contours, thus invalidating our derivation. It is important to note however, that the inner-most and outer-most regions, where there contours are self-similar do correctly reproduce the original profile function. Fortunately, the influence of each individual contour of the overall density profile is limited. Each contour only affects contours interior to itself, and has the highest influence on adjacent contours. Thus, in our derivation, as one moves from the outermost shells to the innermost, a change in the value of ϵ will only begin

to have an effect at the contour where the change first occurs, and its influence will decline as we move further into the interior. We refer to this change in contour shape as an ϵ discontinuity. Assuming only one such discontinuity occurs within a given map (so that there are only two contour shapes present), the derived volume density profile should still be correct in the region outside of the discontinuity. The discontinuity will invalidate the derived profile interior to itself, but as its influence weakens the innermost region of the derived profile may still be accurate, as in Figure 4.4d. This phenomenon is frequently present when dealing with real data, and is illustrated further in Section 4.5.

4.4.3 Understanding Uncertainties and Distinguishing Real Features From Noise and Systematic Effects

Sections 4.3 and 4.4 have proven that, under ideal conditions, and in the absence of noise, our technique can accurately derive the shape of the radial volume density profile. However, such idealized circumstances rarely occur in nature so it is important to be able to distinguish real data from noise and systematic effects.

Traditionally, one would assign an uncertainty to each measurement in the derived profile in order to determine which points are likely to be real measurements. However, a serious shortcoming of our method here is that we are unable to assign such uncertainties. Many methods were tried, however the root problem is that we are unable to properly assign an accurate uncertainty to the N vs. A measurements for the contours. Even assuming that all contours ultimately have the same shape, systematic noise affects such contours in ways

that are difficult to quantify. Each of the above simulated data sets, are made with different levels of systematic noise in order to illustrate its effects on the solutions. Figure 4.2 has minimal noise equivalent to 1% of the peak intensity, resulting in a near perfect derived profile. Figures 4.3a-b contain 3% noise which is sufficient to add some irregularity to the shapes of the observed contours. Those irregularities are most evident in the smallest contours, manifesting as slight offsets in the innermost regions of the radial density profile.

The 5% map in Figures 4.3c-d shows a new phenomenon. Here, the noise is such that the innermost contour is broken into two pieces which are unusable. As a result, the derived profile has no measurements interior to $r' = 0.3a_0$. Further, there are larger irregularities in the derived profile. These are caused by individual pixels with a significantly different signal compared to their surroundings. Contours will tend to bend around such pixels, until a certain column density threshold is reached and the contours snap onto the other side of the pixel. This phenomenon may be recognized in that all the irregularities will have roughly the same width in the derived profile, corresponding roughly to the width of each pixel in the map as evident in Figure 4.3d. Figures 4.4a-b show a more difficult case where noise is 10% of the peak signal. The object in the map can be difficult to discern under such conditions. The systematic noise will prevent the construction of the innermost contours, but may also prevent the formation of contours in other regions leading to gaps in the derived profile such as in Figure 4.4b. It is important to note that the gaps did not prevent the derivation of the correct profile in the regions where contours could be formed.

Systematic noise in the column density maps does not contribute much to the small-scale uncertainties between individual points in the derived profile.

A much more immediate difficulty is that systematic noise prohibits the formation of valid contours. As a result, we have not yet found an accurate method of relating systematic noise in the map to the uncertainties for each individual point in the derived profile.

Changes in contour shape introduce a bias to the resulting profiles, as in Figure 4.4c-d. No reliable method for removing such bias is apparent. However, the bias seems to be localized to only those regions of the derived profile immediately interior to the ϵ discontinuity. As a result, the innermost portion of the derived density profile in Figure 4.4d agrees well with the original profile. How these ϵ discontinuities manifest themselves is best illustrated with real data in Section 4.5.

4.5 Derivation of Volume Density Profiles of Molecular Clouds Using Real Data

Star formation theory abounds with open questions, many of which are related to the process by which molecular clouds collapse. Of particular interest is the balance between forces which contain the cloud such as gravity or external pressure, and support mechanisms such as temperature and pressure, turbulence, angular momentum, magnetic fields, etc. A cloud's density distribution is central to understanding this balance. Thus measuring both the gas and dust components to obtain the distribution of the total proton count is of critical importance, representing a long-standing and active field of study.

The Bonnor-Ebert Sphere represents one of the earlier attempts at mod-

eling molecular clouds [Bonnor, W.B. (1956), Ebert, R. (1955)]. This model assumes an isothermal sphere in equilibrium and bounded by some external pressure. Even such a simple model yields powerful insights, such as that radial volume density profiles in molecular clouds should resemble power laws with an approximate $n \ \alpha \ r^{-2}$ relationship between radius and volume density within a cloud. This assertion has been confirmed as approximately correct through innumerable numerical simulations and observations. Several recent works have utilized Bonnor-Ebert spheres, or some derivative thereof, such as [Evans et al. (2001)],[Alves et al. (2001)], or [Teixeira et al. (2005)]. Similar conclusions are obtained by methods independent of the Bonnor-Ebert sphere such as [Arquilla & Goldsmith (1985)]. While such models are excellent approximations, clouds which closely resemble the Bonnor-Ebert sphere, such as B68 [Alves et al. (2001)], are exceedingly rare. While the majority of clouds have been found to be approximately governed by power laws with an exponent of two, there is considerable variation in the value of the exponent both among different clouds, and within different regions of the same cloud. Precise measurements of the exponents in each cloud speak to the significance of the support mechanisms. It has been convincingly demonstrated that clouds in different evolutionary states exhibit different density distributions, most recently by [Liu et al. (2012)], and [Wu et al. (2012)]. [Liu et al. (2012)] made a strong case for the urgent need of investigations of density distributions and support mechanisms in pre-stellar cores in light of new data from Planck.

We have chosen to demonstrate our technique using total proton counts in molecular clouds due to their well-known power-law nature which may be used to validate the technique. By not assuming a geometry, we remove a significant source of bias present in all previous observations, thus obtaining more accurate

measurements of power-law exponents which are currently an active field of study. The relatively small sample size here is used for demonstration purposes, while a more focused study will be presented in forthcoming publications.

It is assumed that under most, though not all, circumstances that gas and dust are fairly well mixed in the diffuse ISM and in molecular clouds. Most atomic transition lines are too energetic to be observable in molecular clouds. Further, the abundance of atomic species in a cloud is often highly dependent on chemistry due to the formation of molecules. Thus atomic species are generally poor tracers of the total proton count in clouds. Some molecular species, such as H_2 or ^{13}CO are generally good tracers of the total proton count in molecular clouds. However, H_2 cannot be directly measured in clouds unless through absorption against a background source. ^{13}CO requires us to determine its excitation temperature to obtain column densities. Further, ^{13}CO has been shown to freeze onto dust grains at higher densities [Pineda et al. (2010)]. Neither atomic, nor molecular species are ideal tools for measuring the total proton count in molecular clouds. While not without its limitations, dust provides a well-tested, proven alternative. Estimating total proton column densities through stellar reddening avoids the need to determine temperatures and may be used ubiquitously throughout a cloud assuming sufficient background stars are visible. A careful study by [Goodman et al. (2009)] compared dust extinction, Near-Infrared Emission, and ^{13}CO emission as probes of the total proton count. After a detailed examination they concluded that dust extinction provided the simplest and most reliable probe. We have thus decided to demonstrate the utility of our technique through dust extinction. Methods for deriving total proton column densities through stellar reddening data are well-studied and widely used [Skrutskie et al. (2006)]. The 2MASS catalog presents a widely accessible,

and comparatively uncontroversial method for obtaining total proton column density maps.

The data for two of the clouds (B133, and L466) were derived by the authors from the raw 2MASS stellar reddening catalog using an implementation of the NICER method [Lombardi & Alves (2001), Chapman et al. (2009)]. Maps for the other clouds (L1765, L1709, B5, NGC1333) were obtained directly from the publicly available 2MASS maps [Skrutskie et al. (2006)]. All maps derived from the public catalog use the same beam size of 3 arcminutes. The maps for B133 and L466 use a 1 arcminute beam. L1765, and L1709 are part of the Ophiuchus Complex, while B5 and NGC1333 are part of the Perseus complex. Each of these four clouds are in regions with substantial background extinction and are accompanied by neighboring features. B133 and L466 are more isolated clouds with comparatively little background extinction or neighboring features.

The scheme used in Figure 4.5 is used to describe each of the clouds in this study. Figure 4.5a represents the column density map for L1756, along with some sample contours drawn. Column density contours are applied throughout the map and filtered as described in Section 4.4 to produce the column density vs. area (N vs. A)plot in Figure 4.5b. It is apparent that there are three different behaviors in the N vs. A plot, therefore each measurement has been coded with a symbol and color. This color and symbol scheme is applied throughout the whole Figure. The colors of the contours drawn on the column density map correspond to the same column density levels as the colors in the N vs. A plot. Figure 4.5c is a diagnostic plot similar to Figure 4.2c. The derived volume density profile is depicted in Figure 4.5d. In contrast to the simulated data in Figure 4.2d, n_0 and a_0 for the real cloud are not known, and thus the plot is scaled in

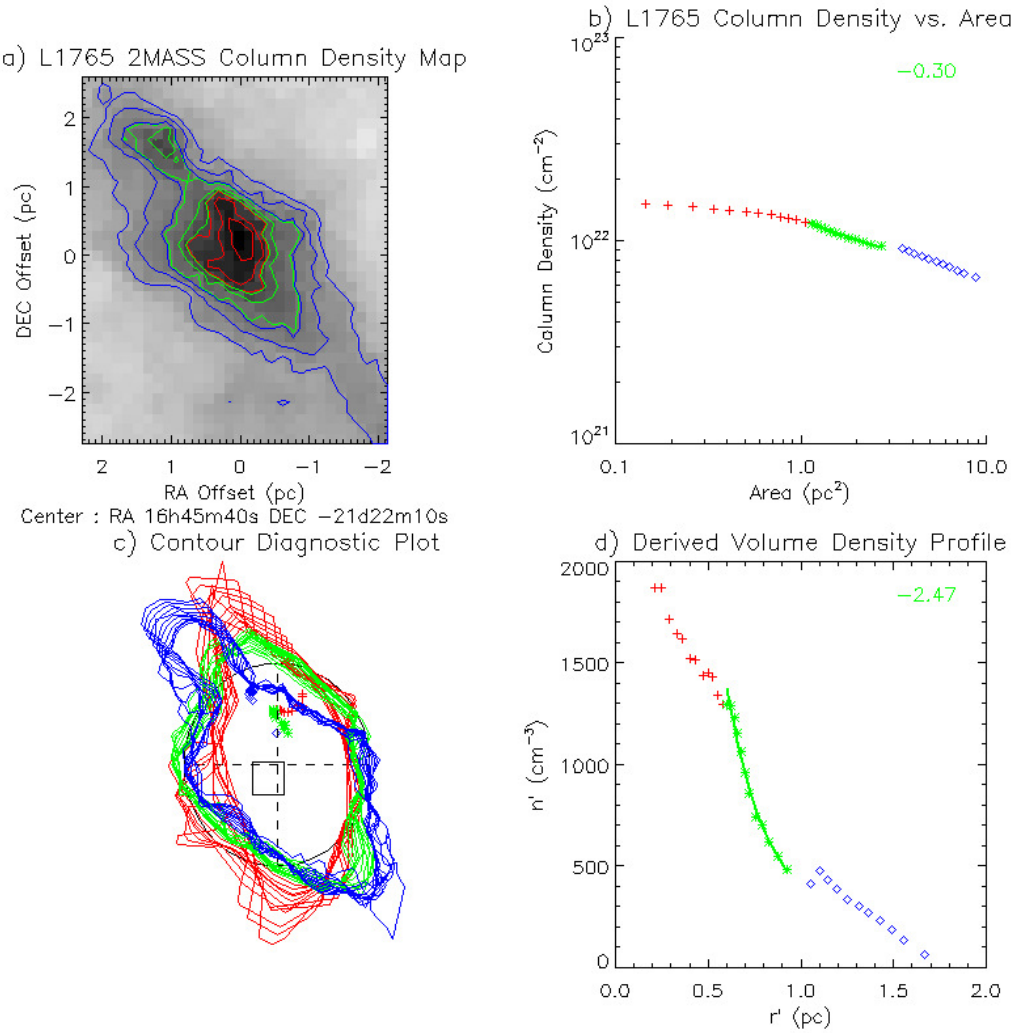

Figure 4.5: a) L1756 Column Density map. Darker pixels represent greater column density. Sample contours are drawn, with each color representing an individual contour group. b) N vs. A plot with derived from contours actually used in the derivation, color groups correspond to the coloring in a. The fitted line(s) correspond to simple power-law fits for each color-group with the exponent(s) printed in the legend, and are only drawn through segments which are believed to be trustworthy. c) Contour Diagnostic Plot similar to that in Figure 4.2a. d) Derived volume density profile. The fitted line(s) correspond to simple power-law fits for each color-group with the exponent(s) printed in the legend, and are only drawn through segments which are believed to be real.

terms of n' and r'.

Three regions are evident in L1765 with red crosses representing the highest column density contours, blue representing the outer-most contours, and green in the middle. The changes in behavior between the three groups are in fact characterized by two ϵ discontinuities. In the case of L1765, only the green data are believed to be significant. The red group represents the inner core. As in the column density map and the contour diagnostic plot, the red contours are not self-similar. There are too few pixels to properly define these contours, and thus they are not reliable measurements. Experimentation with real data reveals that the smallest contours must have an area greater than approximately 25 Nyquist-sampled pixels to be sufficiently well defined to be usable. With L1765, these innermost contours are displayed as an example, they are simply removed from consideration in the other clouds. The blue group represents the outermost region of the cloud. It is not a confident representation of the volume density profile because the blue contours reach the edge of the map, and seem to encompass a smaller, neighboring source.

The map shows green contours centered around the main cloud, as well as separate contours along the secondary clump. The blue contours however encircle the secondary clump as well. This technique cannot correctly function where there are two cores. As a result the blue contours and the related data cannot be trusted. The diagnostic plot reveals that only the green contours around the main cloud are used in the derivation.

The green group in L1765 seems to exhibit a very good power law with slope -0.3 in the $Nvs.A$ plot. This slope was arrived at through a simple linear fit on the log-log scale and the fitted line is drawn in green in Figure 4.5b. From

Section 4.3 it is expected that if the N vs. A exhibits a power-law behavior, then so should the derived volume density profile. Figure 4.5d indeed shows that the green region's volume density profile function follows a power law with slope -2.47. Note that the density profile plot is not on a log-log scale.

Thus we are able to determine the shape of the volume density profile in the intermediate region of the cloud (the green group), where the contours are well-defined, self-similar, and include only one core or clump. A reasonable concern is how can the green region be trusted when the red and blue are not. The red measurements are interior to the green ones, and thus have no effect at all on the green measurements. Equation 4.17 reveals that the depth of each shell is roughly constant in the region interior to the shell, and thus so is its contribution to all interior shells in the derived profile. The primary contribution of the blue measurements is to add an approximately constant volume density to the interior green and red measurements during the derivation process. However, that constant contribution is irrelevant unless we know the specific geometry of the cloud. Only the changes in the shell depth near the edge of each shell can alter the shape of the derived interior profile. Therefore, only the few inner-most points in the derived profile interior to the ϵ discontinuity are affected. Our derived profile only yields values for n' and r' which are scaled by unknown geometry-dependent constants. Based on Figure 4.5d, we cannot say that at a radius of 0.9 pc, the volume density within L1765 is equal to $500 cm^{-3}$, nor is that the goal of this research. We can however say with a good degree of confidence that in those regions of the main cloud encompassed by the green contours in Fig 4.5a, or approximately the middle third of the cloud radially, the volume density profile is governed by a power law with exponent -2.47. If, and only if, the cloud is assumed to be approximately spherical, and only then, n' and

r' may actually represent similar values to the real n and r. Without geometry information however, we can only be certain that the green region of the cloud is governed by the profile shape in the derived profile.

The fact that we observed a strict power-law within a molecular cloud is in line with previous observations made through other methods. It is both encouraging and disconcerting that the derived profile follows a power law quite so well. It is encouraging to see that a real map, with real data, will produce an orderly volume density profile function (in the green region) and that a power-law is observed in accordance with previous studies. However, it is necessary to make certain that the power-law is not somehow a systematic effect of our technique or of the data itself.

Therefore it is necessary to look at additional clouds to determine their behavior, and verify the validity of our technique.

Figure 4.6 represents L1709. In this case, the region interior to the red group is not shown as those contours have too small an area to be useful. The green contours however, are not trusted as they are influenced by the secondary peak at the edge of the map. The contours for the red group in Figure 4.6c exhibit a remarkable self-similarity in shape and center position even though they vary in area from 0.3 to 0.7 square parsecs. Similarly to L1765, the derived profile exhibits a strong power-law with a slope of -2.43.

The analysis for B5 is depicted in Figure 4.7. The blue and green regions are not trusted in this case because they encompass two secondary clumps in the top, and bottom right regions of the map. The red contours do not exhibit quite the same level of self-similarity as found in L1756 and L1709 due to the

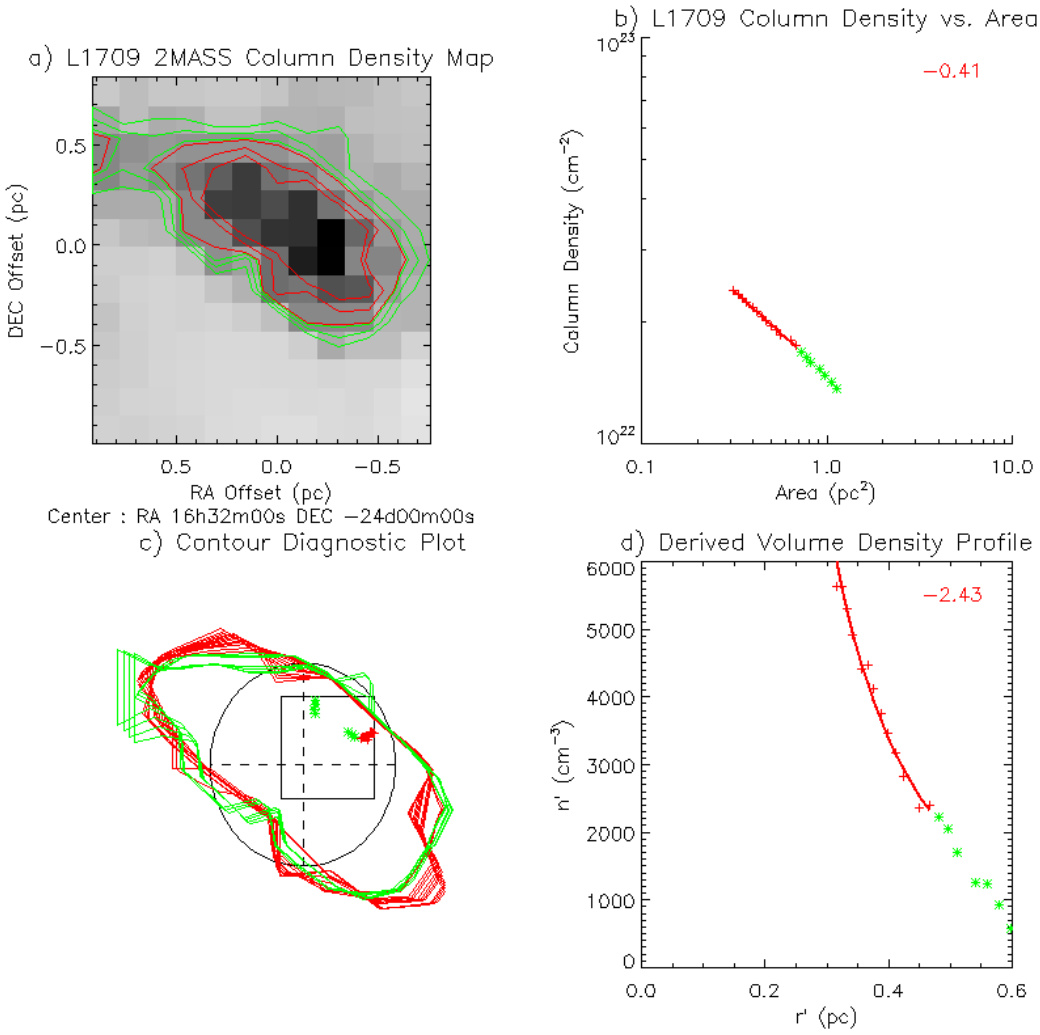

Figure 4.6: L1709 Represented similarly to Figure 4.5

distension in the bottom right region. As a result, even the red contours may be somewhat suspect, however the distension corresponds to a variance of less than 5% in the value of ϵ among the red contours. The red region again corresponds to a power law with slope of −2.15.

The clouds examined thus far have all belonged to the Ophiuchus and Perseus complexes and have been surrounded by neighboring clumps which prevented us from measuring the density profiles in the outermost regions of

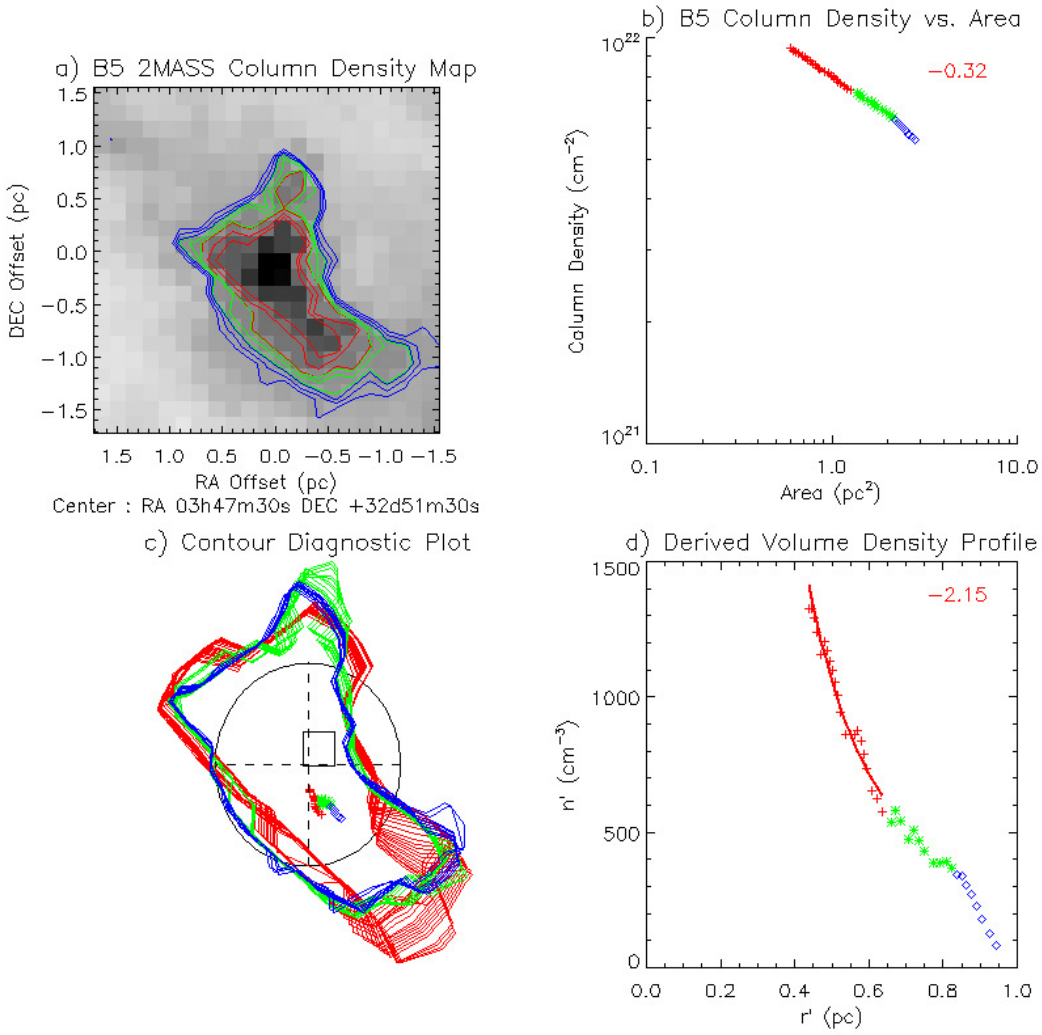

Figure 4.7: B5 Represented similarly to Figure 4.5

the clouds. Furthermore, they have all exhibited a very similar power-law behavior, while originating from the same data source, which raises concerns that perhaps the way they were gridded, or the reduction method, may somehow be influencing the results. Hence, we located two clouds (L466, and B133) which are isolated, and used an independent data reduction while gridding the maps to 1 arcminute beams. The reason why a 1 arcminute beam was not used for all clouds is that with 2MASS data there are often no visible stars in the regions with highest extinctions when using such a small beam. Locating clouds where

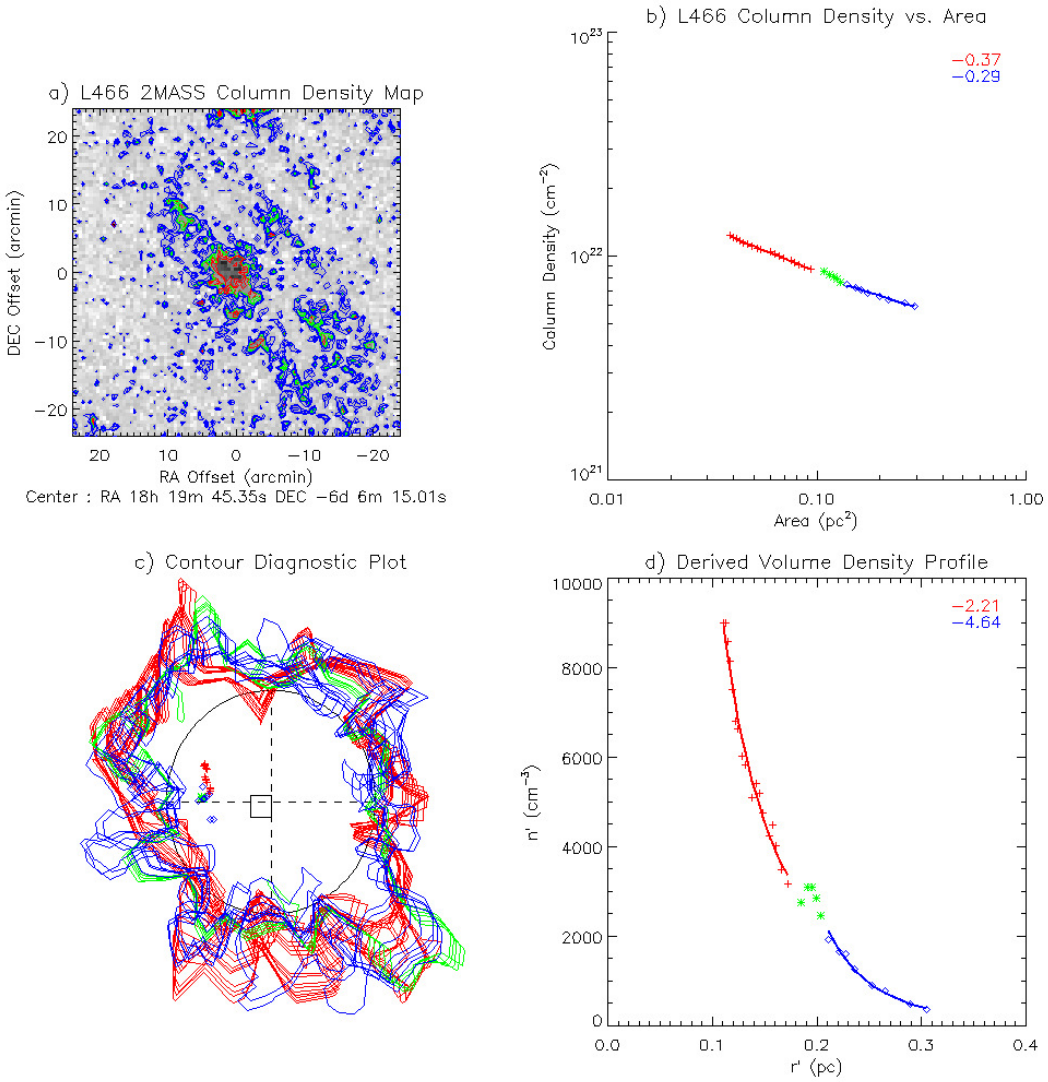

Figure 4.8: L466 Represented similarly to Figure 4.5

sufficient stars were visible in the 2MASS data with such a small beam, that are also relatively isolated was a non-trivial task.

Figure 4.8 represents L466. In this case, there are no adjoining clumps, or background extinction. Thus we were able to utilize a much wider range of contours both in the interior and exterior regions of the cloud. Here, both the red and blue regions are trusted, while the green region corresponds to an ϵ

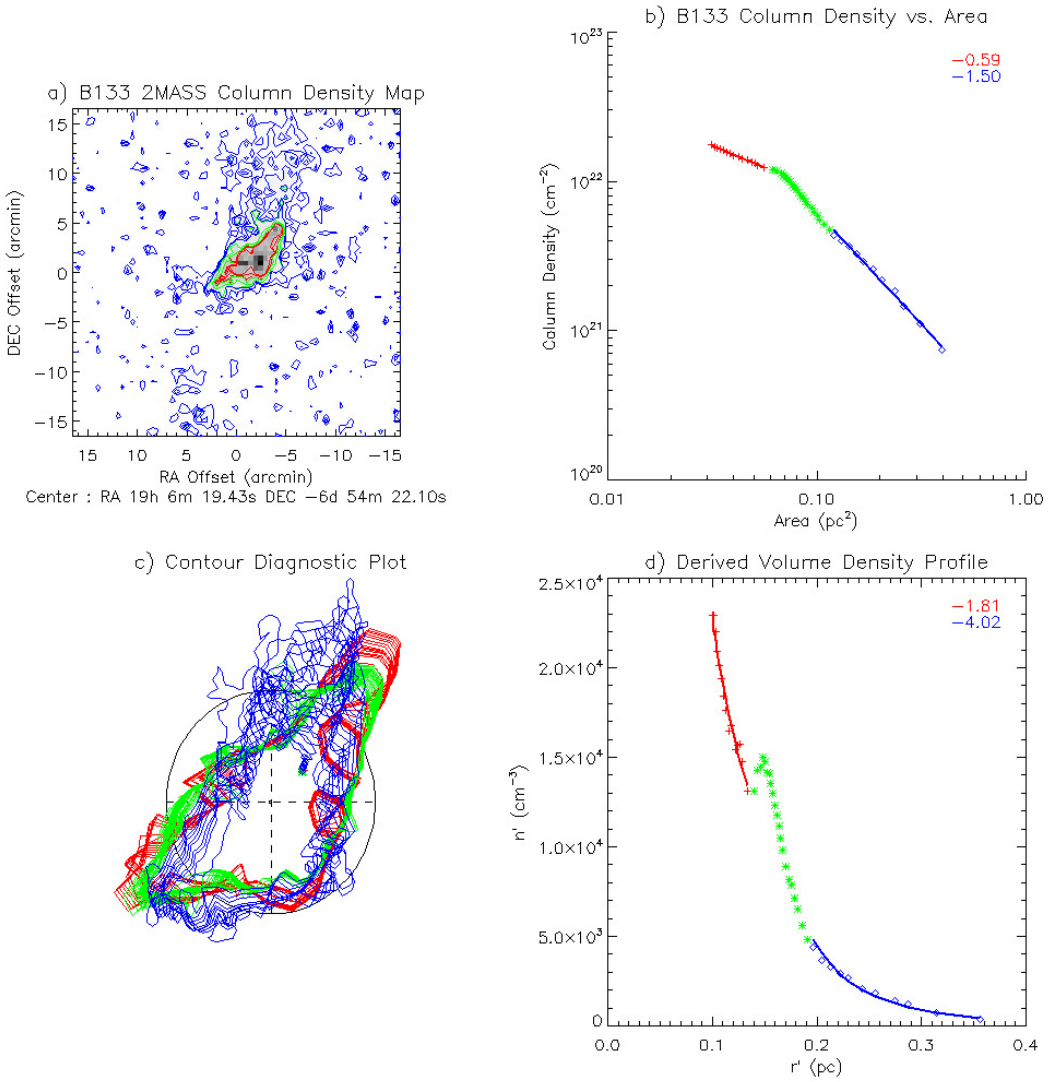

Figure 4.9: B133 Represented similarly to Figure 4.5

discontinuity and is not trusted. Here, the red region exhibits the same behavior as the previous clouds with a power-law slope of −2.21. The outermost, diffuse region of the cloud however also follows a power-law, but with a slope of −4.64.

Figure 4.9 reveals that in B133 we can measure the density profile in the outermost region of the cloud. Similarly to L466, there seem to be two power laws present in the red and blue regions with slopes of −1.81, and −4.02. The

green region is again the site of an ϵ discontinuity (significantly larger than in L466) and cannot be trusted.

What is the meaning of the two power-laws in the two clouds (L466 and B133) where we have been able to confidently measure the radial profile in the diffuse region of the cloud? How can two distinct power laws exist within the same cloud? This kind of discontinuity can be troubling. Previous researchers have noted that attenuated power-laws can well describe such clouds, while exhibiting different localized power laws in individual regions [Pineda et al. (2010)].

It may be possible that an attenuated power law, such as that used in Equation 4.22 may accurately represent these clouds. However, there is insufficient data to fit n_p to the derived profile from L466 and B133 since the innermost region is still unmeasured and n_p has three free parameters (n_0, γ, and a_c). Using three free parameters it is not possible to come up with a constrained fit for L466 and B133. However, the total mass of the cloud may be used to constrain this to a two-parameter problem utilizing

$$M = 4\pi \int_0^\infty n(r) r^2 dr = 4\pi n_0 \int_0^\infty \left(1 + \frac{r^2}{a_c^2}\right)^{\frac{-\gamma}{2}} r^2 dr \ , \tag{4.36}$$

which may be integrated using some creative manipulation of the ${}_2F_1$ Hyper-Geometric function to yield

$$M = \pi^{\frac{3}{2}} n_0 a_c^3 \left(\frac{\Gamma(\gamma/2 - 1)}{\Gamma(2)}\right) \ , \tag{4.37}$$

where Γ represents the Gamma function ($\Gamma(a+1) = a!$).

Equation 4.37 permits us to turn the attenuated power-law fit into a two parameter problem using a cloud mass measured from the column density map.

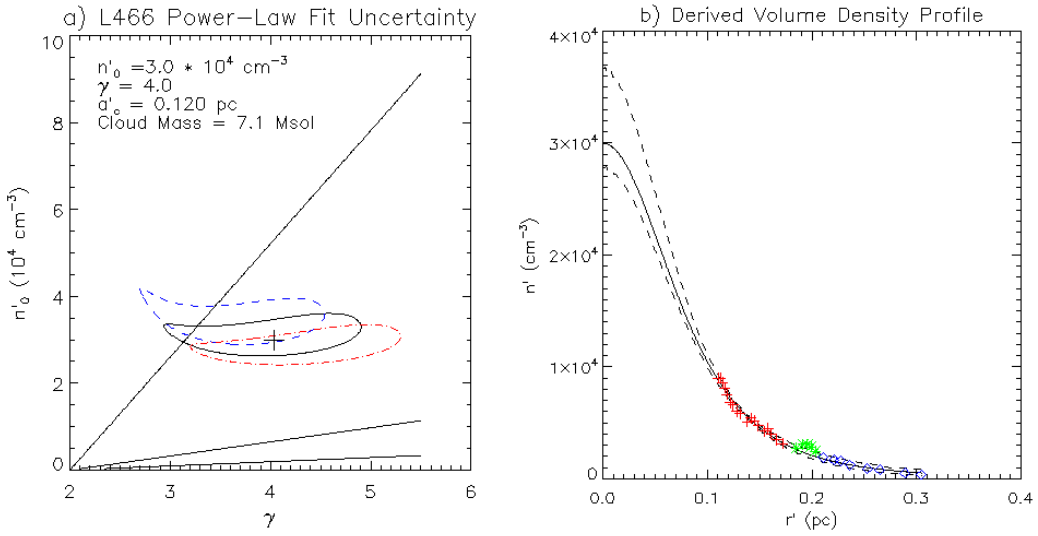

Figure 4.10: The results of the attenuated power-law fit for L466. The green region is ignored during the calculations. a) Represents a map of the fit residuals on a map as a function of γ and n'_0. The cross represents the position of the best fit with the lowest residual. The black contour represents the 1σ uncertainty for the fit. The blue and red contours represent the uncertainties considering masses respectively 5% lower, and higher than the measured value. The straight lines represent positions where a'_c equals 0.1, 0.2, and 0.3 parsecs in a clockwise order. b) The derived density profile (points) along with the fitted attenuated power-law (solid line) and the 1σ uncertainty (dashed lines).

γ and n'_0 seemed to be the most appropriate free parameters to use. It can be shown using the derivation in Section 4.3 that it is appropriate to use n'_0 and a'_c along with the cloud Mass even though geometric information is entangled in those parameters.

Figures 4.10 and 4.11 present the results of such fits. The left panels in each figure represent residuals maps. The best fit for values of n'_0 and γ is represented by a cross. The contours represent the 1σ uncertainties calculated from the residuals and are not necessarily symmetric. There may be some uncertainty

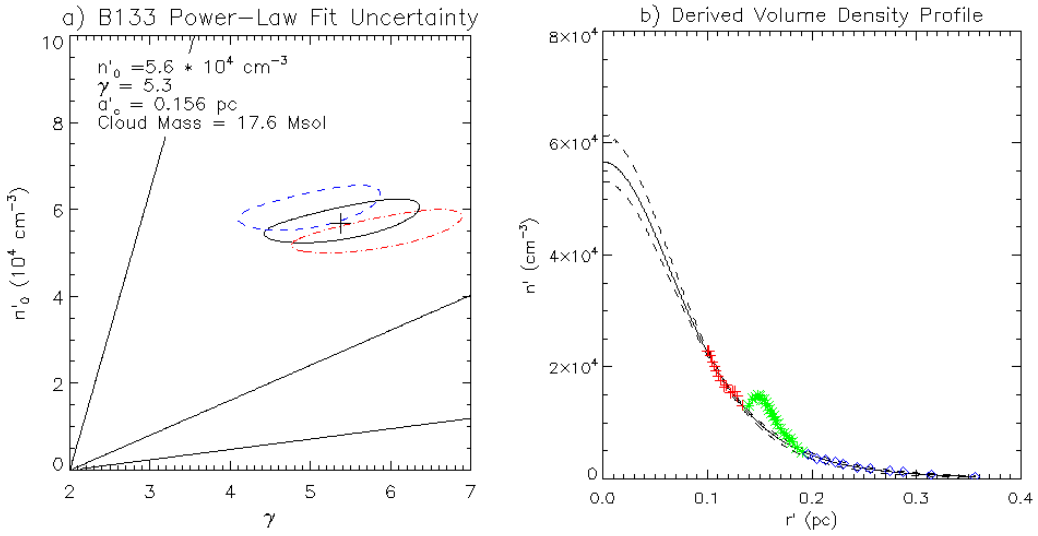

Figure 4.11: The results of the attenuated power-law fit for B133 represented similarly as in Figure 4.10.

in determining the masses of these clouds from the column density maps, due to background extinction, biases, and ambiguity in defining the edges of each cloud. This uncertainty is likely to be small in most cases. However, the blue and red contours correspond to alternate solutions with masses 5% lower, and higher from the measured value in order to illustrate the effect. While mass constrains the value of a_c' for any given n_0' and γ, lines where a_c' equals 0.1, 0.2, and 0.3 parsecs are drawn with the 0.1 parsec line closest to the vertical axis. The best-fit curves (solid line) are plotted in the right panels over the derived profiles, with the 1σ uncertainty bounds marked by dashed lines. The uncertainty bounds are not necessarily symmetric as they are not necessarily gaussian and are calculated using all possible solutions, not just the best fit.

In both clouds, the exterior (blue) and interior (red) regions can be very well fit by attenuated power laws. It is a peculiarity of the attenuated power-law model that there may be a great deal of uncertainty in the values of γ which,

in combination with a'_c, and n'_0 can produce very similar results. The greatest uncertainty in the fit occurs in the innermost core of each cloud, as expected. There is nothing in the data which would suggest that the innermost regions of the clouds follow the fitted profile, as there is no data there. However, these fits do show that an attenuated power-law could explain why two different regions within the same cloud could appear to follow very different localized power-laws.

4.6 Comparison With Previous Methods and Practices

This technique may be applied to many fields of study. In the previous section studied the total proton volume density radial profiles in molecular clouds. Therefore we shall compare our technique to some previous attempts at discerning the internal structure of such clouds. To our knowledge, no one has previously applied a geometry-independent method for measuring such volume density radial profiles. Since molecular clouds rarely resemble simple geometries, the imposition of geometric assumptions has been especially problematic in this field. In fact, most studies involving the internal structure of molecular clouds have limited themselves to studying the distribution of the observed column densities. Due to the large volume of work utilizing this approach it is now well known that molecular cloud total proton column densities generally have probability density functions (PDFs) that exhibit log-normal behavior [Ridge et al. (2006), Froebrich et al. (2007), Wong et al. (2008), Goodman et al. (2009), Kainulainen et al. (2009), Tassis et al. (2010)],
[Liu et al. (2012)]. Clouds which have already initiated star formation also exhibit power-law tails in their PDFs [Kainulainen et al. (2009),

Froebrich & Rowles (2010)]. These tails may be related to local collapsing sites in turbulent flows [Ballesteros-Paredes et al. (2011)]. They may also be indicative of the evolution from turbulence dominated diffuse regions to denser regions which may be collapsing [Ballesteros-Paredes et al. (2011)]. The volume of literature in this field, especially in recent years, speaks to its significance. This avenue of study has yielded many invaluable insights, however it is indirectly trying to discern the internal structure of these clouds. Numerous numerical simulations are used to construct column density maps for comparison with observations instead of directly comparing the volume density structure [Norlund & Padoan (1999), Klessen (2000), Ostriker, Stone, & Gammie (2001), Li et al. (2004)]. It may be more useful to compare volume density behavior against numerical simulations, however previous methods of obtaining this behavior from observed data have been too limited for such direct comparisons to be widely used.

Due to the desire to have more direct information on the internal structure of these clouds, various methods have been used to get volume density estimates despite their inherent limitations. The simplest and most common method involves estimating the object's shape from a column density map to arrive at an educated guess for its depth along one or more lines of sight. [Liu et al. (2012)] and [Wu et al. (2012)] are among many recent papers which have used a similar method. This method is usually used only along a single line of sight, typically the center, due to the uncertainties in estimating an object's three-dimensional shape. This method yields only the mean volume density along the line of sight, and is directly influenced by geometric assumptions. It yields no information on how volume density varies within a cloud.

Understanding the internal structure of clouds allows us to determine the relevant physics and chemistry. Many studies have sought to do this by assuming some geometry for the cloud and comparing it to an observed column density map in order to produce a best-fit radial profile function. Spheres and ellipsoids are most commonly assumed. Early examples are the Bonnor-Ebert Sphere [Bonnor, W.B. (1956), Ebert, R. (1955)] or the study by [Arquilla & Goldsmith (1985)]. More recent examples of this methodology are found in [Pineda et al. (2010)], and [Dapp & Basu (2009)]. [Pineda et al. (2010)] in particular shows how successfully this method can be applied to the study of dust volume densities in molecular clouds. The primary advantage of this method is that it allows us to arrive at a volume density radial profile. However, it is often difficult to reconcile the idealized geometric assumptions with the actual objects studied. Such methods are therefore often constrained to only those objects whose two-dimensional projections at least resemble the idealized geometric assumptions. [Alves et al. (2001)] found that only B68 seemed to provide an excellent fit to the Bonnor-Ebert Sphere in their survey. Any deviations from the assumed geometry manifest themselves in the derived radial profiles as bias in ways that are often unpredictable, and are thus frequently ignored or simply misinterpreted as uncertainties. If one assumes a sphere then any deviations from a sphere will manifest themselves upon the derived radial profile function. Since the object's true geometry is unknown, these manifestations are unpredictable.

By assuming only that the object is optically thin and can be described using a single radial profile function, we show in Sections 4.2, and 4.3 how the derived profile function's shape is geometry-independent while all the geometric information is contained in the absolute values which scale the derived profile

(G and χ). Disentangling the profile shape from its absolute values permits us to remove any bias due to manifestations of an imperfect geometric assumption on the profile shape, yielding improved results. It is still possible to estimate G and χ by assuming a geometry and thus scale the derived the radial profile. In this manner our technique is at least equivalent or better than previous methods.

Avoiding the geometric manifestations offers subtle, yet significant advantages. If one assumes a particular geometry then they are constrained to studying only those objects which at least resemble that geometry on a two-dimensional projection. No molecular clouds resemble idealized geometric shapes. Hence geometric assumptions will always produce manifestations, even if the study is limited to a carefully selected group of objects that most closely resemble the assumed geometry. [Pineda et al. (2010)] represents meticulous research of a very high quality, where the target clouds were carefully selected to match the assumed geometry (in their case, a sphere). Despite the difference in scales, comparing Figure 11 in [Pineda et al. (2010)] to Figures 4.5d, 4.6d, 4.7d, 4.8d, 4.9d, 4.10b, and 4.11b in this paper shows that our derived profiles (in the trusted regions) resemble power laws much more closely than theirs. We hypothesize that most of the features visible in Figure 11 of [Pineda et al. (2010)] that deviate from their power-law fit are due to geometric manifestations.

In comparison, our clouds have much more varied shapes and sizes than theirs. [Pineda et al. (2010)] went to great lengths to meticulously analyze their data to remove observational biases as well as a multitude of other effects, while we only took the publicly available data and performed no such corrections. Further, their method takes greater effort to implement from a numerical per-

spective than the one proposed here. Yet, our derived profiles resemble power-laws much more closely than theirs. Avoiding the geometric assumption, and its manifestations yields a significant improvement in results.

4.6.1 Limitations

There are several limitations to using this technique. Some of these also apply to similar methods, while others require serious consideration when interpreting derived profiles.

Our technique relies on the self-similarity of column density contours, limiting which sources may be studied. It is important to note that this self-similarity assumption is always implied, though rarely explicitly stated, whenever one assumes that an object may be described using a single radial profile function. All methods which assume a specific geometry, rely on self-similarity as well. Without a geometric assumption, our technique is applicable to a wider range of objects. Qualitatively it seems that at least some portions of a great many astronomical objects exhibit self-similarity in their column density contours.

Just as no objects perfectly resemble idealized geometric shapes, similarly none show perfect self-similarity in their column density contours. Such imperfections manifest in the derived profiles as ϵ discontinuities. Since our method derives the radial profile through an iterative process, originating at the interior and progressing to the interior of a cloud, only those points interior to the discontinuity are affected. As the contribution from each exterior point to a specific interior point decreases with distance, only those points immediately interior to the ϵ discontinuity are affected. In this manner, the discontinuities behave in

a predictable manner. Further, they are simple to identify by changes in contour shapes, as well as their recognizable manifestations on the derived radial profiles. ϵ discontinuities can still prevent us from studying significant portions of the derived profiles as demonstrated by the green, untrusted regions in Figures 4.5d, 4.6d, 4.7d, 4.8d, 4.9d, 4.10b, and 4.11b. The same ϵ discontinuities are present in geometry-dependent methods, however in those cases their effects are mostly unpredictable and difficult to identify.

No appropriate method is yet evident for assigning accurate uncertainties to individual points in the derived profiles, presenting a significant limitation to our technique. The primary difficulty is due to the source of the uncertainties. As shown in Section 4.4.2, noise in the column density map is much more likely to prevent the construction of contours than to produce significant uncertainties in the derived profile. To even derive such uncertainties derived from noise one would have to assign uncertainties to the contour areas. Any stochastic method of doing so would be invalidated by the variations in profile shapes accompanying ϵ discontinuities. Finally, the effects of ϵ discontinuities, where present, are generally much larger than any uncertainties introduced through noise in the maps. As a result of this inability to assign accurate uncertainties, the identification of real features in a given profile is a nuanced task, as evidenced by the approach in the previous sections.

The difficulty in forming contours of only a small number of pixels forces us to ignore the data within the innermost core of each object by limiting the span of any derived profiles. As the core density is often of the most interest, this is a significant drawback. It may be possible to construct N vs. A without using contours, however no reliable method is presently available.

Molecular clouds in particular are often grouped in regions where multiple clouds, with separate cores may overlap. Anytime there is more than one core, or center position within a region it becomes impossible to exactly specify the cloud using just a single radial profile. Thus it is necessary to only use those objects that are relatively isolated, and have a well defined center with a single core. This limitation is present regardless of whether using our method or those that require a geometry assumption. Fortunately, the presence of such secondary cores is readily apparent through ϵ discontinuities, and the affected data points in the derived profiles can be identified and ignored.

4.7 Discussion

This paper has presented a novel new method for determining the shapes of the radial volume density profiles of objects such as molecular clouds without making assumptions about their geometry. While the method was applied here only to dust extinction maps of molecular clouds, it is highly generalized and may be applied to any objects, and any observable quantities that satisfy the assumptions in Section 4.2. Those assumptions may be briefly summarized as requiring that the object can be described using a single radial profile function as well as the validity of Equation 4.1. As such, this method may be widely useful in a number of fields. The method relies on using only a single column density map, which necessarily cannot uniquely define a three-dimensional object whose geometry is unknown. It is a fortunate mathematical peculiarity that makes this method possible in that it embeds all of the object's geometric information, and no information about the shape of the radial profile function, into two dependent scalars, G and χ. These constants scale the derived $n'(r')$ profile

to the cloud's original function $n(r_{rc})$. Values for G and χ can only be determined with knowledge of an object's geometry, however the shape of the derived radial profile can be derived accurately within the bounds of the assumptions in Section 4.2.

Those methods which rely on geometric assumptions necessarily introduce an often significant, yet difficult to predict bias due to deviations from idealized geometries. Our method yields the maximum amount of information attainable without the introduction of such a bias. This is achieved without employing any additional assumptions which are not present in previous methods for deriving radial volume density profiles. Our method is limited in several ways, the chief of which is the presence of ϵ discontinuities which arise due to variations in contour shapes as a result of the failure of assumption 2. Figure 4.4b best represents how ϵ discontinuities manifest. In that instance self-similarity is satisfied only in the outer-most and core regions of the cloud. Regions of the derived profile immediately interior to the ϵ discontinuities are affected, while exterior regions and those sufficiently far to the interior of the discontinuities still maintain their shape. It is a simple to discern these discontinuities either through monitoring contour shapes, or calculating ϵ numerically for each contour, however significant portions of the derived profiles may be untrustworthy due to their presence. If one were to assume the simulated object in Figure 4.4a were a sphere, the ϵ discontinuities would still be presented, but manifested in a less obvious, and more unpredictable manner. Despite its limitations, our method presents the best option for discerning the shape of the radial profile in those situations where it is suitable for use.

Section 4.3 presents an analytic derivation from basic principles, while Sec-

tion 4.4 bolsters the derivation through tests using simulated data. All the clouds studied here exhibited similar behavior with power laws present in each. All clouds exhibited power-laws with similar slopes ranging from -1.8 to -2.5 in their middle regions. We believe that these power-laws are not a systematic effect since analytic derivation, and numeric simulations show that the technique should be capable of properly deriving any kind of radial profile function. The clouds analyzed originated from two different data sets, which were reduced independently and gridded using two different beam sizes with no discernible difference in the derived power-laws. Due to these circumstances it is reasonable to conclude that the method described here is accurately deriving the shapes of the volume density profiles for these clouds within the trusted regions.

We chose to demonstrate the technique using 2MASS data on molecular clouds since they were well known to exhibit simple power laws and the 2MASS data set is relatively well understood, thus minimizing the risks of extraneous circumstances obfuscating the results. As discussed in Section 4.5, the internal structure of molecular clouds is a long-standing and highly active field of study. The total proton density is of particular interest as it contains information on support mechanisms as well the formation rates of molecules such as H_2, or ^{13}CO. We found that a great many clouds exhibit ϵ discontinuities and that it is a non-trivial task to locate clouds which are relatively isolated. We further found that all clouds exhibit at least one region where contour self-similarity holds and were surprised at just how self-similar these contours are. While we did not display the data for all clouds studies in this paper, it seems that quite often there are regions where the cloud's column density contours exhibit remarkable self-similarity accompanied by sharp changes in contour shape (ϵ

discontinuities) between regions.

Most clouds grouped within larger complexes, such as Taurus, or Perseus are surrounded by large-scale extinction which prohibits the study of the exterior regions. Those clouds exhibited well-behaved, and expected power laws roughly of order 2. Isolated clouds, like B133 and L466 however offer the ability to examine the diffuse, exterior regions of these clouds, showing much steeper power laws. Previous research has pointed toward different power-laws being observed in different regions of molecular clouds. These observations are consistent with attenuated power-laws, as shown through the fits done in Section 4.5. [Pineda et al. (2010)] found very similar results despite using a geometric assumption. While ϵ discontinuities are not as apparent in the derived profiles due to their spherical assumption, and neither is the sharp change in power laws visible through our method, they did find that different regions of their derived profiles were characterized by different localized power laws. They, like previous studies, found that the derived profiles are best fit through attenuated power-laws as we did as well in Section 4.5.

A key difference is that our method shows that there does not appear to be a gradual change in the derived local power laws, but rather sudden shifts where the interior profile may follow a power law of 2, followed by an ϵ discontinuity, and a much steeper power law of 4 in the exterior regions. That this sudden break accompanies a stark shift in contour shapes is intriguing. With only two isolated clouds, there is insufficient data within this paper to draw conclusions, and that is beyond the scope of demonstration of the technique. However, it raises an interesting question. If it can be proven that this is a common characteristic when observing isolated molecular clouds with 2MASS data, and is not

some kind of artifact of the column density maps or the technique for deriving radial profiles, then is there a real effect which produces a sudden change in the density behavior of these clouds. One possibility may be that perhaps the nature of the dust particles changes at lower densities, thus producing a sharper drop in observed extenction. Perhaps one of the cloud's support mechanisms ceases to be effective at a certain point leading to a steeper drop in density in the exterior. It may also be possible that the interior of the cloud is undergoing gravitational collapse while the exterior is not. An approach to these questions is reserved for a further publication using a much larger sample size. Currently we can say that we have no reason to believe that this change in local power laws is due to biases within the data or our reduction technique within the bounds of the limitations discussed throughout the paper as we have tested the technique using a variety of geometries, profile shapes, beam widths, and reduction techniques. There is nothing in the analytical derivation suggesting that such a phenomenon should be produced as a side-effect. Further, numerous previous studies have found that the localized power law seems to change within different regions of individual clouds, they simply may not have been able to discern how sharp the change is due to their use of geometric assumptions.

4.8 Acknowledgements

This publication makes use of data products from the Two Micron All Sky Survey, which is a joint project of the University of Massachusetts and the Infrared Processing and Analysis Center/California Institute of Technology, funded by the National Aeronautics and Space Administration and the National Science Foundation.

CHAPTER 5

PLACING LOWER LIMITS ON MOLECULAR CLOUD AGES USING MODELLING AND OBSERVATIONS

5.1 Introduction

While it is generally understood that stars form in collapsing clouds of gas and dust, many details of the process are poorly understood. Gravity acts to collapse the clouds, while gas pressure, magnetic fields, rotational momentum, and other forces act in opposition. It is difficult for us to directly measure even the basic parameters of these clouds like density, temperature, or magnetic field strength, thus making it a challenge to understand how various forces relate to one another within a cloud, especially in their magnitudes. We may approach the problem by estimating the time scale for the collapse process from when a cloud is mostly diffuse, atomic gas until stars are formed. Cloud ages, and the collapse timescale have long been studied ([Shu (1973), Heiles et al. (1988), van der Werf et al. (1988)], and many others). Advances in observational techniques have renewed intense interest in the field. [Goldsmith & Li (2005), Pineda et al. (2010), Pagani et al. (2013), Brunken et al. (2014)] represent some of the most recent efforts to measure cloud ages using four independent methods: the atomic to molecular Hydrogen ratio, ^{13}CO depletion onto dust grains, deuterium fractionation of N_2H^+, and the ratio of ortho-H_2D^+ to para-H_2D^+ respectively. We do so by placing lower limits on observed clouds' ages using new techniques that measure the ratio of atomic to molecular Hydrogen gas within each cloud, and model the expected evolution.

The primary means by which HI is converted to H_2 is by formation on

dust grains. Since the properties of dust grains are poorly known there is significant variance in estimated rates of H_2 formation (see discussion in [Goldsmith & Li (2005)]). It is clear however that the formation rate is highly dependent on density. Any H_2 that is formed will be disassociated when exposed to a UV field, therefore H_2 only exists in shielded regions of the cloud where typically $A_v > 1$. Since such photo-dissociation only occurs in the diffuse exterior of clouds, it will be ignored for the purposes of this paper. Cosmic rays can penetrate deep into the interiors of clouds to disassociate H_2, however those rates are also poorly known due to uncertainties in the cosmic ray flux. [Goldsmith & Li (2005)] shows that using only H_2 on dust grains, and cosmic ray dissociation one can arrive at typical conversion timescales of between 10^5 and 10^7 years. We utilized the same model as expressed in Equation 19 of [Goldsmith & Li (2005)] to determine the HI abundance as a function of time throughout this paper.

Here we define chemical age as the amount of time during which there was sufficient shielding from the external UV field for HI to convert to H_2. Several unknowns limit how well we can estimate a cloud's chemical age, one of which is how a cloud's density and size vary over time. In this paper we will simply assume that a given cloud's size and density have remained constant since the time when the cloud was entirely atomic. If we also assume that clouds only collapse or remain stable after they have sufficient self shielding to begin producing H_2 then our estimate of the chemical age will in fact present us with a lower limit of the cloud's true age. All chemical age estimates presented in this paper are lower limits due to this assumption.

Typical temperatures within the shielded regions of molecular clouds are on

the order of 10K, and thus too cold for H_2 to readily emit at any transition lines. It is common to estimate H_2 column densities either by comparing to the dust column densities and assuming a constant dust to gas ratio, or by using ^{13}CO emission as a tracer. [Krco & Goldsmith (2010)] shows that different clumps, and velocity components along the same line of sight can often have very different HI to H_2 ratios, but dust does not permit us to distinguish between different velocity components along the same line of sight. Thus we have chosen to build the model below with the expectation that H_2 abundances are estimated using ^{13}CO as a tracer. ^{13}CO is generally considered to be a less reliable method due in part to ^{13}CO depletion onto dust grains, however we will show that for this model the effect is minimal.

It is difficult to measure the HI content of molecular clouds due to the extensive presence of background HI emission throughout the galaxy. It is possible to see HI in absorption against bright background sources, but most clouds do not have any suitable background sources available. The cold HI within the shielded regions of molecular clouds will self-absorb against the 21cm emission from the warm galactic background. This HI self-absorption (HISA) is a long-studied phenomenon. [Garzoli & Varsavsky (1966)] first showed that HI column densities seemed to decrease in regions of high optical extinction. [Heiles (1969)] subsequently found the first instance where a narrow HI absorption feature coincided in position and velocity with a wider OH emission feature. [van der Werf et al. (1988)] used interferometry to map L134 and found that the HI absorption closely resembled the shape of the cloud. Since then there have been a great many studies that examined the relationship between HI absorption and molecular emission.

[Li & Goldsmith (2003)] first used the term HI Narrow Self-Absorption (HINSA) to describe that subset of HISA which can be strongly correlated with associated molecular emission in position, velocity, and linewidth. [Krco et al. (2008)] developed an improved method for determining HINSA column densities by exploiting the very close relationship between ^{13}CO emission and HINSA. [Krco & Goldsmith (2010)] then applied that same technique to a survey of nearby clouds with 21cm data from the Green Bank Telescope (GBT) and ^{13}CO data from the Five College Radio Observatory (FCRAO). Ultimately, [Krco & Goldsmith (2010)] yielded the HI/H_2 mass ratios for individual clumps and velocity components within several clouds.

In this paper we will develop a model to estimate lower limits for the chemical age of clouds listed in Table 4 of [Krco & Goldsmith (2010)]. We will use the same naming convention for clouds and clumps as found there. The H_2 masses there were estimated using ^{13}CO as a tracer. Section 5.2 describes the model used. Observed HINSA and H_2 masses of the clouds from [Krco & Goldsmith (2010)] are then applied to the model in Section 5.3. The results, and implications are then discussed in Section 5.4. Section 5.5 then briefly summarizes the conclusions which may be drawn as a result.

5.2 Model Description

5.2.1 Motivations and Considerations Regarding Data, Techniques, and External UV fields

HINSA, by definition are those HISA features which are closely correlated to molecular emission [Li & Goldsmith (2003)]. Of all the molecular emission lines which have been compared to HINSA, ^{13}CO has been found to have the closest relationship. In fact the correlation between HINSA and ^{13}CO velocities, non-thermal line widths, and position is remarkable. To our knowledge, there are no convincing positions where HINSA has been observed where there was not any associated ^{13}CO emission, and according to the survey in [Krco & Goldsmith (2010)] and other research, definite HINSA features were observable in approximately 80% of directions where ^{13}CO was detected. This close correlation leads us to conclude that ^{13}CO and cold HI are probably located in similar regions of each cloud, thus making ^{13}CO a better candidate as a tracer of H_2 and the total proton column densities than using dust extinction.

We have chosen to use HINSA data acquired by the method in [Krco et al. (2008)] that was used to produce the results in
[Krco & Goldsmith (2010)]. This technique uses the observed ^{13}CO emission as a template to better extract HINSA measurements. In contrast to techniques which do not use molecular templates, including those that use dust extinction to derive atomic to molecular gas ratios this method allows us to derive independent measurements of the ratio for each individual clump and velocity component within a cloud. [Krco & Goldsmith (2010)] observed large variations in

the $HINSA/H_2$ ratios within different clumps and velocity components which would appear to belong the same cloud. While it is impossible to prove for any particular cloud that individual clumps are not simply separate structures along the same line of sight, the prevalence of this occurrence would seem to indicate that in at least some instances there really are different clumps and velocity components within the same cloud that exhibit very different $HINSA/H_2$ ratios. In [Krco & Goldsmith (2010)] we postulated that this phenomenon may be explained by different portions of a cloud having formed at different times, or collapsing at different rates. However, no satisfactory explanation was evident. One of the goals of this paper is to further examine this problem.

[Krco & Goldsmith (2010)] showed that comparing HINSA and H_2 column densities on a logarithmic plot showed large variations in the slopes of the relationship. In some instances it even appeared that the $HINSA/H_2$ ratio was higher along lines of sight with greater H_2 column densities. Further modelling has shown that phenomenon may likely be a result of the cloud's shapes and orientations. According to [Goldsmith & Li (2005)] cosmic ray dissociation of H_2 would produce a constant HI volume density of $2cm^{-3}$ throughout those regions of a cloud that had reached steady-state, and that this HI volume density would be independent of the total proton volume density. If this is true, then a disk shaped cloud might exhibit very different $HINSA/H_2$ column density ratios depending on what inclination the cloud was viewed at. For this reason it was necessary to develop a geometry-independent method for estimating cloud ages.

The H_2 formation rate is highly dependent on dust, or total proton volume density. The ideal way to measure cloud age would be to know what fraction

of a cloud's mass exists at what densities through out the cloud's history. Since we do not reliably know the history, or rate of collapse of any of our clouds we can only make the assumption that the current density distribution is unchanged since the cloud's formation. This assumption leads us to underestimate a cloud's age if that cloud was less dense in the past, as expected. Hence our estimates will only produce lower limits on the age in this paper. It is still necessary to determine the cloud's fractional mass as a function of total proton volume density throughout the cloud in a geometry-independent manner. To this end we developed a technique in [Krco & Goldsmith (2014)] that allows us to measure the shapes of radial volume density profiles of clouds in a geometry-independent manner. We found there that attenuated power laws fit the observed clouds very well, however in order for the technique to be successful the clouds have to meet several criteria which are discussed in [Krco & Goldsmith (2014)]. Ideally, we would use the observed radial volume density profiles to get the fractional mass as a function of total proton volume density for each cloud. Unfortunately we found that our available ^{13}CO data for the clouds for which we have *HINSA* maps does not meet those criteria to confidently obtain the radial total volume density profiles for each cloud. Further, using single dish data with the largest telescope available (Arecibo) on the nearest clouds at 21cm does not sufficiently resolve the individual clumps within any clouds to obtain HINSA volume density profiles. The model we present here uses the total observed HINSA and H_2 masses for the mapped clouds in [Krco & Goldsmith (2010)], and the largest possible, realistic range of parameters describing an attenuated power law radial total proton volume density profile to arrive at estimates of the lower limits of the clouds' ages. We will primarily use spherical models in this paper, and will show that when using total

cloud masses while determining only the lower limits on ages it is sufficient to use spherical models.

External UV fields have significant effects on the development and properties of molecular clouds. It is expected that even relatively weak UV fields can disassociate H_2, thus affecting the HI to H_2 ratio within a cloud. [Goldsmith et al. (2007)] modelled one-dimensional slabs and included photodissociation due to an external UV field. Based on that model it is expected that the observed HI spectra will exhibit characteristic "wings" due to warmer HI gas, with larger thermal and non-thermal line widths, at the edges of clouds where the UV field may penetrate. None of our observations of HINSA features exhibit any convincing presence of such "wings" in their spectra. From this we conclude that external UV fields typically do not penetrate deep enough within a cloud as to reach the HI gas that is responsible for producing HINSA features. Therefore we have chosen not to model the effects of external UV fields in this model. If UV fields do play a significant role on the measured HINSA abundances then they would increase the observed $HINSA/H_2$ ratio, meaning that our model underestimate the ages of our clouds. As we are only limited to placing lower limits on cloud ages we feel justified at this time in ignoring the influence of external UV fields.

5.2.2 Definitions

When referring to cloud ages throughout this paper, we will be referring to chemical ages which we define as following:

The chemical age of a cloud refers to the time that has elapsed since the cloud last

reached sufficient density for its interior to be sufficiently shielded from the external UV field to produce molecules in abundance, as reflected by the ratio between atomic and molecular hydrogen in the sufficiently shielded regions of the cloud. As we do not know how a cloud's size and density evolved over time we assume that they have remained constant. Under the assumption that the clouds were less dense in the past, all of our chemical age estimates will in fact be lower limits due to the fact that H_2 formation is quicker at higher densities.

Due to cosmic ray dissociation a cloud should have a non-zero HI abundance throughout. In the dense interior of a cloud, the HI gas is expected to be cold (10K), and H_2 and other molecular should be present. In the outer, diffuse regions where there is not sufficient shielding to block out the UV field there should not be significant quantities of molecules, while the HI gas should be warm (100K). For the purposes of determining chemical ages, we are only interested in those regions of the cloud sufficiently shielded for the atomic to molecular conversion to take place. More specifically, due to the very close observed correlation between HINSA absorption and ^{13}CO emission, our model is limited to only those regions where ^{13}CO is likely to exist in observable quantities. Characterization of these regions is further developed in the following sections. *When referring to HINSA masses and densities we refer only to those HI atoms that are sufficiently cold to absorb the background 21cm emission*. Depending on a cloud's position and galactic longitude the background 21cm emission may vary from approximately 50K to 200K. In [Krco & Goldsmith (2010)] we found that our ability to detect HINSA features is not significantly affected by this variation within the range of cloud distances studied so far (approximately 140 to 950 parsecs).

In this paper we are dealing primarily with spherical models. We compute, and define the optical depth (A_v) by integrating the total proton volume density radially from a certain radius out to infinity. This is different from values of A_v integrated along a line of sight direction. The amount of the external UV-field present in a region of $A_v = 1$ is significantly lower by this definition than if it were calculated by integrating through a 1-dimensional slab. This is because the radial direction is the shortest path to the "surface" in a spherical model, while all other paths would have significantly higher extinctions.

Per the terminology in [Krco & Goldsmith (2010)] we consider that clouds are composed of velocity components and clumps. Two or more clumps may be part of the same velocity component. We practice the same naming conventions here as used in [Krco & Goldsmith (2010)].

5.2.3 Attenuated Power Laws

It is generally well established that the radial volume density profiles of molecular clouds resemble power laws. In [Krco & Goldsmith (2014)] we used a new technique to measure the shapes of clouds' total proton volume density radial profile functions and found that they are very well approximated by attenuated power law functions of the form

$$n(r_{rc}) = n_0(1 + r_{rc}^2)^{-\gamma/2} \ . \tag{5.1}$$

The origin, usage, derivation, and characterization of the above function and its parameters are described in detail in [Krco & Goldsmith (2014)]. n_0 repre-

sents the volume density at the cloud center. γ is the power-law coefficient. r_{rc} is a dimensionless parameter which describes the ratio between the distance from some point to the cloud center and a certain core radius (a_c) which defines the size of the "flattened" region near the center of the cloud. a_c need not be a constant, thus allowing for non-spherical models. In the case of a sphere however, r_{rc} may be expressed simply as $r_{rc} = r/a_c$, where r is the distance from the cloud center and a_c is a constant core radius. This representation allows us to describe generalized, non-spherical geometries, though we will mostly use spheres throughout this paper.

We saw in [Krco & Goldsmith (2014)] that clouds are well represented by attenuated power laws regardless of their shapes or sizes. Based on that paper and previous research [Pineda et al. (2010)] we can conclude that typical values for a cloud may be similar to those used in Figure 5.1.

These values of γ are much higher than those typically quoted in the literature, which are 2. Most studies of molecular clouds use regular power laws. However, clouds seem to exhibit different localized values of the power-law coefficient throughout their profiles as seen in [Krco & Goldsmith (2014)] (Figures 8,9,10, and 11). An attenuated power law more accurately describes the observed profiles, and exhibits varying localized power laws with coefficients ranging from 0 at the cloud center to γ at ∞. Due to the presence of the a_c parameter, attenuated power laws are not highly dependent on the value of γ. This is evident in Figure 10 for L466 of [Krco & Goldsmith (2014)] where even though the 1 σ uncertainty spans values of γ ranging from 3 to 5, there is no drastic effect on the produced profiles. A function with $\gamma = 3$ can fit the observed data just as well as function with $\gamma = 5$. Similar behavior is seen in Figure 11 for B133

in [Krco & Goldsmith (2014)]. While this behavior may be counter-intuitive, it is an important aspect of attenuated power laws.

It is difficult mathematically to work with attenuated power laws, therefore we solve our models numerically and use Figure 5.1 to elucidate some of their subtle properties which shape how our model is constructed. Figure 5.1 illustrates the results of four spherical cloud models using an attenuated power law such as in Equation 5.1. The model represented by black, solid lines uses values of n_0, a_c, and γ which may be considered typical based on previous observations.

Model boundaries are in important consideration. Due to the strong correlation between ^{13}CO and HINSA we only model those regions where ^{13}CO is likely to exist. These regions are bounded both by the critical density for ^{13}CO of approximately $1000cm^{-3}$, and sufficiently high A_v to provide shielding from external UV fields. Figures 5.1a, and 5.1b show the behavior of total proton volume densities and A_v as a function of radius in each of the four models. All three parameters significantly affect the expected radius of the models, but the change in γ seems to have the most significant effect. In each case, the expected radius is a few times the value of a_c. Figure 5.1c shows the direct relationship between volume density and A_v. In each of these four models, volume density of $1000cm^{-3}$ is reached in regions where $A_v < 1$. Especially in the case of the blue model with increased γ, $n = 1000cm^{-3}$ where $A_v = 0.12$. In that instance there is sufficient density for ^{13}CO emission, however any external UV field would certainly destroy any molecules and heat up the HI past the point where it could produce HINSA. By using lower values of gamma (2-3), and larger core radii it is also possible to produce clouds where $A_v > 1$ in regions where the total proton volume density is below the critical value for ^{13}CO. Therefore, we have chosen

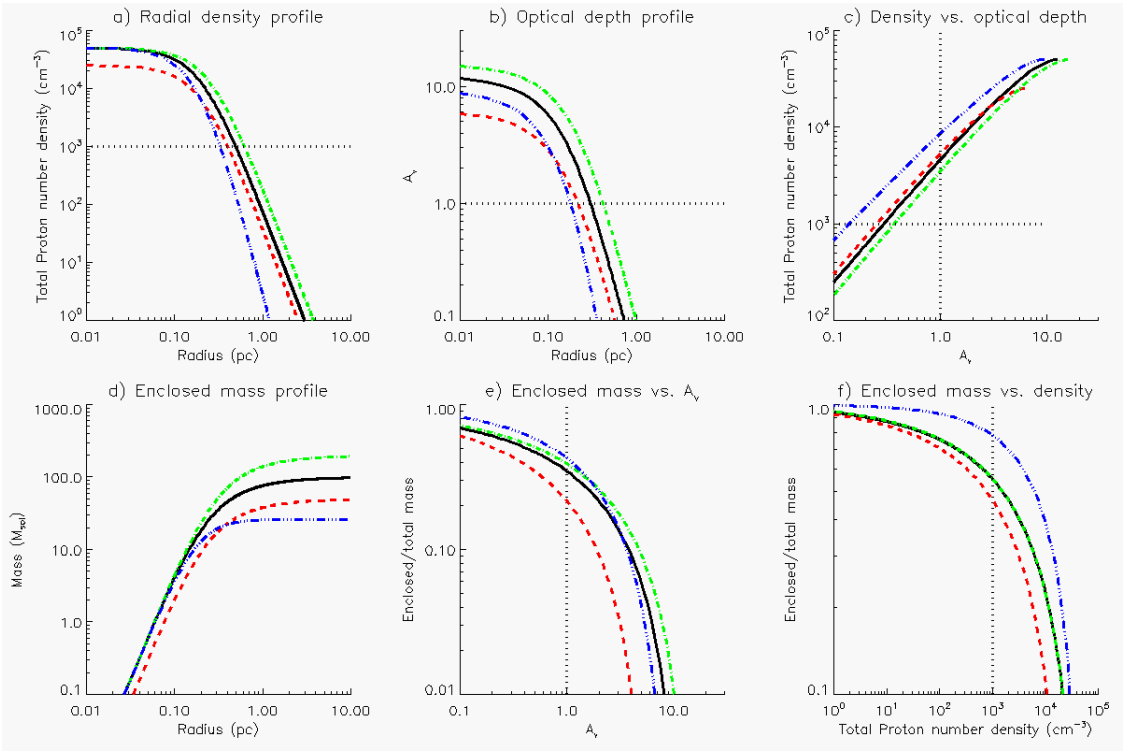

Figure 5.1: Four spherical modeled clouds, where one parameter has been altered in each of the three colored models in comparison to the original (black, solid line) model. The original model uses values of $n_0 = 5 * 10^4 cm^{-3}$, $a_c = 0.2pc$, and $\gamma = 4$. The red, dashed model uses a lower core density with $n_0 = 2.5 * 10^4 cm^{-3}$. The green, dash-dotted model uses a larger core radius at $a_c = 0.2 * 2^{1/3} pc$. The blue, triple-dotted model uses a steeper power law exponent with $\gamma = 6$. a) Represents the total proton volume density as a function of radius for each cloud. b) Shows the optical depth (A_v) as a function of radius as measured by integrating the total proton column density radially to the nearest surface of the cloud. c) Density as a function of optical depth. d) Mass in solar units enclosed within a specific radius for each cloud. e) The percentage of the mass enclosed within a certain optical depth. f) The percentage of the total mass enclosed within a certain volume density.

to bound our model using both a minimum total proton volume density and a minimum value of A_v. Any regions within a cloud which do not meet both these criteria are not considered as they will not produce HINSA absorption, or ^{13}CO emission.

The fraction of a cloud's mass that exists at each density is critical to how the cloud's ratio of total HINSA and H_2 masses evolve over time. Figure 5.1d shows that roughly half of a cloud's mass is contained within the core as defined by the core radius (a_c). Similarly, only a few to ten percent of a cloud's mass is contained within the region where the density profile is flattened. This leads us to believe that the value of γ should have a stronger, non-linear effect on a cloud's $HINSA/H_2$ mass ratio, whereas the core density should only have a roughly linear affect since outside of the flattened region it simply scales the density profile. Figures 5.1e, and 5.1f show that approximately only half of a cloud's mass will be in regions where the volume density and A_v criteria are met. We expect the other half of the cloud to contain little to no ^{13}CO and HI too warm to produce HINSA. Adjustments in H_2 measurements for ^{13}CO depletion are made here as described in [Krco & Goldsmith (2010)]. Comparison with [Pineda et al. (2010)] show that ^{13}CO depletion is only significant in the densest regions of each cloud, which comprise a small fraction of each cloud's total mass. As our model will be dependent only on total cloud masses, the effects of ^{13}CO depletion are small compared to the other sources of uncertainty.

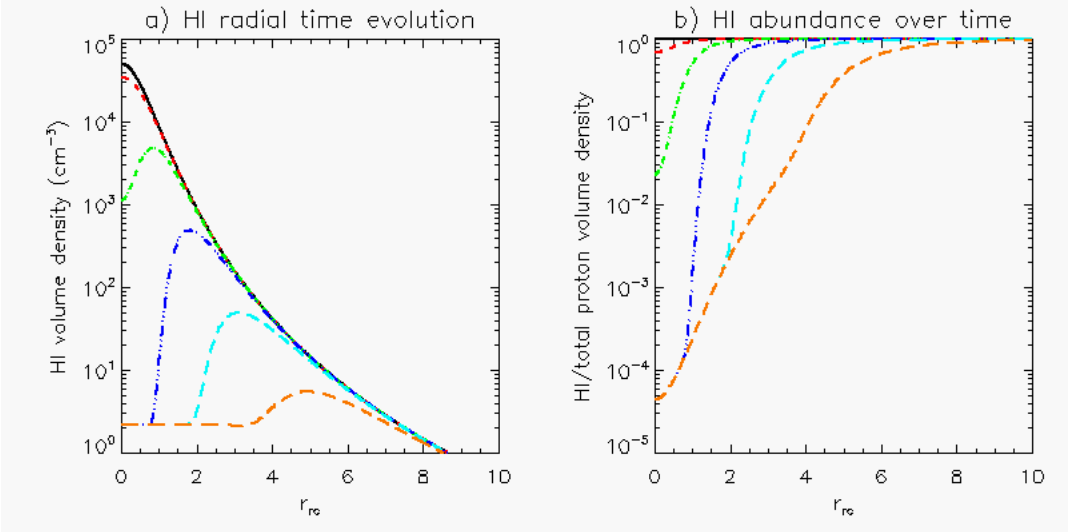

Figure 5.2: HI volume density and fractional abundance as a function of r_{rc} at times t=0, 10^4, 10^5, 10^6, 10^7,and 10^8 years. This model uses a spherical cloud with attenuated power parameters of $n_0 = 5 * 10^4 cm^{-3}, a_c = 0.2pc, \gamma = 5$.

5.2.4 Time evolution

As we are excluding the effects of photo dissociation due to external UV fields, the most appropriate method for modelling the time evolution of the HI to H_2 conversion is that developed in [Goldsmith & Li (2005)]. We use the same values for the H_2 formation rate ($1.2 * 10^{-17} cm^3 s^{-1}$) and the cosmic ray ionization rate of ($5.7 * 10^{-17} s^{-1}$). These rates directly determine both the steady-state HI volume density and the conversion timescale. The use of different rates is examined in the Discussion Section.

Figure 5.2 shows how the HI abundance evolves over time for a spherical attenuated power law cloud with typical parameters. The black line shows the HI abundance at $t = 0$ years, which is approximately equal to the total proton volume density. As expected we see that the interior of the cloud, which is the most dense converts its HI to H_2 rather quickly in comparison to the outer

diffuse region. Nearly the entire core, as defined by $r_{rc} = 1$ has reached steady state within the first 1 Myr. The outer regions however do not reach steady-state even after 100 Myrs.

For this model, the boundaries at which HINSA and ^{13}CO emission cannot be produced occur at approximately $r_{rc} = 2$. Any material outside of $r_{rc} = 2$ would not produce either ^{13}CO emission or HINSA. Evidently, by 10 Myrs nearly all the HI that can produce HINSA would have reached its steady-state volume density of $2cm^3$. This lends credence to the hypothesis that the variation in column density slopes observed in [Krco & Goldsmith (2010)] are due to the fact that significant portions of the observed clouds have reached steady-state, and HINSA column densities are directly proportional to depth along the line of sight.

There is an inversion point in the HI volume density which travels outward from the center of the cloud with time. If we could directly measure HI radial volume density profiles, this inversion point would be a useful marker of a cloud's age, however that is impossible without interferometric 21cm data which is not available at this time. As a result we can only compare in this paper, the total masses of both HINSA and H_2 for any individual cloud.

5.2.5 Parameter Limits and Appropriate Cut-off Boundaries

We cannot directly determine the core density, core radius, or the power-law coefficient of our individual clumps. We can estimate the total proton mass of each clump using ^{13}CO as a tracer (while accounting for ^{13}CO depletion) as done in [Krco & Goldsmith (2010)]. Therefore, for each cloud's specific mass

we construct a range of models using all the reasonable possible values of n_0, a_c, and γ. The known mass reduces the number of unknown parameters to two, for which we have chosen to use n_0, and γ, while the necessary a_c is then computed from the parameters and the cloud's mass.

We must set an appropriate range of possible values for n_c and γ. In general we consider the minimum possible value for the core density to be $10^3 cm^{-3}$ as that is the ^{13}CO critical density. It is difficult to realistically construct anything but the largest clouds (several tens of thousands of solar masses) using core densities greater than $10^6 cm^{-3}$. For values of $\gamma < 3$, attenuated power laws produce infinite masses. We have arbitrarily chosen to use an upper limit of $\gamma < 7$ as the steepest conceivable power law coefficient that can be expected in realistic clouds. Higher values of γ produce clouds which are essentially uniform in density throughout the core with a very steep drop off near the edges. The parameter space is further limited for each cloud by its mass. If the mass is too large then using $n_0 = 10^3 cm^{-3}$ may require an a_c that is many times larger than the observed cloud on the sky. Similarly, if the mass is too low, and γ too high then the cloud cannot produce a large enough region with sufficient A_v to shield from the external UV field and form molecules. In each cloud we use the largest possible range of values for n_0, and γ that produces models that might resemble a realistic cloud. For most of our clouds this results in a ranges of $1.5 * 10^3 cm^{-3} < n_0 < 10^6 cm^{-3}$, and $3 < \gamma < 7$.

We only observe the ^{13}CO emission and HINSA for each cloud. As shown in Figure 5.1, the region we can observe will typically only encompass approximately half of a cloud's total mass. Therefore it is necessary to appropriate boundaries to our models. We have chosen to use the ^{13}CO critical density and

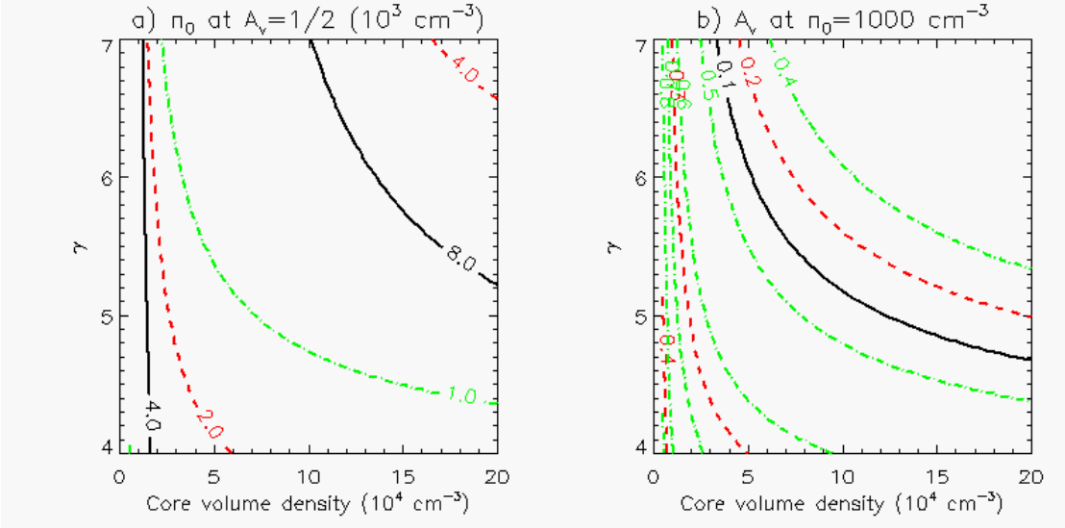

Figure 5.3: The relationship between n_0 and A_v for three different clouds with masses of 10, 100, and 1000 M_{sol} represented by black (solid), red (dashed), and green (dash-dotted) lines respectively for a range of values of n_0, and γ. Contours in a) show the value of the total proton volume density at the radii where $A_v = 1/2$ for each combination of n_0 and A_v in units of $10^3 cm^{-3}$. Contours in b) show the value of A_v at the radii where the volume density is $10^3 cm^{-3}$.

a minimum value of A_v as our bounding parameters. Figure 5.3 shows that depending on a cloud's mass there are significant differences in the relationship between these two boundaries. For the $10M_{sol}$ cloud, there are significant regions where the volume density is sufficient for ^{13}CO, but there is insufficient A_v to shield the cloud. At $A_v = 1/2$, volume densities have values between 4 and 8,000 cm^{-3}. Similarly at those radii where the volume density is $10^3 cm^{-3}$, there is only about 0.1 magnitudes of A_v. For the much larger, $1000M_{sol}$ cloud, it is much easier to build up sufficient A_v at lower densities so that it is possible to have clouds with volume densities of $10^3 cm^{-3}$ at radii where $A_v = 1/2$. The largest of the clumps in our survey have over $10^4 M_{sol}$, while the smallest are just above $10M_{sol}$. In clouds smaller than $10^3 M_{sol}$, the A_v will be the primary determinant of the boundary while the volume density will be the primary determinant in

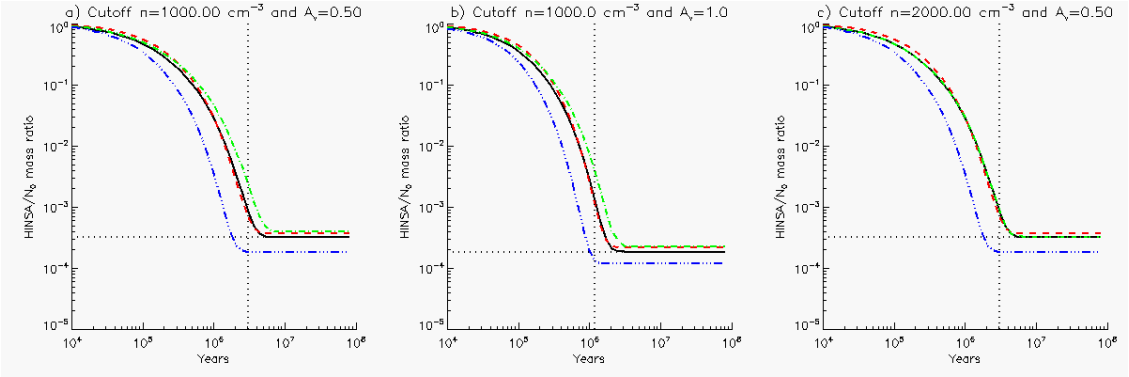

Figure 5.4: Time evolution for the four cloud models used in Figure 5.1. Each figure shows how the HINSA mass compares to the total proton mass (as measured by ^{13}CO emission for each cloud). Panel a) bounds the models using a cutoff n of $10^3 cm^{-3}$ and $Av = 1/2$. Panel b) uses a higher A_v boundary, while panel c) uses a higher volume density boundary. The horizontal and vertical dotted lines reflect the steady-state mass fraction of HI, and the time at which the HINSA mass fraction reaches 10^{-3} for the black model.

larger clouds. Hence we have chosen to define the boundary for all our models such that volume density must exceed $10^3 cm^{-3}$, and A_v must be larger than $1/2$.

Since we have chosen to compute A_v radially to the surface, a value of $1/2$ would correspond approximately to an extinction of 1 magnitude when viewed along the line of sight from Earth, depending on the cloud's geometry. This is consistent with previous observations. Figure 5.4 shows how the fractional mass of HINSA changes with time for each of the clouds modelled in Figure 5.1. Results using three different boundary conditions are shown. The volume density boundary affects only the results for the most massive, green model ($200 M_{sol}$), while the A_v boundary has the strongest influence on the smallest clouds. In both cases, increasing the cut-off values for n or A_v leads us to deduce a younger age for each cloud. Both boundary conditions have significant

effects on our model, however we believe that $A_v > 1/2$ and $n > 10^3 cm^{-3}$ are the most appropriate values to use.

5.2.6 Effects of Cloud Geometry

Thus far we have only modelled spherical clouds, however real clouds rarely resemble spheres, and our formulation of r_{rc} from [Krco & Goldsmith (2014)] allows us to model clouds with arbitrary geometries. Figures 5.5, and 5.6 represent four spheroid cloud models with identical masses and attenuated power law parameters, but different shapes. The spheroids are constructed using the formulation in [Krco & Goldsmith (2014)]. This formulation is dependent on the assumption that within an individual cloud or clump, surfaces of equal volume density all share the same shape, orientation, and center position. Observed clouds seem to follow this assumption reasonably well.

For non-spherical clouds it becomes much more difficult to estimate the A_v within any point in the cloud. If we do not include any A_v boundary conditions, then according to this formulation each cloud will have the same mass distribution when compared to how much mass is located at each density. This will be true regardless of orientation, or shape. Indeed, Figure 5.5 shows that without an A_v boundary condition the time evolution of each cloud is identical.

When the same $A_v > 0.5$ boundary condition is included for all four clouds as in Figure 5.6, then the clouds' time evolutions begin to diverge. In a spherical cloud, a particular value of A_v will always correspond to one and only one value of n throughout the entire cloud. For a non-spherical cloud, this is no longer true. If we observe a cloud with these parameters, and a HINSA fractional mass

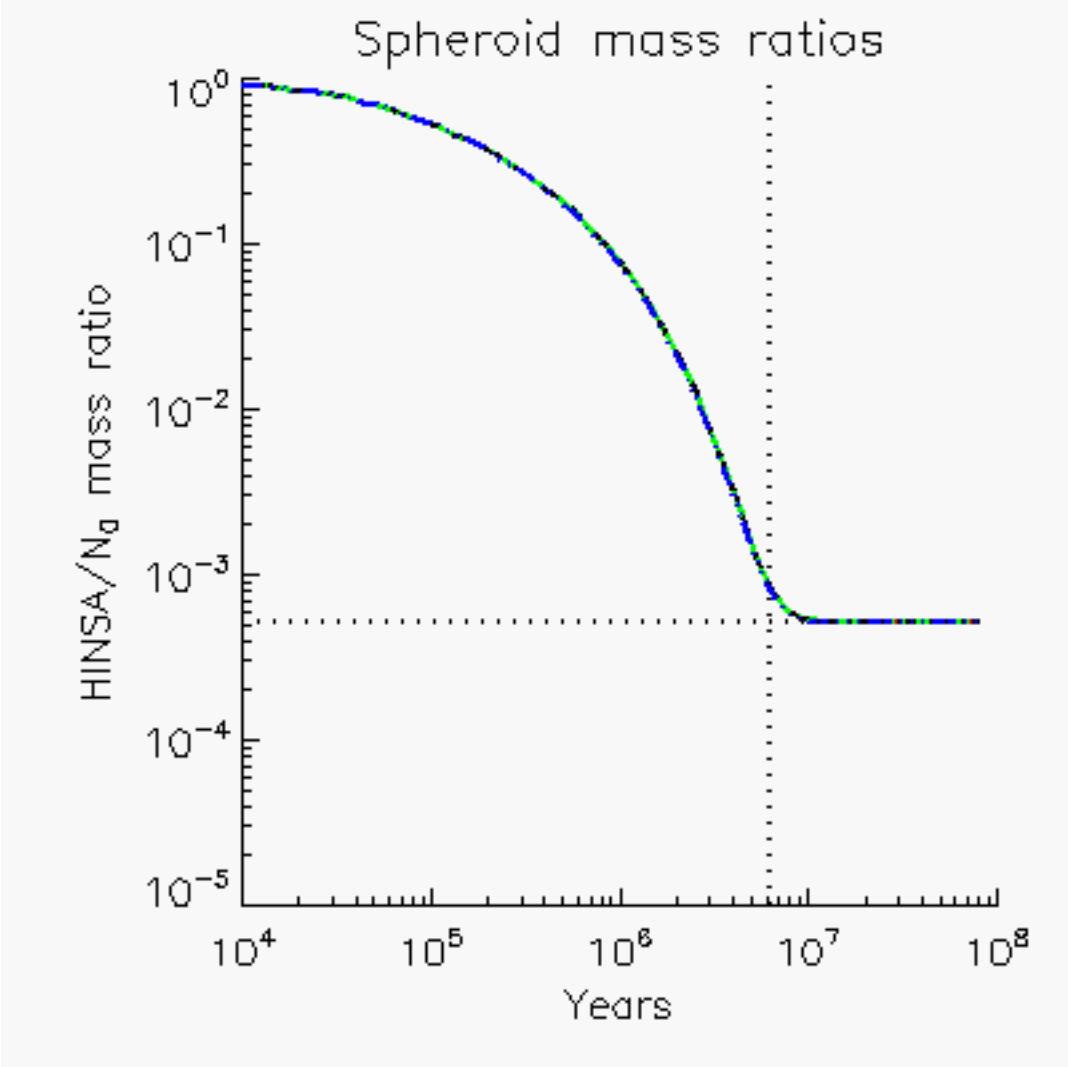

Figure 5.5: The time evolution of four modelled clouds (all of which overlap) using the spheroid formulation in [Krco & Goldsmith (2014)]. Each cloud has the same attenuated power law parameters, and total mass as the black (solid) model in Figure 5.1. The black (solid) line represents a spherical cloud ($\alpha = 1$). The red (dashed) line represents an oblate spheroid ($\alpha = 0.5$). The green (dash-dotted), and blue (triple-dotted) lines represent prolate spheroids with α values of 2, and 3 respectively. No A_v boundaries were used in all four models (only the $n > 10^3 cm^{-3}$ cut-off was used), therefore all have identical time evolution, and all four models overlap. The horizontal, and vertical dotted lines represent the steady-state HINSA fractional mass, and the time at which the HINSA fractional mass reaches 10^{-3} for the black (solid) model.

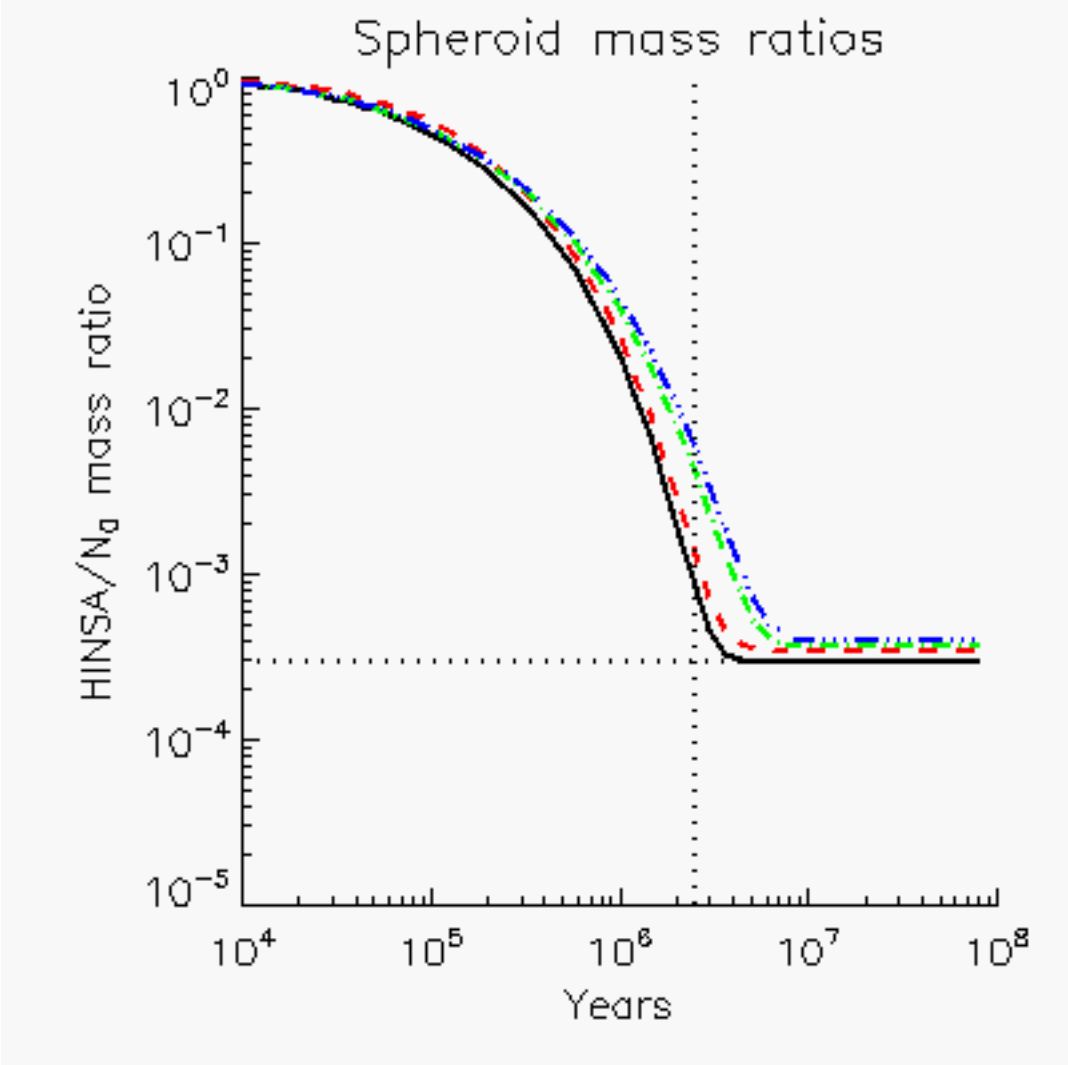

Figure 5.6: The same cloud models as in Figure 5.5 except in this instance boundaries using cut-off values of $n > 10^3 cm^{-3}$ and $A_v > 1/2$ were used. The spherical model results in the lowest age estimate.

of 10^{-3}, assuming the cloud is a sphere would lead us to conclude its age to be 2.5 Myrs. Assuming that the cloud has any other shape would lead us to a higher age estimate. This is due to the fact that spheres have the smallest surface area of any shape. As we are only able to determine the lower limits on cloud ages in this paper, we proceed to assume that all of our clouds are spheres. We later show how additional information on cloud geometries can yield more precise ages.

5.3 Application to Observed Clouds

In [Krco & Goldsmith (2010)] we summarized the survey results covering 9 mapped clouds by noting the total HINSA and H_2 masses of each component, as well as each cloud as a whole. The HINSA masses were arrived at through direct measurement of the HINSA features using the method developed in [Krco et al. (2008)]. The H_2 masses were estimated using ^{13}CO as a tracer while adjusting for depletion as described therein. The same clouds and naming conventions are used here. The total proton masses, and the HINSA mass ratios used here are listed in Table 5.1. The numbers differ slightly ($< 1\%$) from those in [Krco & Goldsmith (2010)] as we have since then developed an improved method of differentiating between different components, and signal which may not belong to the cloud.

From the observations in [Krco & Goldsmith (2014)] it is reasonable to assume that the total proton radial volume density functions of each component resemble an attenuated power law. However, we do not know the core density, radius, or the value of γ for any of the components. For each component we

create an group of cloud configurations using the observed total proton mass, and an array of values for the core density and γ within the ranges described in Section 5.2. All components are assumed to be spheres. The core radius (a_c) is computed for each configuration such that the model's total proton mass, as measured through ^{13}CO observations matches the observed mass. The HINSA mass abundance is then calculated as a function of time for each cloud configuration using the model from Section 5.2. Comparison with the observed HINSA mass then yields an age estimate for each cloud configuration.

Figures 5.7 - 5.16 detail the results of our analysis for clouds L134, L204, and L462. Table 5.1 summarizes the results for all the clouds. Each cloud is divided into one or more components. Each numbered component represents a separate velocity component, or clump which could be identified as distinct either in velocity or sky position. The LOS component in each cloud represents the sum total of all clumps and velocity components along the line of sight encompassed by the cloud, with exclusions having been made to separate those signals which appear to belong to other clouds. The number of pixels with both ^{13}CO and HINSA signal are summed for each component. As ^{13}CO and HINSA are highly spatially correlated the sums for both species are very similar. Averaging the two species yields an observed area (A) for each component. We define the observed radius (R_{G1}) as $R_{G1} = \sqrt{A/\pi}$. This notation is in reference to the G parameter defined in [Krco & Goldsmith (2014)]. For any component of arbitrary shape which satisfies the assumptions in [Krco & Goldsmith (2014)] we may define a mean radius R_m by integrating over all directions in spherical coordinates from the cloud's center position to find the mean distance at which signal is produced based on the volume density and A_v limits discussed in the previous sections. We cannot know the true value of R_m without knowing each

cloud's three-dimensional shape. In the case of a sphere $G = 1$, and therefore $R_{G1} = R_m$. If the cloud is non-spherical, and its projected area along our line of sight is greater than the projected area averaged over all perspectives (such as a disk viewed face-on) then $R_{G1} < R_m$, and $G < 1$.

Figures 5.7 - 5.16 are organized in an identical fashion. Panel a) in each figure represents the modelled HINSA mass fraction as a function of age. The red, dashed lines designate the boundaries of the possible values of the HINSA mass fraction for each Age using all configurations. Averaging the HINSA mass fraction for all configurations at each Age yields the mean HINSA mass fraction designated by the black, solid line. In the absence of any other information, it is equally likely for each configuration to be the one that best represents the component. In this case, the mean HINSA fraction would represent the most likely time evolution of the component. However, it is unlikely that this is true. The horizontal, blue solid line designates the observed HINSA mass fraction. Each configuration requires a different value of a_c in order to produce an object with the correct mass, and therefore results in a component of a different R_m. The blue, dash-dotted line represents that configuration which results in a value of R_m that is closest to R_{G1}. Thus, if a component's true geometric shape resembles a sphere, then the configuration represented by the blue, dash-dotted line is the most likely to the most accurate representation.

Panel a) best represents the viable results which may be derived using this model. Without further information, the only result which we can present with significant confidence is the minimum possible age for each component (Age_L) assuming that the component's core density and γ fit within the parameter range defined in Section 5.2.5. Age_L may be determined by the earliest inter-

section of the blue, horizontal line (The measured HINSA mass fraction) and the red, dashed lines which represent all possible configurations within the defined parameter space. In the case of Component 0 of L134 (L134-0, Figure 5.8), $Age_L = 0.76Myr$. We may also say, with some confidence, that if L134-0 resembles a sphere, then the component has most likely already reached its steady-state (SS) HINSA mass fraction, and is likely older than 7 Myr. In the case of L204-1 (Figure 5.12 we may further conclude that it most likely does not resemble a sphere, as according to our model the SS HINSA mass fraction for a sphere of that cloud would be greater than that which is observed.

Knowing only the mass of each component, and the HINSA mass fraction limits us to using a large parameter space to describe the attenuated power law within each model. Having further information on a specific component can help us narrow that parameter space and better constrain Age_L. In this paper we have modelled our clouds as spheres when determining the distribution of mass with respect to volume density which is the primary determinant of the *HI* to H_2 conversion rate. However, [Krco & Goldsmith (2014)] shows that molecular clouds seem to obey the self-similarity properties described therein. It can be shown that with such self-similarity, a cloud's geometry will not affect its mass distribution with respect to volume density. If a cloud's internal structure can be described using a single radial volume density profile function, then the proportion of its mass which exists at each volume density will be the same regardless of its shape. Therefore, even if a cloud is non-spherical it should possess the same mass distribution as determined by our model assuming that we correctly determine the attenuated power law parameters. We have also assumed that our models are spherical with regards to determining where to place our boundary conditions, as we have shown that this assumption leads to

the lowest age estimates 5.2.6. If the clouds are non-spherical, then they will be older than our age estimates and the value of A_L we derive should still be valid. Since we know that no molecular cloud is a perfect sphere, we should then consider how we may constrain our estimates of A_L with further information on each component's geometry.

Panels b), and c) in Figures 5.7 - 5.16 serve to illustrate how this may be accomplished. Panel b) described the relationship between a cloud's R_m and its core volume density. Aside from the boundary conditions imposed by our A_v limit, this relationship should be true regardless of the cloud's shape (this may be shown using the formulation in [Krco & Goldsmith (2014)] for any shapes which abide by the assumptions therein). For each value of the core volume density, there is a range of possible R_m values determined by the possible values of γ, and by extension a_c. This range is depicted by the two black, solid lines in panel b). The blue, horizontal dash-dotted line represents where $R_m = R_{G1}$. The green, horizontal triple-dotted lines represent where $R_m = R_{G1} * 2^{1/2}$ and $R_m = R_{G1} * 2^{-1/2}$. These lines represent the range of R_m values where, depending on cloud shape and orientation, it may be said that the area of the cloud as observed from Earth may be approximately twice, or one half of what it may be from another perspective. They are meant to represent the range of R_m values where the component is considered to be not too different from a sphere. In the case of L204-1 (Figure 5.12), panel b) indicates that if we could determine that $R_m = R_{G1}$, we could then constrain the cloud's possible core density to values between approximately $5 - 15 * 10^4 cm^{-3}$, as only those values could produce a component with the correct mass using $3 < \gamma < 7$. Similarly, if we could determine that L204-1's core density was equal to $10^5 cm^{-3}$, then most likely $.5pc < R_m < .7pc$. Either of these conclusions, which may be possible to obtain with additional

information, would significantly constrain the parameter space of our model and our estimate of Age_L. In the case of L462-0 (Figure 5.14), panel b) leads us to conclude that it is highly unlikely that this component is a sphere. The cloud's core density would have to be too low to produce ^{13}CO emission in order to comprise such a large cloud with sufficient mass if it was indeed shaped like a sphere.

We have found that R_m is the best parameter by which to constrain ages. R_m is dependent on the cloud mass, and all three of the attenuated power law parameters. Determining an individual parameter, such as the core density, γ, or even a_c does constrain the ages as well since each parameter by itself has too small an influence on the mass distribution of a cloud. Panel c) illustrates how R_m for each configuration correlates with the calculated age when compared to the observed HINSA mass fraction. Each point represents an individual configuration, with its distinct core density and γ. The black, solid, horizontal line (where present) represents that range of R_m values which result in the cloud reaching steady state. The vertical green and blue lines represent the same values of R_m as in panel b). As expected, the computed ages increase with greater R_m (and thus lower core volume densities). The computed ages are very well constrained by R_m. With additional data we may be able to constrain a component's geometry, or its core density. Either of those constraints would allow us to better estimate each component's R_m, and improve our age estimates. This may be possible to accomplish using interferometric HINSA data, and will be the focus of the researcher's future efforts.

For brevity, detailed plots of the results are shown only for three clouds (L134, L204, and L462) which are representative of the rest of the survey. Com-

plete results for all clouds are summarized in Table 5.1.

5.4 Discussion

5.4.1 HINSA constraints

We have discovered that the HINSA mass measurements place constraints on the possible values of the core density, and γ beyond those discussed in Section 5.2.5. Since we expect that the cosmic ray flux produces a steady-state constant volume density of HINSA (approximately $2cm^{-3}$), we have found that there is an upper limit to the possible values of R_m. This R_m upper limit is reached when a given component is so large that even at steady-state its total HINSA mass exceeds that which is observed. This limit is reached in nearly all of our modelled components and constrains the parameter space for the core volume density and γ, resulting in all of our estimates of Age_U being either at or very near steady state in Table 5.1. Typically this limit prohibits the most massive components from having core densities less than $10^4 cm^{-3}$.

This limit also constrains the maximum R_m in the least massive components. We have found that if a component's total proton mass is less than approximately $15M_{sol}$, the maximum R_m is so small that it is impossible to construct a model with sufficient self-shielding to produce molecules or ^{13}CO emission. As a result we were forced to exclude 5 of the least massive components observed in [Krco & Goldsmith (2010)] from this analysis (L134-2, L1757-4, L1757-5, L460-2, and L460-3). The reason for this phenomenon is unclear, however three primary possibilities present themselves:

- a) We obtained our distance estimates from the existing literature as described in [Krco & Goldsmith (2010)]. Underestimating a cloud's distance would result in us underestimating both the the total proton and HINSA masses equally. Four of these components are between $10 - 12 M_{sol}$, and a 50% error in their distances might mean that their masses are indeed over the $15 M_{sol}$ limit. Such distance errors may be possible. However, $L1757 - 4$ would have to be more than 10 times more distant than our present estimate. This may indicate that $L1757 - 4$ does not belong to $L1757$ at all, but is simply located along the same line of sight. Its HINSA mass fraction is the highest of all the $L1757$ components, and may support that hypothesis.
- b) It may be that our HINSA, or ^{13}CO column density measurements are wrong, especially since we lacked a good method of measuring each component's temperature. However, in each of these 5 components, the signal-to-noise ratio is well above five. We do not believe that the HINSA, or ^{13}CO measurements alone are at fault since the HINSA mass fractions in all five components are in line with those of other components, and it is unclear what measurement error would reasonably produce such an under-estimate of both the HINSA and ^{13}CO masses.
- c) Our models assume that each component is self-shielded. It may be possible that the neighboring, larger components are providing shielding from the external UV field. This would allow for a much larger region to produce HINSA and ^{13}CO emission.

a) or c), or some combination of all three seem as the most likely explanations. In order to test c), we have tried modelling all five of the components without an A_v boundary conditions and found that it is still very difficult, but not impossible to construct models that would fit the four more massive components. We could

not construct a model that would fit $L1757-4$ under any conditions. There may be further indications that support the shielding hypothesis, as discussed in Section 5.4.3.

5.4.2 Confidence, and Sources of Uncertainty

Measurements of both the ^{13}CO, and HINSA masses are fraught with many sources of uncertainty, including distance, and temperature estimates among others. As this work builds on that data it too inherits those uncertainties. Our inability to provide accurate HINSA measurement uncertainties (as described in [Krco et al. (2008)], and [Krco & Goldsmith (2010)]), carries directly into this work. Uncertainties that result from using ^{13}CO as a tracer for H_2, such as the ^{13}CO to H_2 conversion ratio, and ^{13}CO depletion onto dust grains also contribute. It was evident from our first observations that there were large variations in the HINSA to ^{13}CO and OH column density ratios HINSAGBT. Even along a single line of sight there are frequently two or more components which may have ^{13}CO, ^{12}CO, $C^{18}O$, or OH emission signals of similar strength while the accompanying HINSA features may have very different signal strengths between the same velocity components. To answer why this occurs, it is necessary to be able to separate and independently measure all velocity components along each line of sight. We could have chosen to use different, less robust, methods of measuring HINSA column densities that would allow us to more appropriately assign accurate uncertainty estimates. Those methods would not have allowed us to differentiate between different velocity components as HINSA features often overlap in velocity and it is necessary to use a molecular template to properly separate them as in [Krco et al. (2008)]. We may have used dust extinction

to better estimate total proton column densities, but doing so would have also prevented us from differentiating between velocity components. We have chosen our methods in order to be able to answer why there are such large HINSA to molecular column density ratio variations in different velocity components along the same line of sight as discussed in Section 5.4.4.

As we do not know how the mass distribution of these clouds evolved over time, we make the assumption that the clouds' current structure has remained constant, leading us to lower limit estimates of their ages. Each aspect of the model is organized with this goal in mind, thus the only results which we may have significant confidence in are the the lower age limits (A_L). All other results are secondary, and only used to illustrate interesting phenomena, or how the models may be improved with additional data. We have chosen to model the clouds as spheres when considering A_v limits as that leads to the lowest age estimates (Section 5.2.6. Spheres have the smallest surface areas, and thus the smallest fraction of each cloud is exposed to the external UV field. All other shapes have larger surface areas, and while UV fields might not be able to penetrate deeper, the regions which they do penetrate are necessarily a larger fraction of the cloud's mass. As such penetration prevents ^{13}CO emission, and HINSA it excludes those regions from consideration. The outer regions have the greatest HI/H_2 fractions. Excluding them lowers the total HINSA mass fraction, thus leading to higher age estimates.

The H_2 formation (k') , and cosmic ray ionization (ζ_{H2}) rates are both poorly known even though both are subjects of intense study. We have chosen to use the same rates as in [Goldsmith & Li (2005)] as those represent mid-range values. It is entirely possible that both rates are off by a factor of 2 or more, or

that they may even vary from cloud to cloud, or within different regions of individual clouds. In the higher density regions, where most of the material resides ($n_0 > 10cm^{-3}$), the timescale for HI to H_2 conversion may be expressed as HINSA2

$$\tau = \frac{1}{2k'n_0} \ . \tag{5.2}$$

To first order, any changes to k' will inversely scale all of our age estimates. As our value of k' may be off by a factor of 2, all of our age estimates may be off by a similar value. The steady-state HI volume density may be expressed as HINSA2

$$n_{HI} = \frac{\zeta_{H2}}{2k'} \ . \tag{5.3}$$

None of our estimates of A_L approach the steady-state values, and therefore are not affected by the steady state volume density. Considering equations 5.2, and 5.3 we can conclude that the cosmic ray ionization rate does not significantly affect our estimates of A_L, and that the H_2 formation rate is, to first order, inversely proportional to our estimates of A_L.

5.4.3 Mean Radii and Observed Sizes

The R_{range} column in Table 5.1 represents the minimum and maximum values of R_M for all cloud configurations which could be constructed using the restrictions discussed in Sections 5.2.5, and 5.4.1. If R_M was smaller than this range, then the clouds would generally be too small to achieve enough self-shielding to produce the observed amount of ^{13}CO. For R_M to exceed this range the clouds would generally have to possess more than the observed amount of HINSA even at steady-state, or too low a density to produce ^{13}CO emission. Table 5.1 shows that all of our R_{G1} values are either near, or exceed the maximum values

of R_{range}. If our model, and understanding of these clouds are correct, then this would lead us to conclude that all clouds are preferentially oriented toward us in a manner that maximizes their observed area. As these clouds are located in different regions of the galaxy, and have very different sizes, this seems unlikely. There is a clear bias present, the reasons for which are not clear.

One explanation is that we have overestimated ζ_{H2}, and therefore the HI volume density at steady-state (Equation 5.3). Reducing ζ_{H2} by half would proportionally reduce the steady-state HI volume density, permitting R_{range} to increase by a factor of $2^{1/3}$ (26%). Such an adjustment would allow for many R_{G1} values to fit within R_{range}, however the smallest components ($< 50 M_{sol}$) would still have volume densities too low for ^{13}CO emission. As both conditions must be met, the bias cannot be explained by this possibility alone.

It was necessary to define a bounding region for each component where both ^{13}CO emission and HINSA would be produced based on total proton volume density and A_v to the surface. This approach assumes that each component is entirely responsible for its own shielding. It is also possible, and perhaps likely, that the different components within a cloud contribute to one another's shielding from the external UV field. This would have the effect of expanding the region where ^{13}CO emission and HINSA would be produced past our estimates, and would increase our estimates of R_{range}. As noted in Section 5.2.5, the A_v boundary condition takes precedence only in clouds that are less than $10^3 M_{sol}$, which does not include components 0,1, and 2 of L1029. In each of those components $R_{G1} > R_{range}$, however those are only three components within the same cloud and the cloud's geometry and orientation may well account for the value of R_{G1}. To better determine if self-shielding is responsible for the large values

of R_{G1} we need a larger survey with more components greater than $10^3 M_{sol}$. If massive clouds are found to also preferentially have $R_{G1} > R_{range}$ then another effect is likely responsible.

L392 comprises of only a single velocity component which is roughly circular in shape on the sky, yet its R_{G1} is nearly twice greater than R_{range}. Neither shielding by neighbouring components, nor overestimation of ζ_{H2} can explain this discrepancy. It may simply be that the cloud is shaped like a thin disk and we are viewing it head-on. Additional information on the geometry, or core density of this cloud would prove valuable.

5.4.4 HINSA abundances

One of the primary discoveries of the first HINSA surveys was that $HINSA/H_2$ ratios could vary greatly within different velocity components along the same line of sight, and within the total masses of different components within the same cloud. A goal of this research was to determine if these variations could be explained. Using this model we can demonstrate that large differences in M_{HINSA}/M_0 among components do not necessarily produce large differences in ages due to the dependence on total mass. L204-0 has M_{HINSA}/M_0 more than 7 times greater than that of L204-1, yet its Age_L is 35% greater. HINSA column density, and mass abundances alone are not enough to determine the ages of components. It is necessary to consider each component's total proton mass as well.

Our decision to pursue methods that allowed us to treat each component within a cloud separately has been justified by the results in Table 5.1. In each

case, treating the clouds as a single entity (the LOS component) leads to higher age estimates. L134, and L429 are especially good examples where the individual components have very similar ages, but the LOS component yields a higher age in this case. Two components with the same age will have different M_{HINSA}/M_0 ratios depending on their masses. Adding the two components and treating them as one will not yield the correct age.

We find good agreements between the values of Age_L among components within the same cloud, even when they have different masses and exhibit different M_{HINSA}/M_0 ratios. This may indicate that different components within each cloud formed at approximately the same time and followed similar rates of collapse. The most notable exception is found in L1029. The third component is significantly smaller than the others, and seems to have a younger age. It is unlikely that the difference in Age_L is due to difference in masses between component 3, and components 0,1, and 2 since component 4 has a low mass as well and its Age_L is in agreement with the three larger components. Similarly, other low mass components throughout the survey show greater values of A_L than L1029-3. This may indicate that L1029-3 either began its collapse after the rest of the cloud, or that it has been collapsing more slowly.

5.4.5 L204

It is difficult to validate these results without independent measurements of cloud ages. L204 presents a special opportunity in that it is located close to ζ Oph, an O9 type star surrounded by an HII region. ζ Oph is a runaway from the Sco OB2 complex with an estimated kinematic age of 1.1 Myrs Herbst81.

L204's kinematics indicate that the cloud may have been formed due to ζ Oph's influence. [McCutcheon et al. (1986)] noted the V_{LSR} differential present among different sections of L204, and the inverse relationship between the mass of each section and the velocity presumably imparted by ζ Oph. Using the velocity differential, and associated distances they derived a lower limit for L204's kinematic age of between 0.1 - 0.3 Myrs. As the velocity differential was not imparted instantaneously, L204's kinematic age is likely a few times greater than the lower limit. [Heiles et al. (1988)] concluded that L204 formed behind the expanding shell associated with the North Polar Spur more than 1 Myr ago. [Tachihara et al. (2000)] examined the influence of ζ Oph on L204 and concluded that the most likely method of momentum transfer was due to the photo-dissociation rocket effect. Assuming 100% efficiency, which they note is unlikely, they arrived at lower limits between 0.02 and 0.15 Myrs for six sections of the cloud.

Our chemically-derived lower limits are in agreement with the independent, kinematic estimates above. This agreement indicates that our models are likely approximately correct. It is interesting to note that [Tachihara et al. (2000)] concluded that one portion of the cloud (which corresponds to our L204-1) is more weakly coupled to ζ Oph, and that our model suggests this component is younger than the L204-0 component.

5.4.6 Young Clouds

The highest HINSA mass fraction observed in this survey is $3.8x10^{-3}$ (L1029-1). The lowest value of A_L is 0.32 Myrs (L1757-1). What is happening in the first few

hundred thousand years? Why have we not observed any clouds with HINSA mass fractions of 0.5, or even 10^{-2}. This survey is sufficiently large that it is surprising not to see any clouds in earlier stages of development. The survey was limited to clouds which showed no indication of ongoing star formation and exhibit HINSA features. By definition, HINSA features necessitate the presence of associated molecular emission.

There have been several surveys that showed HISA features with no associated molecular emission, however due to the complexity of the background HI emission spectra it is often difficult to identify whether HISA features are associated with any clouds. As the structure of dust grains is not well known, nor their evolution over time, it is possible that HI begins its conversion to H_2 before ^{13}CO or other molecules can form in observable abundances. It is possible that some of the observed HISA features may belong to clouds in such an early state of development, and they were excluded from this survey by not having associated molecular emission. This hypothesis may be further examined by comparing HISA features with no associated molecular emission to dust extinction maps. A statistical analysis to this survey may reveal whether such clouds might account for the missing young clouds not observed here.

The original survey in [Krco & Goldsmith (2010)] detected HINSA features in 83% of the observed clouds, while [Li & Goldsmith (2003)] found HINSA detections in 77% of the observed clouds in Taurus. [Krco & Goldsmith (2010)] found no relationship between HINSA non-detections and cloud positions, distances, or even background HI emission. There was a distinct relationship between the prevalence of HINSA non-detections and H_2 column densities (Figure 2d in [Krco & Goldsmith (2010)]). H_2 formation on dust grains is most intense

immediately after cloud formation, and results in significant cloud heating. It may be that in the first few hundred thousand years, the H_2 formation rate is so high that the increased cloud temperature inhibits the expression of observable HINSA features. In that case, it may be impossible to observe HINSA features in clouds where the HINSA mass fraction is above 10^{-2}. The 20% non-detection rate found in [Krco & Goldsmith (2010)] and [Li & Goldsmith (2003)] may be due to such young clouds. As such clouds would be in the earlier stages of collapse, and H_2 formation they should exhibit lower H_2 column densities, possibly explaining the correlation between HINSA non-detections and lower H_2 column densities found in [Krco & Goldsmith (2010)]. To ascertain the validity of this hypothesis it would be necessary to examine models of cloud temperatures during the early stages of collapse along with the H_2 formation process to determine whether HINSA features would be visible.

5.5 Summary

- We have presented a model which utilizes the observed HINSA and H_2 masses of molecular clouds to obtain lower limits on their chemical age under the assumption that each cloud's radial volume density profile may be described using an attenuated power law with a wide parameter space bounded by the conditions discussed in Sections 5.2.5, and 5.4.1.
- We have found that there are clear limits to the possible parameters for clouds described with attenuated power-laws as described in Sections 5.2.5, and 5.4.1. The need for self-shielding limits the minimum size of clouds, while the HINSA steady-state volume density limits their maximum size. While these limits encompass a fairly large parameter space,

they are narrow enough to yield some results.

- Our models found that for clouds under $1000 M_{sol}$, A_v is the primary determinant of the extent of the region where ^{13}CO emission may be formed. This is due to there being volume densities $> 10^3 cm^{-3}$ in regions where $A_v = 1/2$. Therefore, the observed ^{13}CO extent for most clumps is governed by their available shielding, and the strength of the external UV field.
- Most of the clouds in this survey have ^{13}CO sizes greater than those that can be produced by our models using only self-shielding. This leads us to believe that neighbouring components may contribute to each other's shielding from the external UV field.
- Another possible explanation is that our estimate of ζ_{H2} may be too high. Reducing ζ_{H2} by a factor of 2 results in most of the components' R_{range} values increasing to the point where they encompass R_{G1}.
- One of the biggest questions arising from the first HINSA observations has been the presence of very different HINSA/^{13}CO column density ratios among different velocity components along the same line of sight, as well as HINSA mass fractions. Here we have shown that such differences are to be expected as components of different total proton masses and the same age will produce significantly different HINSA mass fractions.
- L204 is the only cloud in our survey for which there are dynamical age estimates available. Our results are in agreement with those estimates.
- No clouds have so far been observed with HINSA mass fractions of $4x10^{-3}$ or greater, indicating that we are not seeing the youngest clouds through this method. It may be that such clouds only produce HISA features, or that the heating due to H_2 formation may prevent the observations of any HI Self-Absorption.

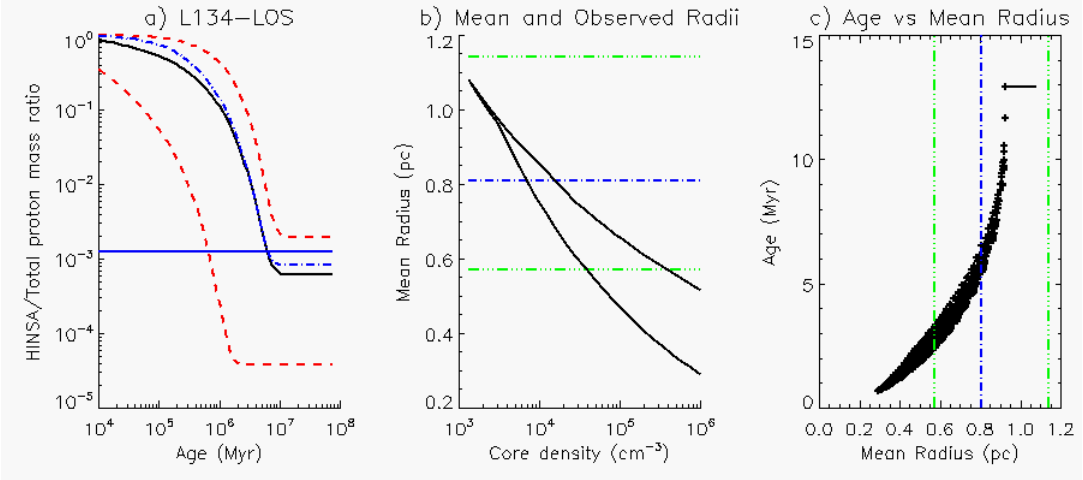

Figure 5.7: Model comparison for L134, Component LOS. Panel descriptions are found in Section 5.3

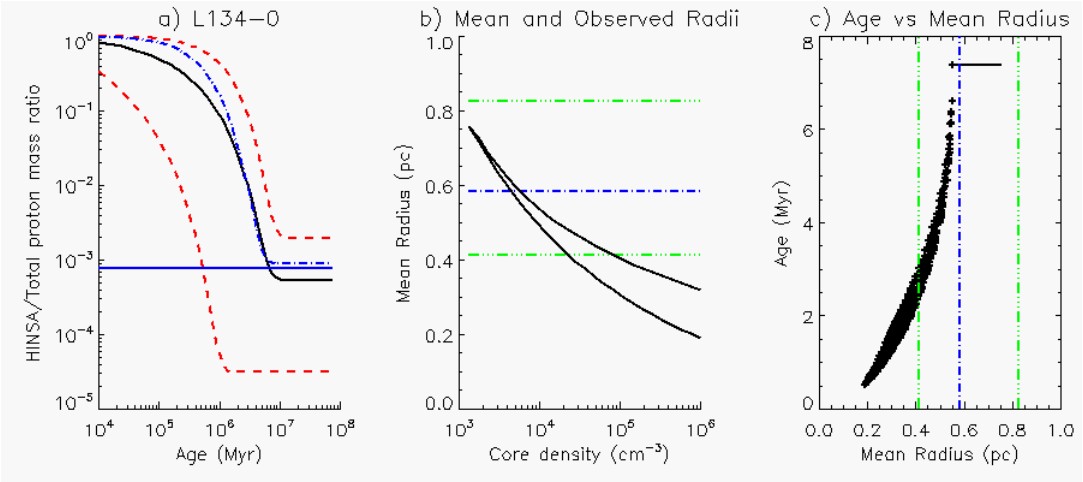

Figure 5.8: Model comparison for L134, Component 0. Panel descriptions are found in Section 5.3

- All of our models reach steady-state HINSA mass fractions within approximately 7 to 15 Myrs.

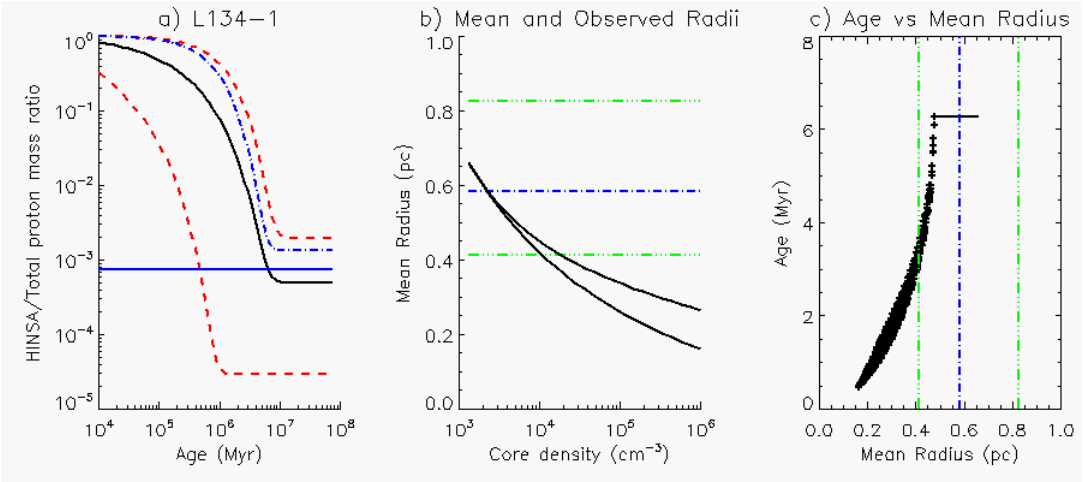

Figure 5.9: Model comparison for L134, Component 1. Panel descriptions are found in Section 5.3

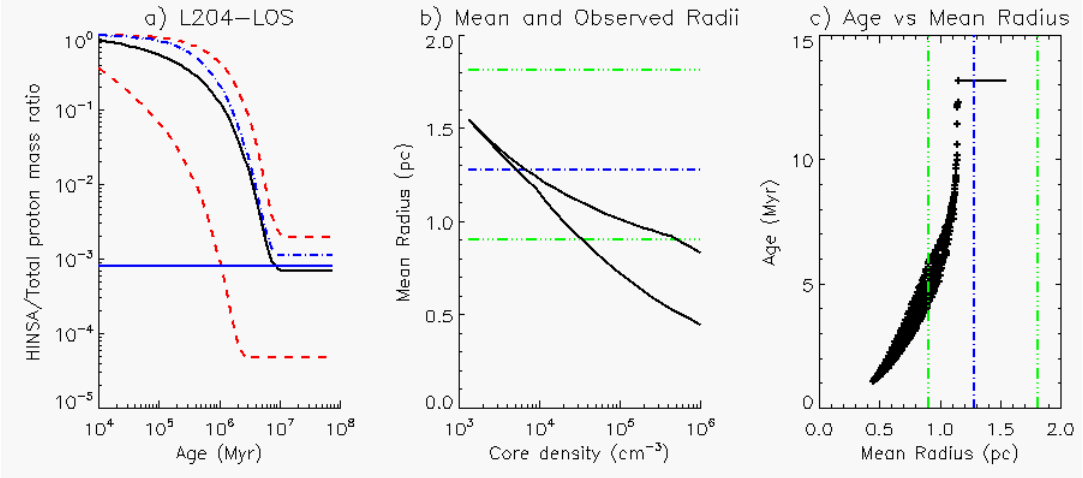

Figure 5.10: Model comparison for L204, Component LOS. Panel descriptions are found in Section 5.3

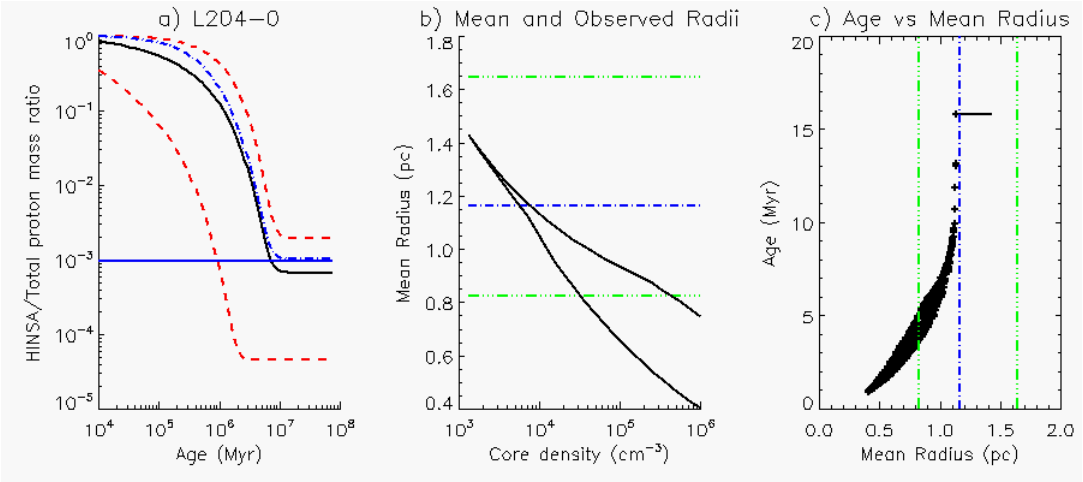

Figure 5.11: Model comparison for L204, Component 0. Panel descriptions are found in Section 5.3

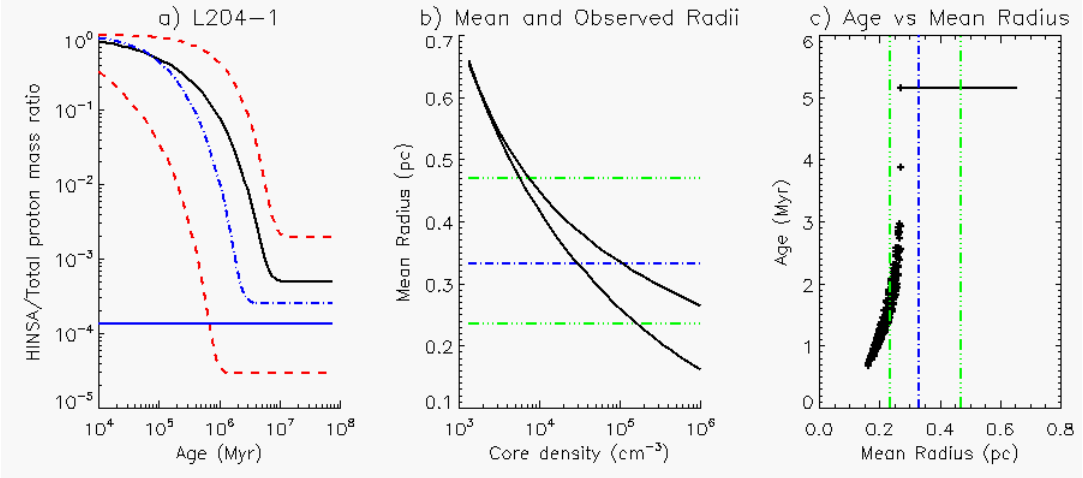

Figure 5.12: Model comparison for L204, Component 1. Panel descriptions are found in Section 5.3

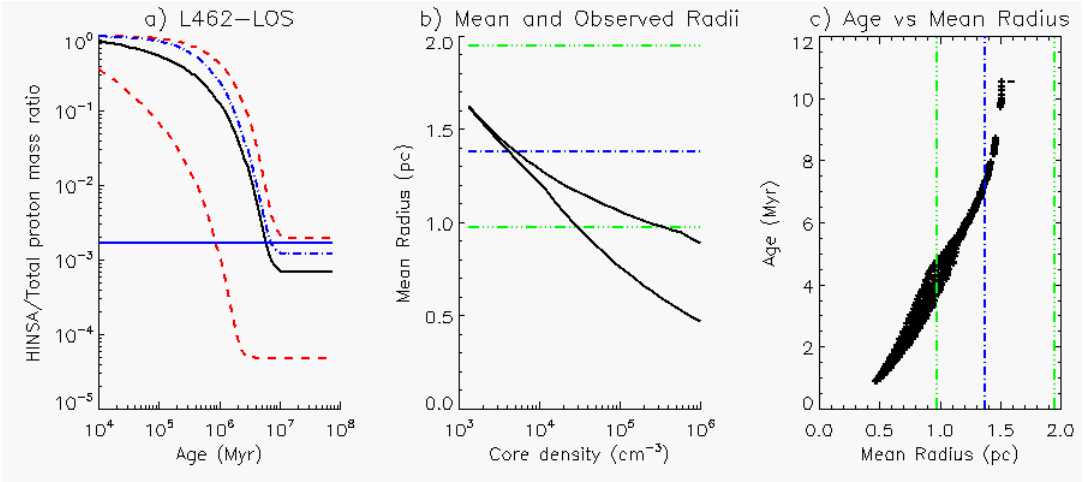

Figure 5.13: Model comparison for L462, Component LOS. Panel descriptions are found in Section 5.3

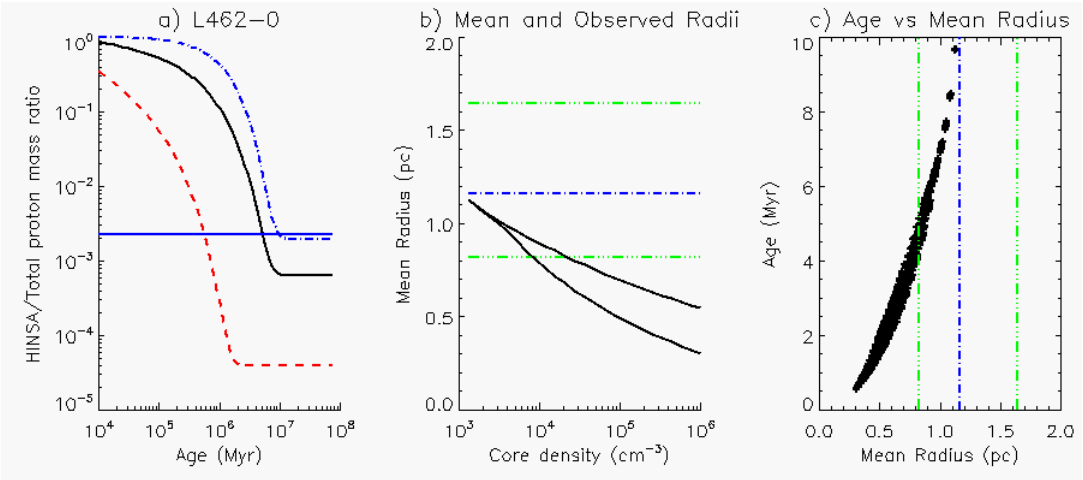

Figure 5.14: Model comparison for L462, Component 0. Panel descriptions are found in Section 5.3

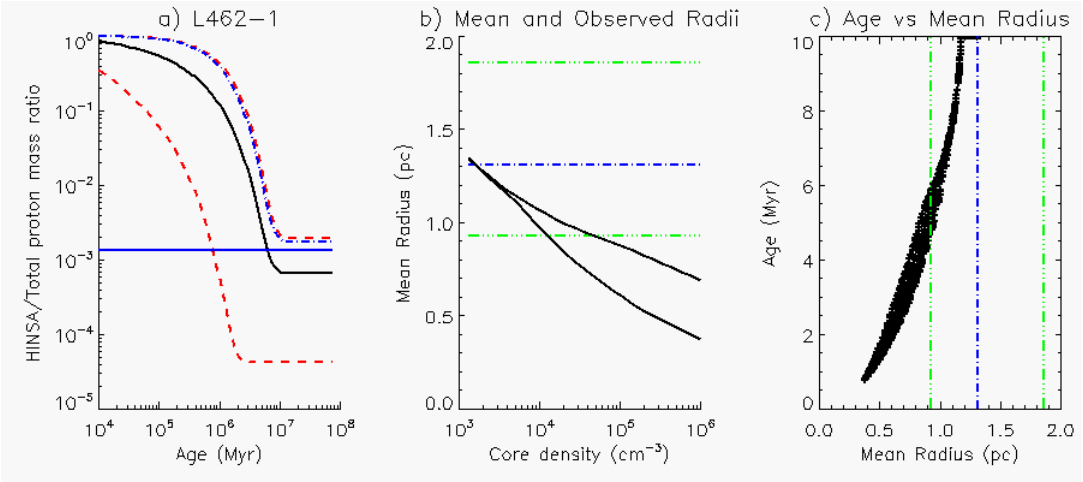

Figure 5.15: Model comparison for L462, Component 1. Panel descriptions are found in Section 5.3

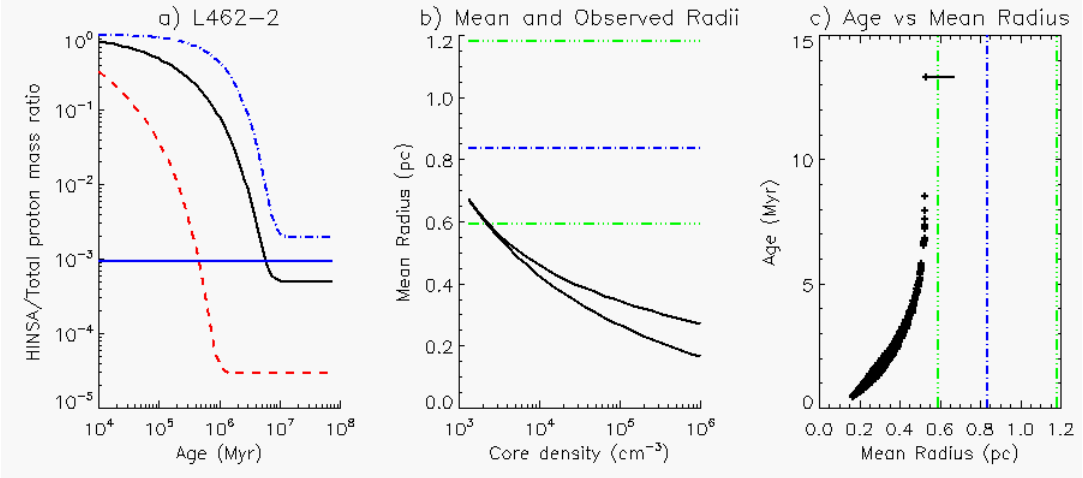

Figure 5.16: Model comparison for L462, Component 2. Panel descriptions are found in Section 5.3

Source	Component	M_0/M_{sol}	$M_{HINSA}/M_0/10^{-3}$	Age_L	Age_U	Age_{mean}	R_{range}	R_{G1}	Age_2
L1029	LOS	6254.01	3.00	1.49	8.20	5.11	1.28 - 3.79	3.76	4.40 - 8.20
L1029	0	1676.65	2.78	1.05	8.52	5.22	0.76 - 2.44	3.31	7.57 - 8.52
L1029	1	1945.13	3.80	0.96	7.51	4.78	0.81 - 2.56	3.56	7.49 - 7.51
L1029	2	2180.25	2.79	1.14	8.49	5.22	0.85 - 2.66	3.58	7.55 - 8.49
L1029	3	24.88	0.40	0.49	SS	SS	0.14 - 0.35	0.59	SS - SS
L1029	4	70.04	0.14	0.88	SS	SS	0.21 - 0.35	0.93	SS - SS
L134	LOS	144.97	1.23	0.66	SS	6.32	0.29 - 0.92	0.80	2.43 - SS
L134	0	49.79	0.76	0.52	SS	6.84	0.19 - 0.55	0.58	2.51 - SS
L134	1	33.36	0.74	0.46	SS	6.51	0.16 - 0.47	0.58	3.25 - SS
L1757	LOS	263.92	1.69	0.71	SS	5.88	0.36 - 1.23	1.25	4.17 - SS
L1757	0	38.30	0.29	0.60	SS	SS	0.17 - 0.36	0.63	SS - SS
L1757	1	21.14	1.77	0.32	13.61	4.37	0.13 - 0.55	0.63	4.58 - 13.61
L1757	2	62.34	2.03	0.43	12.07	4.97	0.20 - 0.81	0.81	3.57 - 12.07
L1757	3	123.76	1.89	0.55	SS	5.43	0.27 - 0.99	0.98	3.79 - SS
L204	LOS	428.23	0.79	1.05	SS	8.54	0.44 - 1.15	1.28	4.25 - SS
L204	0	335.47	0.96	0.92	SS	7.37	0.40 - 1.13	1.16	3.70 - SS
L204	1	32.83	0.13	0.68	SS	SS	0.16 - 0.27	0.33	1.54 - SS
L392	LOS	164.79	0.63	0.81	SS	13.15	0.30 - 0.77	1.43	SS - SS
L429	LOS	254.77	1.91	0.68	SS	5.61	0.36 - 1.25	0.87	1.92 - SS
L429	0	99.60	2.47	0.47	9.03	4.92	0.25 - 0.95	0.84	2.79 - 9.03
L429	1	59.64	2.12	0.42	10.83	4.89	0.20 - 0.80	0.84	4.06 - 10.83
L429	2	72.08	1.01	0.55	SS	6.38	0.22 - 0.68	0.87	4.83 - SS
L460	LOS	258.79	1.39	0.75	SS	6.23	0.36 - 1.17	1.38	5.85 - SS
L460	0	168.34	1.24	0.69	SS	6.37	0.30 - 0.97	1.31	7.80 - SS
L460	1	60.42	1.78	0.45	SS	5.14	0.20 - 0.77	1.10	SS - SS
L462	LOS	491.40	1.65	0.88	SS	6.03	0.47 - 1.51	1.37	3.73 - SS
L462	0	165.31	2.27	0.55	9.68	5.24	0.30 - 1.12	1.16	4.31 - 9.68
L462	1	279.52	1.36	0.77	SS	6.32	0.37 - 1.17	1.31	4.79 - SS
L462	2	34.84	0.94	0.44	SS	5.93	0.16 - 0.52	0.83	SS - SS
L466	LOS	97.77	0.66	0.68	SS	8.66	0.24 - 0.66	0.59	1.79 - SS
L466	0	51.71	0.94	0.51	SS	6.29	0.19 - 0.60	0.59	2.35 - SS

Table 5.1: Summary of results for the studied clouds, using the same data as in [Krco & Goldsmith (2010)]. All ages are in millions of years. All radii are in parsecs. SS designates that the component has reached the steady state. The LOS component refers to the entirety of each cloud within a map, including all clumps and velocity components. Only components with over 20 solar masses are shown. The total proton mass, and the HI to H_2 mass ratios of each cloud are represented by M_0/M_{sol} and $M_{HINSA}/M_{H_2}/10^{-3}$. Age_L, and Age_U represent the lower, and upper limits on the age of each component derived from all possible values of n, and γ. By averaging the HI to H_2 mass ratios derived from all possible values of n, and γ we arrive at Age_{mean}. R_{range} represents the range of possible component radii encompassing all possible values of n, and γ. R_{G1} is the component radius assuming that $G = 1$. Age_2 represents the possible range of ages if $1/\sqrt{2}R_m < R_{G1} < \sqrt{2}R_m$.

CHAPTER 6

SUMMARY OF RESULTS

While this research has taken many years to complete it has yielded significant new insights, provided new techniques and methodologies, and accordingly advanced the state of the field. In the course of several projects, we have answered nearly all of the questions posed when this research began in 2005, as well as discovered some new questions and possibilities for future research. In this chapter we summarize the most significant advancements that have resulted from this research.

6.1 New HINSA measurement Technique

Even though hydrogen is the most abundant species in the universe, it is very difficult to confidently measure the HI content of molecular clouds. The problem lies not in obtaining sufficient signal, but in discerning which HI belongs to a particular cloud. Uncertainties in the background emission, temperature, and even the line profile have prevented rigorous quantitative analysis. [van der Werf et al. (1988)] was among the first to attempt rigorous mapping of the HINSA within an entire cloud. Interferometry offered a seemingly natural method of removing the background emission from L134. It was quickly apparent that variations in the background emission from one end of a cloud to another were usually of the same scale as the HINSA features themselves. [Li & Goldsmith (2003)] and [Goldsmith & Li (2005)] developed a different method whereby they used masks and polynomial fitting to determine the expected background emissions. This method had several difficulties, one of which being the somewhat arbitrary choice of the degree of the polynomial

and the masking regions used for the fitting. Small changes in the fitting parameters could significantly affect the derived HINSA column densities. These uncertainties limited the analysis that could be performed with the data.

It was clear that a more robust method of measuring HINSA column densities was needed in order to undertake a more sophisticated analysis. We knew from previous observations, as well as our own survey [Li & Goldsmith (2003), Goldsmith & Li (2005), Krco & Goldsmith (2010)] that HINSA features were very closely correlated to ^{13}CO emission in velocity, linewidth, and sky position. This correlation was advantageous in creating a new, less arbitrary technique. HINSA features are much narrower in linewidth than HI emission components. Therefore they become the dominant feature in a spectrum when a second derivative with respect to frequency/velocity is taken. This offers another opportunity to measure, and extract HINSA features in an improved technique. The technique described in Chapter 2, takes advantage of these two opportunities to present an improved method for measuring HINSA column densities. Its primary advantages over previous methods are in its accuracy, the lack of arbitrary fitting parameters, and the ability to distinguish between multiple, overlapping components along the same line of sight. The success of this technique yielded improved confidence in HINSA column densities, and thus enabled us to pursue a more sophisticated study of HINSA, and HI/H_2 ratios than had previously been done.

6.2 Viability of HINSA as a Tool of Study

Previous studies of HINSA features had focused almost exclusively on the Taurus Molecular Cloud Complex, and a small number of nearby clouds such as L134 [van der Werf et al. (1988), Li & Goldsmith (2003), Goldsmith & Li (2005)]. When this research began, it was not at all certain that HINSA features were common occurrences as opposed to peculiarities of Taurus, and a few other clouds. It was expected that foreground HI emission could diminish the expression of any HINSA features. However, the strength and properties of this effect were poorly known. Significant questions remained such as whether there would be a limiting distance past which HINSA features could no longer be detected, whether HINSA features are more prevalent toward regions with stronger background emission such as in galactic plane, or toward the galactic core, and whether the 80% HINSA detection rate observed in previous studies would persist in other clouds.

We thus conducted the largest HINSA survey to date in HI and OH using the Green Bank Telescope (GBT) that covered nearly 80 positions in 48 dark clouds with no evidence of ongoing star formation. The target clouds were chosen to have a wide a range of distances (up to 700 pc) and positions. The majority of the clouds were studied using single, or multiple pointings while the most interesting clouds were mapped as the limited telescope time permitted. The accompanying OH data allowed us to identify the observed HINSA features. The survey and the associated analysis are described in Chapter 3. We found that HINSA features do appear to be present in approximately 80% of the observed clouds, and that their occurrence did not appear to show any dependence on sky position or galactic coordinates. We detected HINSA in clouds up to 700 pc

away, and found no discernible increase in non-detections with distance leading us to believe that HINSA features are probably detectable at even greater distances. With this survey we demonstrated the basic utility of HINSA features, and that previous studies were not anomalous.

6.3 The HINSA survey

We followed up the GBT observations with a survey of most of the same sources at the Five College Radio Observatory (FCRAO) using ^{12}CO, ^{13}CO, and $C^{18}O$ emission. ^{12}CO was useful in determining temperatures; ^{13}CO was used as a molecular template for HINSA extraction and to estimate total proton column densities; $C^{18}O$ was too weak and too poorly correlated with HINSA to be of direct use. The GBT and FCRAO surveys greatly expanded the parameters of observed HINSA clouds with respect to size, distance, location, and grouping. We were able to characterize the HINSA features within a large sample of clouds for the first time, accompanied by detailed molecular data. The results of the combined survey are detailed in Chapter 3. We found that HINSA column densities typically vary from $10^{17} cm^{-2}$ to $10^{20} cm^{-2}$ (Figure 3.7). Typically, HINSA features are only present along lines of sight with optical depths due to dust extinction of at least 1 magnitude. In clouds where HINSA is present, it is generally present throughout the entire cloud wherever ^{13}CO is detected. Our survey agreed with previous studies in that it showed strong correlation between HINSA and ^{13}CO emission in sky position, velocity, and non-thermal linewidth [Li & Goldsmith (2003), Goldsmith & Li (2005)].

Many of our prior expectations were confirmed when we examined HINSA

column density abundance ratios (N_{HINSA}/N_{H2}). HINSA column density abundance ratios typically ranged between 10^{-5} to 10^{-2} (Figure 3.10), in line with previous measurements. It is still unclear what phenomenon prevents us from observing lines of sight with higher HINSA abundance ratios. By taking the HINSA to total proton column density ratios, we found that clouds which were grouped together on the sky often tended to have similar HINSA abundances. These similarities led us to consider that the HINSA abundances may reflect the ages of clouds and that the clouds in certain complexes likely formed at approximately the same time.

6.4 Properties of HINSA clouds, and individual clumps

With the ^{13}CO (FCRAO) and HINSA (GBT) data it is possible to examine some of the basic characteristics of HINSA clouds. All but one of the mapped sources exhibit multiple velocity components, and clumps along the same lines of sight. It is apparent that in many cases, different velocity components along the same line of sight have very different HINSA column density abundances, therefore we chose to measure the HINSA abundance ratios within each velocity component and clump independently. Our naming convention is such that there may be more than one clump within each velocity component, but only one velocity component per clump. These clumps have masses that vary from ≈10 to ≈6000 M_{sol}. Not only can the HINSA column density abundances vary significantly along the same line of sight, but the overall HINSA abundances within individual clumps can vary within the same cloud (Table 3.4). We sought to determine whether such differences were evidence that different clumps within the same cloud may have formed at different times.

Since the H_2 formation rate is dependent on the dust and atomic hydrogen densities, it is expected that HI volume densities and abundances would be lowest in cloud cores where the density was highest. Thus regions of higher total proton column density should exhibit lower HINSA abundances. This appears to be the case in general, as evidenced in Figure 3.10b. We expected to be able to relate the slopes of HINSA abundance versus total proton column density for individual clumps in order to determine their ages using a simple chemical model assuming spherical symmetry. On the contrary, Figures 3.12 - 3.28 show that in many clouds the slopes on the N_{HINSA}/N_0 vs. N_0 plots vary significantly, and that the slopes could often be positive. The fact that HINSA abundances could increase at higher total proton column densities indicates that there must be a more complex phenomenon at work than a simple first order approximation of a sphere. We determined that positive slopes could be produced in old, non-spherical clouds where most of the cloud had reached its steady-state abundance. Eventually, the HI volume density in the steady-state regions will stabilize at about 2 cm^{-3} due to cosmic ray dissociation of H_2. This constant HI volume density, if present throughout most of a cloud, when combined with highly aspherical geometries (such as edge-on disks) can produce the observed slopes. From these results, and further testing it is apparent that the HINSA column density abundances, and the associated slopes are highly dependent on the shapes and orientation of the clouds. Therefore, an assumption of spherical symmetry is unsuitable, and it is necessary to develop a geometry-independent method of measuring cloud ages.

6.5 Geometry-independent method of determining cloud density distributions

Due to the geometry dependence on observed column densities, it is necessary to use a different method to determine cloud ages. The only geometry-independent observables available are the total HINSA and total proton masses of each clump. It is expected that the HINSA mass abundance will decrease over time, however the rate of decrease is dependent on the H_2 formation rate, which itself is dependent on the clump's density distribution. It is not possible to obtain an exact estimate of the density distribution of a clump using only a single observable quantity in a column density map since such a map cannot uniquely define a three-dimensional object. However, it is possible to obtain the shape of a radial volume density profile function which can accurately represent the internal structure of a clump to within two geometry-dependent scalars (G and χ). We present a new method to do just that in Chapter 4.

Though there are several caveats, this method permits us to see how the volume density behaves within certain regions of each cloud without knowing or assuming the cloud's geometry, thus allowing for many new avenues of study. We found that this method, and the inherent self-similarity requirement work remarkably well on a wide variety of astronomical objects and observable quantities. In this research we limited ourselves to studying the 2MASS dust extinction maps of nearby molecular clouds. We were able to confirm the conclusions of previous studies in that molecular cloud total proton volume density profiles are governed by power laws, and more specifically that attenuated power laws seem to provide the best fits.

The methods we used to obtain the FCRAO data did not have sufficiently high signal to noise ratio to be able to directly measure the radial density profiles of the clouds in our survey. However, the results using 2MASS data do provide limits on the radial profile function's parameters based on other clouds. These limits could then be used to construct a chemical model for our surveyed clouds.

6.6 Chemical Ages of Surveyed Molecular Clouds, Final Conclusions, and Open Questions

The new technique in Chapter 4 revealed that clouds' internal structure could best be described using attenuated power laws, and provided reasonable limits on the parameters such as power law coefficients, core volume densities, and core radii. Since each cloud's geometry is unknown, we used those parameter limits in combination with the total HINSA and total proton masses observed in Chapter 3 to obtain estimates of lower limits on cloud chemical ages using a simple chemical model which only accounted for the H_2 formation rate on dust grains and dissociation due to cosmic rays. The results of this modeling are presented in Chapter 5. These age estimates are summarized in Table 5.1 and yield many new scientific insights which are detailed in Sections 5.4 and 5.5.

We have succeeded in answering the fundamental questions posed at the start of this doctoral thesis. HINSA features are prevalent in approximately 80% of the observed clouds. The youngest clump in our survey (L1757-1) has a chemical age lower limit of only 0.3 Myrs, while all of our observed clouds will reach their steady state abundances within 7 to 15 Myrs. Most of the clouds appear to have ages ranging from several hundred thousand years, to a few

Myrs which is consistent with most theoretical models, and recent results from [Brunken et al. (2014)]. While our underlying assumption of constant density prevents us from specifying true upper age limits, we have been able to determine that 8 of the clumps in our survey have likely not yet reached their steady-state HINSA abundances. No previous studies have been able to claim that their clouds have not yet reached steady-state. Our results are supported by the agreement with the previously known dynamical age of the cloud L204.

The previously observed differences in HINSA column density abundances for different velocity components along the same line of sight are largely due to the mass of each clump. Clumps of the same age, but different masses will have very different HINSA abundances. In most cases, as evidenced by Table 5.1 the different clumps within each cloud will have similar chemical ages despite differences in size, and HINSA abundances. However, in several cases some of the clumps within a cloud have significantly younger ages in comparison to the other clumps. An excellent example is L1029, where 4 of the clumps (L1029-0, L1029-1, L1029-2, and L1029-4) have very similar ages and a wide range of masses, the fifth clump has a significantly lower age (Table 5.1). This may be an indication that L1029-3, may have formed or begun its collapse after the rest of the cloud. That clumps within a cloud may have different ages indicates that they must each be measured and treated separately. Treating a cloud as a whole will always tend to overestimate its age. Our technique, presented in Chapter 2 is at this time the only HINSA technique capable of differentiating between multiple, overlapping, velocity components along the same line of sight. In addition to the chemical age lower limits, we have also presented indications that many clouds may be significantly aspherical based on their observed HINSA column densities. In Section 5.4 we also present circumstantial evidence that

may indicate that clumps do in fact provide shielding for one another from the external UV field.

While this research has answered most of the questions originally posed, it has opened a few new ones. Chief among these is why we were unable to see any clouds younger than 0.3 Myrs, and why we do not see any clouds with HINSA abundances of 10^{-2} or higher. One possible explanation is that in the cloud's initial stages of collapse, the HI to H_2 conversion is rather quick and releases a great deal of energy in the process. This heating may prevent the HI gas that is present from exhibiting HINSA features. It seems plausible that ^{13}CO may form while the HI gas is too warm to produce absorption, and that these clouds in fact are represented by the 20% of clouds in which we had no HINSA detections, but observed OH emission. Determining the temperatures of those clouds with non-detections should be a top priority of future research. If we can determine that those clouds represent the earliest stage of development, then in combination with the present age estimates we would be able to estimate the total lifetimes of molecular clouds, or at least the lower limits.

In Chapter 5 we showed how we could significantly constrain the age estimates with additional information about cloud structure. As discussed in 5.4, knowing a cloud's mean radius would significantly reduce the range of possible ages derived through our model. While this may be difficult, it may be possible to accomplish using interferometric HI data and multiple molecular tracers. An easier to achieve, but less constraining result would be to obtain the power law coefficients for the present clouds by obtaining ^{13}CO maps with better signal to noise ratio and applying the technique from Chapter 4 to them. Determining the power law coefficients in such a way would reduce the range of possible

ages by approximately a factor of two compared to those shown in Chapter 4.

6.6.1 Future Work

Throughout this thesis we have developed a set of tools for better understanding the cold HI content of molecular clouds, measuring cloud ages, and determining volume density radial profile function shapes. In the long term, we intend to use these to establish a better understanding of cloud evolution, and the associated stages as well as a better understanding of the processes that trigger collapse. Not mentioned in the thesis are the GALFA and FCRAO maps of the Taurus and Perseus molecular cloud complexes which we have obtained. Initial results indicate that they likely had very different formation processes. Taurus in particular exhibits a steep age gradient which appears to be parallel to the galactic plane with the older region being closer to the plane. A full analysis similar to that done here for individual clouds is needed for the entire complex to precisely determine the strength of this gradient.

The ability to determine radial profiles without a geometric assumption is very powerful. If we can use multiple species, it should be possible to obtain estimates of the G and χ parameters even for clouds whose geometry is not known. This would then allow us to do a general estimate of cloud geometry in the whole population of molecular clouds and determine whether they are best represented by sheets, or spheres. We could further perform direct comparisons between multiple species to determine radial profiles of cloud temperatures, thus obtaining a much more complete understanding of these clouds. Comparing ^{13}CO and total proton profiles for individual clouds should allow us to see

the effects of ^{13}CO depletion onto dust grains. Ultimately, we could not apply this technique directly to HI data due to the large size of the GBT beam. Following up with interferometric observations may ultimately allow us to located the transition region (where HI abundance peaks) within an evolving cloud. This would serve as a much better measure of a cloud's age.

APPENDIX A

DESCRIPTION OF HINSA PROCEDURES

For definitiveness, we here describe the process of obtaining molecular parameters to be used as a template as well as the actual HINSA extraction in a step–by–step fashion. We model this description based on our specific observations and available data although the technique can be easily adapted to other circumstances. We obtained ^{12}CO and ^{13}CO data with the 14 m Five College Radio Observatory having a 45″ to 50″ FWHM beam size and the HI data were obtained using the 100 m Green Bank Telescope having a 9′ FWHM beam size.

1. Reduction and Regridding: It is assumed that all data have been properly reduced, calibrated, and regridded.

2. Convolution: Initially the ^{12}CO and ^{13}CO spectra are convolved to a 2′ FWHM beam size in order to improve the signal to noise ratio. A gaussian convolving beam shape is used.

3. CO Fitting (first pass): While assuming a particular gas temperature (10K), emission functions are fitted to all ^{13}CO spectra to obtain their center velocities. These velocities are used to determine the excitation temperature of each ^{13}CO velocity component, using the accompanying ^{12}CO spectrum. The temperatures are derived under the assumption that the ^{12}CO emission is in LTE and optically thick at line center. Then, for ^{12}CO, [Stahler & Palla (2004)]

$$f(T_{kin}) = f(T_{ex}) = \frac{T_{B_0}}{T_0} + f(T_{bg}) \ , \tag{A.1}$$

where the excitation temperature (T_{ex}) is taken to be equal to the kinetic

temperature (T_{kin}), T_{B_0} is the observed brightness temperature at line center, T_0 is the equivalent temperature of the transition (5.5K for the J=1 - 0 transition of ^{12}CO), T_{bg} is the blackbody radiation temperature of the background field (2.7K), and

$$f(T) = \frac{1}{exp(T_0/T) - 1} \ . \tag{A.2}$$

4. CO fitting (second pass): Linewidth, and optical depth are derived for each ^{13}CO emission component using the previously obtained temperatures and center velocities. Subsequently the non-thermal linewidths are obtained using:

$$\sigma^2_{obs} = \sigma^2_{nt} + \sigma^2_{th} \ , \tag{A.3}$$

where σ_{obs} is the observed total linewidth, and σ_{nt} and σ_{th} are respectively the nonthermal and thermal components of the linewidth.

5. Molecular Column Densities: Column densities for ^{13}CO for each component along each line of sight are calculated according to the technique described in [Stahler & Palla (2004)]. H_2 column densities are estimated using a H_2/ ^{13}CO abundance ratio of 7.5×10^5 for these galactic clouds.

6. Estimating Atomic Parameters: The center velocity, non-thermal linewidth, and temperature for the HI gas are determined for each velocity component along each line of sight by convolving the previously obtained ^{13}CO parameters to the GBT 9′ beam as weighted by the ^{13}CO column densities according to:

$$X_{j,comp} = \frac{\sum_i f(\theta_{i,j})\, X_{i,comp}\, N^{13CO}_{i,comp}}{\sum_i f(\theta_{i,j})\, N^{13CO}_{i,comp}} \ , \tag{A.4}$$

where $X_{j,comp}$ represents the temperature, non-thermal linewidth, or center velocity of a particular velocity component at sky position j, i represents all nearby sky positions to be convolved, $f(\theta_{i,j})$ represents the beam response function for angular distance θ between points i and j, and $N_{i,comp}^{^{13}CO}$ represents the corresponding ^{13}CO column density for a particular component at position i. For comparison with HI column densities, the H_2 column densities are similarly convolved without the mass weighting factor.

7. Having estimates of the temperature, central velocity, and linewidth for each HINSA component we can, for any value of the optical depth, remove the HINSA absorption to obtain the background emission using equation 2.1. Since their true ordering along the line of sight is not known, as a matter of definition velocity components with the highest positive velocities are taken to be the most distant.

8. Finally we search for those values of τ_0 and σ_H which minimize the value of equation 2.8 to arrive at our solutions.

BIBLIOGRAPHY

[Alves et al. (2001)] Alves, J.; Lada, C. & Lada, E. 2001, Seeing the Light Through the Dark, The Messenger, 103(1), 15-20

[Arquilla & Goldsmith (1985)] Arquilla, R. & Goldsmith, P. F. 1985, Density Distributions in Dark Clouds, Astrophysical Journal, 297, 436-454

[Ballesteros-Paredes et al. (2011)] Ballesteros-Paredes, J., Vazquez-Semadeni, E., Gazol, A., Hartmann, L.W., Heitsch, F., & Colin, P. 2011, Gravity or turbulence? - II. Evolving column density probability distribution functions in molecular clouds, MNRAS 416, 1436-1442

[Bates (1951)] Bates, D.R. 1961, MNRAS, 111, 303B

[Batrla et al. (1981)] Batrla, W., Wilson, T. L., & Rahe, J. 1981, A&A, 96, 202

[Bok & McCarthy (1974)] Bok, B. J., & McCarthy, C. C. 1974, AJ, 79, 42

[Bonnor, W.B. (1956)] Bonnor, W.B. 1956, Boyle's Law and Gravitational Instability, MNRAS 116, 351

[Bowers et al. (1980)] Bowers, P. F., Kerr, F. J., & Hawarden, T. G. 1980, ApJ, 241, 183

[Brunken et al. (2014)] Brunken, S. et al. 2014, Nature, 516, 219

[Chapman et al. (2009)] Chapman, Nicholas L.; Mundy, Lee G.; Lai, Shih-Ping; Evans, Neal J., II 2009, The Mid-Infrared Extinction Law in the Ophiuchus, Perseus, and Serpens Molecular Clouds, Astrophysical Journal, 690(1), 496-511

[Chini (1981)] Chini, R., A&A, 99, 346

[Clark (1986)] Clark, F. O. 1986, A&A, 164, L19

[Dame & Thaddeus (1985)] Dame, T. M., & Thaddeus, P. 1985, ApJ, 297, 751

[Dapp & Basu (2009)] Dapp, W.B., Basu, S. 2009, An analytic column density profile to fit prestellar cores, MNRAS 395, 1092-1098

[Ebert, R. (1955)] Ebert, R. 1955, Uber die Verdichtung von H I-Gebieten. Mit 5 Textabbildungen, Zeitschrift fur Astrophysik, 37, 217

[Elias (1978)] Elias, J. 1978, ApJ, 224, 453

[Evans et al. (2001)] Evans, Neal J., II, Rawlings, Jonathan M. C., Shirley, Yancy L. & Mundy, Lee G. 2001, Tracing the Mass during Low-Mass Star Formation II: Modeling the Submillimeter Emission from Preprotostellar Cores, The Astrophysical Journal, 557(1), 193-208

[Feldt & Wendker (1993)] Feldt, C., & Wendker, H. J. 1993, A&A, 100, 287

[Felli et al. (1992)] Felli, M., Palagi, F., & Tofani, G. 1992, A&A, 225, 293

[Froebrich et al. (2007)] Froebrich, D., Murphy, G. C., Smith, M. D., Walsh, J., & Del Burgo, C. 2007, A large-scale extinction map of the Galactic Anticentre from 2MASS, MNRAS, 378(4), 1447-1460

[Froebrich & Rowles (2010)] Froebrich, D., & Rowles, J. 2010, The structure of molecular clouds - II. Column density and mass distributions, MNRAS, 406(2), 1350-1357

[Garwood & Dickey (1989)] Garwood, R. W., & Dickey, J. M. ApJ, 338, 841

[Garzoli & Varsavsky (1966)] Garzoli, S. L., & Varsavsky, C.M. 1966, ApJ, 145, 79

[Gibson et al. (2000)] Gibson, S. J., Taylor, A. R., Higgs, L. A., & Dewdney, P. E. 2000, ApJ, 540, 841

[Goldsmith & Li (2005)] Goldsmith, P. F., & Li, D. 2005,ApJ, 622, 938

[Goldsmith et al. (2007)] Goldsmith, P.F., Li, D., & Krco, M. 2007, ApJ, 654, 273

[Goodman et al. (2009)] Goodman, A. A., Pineda, J. E., Schnee, S. L. 2009, The True Column Density Distribution in Star-Forming Molecular Clouds, The Astrophysical Journal, 692(1), 91-103

[Heiles (1969)] Heiles, C. 1969, ApJ, 156, 493

[Heiles & Gordon (1975)] Heiles, C., & Gordon, M. A. 1975, ApJ, 199, 361

[Heiles et al. (1988)] Heiles, C., 1988, ApJ, 324, 321

[Herbst & Warner (1981)] Herbst, W, & Warner, J.W., 1981, AJ, 86, 885H

[Hilton & Lahulla (1995)] Hilton, J., Lahulla, J.F. 1995, A&AS, 113, 325H

[Hollenbach & Salpeter (1971)] Hollenbach, D., & Salpeter, E.E. 1971 ApJ, 163, 155H

[Jackson et al. (2002)] Jackson, J. M., Bania, T. M., Simon, R., Kolpak, M. A., Clemens, D. P., & Heyer, M. 2002, ApJ, 566, L81

[Kainulainen et al. (2009)] Kainulainen, J., Beuther, H., Henning, T., Plume, R. 2009, Probing the evolution of molecular cloud structure. From quiescence to birth, Astronomy & Astrophysics, 508(3), L35-L38

[Kavars et al. (2003)] Kavars, D. W., Dickey, J. M., McClure-Griffiths, N. M., Gaensler, B. M., & Green, A. J. 2003, ApJ, 598, 1048

[Kavars et al. (2005)] Kavars, D. W., Dickey, J. M., McClure-Griffiths, N. M., Gaensler, B. M., & Green, A. J. 2005, ApJ, 626, 887

[Kim & Hong (2002)] Kim, H.G., Hong, S.S. 2002, ApJ, 567, 376

[Klessen (2000)] Klessen, R.S. 2000, One-Point Probability Distribution Functions of Supersonic Turbulent Flows in Self-gravitating Media, The Astrophysical Journal, 535(2), 869-886

[Knapp (1974)] Knapp, G.R. 1974, AJ, 79, 527

[Knapp (1975)] Knapp, G.R. 1975, AJ, 80, 111

[Kolpak et al. (2002)] Kolpak, M. A., Jackson, J. M., Bania, T. M., & Dickey, J. M. 2002, ApJ, 578, 868

[Krco et al. (2008)] Krco, M., Goldsmith, P.F., Brown, R.L., & Li, D. 2008, ApJ, 689, 276

[Krco & Goldsmith (2010)] Krco, M., & Goldsmith, P.F. 2010, ApJ, 724, 1402

[Krco & Goldsmith (2014)] Krco, M., & Goldsmith, P.F. 2014, in publication

[Kun et al. (1994)] Kun, M., Obayashi, A., Sato, F., Yonekura, Y., Fukui, Y., Balazs, L.G., Abraham, P., Szabadoc, L., & Kelemen, J. 1994, A&A, 292, 249K

[Latter & Black (1991)] Latter, W. B., & Black, J.H. 1991, ApJ, 372, 161L

[Lee & Myers (1999)] Lee, C.W., Myers, P.C. 1999, ApJ, 123, 233S

[Leung et al. (1982)] Leung, C.M., Kutner, M.L., & Mead, K.N. 1982, /apj, 262, 583

[Li & Goldsmith (2003)] Li, D., & Goldsmith, P. F. 2003, ApJ, 585, 823

[Li et al. (2004)] Li, P.S., Norman, M.L., Mac Low, M., Heitsch, F. 2004, The Formation of Self-Gravitating Cores in Turbulent Magnetized Clouds, The Astrophysical Journal, 605(2), 800-818

[Lindblad et al. (1973)] Lindblad, P. O., Grape, K., Sandqvist, A., & Schober, J. 1973, A&A, 24, 309

[Liu et al. (2012)] Liu, T.; Wu, Y. & Zhang, H. 2012, Molecular Environments of 51 Planck Cold Clumps in the Orion Complex, The Astrophysical Journal Supplement Series, 202(1), 4

[Lombardi & Alves (2001)] Lombardi, M.; Alves, J. 2001, Mapping the Interstellar Dust with Near-Infrared Observations: An Optimized Multi-Band Technique, Astronomy and Astrophysics, 377, 1023-1023

[Lynds (1962)] Lynds, B.T., , 7, 1

[McCutcheon et al. (1978)] McCutcheon, W. H., Shuter, W. L. H., & Booth, R. S. 1978, MNRAS, 185, 755

[McCutcheon et al. (1986)] McCutcheon, W.H., Vrba, F.J., Dickman, R.L., & Clemens, D.P. 1986, ApJ, 309, 619M

[Minn (1981)] Minn, Y. K. 1981, A&A, 103, 269

[Montgomery et al. (1995)] Montgomery, A. S., Bates, B., & Kemp, S. N. 1995, Irish Astronomical Journal, 22, 186

[Myers et al. (1978)] Myers, P. C., Ho, P. T. P., Schneps, M. H., Chin, G., Pankonin, V., & Winnberg, A. 1978, ApJ, 220, 864

[Norlund & Padoan (1999)] Norlund, A.K., Padoan, P. 1999, in Interstellar Turbulence, ed. J. Franco & A. Carraminana (Cambridge: Cambridge University Press), 218

[Nozawa et al. (1991)] Nozawa, S., Mizuno, A., Teshima, Y., H.Ogawa, & Y. Fukui 1991, ApJ, 77, 647

[Ostriker, Stone, & Gammie (2001)] Ostriker, E.C., Stone, J.M., Gammie, C.F. 2001, Density, Velocity, and Magnetic Field Structure in Turbulent Molecular Cloud Models, The Astrophysical Journal, 546(2), 980-1005

[Pagani et al. (2013)] Pagani, L. et al. 2013, A&A, 551, A38

[Pineda et al. (2010)] Pineda, J. L.; Goldsmith, P. F.; Chapman, N.; Snell, R. L.; Li, D.; Cambresy, L. & Brunt, C. 2010, the Relation Between Gas and Dust in the Taurus Molecular Cloud, Astrophysical Journal, 721(1), 686 - 708

[Reich et al. (1997)] Reich, P., Reich, W., & Fuerst, E. 1997, A&A, Suppl. 126, 413

[Reich & Reich (1986)] Reich, P., & Reich, W. 1986, A&A, 63, 205

[Ridge et al. (2006)] Ridge, N. A.; Di Francesco, J.; Kirk, H. et al 2006, The COMPLETE Survey of Star-Forming Regions: Phase I Data, The Astronomical Journal, 131(6), 2921-2933

[Schmidt (1975)] Schmidt, E.G. 1975, MNRAS, 172, 401

[Shu (1973)] Shu, F. H., IAU Symposium 52, Interstellar Dust and Related Topics, 257

[Shuter et al. (1997)] Shuter, W. L. H., Dickman, R. L., & Klatt, C. 1987, ApJ, 322L, 103

[Simonson & van Someren Greve (1976)] Simonson, S.C. III, van Someren Greve, H.W. 1976, A&A, 49, 343S

[Skrutskie et al. (2006)] M.F. Skrutskie; R.M. Cutri; R. Stiening; M.D. Weinberg; S. Schneider; J.M. Carpenter; C. Beichman; R. Capps; T. Chester; J. Elias; J. Huchra; J. Liebert; C. Lonsdale; D.G. Monet; S. Price; P. Seitzer; T. Jarrett; J.D. Kirkpatrick; J. Gizis; E. Howard; T. Evans; J. Fowler; L. Fullmer; R. Hurt; R. Light; E.L. Kopan; K.A. Marsh; H.L. McCallon; R. Tam; S. Van Dyk; and S. Wheelock, 2006, Astrophysical Journal, 131, 1163

[Snell (1981)] Snell, R. L. 1981, ApJS, 45,121

[Solomon & Werner (1971)] Solomon, P. M. & Werner, M. W. 1971, ApJ, 165, 41

[Stahler & Palla (2004)] Stahler, Steven, W. & Palla, Francesco 2004, The Formation of Stars, (1st ed.;KGaA, Weinheim:WILEY - VCH Verlag GmbH & Co)

[Straizys et al. (1992)] Straizys, V., Cernis, K., Kazlauskas, A., & Meistas, E. 1992, Baltic Astron., 1, 149

[Tassis et al. (2010)] Tassis, K., Christie, D. A., Urban, A., Pineda, J. L., Mouschovias, T. Ch., Yorke, H. W., Martel, H. 2010, Do lognormal column-density distributions in molecular clouds imply supersonic turbulence?, MNRAS, 408(2), 1089-1094

[Tachihara et al. (2000)] Tachihara, K., Abe, R., Onishi, T., Mizuno, A., Fukui, Y. 2000, PASJ, 52, 1147

[Teixeira et al. (2005)] Teixeira, Paula S.; Lada, Charles J. & Alves, Joao F. 2005, From Dusty Filaments to Cores to Stars: An Infrared Extinction Study of Lupus 3, The Astrophysical Journal, 629(1), 276-287

[Uyaniker et al. (1999)] Uyaniker, B., Fuerst, E., Reich, W., Reich, P., & Wielebinski, R., 1999, A&A, Suppl. 138, 31

[van der Werf et al. (1988)] van der Werf, P. P., Goss, W. M., & van den Bout, P. A. 1988, A&A, 201, 311

[Wilson & Minn (1977)] Wilson, T. L., & Minn, Y. K. 1977, A&A, 54, 933

[Wong et al. (2008)] Wong, T., Ladd, E. F., Brisbin, D., Burton, M. G., Bains, I., Cunningham, M. R., Lo, N., Jones, P. A., Thomas, K. L., Longmore, S. N., Vigan, A., Mookerjea, B., Kramer, C., Fukui, Y., Kawamura, A. 2008, Molecular line mapping of the giant molecular cloud associated with RCW 106 - II. Column density and dynamical state of the clumps, MNRAS, 386(2) 1069-1084

[Wu et al. (2012)] Wu, Y.; Liu, T.; Meng, F.; Li, D.; Qin, S.-L. & Ju, B.-G. 2012, Gas Emissions in Planck Cold Dust Clumps: a Survey of the J = 1-0 Transitions of ^{12}CO, ^{13}CO, and $C^{18}O$. The Astrophysical Journal, 756(1), 76